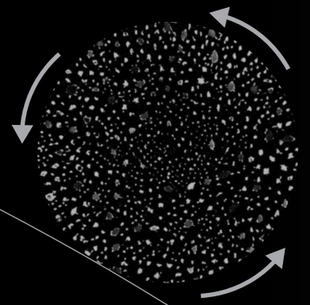
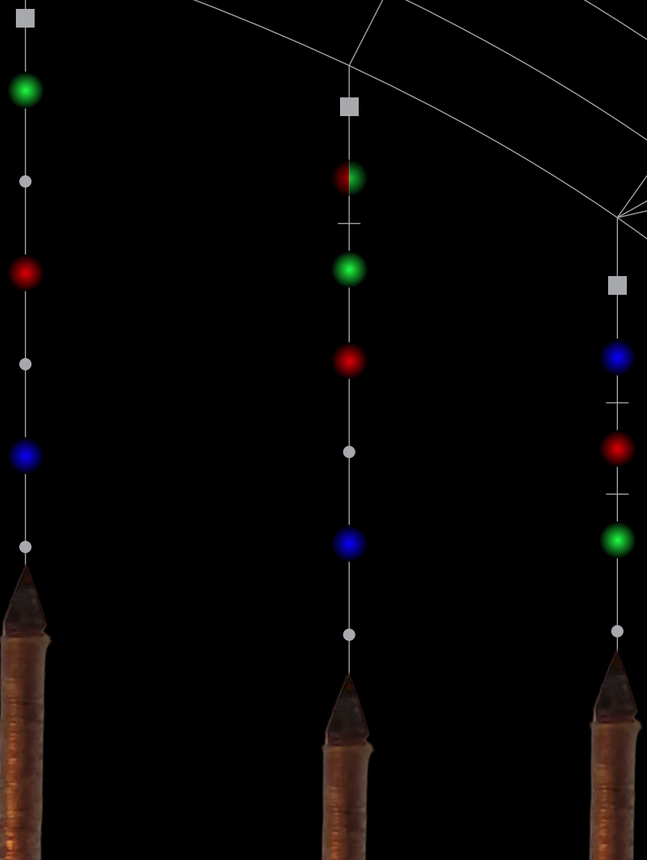
UNIVERSITY OF TWENTE.



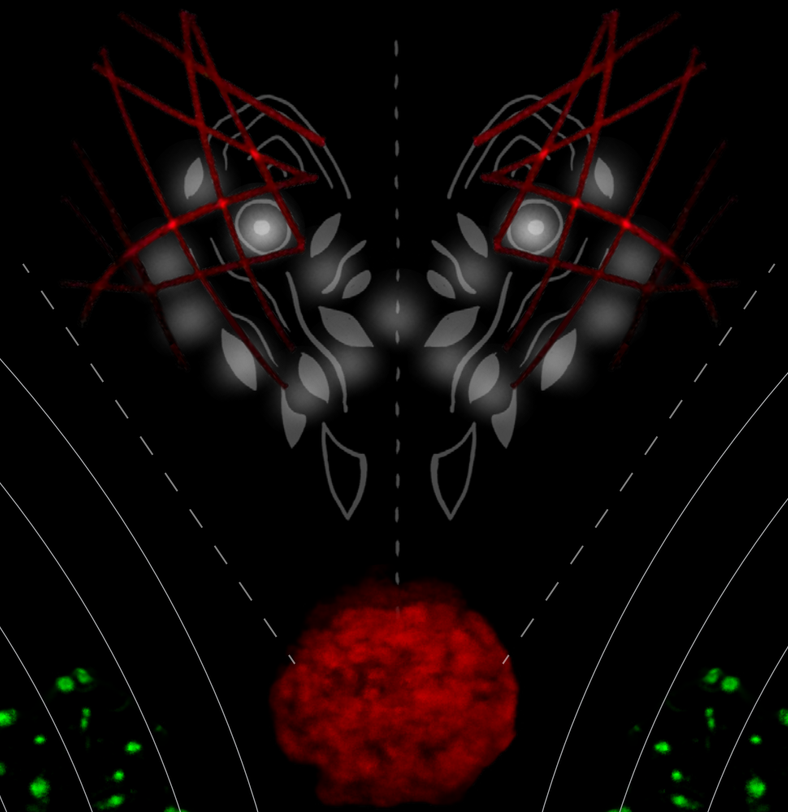


MAGNETS AND LIGHT: A JOURNEY INTO THE MICROWORLD

JUAN HUAROTO SEVILLA

MAGNETS AND LIGHT

A JOURNEY INTO THE MICROWORLD

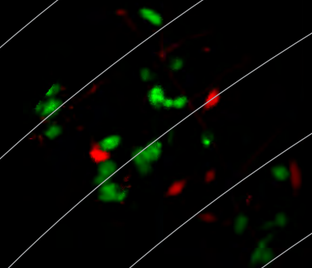


JUAN J. J. HUAROTO SEVILLA

Invitation

I cordially invite you to attend the public defense of my doctoral dissertation entitled

MAGNETS AND LIGHT: A JOURNEY INTO THE MICROWORLD



on the 16th of november 2026
at 14:30
in the Prof. dr. G. Berkhoffzaal,
the Waaier, University of Twente

Juan J. J. Huaroto Sevilla
j.j.j.huarotosevilla@utwente.nl



Paranymphs:
Yu-Hsiang Lin
Carlos Olaya

MAGNETS AND LIGHT

A JOURNEY INTO THE MICROWORLD

Juan Julian Jesus Huaroto Sevilla

MAGNETS AND LIGHT

A JOURNEY INTO THE MICROWORLD

DOCTORAL THESIS

to obtain
the degree of doctor at the University of Twente,
on the authority of the Rector Magnificus,
prof. dr. ir. A. Veldkamp
on account of the decision of the Doctorate Board,
to be publicly defended
on Monday the 16th of November 2026 at 14:30 hours

by

Juan Julian Jesus Huaroto Sevilla

born on the 30th of May, 1992
in Trujillo, La Libertad, Peru

This doctoral thesis has been approved by:

Promotors
prof. dr. S. Misra
prof. Dr.-Ing. J. Arens

Copromotor
prof. dr. ir. G.R.B.E. Römer

Cover design: Juan J. J. Huaroto Sevilla
Printed by: Ipskamp Printing, Enschede
ISBN (print): 978-90-365-7193-7
ISBN (digital): 978-90-365-7205-7
DOI: https://doi.org/10.3990/1.9789036572057

©2026 Juan Julian Jesus Huaroto Sevilla, The Netherlands. All rights reserved. No parts of this thesis may be reproduced, stored in a retrieval system or transmitted in any form or by any means without permission of the author. Alle rechten voorbehouden. Niets uit deze uitgave mag worden vermenigvuldigd, in enige vorm of op enige wijze, zonder voorafgaande schriftelijke toestemming van de auteur.

GRADUATION COMMITTEE:

Chair/Secretary:	prof. dr. ir. H.F.J.M. Koopman *University of Twente*
Promotors:	prof. dr. S. Misra *University of Twente*
	prof. Dr.-Ing. J. Arens *University of Twente*
Copromotor:	prof. dr. ir. G.R.B.E. Römer *University of Twente*
Committee Members:	prof. dr. ir. H.L. Offerhaus *University of Twente*
	prof. dr. J.M.J. den Toonder *Eindhoven University of Technology*
	prof. dr. P. Lambert *Université Libre de Bruxelles*
	prof. dr. S. Manohar *University of Twente*

This work is part of the research project **MAESTRO** funded by the European Research Council (ERC) under the European Union's Horizon 2020 Research and Innovation programme, grant number 866494.



MAESTRO



Funded by
the European Union



European Research Council

Established by the European Commission

Dedicated to the memory of land defenders
and to every act of resistance that rises against hegemony.

May knowledge always serve liberation,
and never submission.

Summary

Microrobotics explores the use of untethered micro-agents at sites that conventional instruments cannot easily reach. Potential applications include targeted therapy, tissue sampling, and assisted reproduction. However, guiding these miniaturized agents requires control of their motion and information about their position and interactions with biological surroundings. This thesis pairs magnetic actuation with fluorescence imaging to address these complementary needs.

Magnetic fields penetrate biological tissue and exert forces and torques on magnetically responsive agents without physical contact. However, external electromagnetic platforms can have large footprints and high power requirements. Bringing miniaturized magnetic sources close to the agents offers a route to localized actuation with compact hardware and lower power requirements. The actuation problem also extends to the agents themselves: individual agents have limited force and payload capacities, while coordinated collectives can perform tasks beyond the capabilities of a single agent.

Fluorescence imaging uses fluorescent labels to distinguish micro-agents and selected biological structures by color. Following their motion and interactions requires sufficient imaging speed, but multicolor imaging often separates fluorescent signals by acquiring channels sequentially. As more channels are added, the effective frame rate decreases. Extending observation through biological tissue introduces light scattering, which limits imaging depth and contrast. For agents in confined anatomical regions, observation also depends on bringing the imaging optics close to where they operate, beyond the practical reach of conventional benchtop microscopes.

This thesis develops magnetic actuation and fluorescence imaging strategies, progressing toward their integration for image-guided microrobotics in biologically relevant environments. The thesis is structured into three parts and eight chapters. Magnetic actuation is developed in **Part I**, and its integration with fluorescence imaging is pursued across **Part II** and culminates in **Chapter 6**. The three parts are titled after songs from the classic rock, progressive rock, and post-rock genres, used as reflective markers for each stage of the thesis: magnetic actuation, fluorescence imaging, and the tran-

sition toward future directions.

Chapter 1 introduces the general concepts and research objectives that guide the thesis. **Part I**, ***Invisible touch***, focuses on magnetic actuation. **Chapter 2** introduces local magnetic actuation using miniaturized electromagnets. This approach offers a compact, low-power alternative to bulky external platforms. **Chapter 3** turns to the collective behavior of magnetic micro-agents. Here, non-uniform magnetic fields drive coordinated dynamics in groups of magnetically responsive microparticles.

Part II, ***Any colour you like***, addresses fluorescence imaging for microrobotics, with each chapter demonstrating its contribution in the context of magnetically actuated micro-agents. **Chapter 4** presents a deep learning framework that improves the temporal resolution of multicolor fluorescence microscopy, enabling simultaneous real-time observation of micro-agents, biological targets, and their surroundings. **Chapter 5** introduces two-photon microscopy as a tool for visualizing micro-agents through biological tissue, using a near-infrared femtosecond pulsed laser for localized excitation and reduced scattering. **Chapter 6** extends fluorescence imaging toward in situ operation by developing a two-photon endomicroscopy system for real-time imaging of magnetic micro-agents in *ex vivo* tissue specimens and 3D multicellular aggregates.

Part III, ***The end of the beginning***, closes the thesis with synthesis and outlook. **Chapter 7** revisits the findings across **Chapters 2–6** and traces the convergence of magnetic actuation and fluorescence imaging toward image-guided microrobotics. **Chapter 8** discusses the steps still needed to bring this approach closer to biomedical practice.

Samenvatting

Microrobotica onderzoekt de inzet van ongebonden micro-agenten op plaatsen die met conventionele instrumenten moeilijk te bereiken zijn. Mogelijke toepassingen zijn gerichte therapie, weefselafname en geassisteerde voortplanting. Het sturen van deze geminiaturiseerde agenten vereist echter controle over hun beweging en informatie over hun positie en interacties met de biologische omgeving. Dit proefschrift combineert magnetische aansturing met fluorescentiebeeldvorming om aan deze complementaire vereisten te voldoen.

Magnetische velden dringen door biologisch weefsel heen en oefenen zonder direct contact krachten en koppels uit op magnetisch responsieve agenten. Externe elektromagnetische platforms kunnen echter omvangrijk zijn en een hoog vermogen vereisen. Door geminiaturiseerde magnetische bronnen dicht bij de agenten te plaatsen, kan lokale aansturing worden gerealiseerd met compacte hardware en een lager benodigd vermogen. Het aansturingsvraagstuk betreft ook de agenten zelf: individuele agenten kunnen slechts beperkte krachten uitoefenen en een beperkte lading dragen, terwijl gecoördineerde collectieven taken kunnen uitvoeren die buiten de mogelijkheden van een enkele agent liggen.

Fluorescentiebeeldvorming gebruikt fluorescerende labels om micro-agenten en geselecteerde biologische structuren op kleur te onderscheiden. Om hun bewegingen en interacties te volgen, is een voldoende hoge beeldsnelheid nodig. Bij meerkleurenbeeldvorming worden fluorescentiesignalen echter vaak gescheiden door de kanalen sequentieel op te nemen. Naarmate meer kanalen worden toegevoegd, neemt de effectieve beeldsnelheid af. Bij beeldvorming door biologisch weefsel heen beperkt lichtverstrooiing bovendien de beeldvormingsdiepte en het contrast. Om agenten in besloten anatomische gebieden te observeren, moet de beeldvormingsoptiek daarnaast dicht bij de agenten worden gebracht. Dergelijke gebieden liggen buiten het praktische bereik van conventionele laboratoriummicroscopen.

Dit proefschrift ontwikkelt strategieën voor magnetische aansturing en fluorescentiebeeldvorming en werkt toe naar hun integratie voor beeldgeleide microrobotica in biologisch relevante omgevingen. Het proefschrift is gestructureerd in drie delen en acht hoofdstukken. Magnetische aansturing wordt

ontwikkeld in **Deel I**, en de integratie ervan met fluorescentiebeeldvorming wordt in **Deel II** uitgewerkt en culmineert in **Hoofdstuk 6**. De drie delen zijn vernoemd naar nummers uit de genres classic rock, progressive rock en post-rock, die als beschouwende markeringen dienen voor elke fase van het proefschrift: magnetische aansturing, fluorescentiebeeldvorming en de overgang naar toekomstige richtingen.

Hoofdstuk 1 introduceert de algemene concepten en onderzoeksdoelstellingen die richting geven aan het proefschrift. **Deel I**, ***Invisible touch***, richt zich op magnetische aansturing. **Hoofdstuk 2** introduceert lokale magnetische aansturing met behulp van geminiaturiseerde elektromagneten. Deze benadering biedt een compact, energiezuinig alternatief voor omvangrijke externe platforms. **Hoofdstuk 3** gaat in op het collectieve gedrag van magnetische micro-agenten. Hier sturen niet-uniforme magnetische velden gecoördineerde dynamica aan in groepen magnetisch responsieve microdeeltjes.

Deel II, ***Any colour you like***, behandelt fluorescentiebeeldvorming voor de microrobotica, waarbij elk hoofdstuk zijn bijdrage demonstreert in de context van magnetisch aangestuurde micro-agenten. **Hoofdstuk 4** presenteert een deep learning-raamwerk dat de temporele resolutie van meerkleurenfluorescentiemicroscopie verbetert en de gelijktijdige real-time observatie van micro-agenten, biologische doelwitten en de omgeving mogelijk maakt. **Hoofdstuk 5** introduceert tweefotonmicroscopie als hulpmiddel om micro-agenten door biologisch weefsel heen zichtbaar te maken, met behulp van een nabij-infrarode femtoseconde-pulslaser voor gelokaliseerde excitatie en verminderde verstrooiing. **Hoofdstuk 6** breidt fluorescentiebeeldvorming uit naar toepassing in situ door een tweefoton-endomicroscopiesysteem te ontwikkelen voor real-time beeldvorming van magnetische micro-agenten in *ex vivo* weefselmonsters en 3D multicellulaire aggregaten.

Deel III, ***The end of the beginning***, sluit het proefschrift af met synthese en vooruitblik. **Hoofdstuk 7** blikt terug op de bevindingen uit **Hoofdstukken 2–6** en traceert de convergentie van magnetische aansturing en fluorescentiebeeldvorming richting beeldgeleide microrobotica. **Hoofdstuk 8** bespreekt de stappen die nog nodig zijn om deze benadering dichter bij de biomedische praktijk te brengen.

Scientific output

This thesis is based on the following six peer-reviewed journal articles:

1. **J. J. Huaroto**, M. Richter, M. Malafaia, J. Kim, C-S. Kim, J-O. Park, J. Sikorski, and S. Misra. *MagNeed – Needle-shaped electromagnets for localized actuation within compact workspaces*, Robotics and Automation Letters, vol. 8, no. 6, pp. 3908–3915, 2023.
   DOI: 10.1109/LRA.2023.3273519.
   (Part I – Chapter 2 in this thesis).

2. **J. J. Huaroto**, F. N. Piñan Basualdo, D. L. Roos Ariëns, and S. Misra. *Non-uniform magnetic fields for collective behavior of self-assembled magnetic pillars*, Swarm Intelligence, vol. 19, no. 4, pp. 317-332, 2025.
   DOI: 10.1007/s11721-024-00240-z.
   (Part I – Chapter 3 in this thesis).

3. **J. J. Huaroto**, Y. Jin, N. Roy, and S. Misra. *Real-time multi-color fluorescence microscopy via cross-channel acquisition and deep-learning-based inference*, Advanced Intelligent Discovery, e202500176, 2026 [In Press].
   DOI: 10.1002/aidi.202500176.
   (Part II – Chapter 4 in this thesis).

4. **J. J. Huaroto**, L. Capuano, M. Kaya, I. Hlukhau, F. Assayag, S. Mohanty, G.-w. Römer, and S. Misra. *Two-photon microscopy for microrobotics: Visualization of micro-agents below fixed tissue*, PLoS ONE, vol. 18, no. 8, pp. e0289725, 2023.
   DOI: 10.1371/journal.pone.0289725.
   (Part II – Chapter 5 in this thesis).

5. **J. J. Huaroto**, G.-w. Römer, Ivo M. Vellekoop, and S. Misra. *Two-photon endomicroscopy for image-guided magnetic micro-agents*, Small, vol. 22, no. 56, pp. e75051, 2026.
   DOI: 10.1002/smll.75051.
   (Part II – Chapter 6 in this thesis).

6. **J. J. Huaroto** and S. Misra. *Size and illumination matters: Local magnetic actuation and fluorescence imaging for microrobotics*, Journal of the Indian Institute of Science, vol. 104, pp. 745–763, 2024. DOI: 10.1007/s41745-024-00453-5.
(Chapter 1 and Part III – Chapter 8 in this thesis).

The author also co-authored the following peer-reviewed journal article during the doctoral period:

- T. L. Thomas, J. Bos, **J. J. Huaroto**, V. Kalpathy Venkiteswaran, and S. Misra. *A magnetically actuated variable stiffness manipulator based on deployable shape memory polymer springs*, Advanced Intelligent Systems, vol. 6, no. 2, pp. 2200465, 2024.
DOI: 10.1002/aisy.202200465.

Contents

Summary iii

Samenvatting v

Scientific output vii

1 Introduction: Beyond the visible 1
- 1.1 The microworld . . . 1
- 1.2 Microrobotics . . . 2
- 1.3 Image-guided microrobotics . . . 3
  - 1.3.1 Magnetic actuation . . . 6
  - 1.3.2 Fluorescence imaging . . . 9
- 1.4 Research objectives . . . 13
- 1.5 Thesis outline . . . 16

Part I: Invisible touch 19

2 Miniaturized electromagnets for local actuation 21
- 2.1 Introduction . . . 22
- 2.2 System overview . . . 23
  - 2.2.1 Design of MagNeed . . . 23
    - 2.2.1.1 Electromagnetic actuation strategy . . . 25
    - 2.2.1.2 Needle-shaped electromagnets . . . 26
    - 2.2.1.3 Current-to-field map . . . 29
    - 2.2.1.4 Thermal analysis . . . 31
    - 2.2.1.5 Final design . . . 32
  - 2.2.2 Framework . . . 32
  - 2.2.3 Model validation . . . 34
- 2.3 Experimental demonstrations . . . 34
  - 2.3.1 Localized trapping of a milli-sized agent . . . 36
  - 2.3.2 Localized actuation of a milli-sized agent . . . 37
- 2.4 Conclusions and future work . . . 38

3 Collective behavior of magnetic microparticles **41**
3.1 Introduction 42
3.2 Results and discussions 44
3.2.1 Static magnetic self-assembly 44
3.2.2 Dynamic collective behavior 47
3.2.3 Object manipulation 51
3.2.4 Upstream/downstream locomotion 53
3.2.5 Independent actuation of magnetic pillar clusters . . 55
3.3 Conclusions 57
3.4 Experimental section 57

Part II: Any colour you like **63**

4 Real-time multicolor fluorescence microscopy **65**
4.1 Introduction 66
4.2 Results and discussions 68
4.2.1 Cross-channel acquisition and deep-learning-based inference 69
4.2.2 Real-time imaging of micro-agent-spheroid interactions 71
4.2.3 Channel reconstruction assessment 73
4.2.4 Evaluation 75
4.2.5 Fluorescence-guided real-time tracking 78
4.2.6 Three-color fluorescence microscopy 80
4.2.7 Performance with morphology-matched spheroids . . 83
4.3 Conclusions 86
4.4 Experimental section 86

5 Two-photon microscopy for microrobotics **103**
5.1 Introduction 104
5.2 Results 107
5.2.1 Spectrum analysis of fluorescent micro-agents 107
5.2.2 Two-photon microscopy of micro-agents 108
5.2.3 Laser-tissue interaction 109
5.2.4 Visualization of micro-agents through biological tissue 111
5.2.5 Continuous visualization of magnetic electrospun fibers 114
5.3 Conclusion 116
5.4 Experimental section 117

6 Two-photon endomicroscopy for image-guided magnetic microrobotics **123**
6.1 Introduction 124
6.2 Results and discussions 126
6.2.1 Endomicroscopy system 126
6.2.2 Engineering and characterization of electrospun precursor fibers 131
6.2.3 Real-time two-photon endomicroscopy of magnetic micro-agents 133
6.2.4 Micro-agent detection through biological tissue . . . 136
6.2.5 Image-guided re-centering of a HeLa cell spheroid during micro-agent interaction 140
6.3 Conclusions and future work 142
6.4 Experimental section 143

Part III: The end of the beginning **167**

7 Discussion and conclusions **169**

8 Outlook **177**
8.1 Toward living biological environments 177
8.2 Multimodal imaging 178
8.3 Toward endomicrorobotic instruments 178
8.4 Multiscale closed-loop control 180
8.5 Clinical relevance 180

References **183**

Acknowledgments **219**

About the author **227**

CHAPTER 1

Introduction: Beyond the visible

Many medical procedures require acting at specific sites inside the body that conventional instruments cannot easily reach. In therapy, systemic administration distributes a drug throughout the body, but the dose is then limited by toxicity to healthy tissue [1]. Localized therapies instead act on a target region, sparing surrounding tissue and widening the therapeutic window [2]. Similar demands for site-specific access appear in other procedures, such as tissue sampling and assisted reproduction [3], [4]. These procedures take place in deep, confined, or cellular-scale regions, sometimes at scales far below those of ordinary tools, in a "world" too small to access or manipulate directly. This chapter introduces the technological context, objectives, and structure that shape the chapters that follow.

1.1 The microworld

The microworld lies outside ordinary human perception, difficult to access, not because it is far but because it is small: structures below the eye's resolution limit, around 100 micrometers, require specialized instruments to observe [5]. The invention of the microscope extended human vision beyond such natural limits, making this domain accessible to observation [6]. Modern microscopy techniques reveal structures across a wide range of biological and physical scales, from individual atoms and molecules to cells and tissues. Such progress is supported by a diverse set of imaging modalities*, including optical, electron, X-ray, and atomic force microscopy [7]. Among these, optical microscopy is widely used for imaging biological

*In this thesis, modality refers to a technique defined by its underlying physical principle, used either for imaging (e.g., fluorescence microscopy, ultrasound) or for actuation (e.g., magnetic fields, acoustic waves). In Chapter 3, actuation modality refers more specifically to a magnetic field configuration that produces a reproducible collective response of self-assembled magnetic pillars (Table 3.1). The tasks enabled by these responses, such as object manipulation and locomotion, are referred to as functionalities.

samples due to its high temporal resolution, specificity, and compatibility with living systems [8]. Yet optical microscopy remains constrained by the available contrast mechanisms, diffraction-limited spatial resolution, and the requirement for a direct line of sight to the sample. In biological samples, scattering and absorption restrict imaging to thin, optically accessible regions, leaving deeper or confined sites unresolved [9]. Addressing these limitations has driven continuous advances in imaging technology, including super-resolution microscopy, multi-photon imaging, computational imaging, and artificial intelligence-assisted methods [10]. But observation is only one objective; understanding the microworld has increasingly motivated efforts to act within it. As with the exploration of space and the deep sea, observation has historically preceded action.

1.2 Microrobotics

The transition from observing the microworld to acting within it motivates the development of microrobotics as the field dedicated to the design and operation of robotic systems at micrometer scales [11]. From untethered micro-agents[†] and miniaturized devices to robotic platforms for microscale manipulation [12]–[14], microrobotics bridges robotics and the microworld, enabling interaction with structures that conventional instruments cannot reach. While microrobotics has developed rapidly over recent decades, the aspirations behind the field predate its experimental realization.

Long before microrobotics became experimentally plausible, fiction imagined miniaturized travel through the human body. *Fantastic Voyage* and *Innerspace* are well-known examples [15], [16]. In both narratives, inner biological environments are spaces for exploration and intervention, where technology enables action from within. A related perspective appears in scientific thought: in *There's Plenty of Room at the Bottom*, Richard Feynman draws attention to the small scale as a place of physical and technological

[†]In this thesis, a micro-agent refers to an untethered particle or structure with characteristic dimensions from approximately 1 µm to below 1 mm, which is either responsive to external stimuli (active) or not (passive). The micro-agents used here are functionalized only for actuation and fluorescence imaging. Chapters 2 and 3 also use millimeter-sized objects for proof-of-concept experiments: a 1 mm magnetic bead (milli-sized agent) and a 2 mm glass bead (passive object). In Chapter 4, cell spheroids are referred to as passive biological agents.

possibility [17]. Although this lecture does not describe microrobotics in its present form, it supports the broader idea that meaningful function and control can emerge far below the scale of direct human action.

Advances in microfabrication [18], materials [19], wireless actuation [20], and imaging [21] have since turned these early visions into experimentally validated microrobotic systems. Among these systems, untethered micro-agents have emerged as a subclass capable of navigating without physical connections to external instruments. Conventional instruments, such as catheters, guidewires, and endoscopes, access internal sites through a physical link to an external operator. This link bounds how far the instrument travels, set by its length, stiffness, and the size and tortuosity of the access path. Untethered micro-agents have no such link: their operating range is instead set by their own size and by the extent over which they can be actuated from outside. Recent studies envision these micro-agents for clinical applications such as targeted drug and gene delivery [22], [23], localized chemotherapy [24], [25], tissue sampling [3], [26], and assisted fertilization [4], [27] (Figure 1.1). For these applications, successful implementation depends on the observation and control of micro-agent position, behavior, and interactions with biological environments. Addressing this need is the goal of image-guided microrobotics.

1.3 Image-guided microrobotics

Image-guided microrobotics integrates image-based feedback with the actuation and control of untethered micro-agents. Without imaging, actuation lacks information about the agent's position, behavior, and interaction with its surroundings. Without actuation, imaging remains observational. Integrating the two, therefore, turns untethered microrobotic motion into image-guided navigation and manipulation. This approach uses image-based feedback to inform control decisions about actuation, imaging configuration, sample positioning, or a coordinated combination of these. For example, image-based feedback can guide the actuation system to steer micro-agents toward a target, adjust the imaging system to keep them in view during operation, or reposition the sample to maintain alignment with both the actuation and imaging fields. Figure 1.2 summarizes the image-guided microrobotics framework, including representative actuation and imaging modalities used in the field.

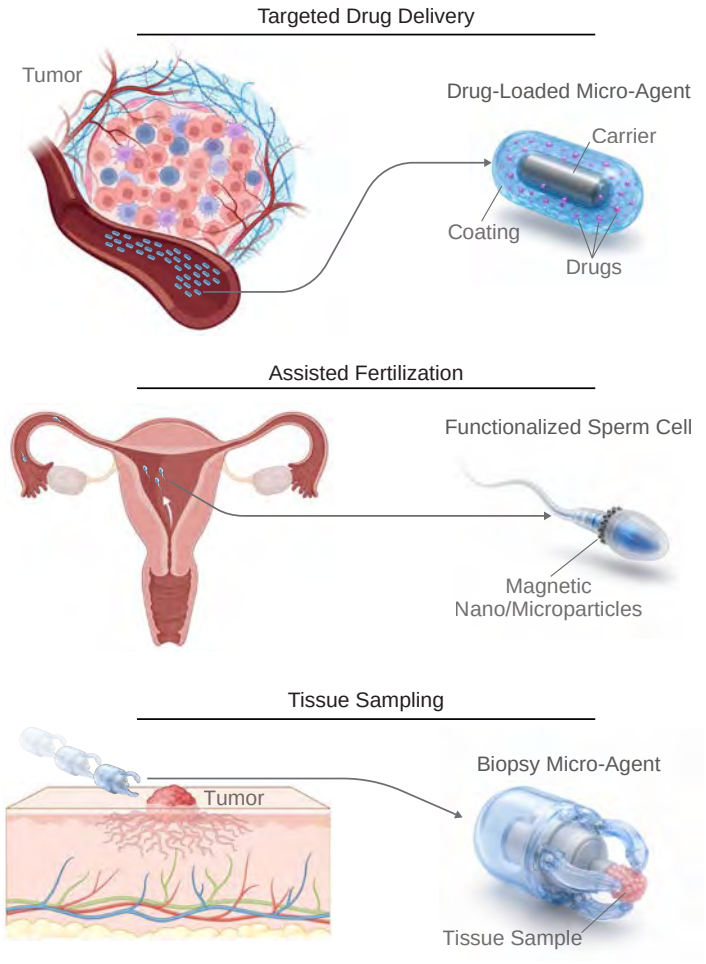


Figure 1.1: Representative clinical applications envisioned for untethered micro-agents. Examples include targeted drug delivery to a tumor microenvironment, assisted fertilization, and biopsy of cancerous tissue. The schematics pair each application with a representative micro-agent design adapted for payload transport, cellular-scale assistance, or tissue sampling. The elements presented in this figure were prepared/generated using BioRender.com and DALL·E 3. All elements were reviewed and edited by the author for scientific accuracy.

The development of image-guided microrobotics has drawn from a wide range of actuation and imaging modalities. On the actuation side, physical principles such as magnetic fields [28], [29], acoustic waves [30], [31], light [32], [33], chemical gradients [34], [35], thermal stimuli [36], [37], and

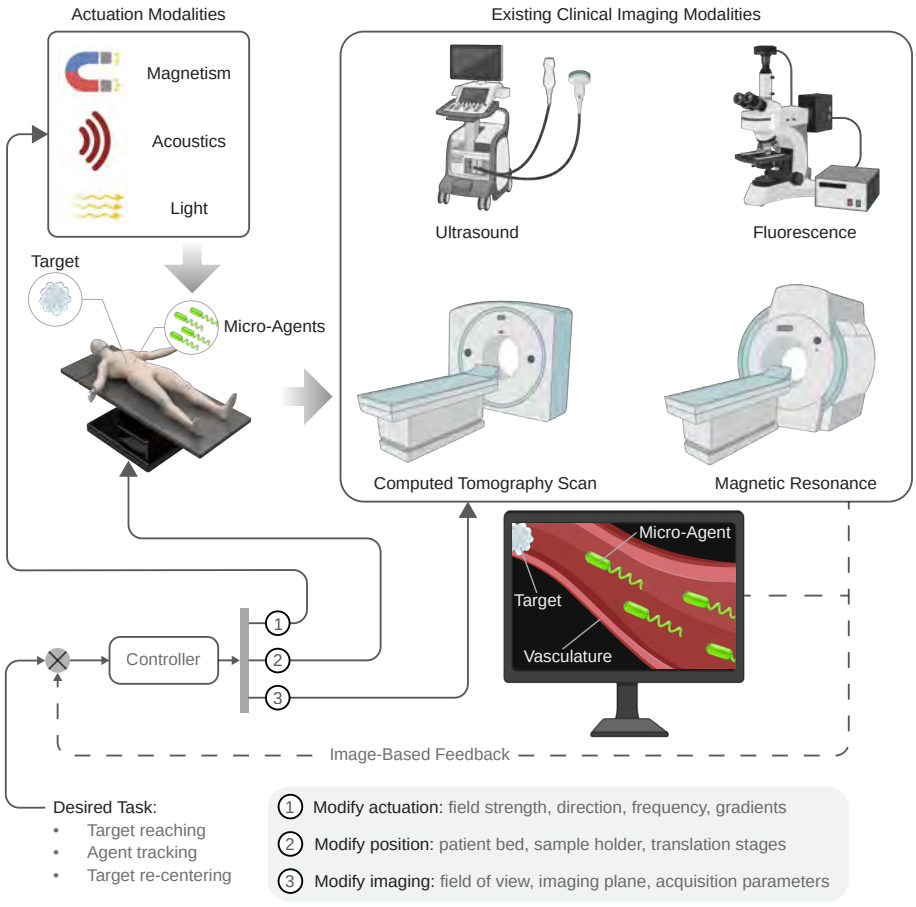


Figure 1.2: Schematic of image-guided microrobotics within the human body. Representative actuation modalities, including magnetism, acoustics, or light, provide external stimuli for micro-agent operation, while imaging modalities, including ultrasound, fluorescence imaging, computed tomography, or magnetic resonance imaging, provide observations of the micro-agents, biological targets, and surrounding structures. Image-based feedback closes the loop by comparing the observed state with the task objective, such as target reaching, agent tracking, or target re-centering. The numbered outputs indicate possible control actions informed by this feedback: (1) modification of actuation parameters, (2) physical positioning, and (3) imaging configuration. These actions may be used individually or in coordinated combinations. The elements presented in this figure were prepared using BioRender.com.

electrical fields [38], [39] have been explored. On the imaging side, both ionizing and non-ionizing modalities have been applied, ranging from X-ray

computed tomography [40] and positron emission tomography [41] to ultrasound [42], magnetic resonance imaging [43], photoacoustic imaging [44], and optical techniques including fluorescence imaging [45], [46]. From this range of modalities, actuation and imaging are chosen deliberately, balancing trade-offs among actuation range, spatial selectivity, imaging resolution, penetration depth, and biological compatibility for the intended application.

In the context of image-guided microrobotics for localized treatment, micro-agent deployment poses two core requirements: (1) the micro-agents must be actuated at a distance, through tissue, without physical links; and (2) the micro-agents, the biological target, and the surrounding tissue must be resolved as separate components. This thesis pairs magnetic actuation with fluorescence imaging to meet these requirements. Magnetic actuation enables remote, biocompatible, and precise control of micro-agents, addressing the first requirement [47]. Fluorescence imaging provides specific, high-contrast visualization of labeled components, addressing the second [48]. Beyond their individual roles, magnetic actuation and fluorescence imaging share a basis in electromagnetic interactions with matter, though they operate in different physical regimes [49], [50]. Low-frequency magnetic fields couple to magnetic micro-agents to exert forces and torques, while optical-frequency fields excite fluorophores to produce image contrast. Prior work pairing magnetic actuation with fluorescence imaging for microrobotics has relied on external actuation platforms and benchtop microscopes. These configurations, however, limit micro-agent deployment in confined or deep regions. This thesis develops each modality and works toward their integration for image-guided microrobotics in biologically relevant environments.

1.3.1 Magnetic actuation

Magnetic actuation relies on the generation of external magnetic fields and gradients that remotely interact with magnetic micro-agents [29], [51]. Formally, a micro-agent carrying a magnetic moment ($\boldsymbol{\mu} \in \mathbb{R}^3$) placed in an external magnetic field ($\mathbf{B} \in \mathbb{R}^3$) experiences a wrench ($\mathbf{W} \in \mathbb{R}^6$) [52]:

$$\mathbf{W} = \begin{bmatrix} \mathbf{F} \\ \mathbf{T} \end{bmatrix} = \begin{bmatrix} \nabla(\boldsymbol{\mu} \cdot \mathbf{B}) \\ \boldsymbol{\mu} \times \mathbf{B} \end{bmatrix}, \tag{1.1}$$

where $\mathbf{F} \in \mathbb{R}^3$ and $\mathbf{T} \in \mathbb{R}^3$ denote the magnetic force and torque, respectively. The magnetic moment can be permanent, as in hard-magnetic agents, or field-induced, as in soft-magnetic agents, for which $\boldsymbol{\mu} = \boldsymbol{\mu}(\mathbf{B})$ up to saturation [53]. In the induced case, a net torque requires that the moment not be collinear with the field, which typically follows from shape or material anisotropy. Spatial gradients in the magnetic field generate a force that contributes to translational motion. The torque tends to align the magnetic moment with the applied field, contributing to rotational motion. Two principal sources are used to generate the fields and gradients (Figure 1.3(A)) [28], [47]. First, in an electromagnet operated within a calibrated, non-saturating regime, the magnetic field at a position ($\mathbf{r} \in \mathbb{R}^3$) can be approximated as linear with respect to the applied current ($I \in \mathbb{R}$) [54]:

$$\mathbf{B}(\mathbf{r}, I) \approx \mathbf{b}(\mathbf{r})\, I, \tag{1.2}$$

where $\mathbf{b}(\mathbf{r}) \in \mathbb{R}^3$ is the current-to-field map. This map depends on the electromagnet geometry and magnetic properties, and can be modeled using dipole or multipole approximations [49], [52]. Second, in permanent magnets, the magnetic field ($\mathbf{B}(\mathbf{r})$) is generated by the material magnetization and varies spatially according to the magnet geometry and magnetization distribution. A time-varying magnetic field can be produced by mechanically rotating the permanent magnet at angular velocity ($\Omega \in \mathbb{R}$). For a magnet rotating about a fixed axis, the field at position ($\mathbf{r}$) and time ($t \in \mathbb{R}^+$) can be expressed as [55], [56]:

$$\mathbf{B}(\mathbf{r}, t) = \mathbf{R}(\Omega t)\, \mathbf{B}_0\big(\mathbf{R}^T(\Omega t)\mathbf{r}\big)\,, \tag{1.3}$$

where $\mathbf{B}_0(\mathbf{r}) \in \mathbb{R}^3$ is the static field map of the magnet in its reference orientation, and $\mathbf{R}(\Omega t) \in SO(3)$ is the rotation matrix describing the magnet orientation. Magnetic actuation systems can be built from electromagnets, permanent magnets, or hybrid combinations. Regardless of the magnetic source, these systems are commonly organized as stationary or mobile actuation architectures. Stationary platforms provide reproducible magnetic field distributions within a defined workspace, while mobile or robotic platforms extend coverage by repositioning the magnetic source (Figure 1.3(B)) [57], [58]. These architectures define the spatial distribution of magnetic fields relative to the micro-agents.

Magnetic actuation can guide individual micro-agents through steering, pulling, and dragging, and can also coordinate collective behavior among

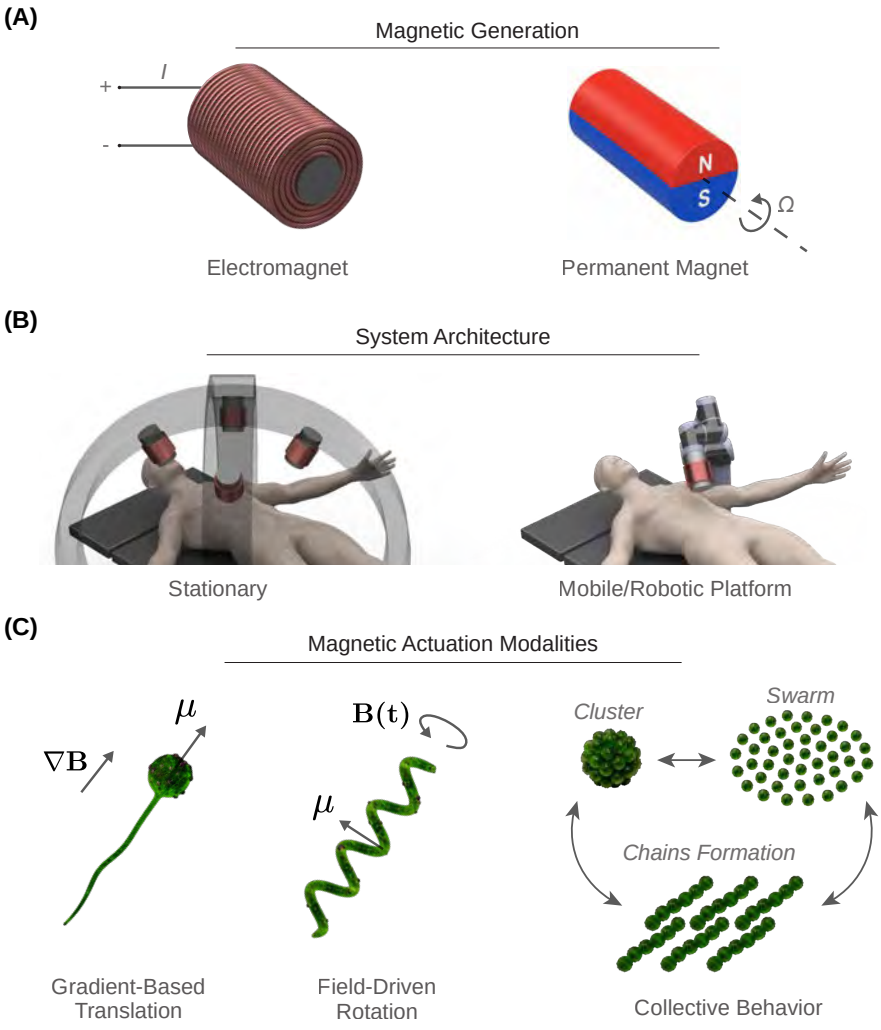


Figure 1.3: Magnetic actuation in microrobotics. (A) Magnetic generation through electromagnets, where the field is controlled by an electric current (I), and permanent magnets, where time-varying fields are produced by mechanical rotation at angular velocity (Ω). (B) System architecture based on stationary platforms with fixed coil arrangements, or motorized and robotic platforms that reposition the magnetic source. (C) Field gradients ($\nabla\mathbf{B}$) generate translational forces on micro-agents carrying a magnetic moment ($\boldsymbol{\mu}$), while time-varying magnetic fields ($\mathbf{B}(t)$) generate torques that drive rotation and propulsion. Magnetic interactions between multiple agents enable collective behavior, including cluster formation, swarm organization, and magnetic self-assembly. The elements presented in panel (C) were generated using DALL·E 3.

multiple agents (Figure 1.3(C)). As shown in Equation (1.1), both the magnetic force and torque depend on the magnetic moment of the micro-agent. For a given magnetization, the magnetic moment scales with the volume of magnetic material. For geometrically similar agents with a fixed magnetic volume fraction, the magnetic force therefore scales as L^3 at a fixed applied field gradient, where L is the characteristic agent size. In low-Reynolds-number flow, viscous drag scales as L at fixed fluid viscosity and relative velocity, neglecting wall effects [59]. Under these assumptions, reducing the agent size from 1 mm to 10 μm decreases the magnetic force by six orders of magnitude and the force-to-drag ratio by four. Consequently, the actuation capability of a single agent is limited, constraining its payload capacity and ability to navigate through biological fluids. The ratio between torque-driven and gradient-driven actuation scales as $|\mathbf{B}|/(L\,|\nabla\mathbf{B}|)$, which favors time-varying fields over gradients as agents become smaller [59]. On the source side, geometrically similar electromagnets operating in a linear magnetic regime produce approximately size-independent field gradients at constant current density when evaluated at correspondingly scaled positions. Smaller coils can also support higher current densities under suitable cooling conditions because heat dissipation becomes more favorable relative to their volume [60]. This scaling motivates bringing miniaturized magnetic sources close to the target. Collective systems address the limited actuation capability of individual agents by distributing the actuation task across many magnetically responsive agents [61]. In such systems, the applied field induces a magnetic response in each agent, while inter-agent magnetic interactions lead to field-dependent organization into chains, clusters, pillars, or swarms. These collectives enable large-scale transport, distributed manipulation, and adaptive reconfiguration [62]–[65].

1.3.2 Fluorescence imaging

After magnetic actuation establishes how micro-agents can be manipulated, fluorescence imaging provides the optical basis for identifying micro-agents and surrounding biological structures. This imaging modality exploits a photophysical process in which a fluorescent molecule, known as a fluorescent dye or fluorophore, absorbs light and re-emits it [66], [67]. Each fluorophore has characteristic excitation and emission spectra, enabling specific labeling and discrimination of distinct targets. The efficiency with which

a fluorophore converts absorbed photons into emitted light is quantified by the quantum yield ($\Phi \in [0, 1]$):

$$\Phi = \frac{N_{\text{em}}}{N_{\text{abs}}}, \tag{1.4}$$

where N_{em} and N_{abs} are the numbers of emitted and absorbed photons, respectively. The quantum yield depends on the fluorophore composition and its local environment [68]. Together with the absorption cross-section, it contributes to the intrinsic brightness of a fluorophore. The absorption cross-section quantifies the efficiency of light absorption, and its value depends on whether excitation occurs through the absorption of one photon or the near-simultaneous absorption of multiple photons. While higher-order processes involving three or more photons exist, this thesis focuses on one-photon and two-photon excitation (Figure 1.4(A)).

In one-photon fluorescence imaging, the fluorophore absorbs a single photon and re-emits at a longer wavelength [69]. The shift from excitation wavelength ($\lambda_{\text{ex}} \in \mathbb{R}^+$) to the emission wavelength ($\lambda_{\text{em}} \in \mathbb{R}^+$), known as the Stokes shift ($\Delta\lambda$), is defined as:

$$\Delta\lambda = \lambda_{\text{em}} - \lambda_{\text{ex}}. \tag{1.5}$$

The Stokes shift enables optical filters to reject the stronger excitation light while transmitting the weaker fluorescence signal, providing the spectral separation required for fluorescence imaging [66]. The detected fluorescence intensity ($F_{1\gamma} \in \mathbb{R}^+$) scales linearly with the excitation intensity ($I_{\text{ex}} \in \mathbb{R}^+$):

$$F_{1\gamma} \propto \sigma_{1\gamma} \cdot \Phi \cdot I_{\text{ex}}, \tag{1.6}$$

where $\sigma_{1\gamma}$ is the one-photon absorption cross-section of the fluorophore. However, one-photon excitation in biological samples is affected by scattering, absorption, and out-of-focus fluorescence, which limit imaging depth and contrast [70].

Two-photon fluorescence imaging mitigates these effects by using near-infrared photons that scatter less in tissue, enabling fluorescence generation at greater depths. This approach relies on the near-simultaneous absorption of two near-infrared photons, and the detected fluorescence intensity ($F_{2\gamma} \in \mathbb{R}^+$) scales quadratically with the excitation intensity:

$$F_{2\gamma} \propto \sigma_{2\gamma} \cdot \Phi \cdot I_{\text{ex}}^2, \tag{1.7}$$

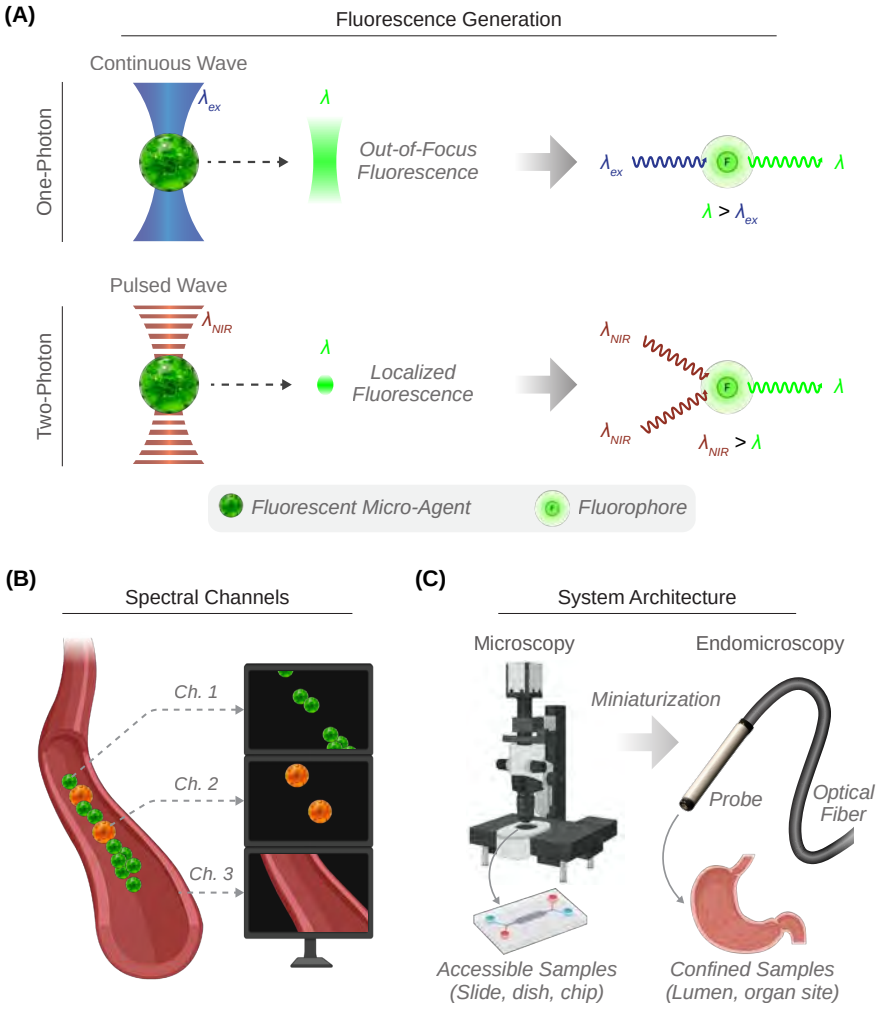


Figure 1.4: Fluorescence imaging in microrobotics. (A) Fluorescence generation through one-photon and two-photon excitation. One-photon excitation commonly uses visible excitation light (λ_{ex}) and can generate fluorescence outside the focal region. Two-photon excitation uses near-infrared pulsed excitation (λ_{NIR}) to concentrate fluorescence generation near the focal volume. The schematics distinguish fluorescence from labeled micro-agents at the sample level and photon absorption/emission at the fluorophore level. (B) Spectral channels are used to resolve differently labeled sample components, such as micro-agents, biological targets, and surrounding structures. (C) Representative fluorescence imaging architectures, including benchtop microscopy for accessible samples and fiber-based endomicroscopy probes for confined anatomical sites. Fluorescence micro-agents depicted in panel (A) were generated using DALL·E 3.

where $\sigma_{2\gamma}$ is the two-photon absorption cross-section, typically several orders of magnitude smaller than $\sigma_{1\gamma}$ [71]. Because $F_{2\gamma} \propto \sigma_{2\gamma}$ scales with the square of the intensity, excitation is confined to the focal volume, suppressing the out-of-focus fluorescence that limits one-photon imaging and providing intrinsic optical sectioning. This low cross-section requires very high excitation intensity at the focus. In practice, this is achieved using femtosecond pulsed lasers sources to deliver pulses of duration ($\tau \in \mathbb{R}^+$) on the order of 100 fs, concentrating the optical energy in time [72]. For a fixed average power, shorter pulses increase the peak intensity of each pulse. This enhances the two-photon fluorescence signal because $F_{2\gamma}$ depends quadratically on I_{ex}. However, maintaining this peak intensity through the imaging system is non-trivial. Chromatic dispersion in optical components and biological media broadens τ, reducing the peak I_{ex} at the focus and lowering $F_{2\gamma}$ [73].

Fluorescence imaging also enables spectral discrimination among sample components. In multicolor fluorescence microscopy, labeled components are visualized in separate channels by detecting fluorescence emission within distinct spectral bands (Figure 1.4(B)). In one-photon fluorescence microscopy, this separation is achieved by selecting excitation sources and emission filters matched to each fluorophore. Channels are commonly acquired sequentially to reduce spectral crosstalk and accommodate limited detector availability. This approach, however, reduces the effective frame rate approximately in proportion to the number of channels. Multi-detector configurations and spectral unmixing can partially mitigate this trade-off, although they introduce additional constraints in system complexity, cost, and signal separability [74], [75]. In two-photon fluorescence microscopy, fluorophores with sufficient two-photon absorption at the selected near-infrared excitation wavelength can be excited simultaneously and detected in separate emission channels [72]. For fluorophores with more distinct spectra, multiple excitation wavelengths are used [45]. Each fluorophore has its own two-photon excitation spectrum, which is broadly red-shifted but not simply twice its one-photon counterpart [76]. Multiphoton microscopy can also enable label-free contrast via second-harmonic generation from non-centrosymmetric structures such as collagen [77], and through autofluorescence from endogenous molecules such as nicotinamide adenine dinucleotide (NADH) and flavin adenine dinucleotide (FAD) [78]. In microrobotics, fluorescent labels and label-free contrast mechanisms can provide

complementary optical channels for distinguishing micro-agents, biological targets, and surroundings.

The ability to distinguish labeled components in microrobotic applications depends not only on the fluorophores, excitation regime, and contrast mechanism, but also on the imaging platform (Figure 1.4(C)). Fluorescence-guided microrobotic experiments have primarily been demonstrated using benchtop microscopes [45], [79]. These systems can provide high spatial resolution, sensitive fluorescence detection, and configurable spectral filtering. However, optical access through biological tissue is fundamentally limited by light scattering and absorption. As a result, only thin or transparent samples can be imaged, and observation in deeper or confined anatomical sites becomes difficult. Endomicroscopy addresses this constraint by bringing the imaging optics inside the human body, using miniaturized fiber-based probes or compact lens systems [80], [81]. Fluorescence endomicroscopy is well established in clinical applications such as gastrointestinal and pulmonary diagnostics [82], [83], yet its use for microrobotic guidance remains comparatively limited.

1.4 Research objectives

The preceding sections establish the conceptual framework that motivates the main aim of this doctoral thesis:

Thesis aim

Develop magnetic actuation and fluorescence imaging strategies toward image-guided microrobotics in biologically relevant environments.

To address this aim, five research objectives (ROs) are formulated, progressing from each modality to their integration.

Miniaturized electromagnets generate localized fields close to the target actuation site, offering a compact alternative to the large external platforms typically used in microrobotics [58], [84]. Existing miniaturized electromagnetic approaches have demonstrated precise manipulation of individual microparticles, particularly in open microscopy workspaces [85]–[87]. In practice, however, local actuation must also operate within confined geometries, under fluidic conditions, and with compact arrangements of multiple

magnetic sources. This motivates the first research objective:

RO.1

Develop localized magnetic actuation strategies for micro-agent operation within compact workspaces.

The limited payload and force of individual micro-agents motivate collective systems, where many agents act together to perform locomotion, manipulation, and reconfiguration tasks. Magnetic collectives have been demonstrated as microparticle swarms [62]–[65], droplets [88], [89], and self-assembled pillars [90]. Self-assembled magnetic pillars are particularly attractive because they can form from magnetic microparticles without permanent attachment to a substrate. However, their actuation has mainly relied on uniform and time-varying magnetic fields, which limit field shaping and spatially selective actuation. Non-uniform magnetic fields generated by multi-coil electromagnetic systems offer a route to expand their behavior, including morphology reconfiguration, locomotion in fluidic environments, object manipulation, and independent actuation [91], [92]. This leads to the second research objective:

RO.2

Investigate the behavior of magnetic micro-agent collectives under non-uniform and time-varying magnetic fields.

Visualizing dynamic interactions between micro-agents and biological structures requires real-time multicolor imaging. Multicolor fluorescence microscopy enables micro-agents and surrounding biological structures to be resolved in separate spectral channels [45], [69]. In practice, standard multicolor imaging commonly relies on sequential channel acquisition to reduce spectral crosstalk. Yet, this approach reduces the effective frame rate as the number of channels increases [93], [94]. Computational strategies, including spectral unmixing and deep-learning-based fluorescence reconstruction, can recover channel information from mixed or limited measurements [95], [96]. However, these approaches have mainly been demonstrated on static samples or specialized optical platforms. For microrobotic systems, where micro-agents interact with biological structures in real time, these

strategies must support continuous reconstruction at video frame rates while preserving spectral specificity. This motivates the third research objective:

RO.3

Improve the temporal resolution of multicolor fluorescence imaging for micro-agents and biological structures.

Biological tissue introduces an optical barrier for fluorescence-guided microrobotics. One-photon fluorescence microscopy provides high-resolution visualization of micro-agents and surrounding structures, but scattering, absorption, and out-of-focus fluorescence reduce contrast with depth [21], [70]. As a result, fluorescence-based microrobotic studies have mainly been performed in thin or optically accessible samples [45], [74], [79]. Two-photon fluorescence imaging offers a route to extend visualization into scattering biological samples by using near-infrared excitation and localized fluorescence generation at the focal volume (Equation (1.7)) [70]. For microrobotic applications, two-photon fluorescence must support continuous visualization of micro-agents through biological tissue during actuation. This leads to the fourth research objective:

RO.4

Investigate two-photon fluorescence microscopy for continuous visualization of magnetic micro-agents through biological tissue.

Fluorescence microscopy provides detailed visualization of micro-agents and biological targets, but it requires optical access to the target site, which is limited in confined anatomical regions. Fluorescence endomicroscopy addresses this limitation by bringing the imaging probe closer to the target site [83], [97]. In microrobotics, however, endoscopic imaging has so far been limited to standard endoscopic modalities [98]. For microrobotics, two-photon endomicroscopy offers two specific advantages over one-photon fluorescence endomicroscopy. First, the localized excitation of two-photon imaging reduces background noise from scattering tissue and improves contrast between labeled micro-agents and biological structures (Equation (1.7)). Second, a single near-infrared excitation wavelength can

excite multiple fluorophores, enabling dual-color visualization through a compact fiber-based probe [81], [99], [100]. However, miniaturized probes have a small field of view, which makes it difficult to track micro-agents and biological targets during magnetic actuation. Therefore, integration requires feedback control to maintain the target within the field of view during actuation. This motivates the fifth and final research objective:

RO.5

Combine magnetic actuation and two-photon fluorescence endomicroscopy for image-guided microrobotics.

1.5 Thesis outline

The remainder of this thesis is organized into three parts and eight chapters. Table 1.1 indicates which chapters address each research objective.

Table 1.1: Mapping of research objectives (ROs) to thesis Chapters 2–6. A filled marker (●) denotes the chapter that primarily addresses an objective; an open marker (○) denotes a chapter that builds on the work of the filled-marker chapter in the same row. Marker color follows the corresponding chapter color.

	Part I		Part II		
Chapter	**2**	**3**	**4**	**5**	**6**
RO.1	●			○	○
RO.2		●	○		○
RO.3			●		○
RO.4				●	○
RO.5					●

The titles of the three parts are inspired by music that accompanies the conceptual arc of this dissertation: *Invisible Touch* by Genesis (1986), *Any Colour You Like* by Pink Floyd (1973), and *The End of the Beginning* by God Is an Astronaut (2002). These titles function as reflective markers, giving each part a thematic tone while the chapter structure defines the

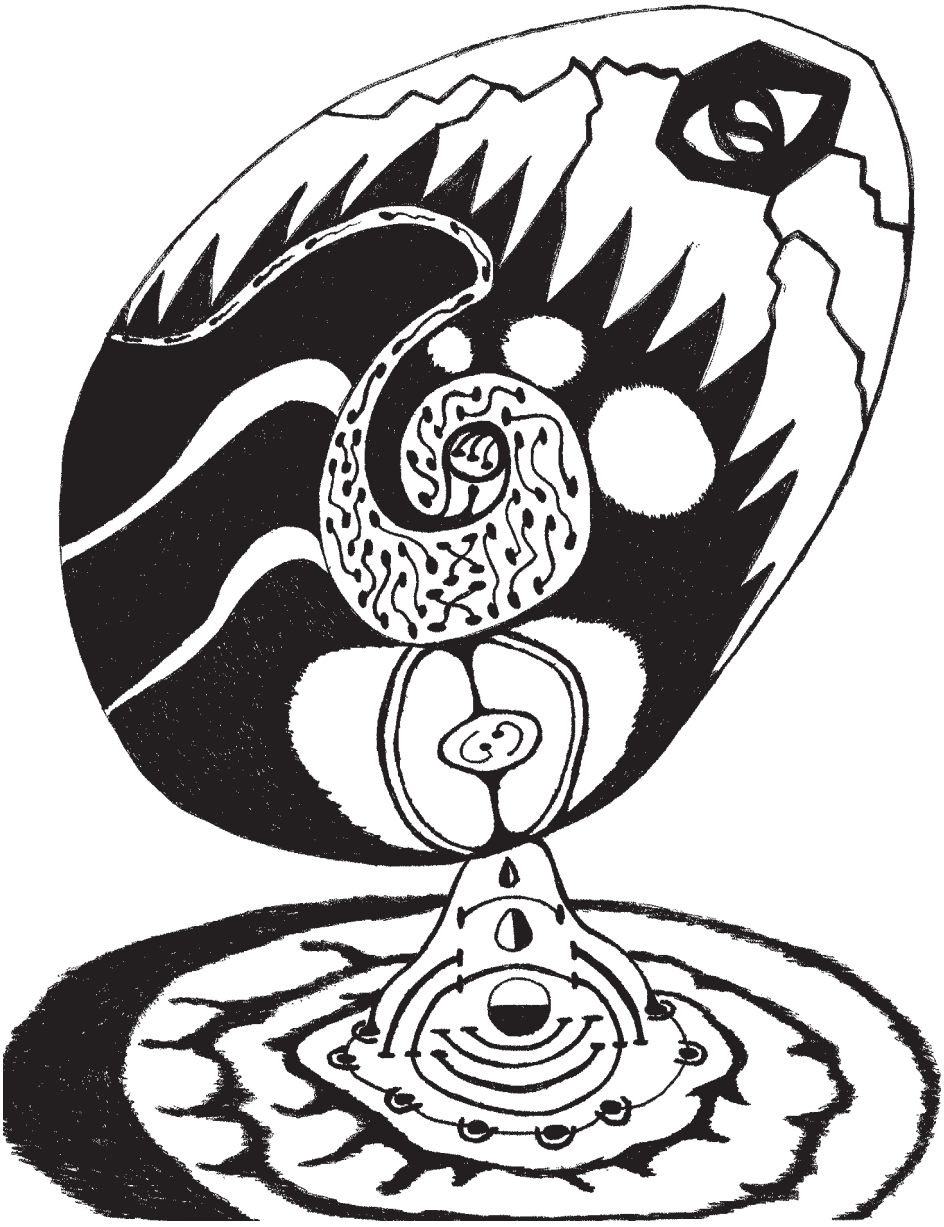
scientific progression. **Part I**, ***Invisible touch***, addresses the actuation dimension of this work, comprising **Chapters 2–3**. **Chapter 2** presents the development of needle-shaped miniaturized electromagnets for localized magnetic actuation within compact workspaces. **Chapter 3** investigates the collective behavior of magnetic microparticles under non-uniform and time-varying magnetic fields, exploring how field shaping can induce coordinated dynamics in self-assembled structures. **Part II**, ***Any colour you like***, addresses the imaging dimension comprising **Chapters 4–6**. **Chapter 4** presents a computational approach to increasing the temporal resolution of multicolor fluorescence microscopy during dynamic interactions between micro-agents and biological structures. **Chapter 5** then extends fluorescence imaging into scattering tissue using two-photon microscopy. **Chapter 6** brings this approach toward in situ operation through a two-photon endomicroscopy system for image-guided magnetic microrobotics. **Part III**, ***The end of the beginning***, comprises **Chapters 7** and **8**. **Chapter 7** synthesizes the main findings of **Chapters 2–6**, identifies the research objectives each addresses, and traces their connections toward image-guided microrobotics. **Chapter 8** outlines the remaining challenges and directions for future work. A single bibliography at the end of the thesis collects the references of all chapters, numbered in order of first citation.

I

Invisible touch

The first part of this thesis turns to acting within the microworld using untethered magnetic micro-agents. At the microscale, making micro-agents move is far from trivial. Direct contact is impractical, onboard power is difficult to miniaturize, and the surrounding medium strongly influences motion. Magnetic actuation addresses these challenges by transmitting forces and torques through space, without wires or physical contact. The title of this part, *Invisible touch*, inspired by Genesis's album of the same name (1986), reflects this principle.

In practice, magnetic actuation introduces its own constraints. Large external platforms can generate controlled fields over defined workspaces, but their scale complicates local, instrument-based actuation. At the collective level, groups of magnetic micro-agents can produce behaviors that single agents cannot. However, controlling a collective also requires shaping its elements, not only moving the group as a whole. The next two chapters address these constraints: **Chapter 2** describes localized magnetic actuation with compact electromagnetic sources (**RO.1**). **Chapter 3** examines self-assembled magnetic collectives that organize and move under non-uniform fields (**RO.2**).



CHAPTER 2

Miniaturized electromagnets for local actuation

The following chapter is adapted from: ***J. J. Huaroto****, M. Richter, M. Malafaia, J. Kim, C-S. Kim, J-O. Park, J. Sikorski, and S. Misra. MagNeed – Needle-shaped electromagnets for localized actuation within compact workspaces, Robotics and Automation Letters, vol. 8, no. 6, pp. 3908-3915, 2023.*
The text, figures, and tables have been adapted for inclusion in this doctoral thesis.

Abstract

Electromagnetic actuation of micro-/milli-sized agents has traditionally relied on large electromagnets positioned at considerable distances from the agents. As a result, the electromagnets consume kilowatts of power to overcome the limited generation of magnetic field gradients. Miniaturized electromagnets offer an alternative approach for reducing power consumption via localized actuation of micro-/milli-sized agents. Typically, the generation of magnetic field gradients in the vicinity of a miniaturized electromagnet is comparable with traditional electromagnetic actuation systems. Miniaturized electromagnets can be positioned near target sites in microfluidic channels or *ex vivo* vasculatures. Thereby, localized trapping and actuation of magnetic micro-/milli-sized agents are carried out. This study introduces MagNeed – an electromagnetic actuation system composed of three needle-shaped electromagnets (NSEs). MagNeed can determine compact workspaces by positioning the NSEs at different spatial configurations. Each NSE generates magnetic field gradients (up to 3.5 T/m at 5 mm from the NSE tip axis) while keeping a maximum power consumption (0.5 W) and temperature (< 42 ^{o}C). MagNeed is complemented by a framework that reconstructs the pose of the NSEs. Experiments test MagNeed and framework on a transparent Teflon tube (5 mm inner diameter). MagNeed demonstrates localized trapping and actuation of a 1 mm NdFeB bead against a flow of water and silica gel particles (1-3 mm diameter).

2.1 Introduction

Contactless actuation of micro-/milli-sized agents can open up novel treatments in medicine through autonomous navigation [101], targeted therapy [102], and surgery [103]. Among various contactless actuation methods (e.g., magnetic [28], acoustic [104], and thermocapillary [105]), remote magnetic manipulation has been proposed for propelling micro-/milli-sized agents within microfluidic channels and *ex vivo* vasculatures [98], [106]. Magnetic actuation excels in robust and precise control of micro/milli-sized agents [92], [107]–[109] by utilizing either permanent magnets or electromagnets distributed around a workspace [58].

The past decade has seen a rapid development of electromagnetic actuation systems for micro-/milli-robotic applications such as localized delivery of biological samples [110], micromanipulation of cells [111], and biopsy [112]. Such actuation systems require multiple electromagnets to allow multi-degrees of freedom actuation [92], [108]. In addition, various mathematical models have been proposed for design and calibration [52], [54], [113]. Electromagnetic actuation systems are primarily arrangements of stationary/mobile electromagnets surrounding a workspace [92], [108], [111], [114]–[116]. The traditional approach to designing electromagnetic actuation systems for micro-robotics follows the trend of using overscaled electromagnets. However, such systems can consume kilowatts of power, increasing the coil temperature and requiring additional cooling mechanisms [92], [114].

Reducing power consumption is particularly relevant when electromagnetic sources are intended to operate close to biological tissue. Resistive losses in the coils generate heat, which must be dissipated while maintaining an appropriate actuator temperature. The associated cooling and power-delivery requirements also constrain integration into compact instruments. The design objective is therefore to generate sufficient magnetic force for a localized actuation task while limiting electrical dissipation and the resulting thermal burden. Bringing miniaturized magnetic sources close to the agent offers a route to this operating regime.

Recent developments in electromagnetic actuation have led to a continued interest in miniaturized electromagnets. The magnetic field gradient generated in the vicinity of a miniaturized electromagnet can be comparable to the values registered in traditional electromagnetic actuation sys-

tems [85]. Besides, power consumption is considerably reduced in three orders of magnitude [85], [117]. Studies on miniaturized electromagnets have proposed needle-like electromagnets to perform independent manipulation of magnetic micro-particles [86], [87]. An actuation system based on electromagnetic needles can provide direct access to enclosed regions. Furthermore, it can generate the force to actuate micro-/milli-sized agents while consuming less power and thus dissipating less heat than traditional systems.

In this study, we introduce MagNeed – an electromagnetic actuation system composed of three needle-shaped electromagnets (NSE). MagNeed creates a compact workspace by positioning the NSEs around a target site (Figure 2.1). The system functionality is validated by addressing two primary aims. (1) To demonstrate the use of NSEs for localized trapping/actuation of a milli-sized agent. (2) To provide a framework to reconstruct the pose of the NSEs. The study begins by introducing the design of MagNeed with an analytical model to describe the near magnetic field and gradients of the NSEs. We validate the analytical model utilizing our framework and magnetic field measurements. The remaining part of the study focuses on the experimental demonstration of MagNeed for localized trapping/actuation of a 1 mm NdFeB bead within a Teflon tube that transports water and silica gel particles.

2.2 System overview

2.2.1 Design of MagNeed

MagNeed is a miniature electromagnetic actuation system to deploy localized actuation of micro-/milli-sized agents within a compact workspace. MagNeed consists of three needle-shaped electromagnets (NSEs) to permit magnetic field and/or gradient control in three-dimensional space [54]. The system development includes four steps: (i) the electromagnetic actuation strategy, (ii) the design of the NSEs, (iii) the current-to-field map to represent the near magnetic field and gradients generated by each NSE, (iv) the thermal analysis of the NSEs.

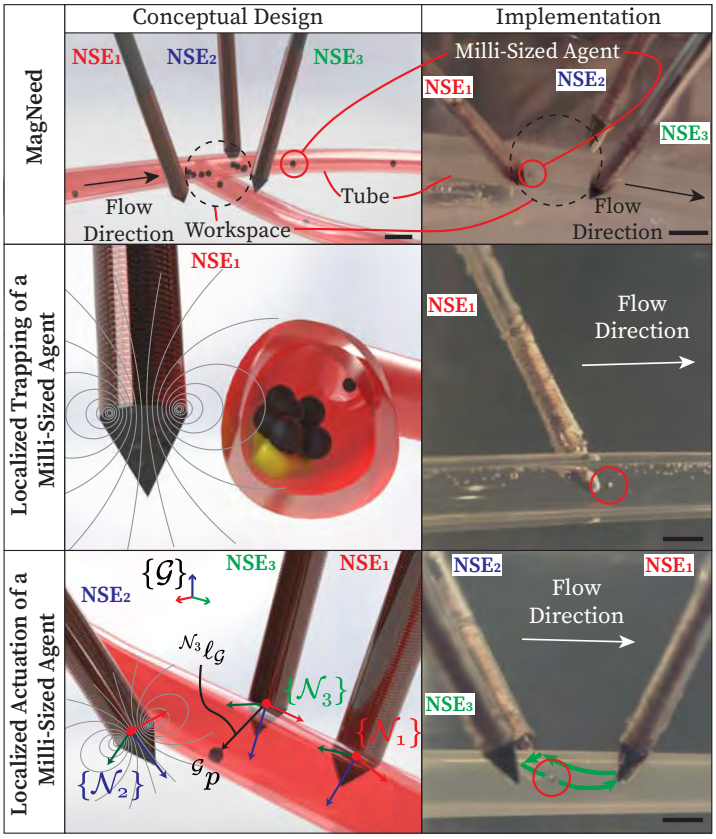


Figure 2.1: Design concept and implementation of MagNeed: three needle-shaped electromagnets (NSEs) positioned around a Teflon tube to define a compact workspace that encloses a target site. A magnetic milli-sized agent is locally actuated in a flowing liquid along the tube. Two applications are envisaged using single and three NSEs (MagNeed): localized trapping and localized actuation of a milli-sized agent. The NSEs frames are $(\{\mathcal{N}_1\}, \{\mathcal{N}_2\}, \text{and } \{\mathcal{N}_3\})$ and $(\{\mathcal{G}\})$ is the global reference frame. The vector $\left({}^{\mathcal{N}_3}\boldsymbol{\ell}_{\mathcal{G}}\right)$ represents the distance between frame $(\{\mathcal{N}_3\})$ and the position of a milli-sized agent $\left({}^{\mathcal{G}}\boldsymbol{p}\right)$ within the workspace. (All scale bars are 5 mm).

2.2.1.1 Electromagnetic actuation strategy

We begin the MagNeed development process by studying electromagnetic actuation principles in the context of micro-/milli-sized agents. The magnetic field generated by a needle-shaped electromagnet ($\boldsymbol{B}(\boldsymbol{p}, I)$) powered by an electrical current ($I \in \mathbb{R}$) exerts a wrench ($\boldsymbol{W} \in \mathbb{R}^6$) over a micro-/milli-sized agent with magnetic moment ($\boldsymbol{\mu} \in \mathbb{R}^3$) and located at a point ($\boldsymbol{p} \in \mathbb{R}^3$). $\boldsymbol{W}$ includes the magnetic force ($\boldsymbol{F} \in \mathbb{R}^3$) and magnetic torque ($\boldsymbol{T} \in \mathbb{R}^3$) and is defined as

$$\boldsymbol{W}(\boldsymbol{p}) = \begin{bmatrix} \boldsymbol{F}(\boldsymbol{p}) \\ \boldsymbol{T}(\boldsymbol{p}) \end{bmatrix} = \begin{bmatrix} \nabla(\boldsymbol{\mu} \cdot \boldsymbol{B}(\boldsymbol{p}, I)) \\ \boldsymbol{\mu} \times \boldsymbol{B}(\boldsymbol{p}, I) \end{bmatrix}. \tag{2.1}$$

For a given magnetization and applied field gradient, the magnetic force scales with the agent's magnetic volume. The corresponding scaling relationships for magnetic agents and electromagnetic sources are discussed in Section 1.3.1. Local frames ($\{\mathcal{N}_k\}$, for $k = 1, 2, 3$) are constructed for each NSE according to a global reference frame ($\{\mathcal{G}\}$) (Figure 2.1). At a point, $\left({}^{\mathcal{G}}\boldsymbol{p} \in \mathbb{R}^3\right)$ concerning the global reference frame, the magnetic field $\left({}^{\mathcal{G}}\boldsymbol{B}({}^{\mathcal{G}}\boldsymbol{p})\right)$ is the sum of the magnetic field generated by each NSE $\left({}^{\mathcal{G}}\boldsymbol{B}_k({}^{\mathcal{G}}\boldsymbol{p})\right)$. The unitary magnetic field $\left({}^{\mathcal{N}_k}\boldsymbol{\beta}_k({}^{\mathcal{N}_k}\boldsymbol{p})\right)$ is generated concerning the local frame of the corresponding NSE. The NSEs are assumed to operate in their linear regions (i.e., the magnitude and components of the magnetic field vary linearly with the current). Hence, the magnetic field in local frames is defined as

$${}^{\mathcal{N}_k}\boldsymbol{B}_k({}^{\mathcal{N}_k}\boldsymbol{p}) = {}^{\mathcal{N}_k}\boldsymbol{\beta}_k({}^{\mathcal{N}_k}\boldsymbol{p}) I_k, \tag{2.2}$$

where $I_k \in \mathbb{R}$, is the current through the kth NSE. In order to compute the vectors ${}^{\mathcal{G}}\boldsymbol{B}_k({}^{\mathcal{G}}\boldsymbol{p})$, we define the rotation matrices $\left({}^{\mathcal{G}}\boldsymbol{R}_{\mathcal{N}_k} \in SO(3)\right)$. This way, ${}^{\mathcal{N}_k}\boldsymbol{p} = {}^{\mathcal{N}_k}\boldsymbol{R}_{\mathcal{G}}\, {}^{\mathcal{G}}\boldsymbol{p} + {}^{\mathcal{N}_k}\boldsymbol{\ell}_{\mathcal{G}}$, where ${}^{\mathcal{N}_k}\boldsymbol{\ell}_{\mathcal{G}} \in \mathbb{R}^3$ are the vectors that represent the distances between the local and global frames (Figure 2.1). Hence, ${}^{\mathcal{G}}\boldsymbol{B}_k({}^{\mathcal{G}}\boldsymbol{p})$ is computed as follows:

$${}^{\mathcal{G}}\boldsymbol{B}_k({}^{\mathcal{G}}\boldsymbol{p}) = {}^{\mathcal{G}}\boldsymbol{R}_{\mathcal{N}_k}\, {}^{\mathcal{N}_k}\boldsymbol{\beta}_k({}^{\mathcal{N}_k}\boldsymbol{p}) I_k. \tag{2.3}$$

According to magnetism principles, field and gradients generated by an electromagnet are stronger at closer distances [85]. MagNeed aims to

achieve localized actuation of micro-/milli-sized agents by defining compact workspaces. Substituting (2.3) into (2.1), we obtain the magnetic force $\left({}^{\mathcal{G}}\boldsymbol{F}({}^{\mathcal{G}}\boldsymbol{p})\right)$ exerted on a micro-/milli-sized agent located at ${}^{\mathcal{G}}\boldsymbol{p}$:

$$ {}^{\mathcal{G}}\boldsymbol{F}({}^{\mathcal{G}}\boldsymbol{p}) = \boldsymbol{\mu}^T \begin{bmatrix} \frac{\partial[{}^{\mathcal{G}}\boldsymbol{\beta}_1({}^{\mathcal{G}}\boldsymbol{p})]}{\partial x} & \cdots & \frac{\partial[{}^{\mathcal{G}}\boldsymbol{\beta}_3({}^{\mathcal{G}}\boldsymbol{p})]}{\partial x} \\ \frac{\partial[{}^{\mathcal{G}}\boldsymbol{\beta}_1({}^{\mathcal{G}}\boldsymbol{p})]}{\partial y} & \cdots & \frac{\partial[{}^{\mathcal{G}}\boldsymbol{\beta}_3({}^{\mathcal{G}}\boldsymbol{p})]}{\partial y} \\ \frac{\partial[{}^{\mathcal{G}}\boldsymbol{\beta}_1({}^{\mathcal{G}}\boldsymbol{p})]}{\partial z} & \cdots & \frac{\partial[{}^{\mathcal{G}}\boldsymbol{\beta}_3({}^{\mathcal{G}}\boldsymbol{p})]}{\partial z} \end{bmatrix} \begin{bmatrix} I_1 \\ I_2 \\ I_3 \end{bmatrix}. \tag{2.4} $$

2.2.1.2 Needle-shaped electromagnets

The second step in MagNeed development involves the design of NSEs capable of generating magnetic gradients to actuate a micro-/milli-sized agent. We compare the magnetic field gradients generated by two NSEs with different core tip geometries: conical and straight (Figure 2.2a). Thereon, we study the optimal core ratio to maximize the magnetic gradients at the tip vicinity of an NSE.

The structure of the NSE follows a steel-cored coil design extended along a section ($l_c \in \mathbb{R}^+$) of the core length ($l_i \in \mathbb{R}^+$) (Figure 2.2a). The central part of the NSE, made out of machined ferromagnetic steel, serves a double purpose. First, it gives structural integrity. Second, it serves as an electromagnet core, amplifying the field generated by a copper solenoid wrapped around its distal part. Finally, an electrothermal coating of polyolefin (0.1 mm thick) wraps the body of the NSE to physically isolate it from the surrounding medium.

In order to visualize the magnetic gradients $\left(\frac{dB_r}{dr}, \frac{dB_z}{dz}, \frac{dB_r}{dz}\right)$ generated by the NSEs with conical and straight-tipped cores, we performed finite element simulations within a region ($\mathbb{A}$) (Figure 2.2(b1)). Table 2.1 provides the geometric parameters used in the simulations. To compare the gradients generated by the NSEs with conical and straight-tipped cores, we compute the differences: $\left|\frac{dB_r}{dr}\right|_c - \left|\frac{dB_r}{dr}\right|_s$, $\left|\frac{dB_z}{dz}\right|_c - \left|\frac{dB_z}{dz}\right|_s$, and $\left|\frac{dB_r}{dz}\right|_c - \left|\frac{dB_r}{dz}\right|_s$. The subscripts "c" and "s" stand for conical and straight-tipped cores, respectively. Figures 2.2(b2)-(b4) show the regions where the differences are greater than 10 mT/m. The black arrow indicates that the NSE with a conical-tipped core improves the generation of gradients at short distances (≤ 0.55 mm) from the core tip (along the z-axis) [84], [118]. Moreover, the base of the conical tip, with a radius ($r_t > r_i$), improves the generation of gradients along the r-axis (Figures 2.2(b2)-(b4)).

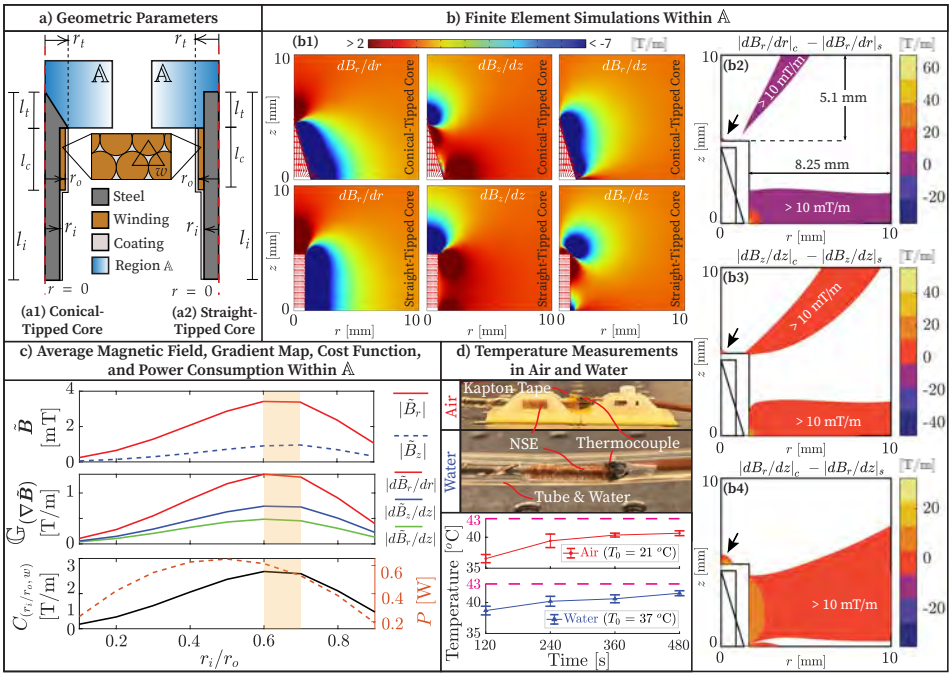


Figure 2.2: Geometric and magnetic properties of needle-shaped electromagnets (NSEs) within MagNeed. a) Geometric parameters of two NSEs with different core tip geometries: conical (a1) and straight (a2). The geometry of the NSEs comprises three parts: steel core, copper winding, and polyolefin coating. The winding is arranged around the core into layers (magnified view), while the coating creates a physical interface between the NSE and the surrounding medium. The subscripts t, c, and i indicate tip, coil, and core, respectively. b) Finite element simulation within the region ($\mathbb{A} = \{r \wedge z \in \mathbb{R}_{\geq 0} : r \leq 10 \text{ mm}, z \leq 10 \text{ mm}\}$). The simulations are realized in finite element software (COMSOL Multiphysics 5.5, COMSOL AB, Sweden) using a current of 1 A. (b1) The magnetic gradients generated by the NSEs with conical and straight-tipped cores within the region ($\mathbb{A}$). (b2)-(b4) The differences of normalized gradients generated by the NSEs with conical ("c") and straight ("s") tipped cores. The differences are plotted within a sub-region of $\mathbb{A}$. The colored regions indicate differences greater than 10 mT/m. The triangle and rectangle at the bottom-left of the graphs indicate the conical and straight-tipped cores, respectively. The black arrows indicate the regions that are close to the tip core. c) Parametric optimization results to identify the optimal core ratio (r_i/r_o), which maximizes the cost function ($C_{(r_i/r_o,w)}$) within $\mathbb{A}$. The colored region represents the optimal interval ($r_i/r_o \in [0.6, 0.7]$) using a wire diameter ($w = 0.2$ mm). d) Temperature measurements in ambient air (21 ^{o}C) and water (37 ^{o}C): the thermocouple probe is located in contact with the NSE tip. The temperature data is acquired using a digital multimeter (U1272A, Keysight Technologies, USA). The NSE is powered using a constant current of 0.75 A for an interval of 480 s. The maximum temperature reported is below 42 ^{o}C, under the 43^{o}C limit.

Table 2.1: Geometric Parameters of the Needle-Shaped Electromagnets (NSEs).

Parameter	Symbol	**Value**
Core Radius	r_i	**0.875 mm**
Coil Radius	r_o	**1.25 mm**
Core Ratio	r_i/r_o	**0.7**
Tip Radius	r_t	**1.35 mm**
Tip Length	l_t	**4.5 mm**
Core Length	l_i	**100 mm**
Coil Length	l_c	**17.5 mm**
Number of Turns	n	**175**
Wire Diameter	w	**0.2 mm**

The simulation results indicate that the NSE with a conical-tipped core can generate strong gradients in the proximity of the core tip. In addition, the improved generation of magnetic gradients along the r-axis suggests that the NSEs can be used for in-/off-axis actuation. This study proposes an optimization-based design to maximize the magnetic field gradients generated by an NSE with a conical-tipped core. The optimization problem has two variables: core ratio ($r_i/r_o \in \mathbb{R}^+$) and wire diameter ($w \in \mathbb{R}^+$) to maximize a cost function $\left(C_{(r_i/r_o,w)} \in \mathbb{R}^+\right)$, which includes the average intensity of the magnetic field gradient $\left(\nabla\tilde{\boldsymbol{B}} \in \mathbb{R}^{3\times3}\right)$ within the region ($\mathbb{A}$). The function $\left(C_{(r_i/r_o,w)}\right)$ is defined by the following expression:

$$C_{(r_i/r_o,w)} = \left|\left|\mathbb{G}_{(\nabla\tilde{\boldsymbol{B}})}\right|\right|_2, \tag{2.5}$$

where the gradient map ($\mathbb{G}_{(\nabla\tilde{\boldsymbol{B}})}$: $\mathbb{R}^{3\times3} \rightarrow \mathbb{R}^3$) is used to obtain the three independent and unequal components of the magnetic field gradient: $\mathbb{G}_{(\nabla\tilde{\boldsymbol{B}})} = \left[\left|\frac{d\tilde{B}_r}{dr}\right|, \left|\frac{d\tilde{B}_z}{dz}\right|, \left|\frac{d\tilde{B}_r}{dz}\right|\right]^T$. The following relationship [119]:

$$n = \left\lfloor \frac{2l_c(r_o - r_i - w)}{\sqrt{3}w^2} + \frac{l_c}{w} - \frac{(r_o - r_i - w)\sqrt{3}}{3w} - \frac{1}{2} \right\rfloor, \tag{2.6}$$

where $\lfloor\rfloor : \mathbb{R} \rightarrow \mathbb{Z}$ is the floor function, computes the maximum number of winding turns ($n \in \mathbb{Z}^+$). The wire diameter (w), the resistivity of the copper wire ($\rho = 1.72\times10^{-8}$ Ω.m), the core radius (r_i), number of turns (n), and the simulation current ($I = 1$ A) are used to estimate the power consumption (P) of the NSE using the formula: $P = I^2\, 8\, \rho\, r_i\, n/w^2$.

The axial symmetry of the NSE allows the 3D geometry to be reduced to a 2D axisymmetric problem in the r–z plane. The model uses the stationary Magnetic Fields interface with quadratic Lagrange elements, solved with a damped Newton method and a direct linear solver to account for the nonlinear magnetization curve of the core material. The winding is represented as a homogenized multi-turn coil and the steel core is modeled with the Soft Iron (without losses) material of the COMSOL library. The NSE is enclosed in an air domain of 50 mm radius and 150 mm height, extending 15 mm below the core base and approximately 30 mm beyond the core tip, with axial symmetry at $r = 0$ and magnetic insulation at the outer boundaries. The full simulation domain is discretized with 51720 triangular elements (average mesh quality of 90%, based on skewness). The mesh within the region ($\mathbb{A}$), where the field and gradients are evaluated, contains 5338 elements with a minimum size of 1 µm and an average mesh quality of 92%. The simulations are carried out within a range of standard wire diameters ($w = 0.1, 0.2, 0.3, 0.4$ mm), an interval of core ratios ($r_i/r_o = [0.1, 0.9]$), and using a current of 1 A. According to the simulation results, the cost function tends to maximize for small wire diameters. However, there is a trade-off with the power consumption (P). In this study, we use a $w = 0.2$ mm diameter wire, which maximizes $C_{(r_i/r_o,w)}$ within the interval ($r_i/r_o \in [0.6, 0.7]$), having a power consumption ($P \in [0.5, 0.6]$ W at 1 A) (Figure 2.2c). Replacing the core material with low carbon steel 1018 changes $C_{(r_i/r_o,w)}$ by less than 2% within this interval and does not shift the optimal interval. For limiting the power consumption to 0.5 W, we chose $r_i/r_o = 0.7$. Final dimensions of the NSE are provided in Table 2.1.

2.2.1.3 Current-to-field map

The magnetic field generated by a needle-shaped electromagnet (NSE) is mapped into a current to reach magnetic actuation over a micro-/milli-sized agent. A high-resolution hall effect sensor (MLX90393, SparkFun Electronics, USA) mounted at the end effector of a collaborative 7-DoF robot (Panda, Franka Emika GmbH, Germany) acquires the magnetic field data within the NSE vicinity. The data is transferred to a microcontroller (Arduino DUE, Arduino, Italy) based on an Atmel SAM3X8E ARM Cortex-M3 CPU, using an I2C interface, and subsequently transmitted to a computer using a serial interface (sampling frequency of 100 Hz). A 3D printed sup-

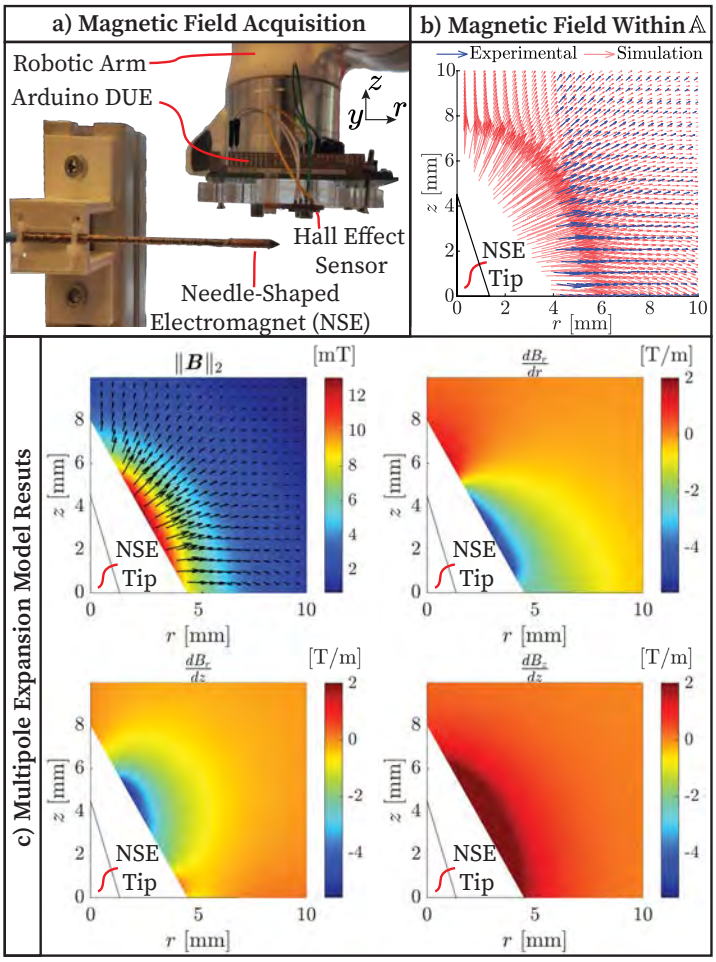


Figure 2.3: Current-to-field map of a needle-shaped electromagnet (NSE): a) The magnetic field acquisition at the distal part of the NSE (i.e., region 𝔸). b) Experimental and finite element data comparison ($R^2 = 0.9414$). c) The multipole expansion model fits the experimental and simulation data ($R^2 = 0.9986$ and $R^2 = 0.9913$ in the r- and z-axis, respectively). The magnetic field and the three non-zero gradient components are plotted using a current of 1 A. At the coordinates ([5, 0] mm), the magnitude of the magnetic field ($\|\boldsymbol{B}\|_2$) and the gradient components $\left(\left|\frac{dB_r}{dr}\right|, \left|\frac{dB_r}{dz}\right|, \left|\frac{dB_z}{dz}\right|\right)$ reach values of 9 mT, 3.5 T/m, 0.09 T/m, and 1.02 T/m, respectively. At the coordinates ([10, 0] mm), magnetic field and gradient components are 2.1 mT, 0.42 T/m, 0.004 T/m, and 0.24 T/m, respectively. The triangle at the bottom-left of the graphs indicates the tip of the NSE.

port is used to hold the NSE horizontally while being powered with 1 A (Figure 2.3a). A longitudinal scan along the y-axis is performed to identify the sagittal plane of the NSE (r-z plane). Thereon, a raster scan path is generated to acquire the magnetic field data in the r-z plane (Figure 2.3b). In order to compute the current-to-field map, the data is bounded within the region ($\mathbb{A}$) using a multi-pole expansion defined by a non-linear scalar potential function ($\Psi(\boldsymbol{p})$) [113]:

$$\boldsymbol{B}(\boldsymbol{p}, I) = \nabla\Psi(\boldsymbol{p})I. \tag{2.7}$$

The unitary magnetic field $\left(\boldsymbol{\beta}(\boldsymbol{p}) \in \mathbb{R}^3\right)$ and its corresponding gradient $\left(\nabla\boldsymbol{\beta}(\boldsymbol{p}) \in \mathbb{R}^{3\times3}\right)$ at a fitting current ($I_f = 1$ A) are defined as follows

$$\begin{cases} \boldsymbol{\beta}(\boldsymbol{p}) = \frac{\nabla\Psi(\boldsymbol{p})}{I_f} \\ \nabla\boldsymbol{\beta}(\boldsymbol{p}) = \left[\frac{\partial\boldsymbol{\beta}(\boldsymbol{p})}{\partial x}, \frac{\partial\boldsymbol{\beta}(\boldsymbol{p})}{\partial y}, \frac{\partial\boldsymbol{\beta}(\boldsymbol{p})}{\partial z}\right]. \end{cases} \tag{2.8}$$

Substituting (2.8) in (2.7), we obtain the current-to-field map for each NSE. The multi-pole model fits the magnetic field data from experimental and simulation results (Figure 2.3b). Yet, the model starts to lack correlation ($R^2 < 0.9$) for coordinates $r < 5$ mm and $z < 8$ mm. Beyond region ($\mathbb{A}$), the magnetic field and gradients tend to zero, which implies that the workspace of an NSE has the shape of a cylinder (radius and height of 10 mm) (Figure 2.3c).

2.2.1.4 Thermal analysis

A surface-temperature limit of 43 °C was adopted as a design criterion for the intended sustained operation of the needle-shaped electromagnets (NSEs). Higher temperatures may be tolerated during shorter exposures, since thermal effects depend on both temperature and exposure duration [120]. The selected ceiling is consistent with the 43 °C limit specified in IEC 60601-1 for applied parts contacting healthy adult skin for 10 minutes or longer [121]. This value serves here as a design benchmark; its suitability for contact with internal tissues requires application-specific assessment. We experimentally test the surface temperature of an NSE by powering it with 0.75 A. The temperature is acquired in ambient air (21 ^{o}C) and water (37 ^{o}C) using a thermocouple probe in contact with the NSE. Figure 2.2d shows the experimental setup and temperature results for an interval of 480

Table 2.2: MagNeed Specifications: Values per Needle-Shaped Electromagnet (NSE).

Specifications	**Value**
Maximum Power [W]	**0.5**
Power per Unit Area Dissipation [mW/mm^2]	**3.9**
Magnetic Field (at 5 mm from tip axis) [mT]	**9** (1 A)
Magnetic Field Gradient (at 5 mm from tip axis) [T/m]	**3.5** (1 A)
Number of NSEs	**3**
Maximum Current [A]	**0.75**
Electrical Resistance [Ω]	**0.84**
Operating Temperature [^{o}C]	$<$ **42**
Workspace per NSE: Cylinder (radius & height) [mm]	**(10 & 10)**

s. Over this interval, the temperature remains below 42 ^{o}C, approaching a plateau in air and increasing slowly in water. Further experiments with currents ($>$ 0.75 A) at least doubled the temperature rise of the NSEs. Thus, we set 0.75 A as the maximum operating current of MagNeed.

2.2.1.5 Final design

The four previous steps served as foundations to determine the design and features of MagNeed. Table 2.2 provides the main characteristics of MagNeed. We highlight the low-power consumption, operating temperature, and magnetic field gradients, which are comparable with state-of-the-art macroscale electromagnetic actuation systems [85], [92], [108], [114]–[117].

2.2.2 Framework

MagNeed can generate different workspace layouts depending on the spatial configuration of the needle-shaped electromagnets (NSEs). Consequently, the system is complemented by providing a framework to reconstruct the pose of the NSEs according to a global reference frame ($\{\mathcal{G}\}$) (Figure 2.4). The pose reconstruction utilizes depth maps and points cloud data to estimate the pose of optical markers attached to the NSE. The data are acquired by a 3D camera (Realsense SR305, Intel, USA) mounted at the end effector of a collaborative 7-DoF robot (Panda, Franka Emika GmbH, Germany). The optical markers are attached at 70 mm from the origin of coordinates of each NSE (Figure 2.4). A post-processing algorithm is implemented in MATLAB (version R2021b, MathWorks, USA) to compute the pose of the optical markers and NSEs [122].

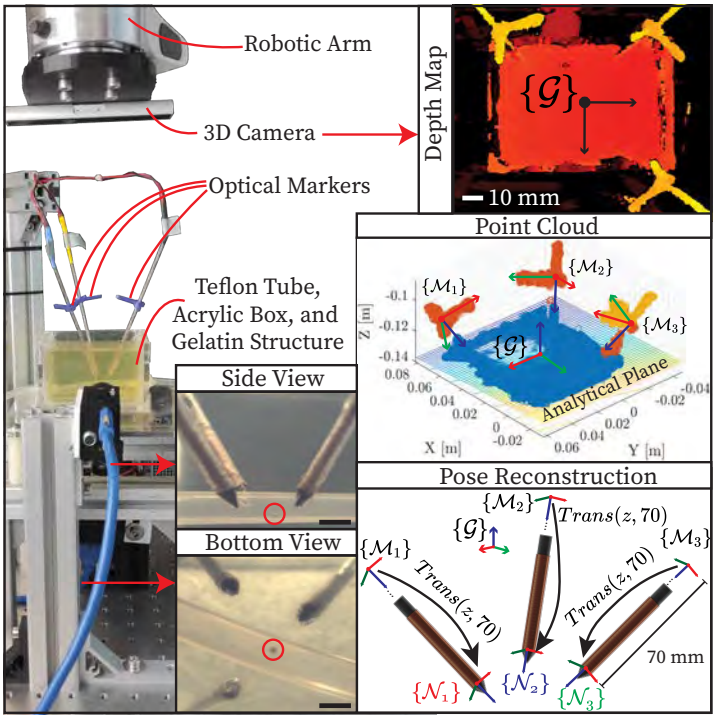


Figure 2.4: Experimental setup to locally actuate a 1 mm NdFeB bead within the Teflon tube. The tube ends are connected to two syringes that can be used to manually or automatically pump water. The current applied to the needle-shaped electromagnets (NSEs) is controlled through servo drives (iPOS4808 BX-CAT, Technosoft S.A., Switzerland). The servo drives are connected to a computer (running Linux Ubuntu 18.04, kernel version 4.19, NVidia QUADRO M2000M GPU, and 32 GB RAM) through an EtherCAT network (control rate of 500 Hz). The imaging of the magnetic bead is acquired by two cameras (grasshopper 3, Teledyne FLIR, USA), which are placed at the bottom and side of the acrylic box. Objective lenses (DF6HA-1S, FUJINON lenses, USA) are assembled to improve the image resolution (350 µm per pixel) in a field of view of 1024 × 1024 pixels^2. Both cameras are connected to the computer via USB 3.1, and a C++ program is implemented using OpenCV 4.5 to simultaneously record videos (acquisition rate of 30 frames per second). The red circles enclose the magnetic bead utilized in the experiments. (The black scale bars are 5 mm). The pose reconstruction of the NSEs uses a 3D camera to acquire depth images and point cloud data. Optical markers are attached at 70 mm from the NSE frames ($\{\mathcal{N}_k\}$, for $k = 1, 2, 3$). The global reference frame ($\{\mathcal{G}\}$), defined on top of the gelatin structure, is identified by fitting the point cloud to an analytical plane equation. The optical marker frames ($\{\mathcal{M}_k\}$, for $k = 1, 2, 3$) are computed by fitting the point cloud to three orthogonal vectors. Finally, a Euclidean translation from ($\{\mathcal{M}_k\}$) to ($\{\mathcal{N}_k\}$) determines the pose of the NSEs. (The color maps indicate the proximity of the point cloud to the 3D camera).

2.2.3 Model validation

The framework is initially tested using a 3D printed structure with three symmetrically spaced cavities to hold the needle-shaped electromagnets (NSEs) (Figure 2.5a). The results of the pose reconstruction showed a maximum error of 6% regarding the inclination angle of the NSEs (50^o). An additional cavity holds a high-precision teslameter probe (3MH3A-500MT, Senis AG, Baar, Switzerland). The teslameter is connected to a computer using a serial interface (acquisition frequency of 125 Hz). The NSEs are powered using sinusoidal currents (amplitude of 0.75 A) while the teslameter probe acquires the magnetic field components (B_x, B_y, and B_z). Figure 2.5b shows the simulated and experimental values of the magnetic field. The error between the experiment and model reaches a maximum of 26.12% corresponding to the z-axis and remains less than 9% for the other axis. We explain such results according to the error propagation from the pose reconstruction. The model correlation is biased by the maximum error values, which are registered at the peak/trough points of the magnetic field results (Figure 2.5b). However, overall the model fits the magnetic field behavior evidence of the root mean square (RMS) error values obtained for each component of the magnetic field ($\boldsymbol{B}$) (Figure 2.5b).

2.3 Experimental demonstrations

MagNeed is tested on a Teflon tube (5 mm inner diameter) that transports water, a 1 mm NdFeB bead (SP0100-50, SuperMagnetMan, USA), and non-magnetic particles (silica gel particles of 1-3 mm diameter). These experiments provide a millimeter-scale proof of concept for localized magnetic trapping and actuation in a confined fluidic channel. The NdFeB bead serves as the magnetically responsive test object, while the silica gel particles serve as nonmagnetic objects for examining interactions during flow and actuation. These materials and dimensions do not reproduce a specific biological environment. Extending the approach to micrometer-scale agents requires assessing the available magnetic force relative to hydrodynamic resistance under the relevant conditions, accounting for the size dependence of magnetic actuation [59]. The needle-shaped electromagnets (NSEs) are positioned around the tube, which is assembled within an acrylic box ($70 \times 90 \times 60$ mm^3). A gelatin structure is cured within the acrylic box to hold

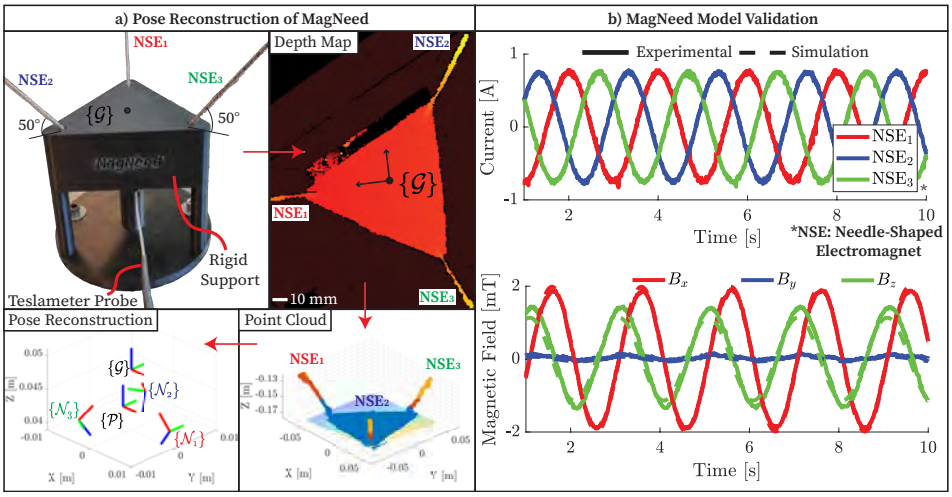


Figure 2.5: a) Pose reconstruction of MagNeed: the rigid support permits the placement of the needle-shaped electromagnets (NSE) and a high-precision teslameter probe (3MH3A-500MT, Senis AG, Switzerland). A 3D camera, located above the rigid support, acquires the depth map and point cloud data of the NSEs and surroundings. The acquired data are used to compute the pose of the NSEs, which are represented by the local frames ($\{\mathcal{N}_1\}$, $\{\mathcal{N}_2\}$, $\{\mathcal{N}_3\}$). The global reference frame ($\{\mathcal{G}\}$) is identified on top of the rigid support. (The color maps indicate the proximity of the point cloud to the 3D camera). b) MagNeed model validation using sinusoidal currents (amplitude: 0.75 A, frequency: 0.5 Hz, phases: 0, $-2\pi/3$, $2\pi/3$) on each NSE. The components (B_x, B_y, and B_z) of the magnetic field ($\boldsymbol{B}$) are acquired according to the teslameter probe frame ($\{\mathcal{P}\}$). The root mean square (RMS) error between simulation and experiments, according to B_x, B_y, and B_z signals, are 0.0047, 0.04, and 0.05, respectively.

the NSEs in a constant spatial configuration (Figure 2.4). The gelatin structure is fabricated by mixing 15% (by-weight) porcine gelatin powder (Dr. Oetker, Germany) with 85% water. The blend is heated up to a temperature of 70 ^{o}C to dissolve the gelatin powder. Finally, the blend is poured into the acrylic box and cured at room temperature. The experiments are conducted using a setup (Figure 2.4) designed for visualizing/tracking the magnetic bead, controlling the current, and reconstructing the pose of the NSEs. In order to test the near magnetic field gradients produced by the NSEs, we create a flow of water and silica gel particles within the tube. This section demonstrates experimentally the localized trapping and actuation applications shown in Figure 2.1. *Please refer to the supplementary video for the demonstration of these experiments.*

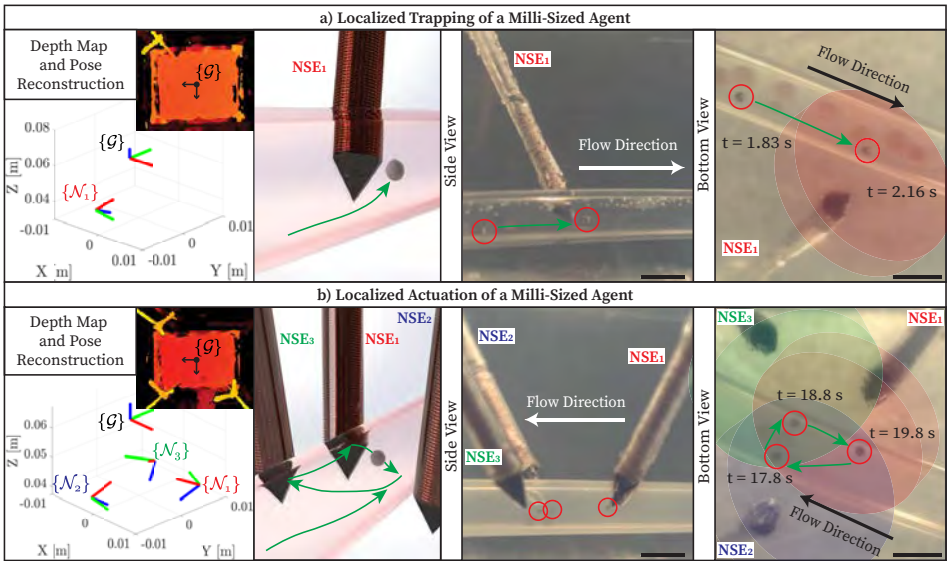


Figure 2.6: Localized trapping and actuation of a 1 mm NdFeB bead within a transparent Teflon tube. a) The magnetic bead moves downstream (t = 1.83 s), then the force generated by a single needle-shaped electromagnet (NSE) (steady current of 0.5 A) pulls the bead toward the inner wall of the tube (t = 2.16 s). The NSE efficiently traps the bead against the flow of water and silica gel particles. b) The magnetic bead performs a periodic motion among three points within the MagNeed workspace while a flow of water and silica gel particles is created along the tube. The NSEs are activated in a round-robin manner (f = 0.25 Hz, duty cycle = 33%, and amplitude of 0.75 A). The red circle encloses the 1 mm NdFeB bead utilized in the experiments. The colored regions at the bottom view illustrate the workspace of each NSE. (All scale bars are 5 mm).

2.3.1 Localized trapping of a milli-sized agent

This experiment shows the potential of a single needle-shaped electromagnet (NSE) for localized trapping of micro-/milli-sized agents in the perfusion of fluid within a microfluidic channel or *ex vivo* vasculatures. We compare the performance and power consumption required to trap a magnetic bead using an NSE and an electromagnetic system composed of 9 coils [92]. A syringe pump (NE-4000, New Era Pump Systems, USA) is used to transport water and milli-sized agents (the 1 mm NdFeB bead and silica gel particles) at a constant flow rate of 100 ml/min. Both NSE and electromagnetic system generate a magnetic force that pulls the magnetic bead to the inner wall of the tube. Our results show that the NSE can efficiently trap a magnetic bead while consuming 8 mW (using 0.1 A) compared to

the 2827 mW of the electromagnetic system. The trapping performance using the NSE is also tested by manually pumping water and silica gel particles (Figure 2.6a). Manual pumping permits the generation of flow rate peaks that cannot be recreated with the syringe pump. Using digital image processing, we estimate the peak flow rate from the observed motion of the silica gel particles, obtaining approximately 376 ml/min. Our results show that the magnetic bead is efficiently trapped and holds its position, while the NSE has a power consumption of 0.21 W (using 0.5 A). To complement the experimental results, we estimate the magnetic and hydrodynamic force scales. Approximating the 1 mm N52 NdFeB bead as a uniformly magnetized sphere with a representative remanence of 1.44 T gives a magnetic moment of approximately 6.0×10^{-4} A m^2. At the characterized reference position $(r, z) = (5, 0)$ mm, the radial magnetic field gradient is 3.5 T/m at 1 A. Assuming a radially oriented magnetic moment and linear scaling of the gradient with current, the corresponding radial magnetic force is approximately 0.21 mN at 0.1 A and 1.05 mN at 0.5 A. For comparison, the drag estimated using the Schiller–Naumann correlation for an isolated sphere at the mean tube velocity is approximately 3 μN at 100 ml/min and 27 μN at the estimated peak of 376 ml/min. These calculations provide approximate force scales; predicting the trapping threshold additionally requires the magnetic force direction, the local flow around the bead, and the effects of wall contact. The experiments establish two operating points for localized trapping: 0.1 A and 8 mW at a pump-controlled flow rate of 100 ml/min, and 0.5 A and 0.21 W during manually generated flow with an estimated peak of 376 ml/min. In the pump-controlled comparison, the NSE consumes approximately 1/350 of the reported actuation power of the nine-coil system for the tested trapping task. These operating points, together with the characterized current-to-field map and coil resistance, provide experimental benchmarks and model inputs for subsequent designs. They do not establish the minimum trapping current or maximum sustainable flow rate.

2.3.2 Localized actuation of a milli-sized agent

In this part of the study, we use MagNeed to actuate a magnetic bead. Each needle-shaped electromagnet (NSE) composing MagNeed has a workspace that covers the Teflon tube region (Figure 2.6). Here, we show two ex-

periments using MagNeed with a maximum power consumption of 0.5 W. (1) Localized actuation of a magnetic bead against a water flow and silica gel particles. (2) The interaction between a magnetic bead and silica gel particles in still water.

In the first experiment, the NSEs are activated in a round-robin manner. Simultaneously, water and silica gel particles are manually pumped along the tube (peak flow rate is approximately 114 ml/min) (Figure 2.6b). We observe that the magnetic bead tends to perform a periodic motion. Yet, when using a low actuation frequency ($f = 0.25$ Hz), the magnetic bead is prone to interact with the silica beads and follow the flow direction. By increasing the actuation frequency up to $f = 1$ Hz, the magnetic bead tends to keep its direction of motion against the flow direction (peak flow rate is approximately 233 ml/min). The capability of MagNeed to actuate a magnetic bead against a flow of water and silica gel particles suggests that our system can be suitable for *ex vivo* experiments using micro-agents in physiological fluid [98].

In the second experiment, we aim to test the force exerted on a magnetic bead to interact with silica gel particles in still water. The magnetic bead and particles are positioned within the Teflon tube, which is surrounded by MagNeed. The NSEs are powered in a round-robin manner using the same currents but a higher frequency ($f = 9$ Hz, duty cycle = 33%, and amplitude of 0.75 A). As a result, the magnetic bead experiences an uncontrolled motion, which is used to collide with and move the silica gel particles. Although the magnetic forces scale with the volume of the magnetic object, MagNeed can generate strong pulling forces that could be applied for impact-based interaction with soft tissues [103].

2.4 Conclusions and future work

This study introduces MagNeed – an electromagnetic actuation system that can determine a compact workspace around a target site using three needle-shaped electromagnets (NSEs). We propose an NSE design and an analytical model to represent the near magnetic field and gradients. Each NSE has a workspace in the shape of a cylinder (radius and height of 10 mm). The overall workspace of MagNeed is determined by the pose of the NSEs, which are computed using a reconstruction framework. The use of NSEs enables the generation of magnetic gradients (up to 3.5 T/m at 5 mm

from the NSE tip axis) that are comparable to those produced by state-of-the-art electromagnetic actuation systems. The surface temperature of an NSE is less than 42 ^{o}C, making MagNeed suitable for *in vitro* and *ex vivo* applications. We experimentally demonstrate the capabilities of MagNeed to locally trap and actuate a 1 mm NdFeB bead within a narrow tube that transports water and silica gel particles. Our results show that MagNeed keeps a maximum power consumption of 0.5 W.

Future studies include the steering of micro-/milli-sized agents using clinical imaging modalities (e.g., ultrasound, computed tomography) as feedback. We also plan to reduce the pose reconstruction uncertainty by implementing a real-time algorithm to classify the point cloud. Moreover, a cell toxicity study testing different bio-compatible coating materials is required to utilize MagNeed in contact with biological tissue. Finally, studying the magnetic field properties by reducing the NSE dimensions and modifying the core materials could lead to flexible NSE potentially applicable for laparoscopy-/endoscopy-assisted navigation of micro-agents.

CHAPTER
3

Collective behavior of magnetic microparticles

The following chapter is adapted from: ***J. J. Huaroto****, F. N. Piñan Basualdo, D. L. Roos Ariëns, and S. Misra. Non-uniform magnetic fields for collective behavior of self-assembled magnetic pillars, Swarm Intelligence, vol. 19, no. 4, pp. 317-332, 2025.*
The text, figures, and tables have been adapted for inclusion in this doctoral thesis.

Abstract

Programmable and self-assembled magnetic pillars are essential to expanding the application domain of magnetic microparticle collectives. Typically, the collective behavior of self-assembled magnetic pillars is carried out by generating uniform and time-varying magnetic fields. However, magnetic field-shaping capabilities employing non-uniform fields have not been explored for magnetic pillars. In this study, we generate non-uniform magnetic fields using a nine-coil electromagnetic system to achieve object manipulation, upstream/downstream locomotion, and independent actuation. We begin analyzing the static magnetic self-assembly of reduced iron microparticles and experimentally derive the average dimensions (height and diameter) of the resulting pillars. Subsequently, we delve into the collective dynamic response under non-uniform and time-varying magnetic fields, unveiling four distinct modalities. In order to demonstrate the versatility of our approach, we extend our study to the two-dimensional manipulation of a millimeter-sized glass bead using a precessing magnetic field describing a Lissajous curve. Moreover, we showcase the ability of magnetic pillars to adapt to confined and dynamic conditions within fluidic tubes. We finally present a noteworthy case where the nine-coil electromagnetic system independently actuates two clusters of magnetic pillars. Our study shows the potential of using non-uniform magnetic fields to actuate self-assembled magnetic pillars, enabling morphology reconfiguration capabilities, object manipulation, locomotion, and independent actuation.

3.1 Introduction

Collective behavior is a widespread phenomenon observed in nature across all scales [123], [124], where groups of individual agents exhibit different coordinated/collective actions [125]. This phenomenon has been studied extensively in fields such as biology [126] and physics [127]. The existence of coordinated behavior can lead to emergent properties not present in the individual agents themselves [128], which has inspired the development of multiple robotic systems [129], [130]. These collective properties can be utilized to accomplish complex tasks and adapt to dynamic environments [62].

In microrobotics, collective systems are advantageous over individual micro-agents since the latter are limited to performing specific tasks [131]. Collective systems can be reorganized *in situ* and accomplish complex actions such as manipulation and cargo transport [65], [132], [133]. Thus, understanding the interaction and self-organization of micro-agents is fundamental to developing novel collaborative applications. Furthermore, contactless actuation methods driven by magnetic fields [134], [135], acoustic waves [136], [137], and light [138] can be implemented under *in vitro* and *ex vivo* conditions, which enables their use in biomedical scenarios.

Magnetic actuation is a promising method for controlling collective systems due to its transparency and biocompatibility [51]. Magnetic collective systems can perform multimodal locomotion [63], morphology reconfiguration [64], object/droplet manipulation [139], [140], and cargo transportation [141]. Inspired from cilia structures in nature, recent studies have proposed magnetic micropillars for generating programmable metachronal waves [142], enhanced object manipulation [143], and liquid/solid transport [144], [145]. Magnetic micropillars are primarily fabricated using replica molding [146], [147] and self-assembly of magnetic soft composites (i.e., a blend of silicone and magnetic microparticles) [143], [144]. Mobile permanent magnets or static arrangements of electromagnetic coils have been used to actuate magnetic micropillar arrays [90]. Although the aforementioned fabrication methods permitted the engineering of the magnetization direction of micropillars, the pillars were attached to a substrate, restricting the morphology reconfiguration of pillars [145]. Finding a strategy to fabricate programmable pillars by magnetic self-assembly techniques is a current challenge in the development process [90].

Self-assembly is the spontaneous organization of individual agents into

a stable configuration. In particular, magnetic self-assembly has been applied to control the collective behavior of magnetic droplets [88], [89], soft ferromagnetic beads [148], and generate programmable pillars [133]. Self-assembled magnetic pillars use uniform magnetic fields for actuation, demonstrating efficient deployment on biological tissue, navigation through uneven surfaces, and cargo transportation [133], [135]. However, the homogeneous characteristics of the magnetic field can limit the field-shaping capabilities and the generation of gradients. Prior work in electromagnetic actuation exploits non-uniform magnetic fields generated by arrangements of multiple electromagnets for independent manipulation of microparticles [91], [92], [149]. Therefore, expanding the application domain of non-uniform magnetic fields to magnetic self-assembled magnetic pillars has the potential to achieve morphology reconfiguration and independent actuation of self-assembled magnetic pillar clusters.

To generate programmable and fabrication-free pillars based on the self-assembly of magnetic microparticles, we exploit the field-shaping capabilities of a nine-coil electromagnetic system [92]. This electromagnetic system can generate time-varying non-uniform magnetic fields to explore novel actuation modalities, which are used for object manipulation and locomotion within fluidic tubes. In order to show the potential of non-uniform magnetic fields, we exploit the spatially selective actuation of the electromagnetic system to perform independent actuation of magnetic pillar collectives. We start analyzing the static magnetic self-assembly of the microparticles by experimentally obtaining the average dimensions of the magnetic pillars. Additionally, we study the pillars' collective dynamic response to non-uniform and time-varying magnetic fields, identifying four primary modalities. Furthermore, we demonstrate that a precessing magnetic field describing a Lissajous curve (i.e., parametric curve composed of two perpendicular sinusoidal signals with different phases and frequencies) can be utilized for the two-dimensional manipulation of a millimeter-sized glass bead. We study the behavior of the pillars in confined and dynamic environments by actuating them within fluidic tubes. We showcase the capability of the nine-coil electromagnetic system by performing independent actuation of two clusters of magnetic pillars. Our results show that non-uniform magnetic fields are a promising approach for actuating self-assembled magnetic pillars, enabling reconfiguration capabilities, object manipulation, locomotion, and independent actuation.

3.2 Results and discussions

The generation of magnetic self-assembly and collective behavior is carried out in a nine-coil electromagnetic system (Figures 3.1A). Microparticles of reduced iron are placed into a polymethyl methacrylate (PMMA) box (base dimensions of 22 × 22 mm^2) along with pure water (i.e., Milli-Q water) and surfactant (details in Experimental Section). The PMMA box containing the microparticles and suspension is located within the electromagnetic system workspace. A constant current is used to power the coil #9 as it generates the magnetic self-assembly of microparticles (i.e., magnetic pillars). Thereon, the coils #1–8 generate non-uniform time-varying magnetic fields and gradients, which trigger the collective behavior of magnetic pillars (Figure 3.1B). The magnetization curve of reduced iron in Figure 3.1C shows negligible remanence (magnetically soft material) and a linear behavior if the applied magnetic field is below 250 mT. The morphology of the microparticles is acquired from scanning electron microscopy, which shows particles with non-uniform diameters (1-5 μm) (Figure 3.1D). In order to study the collective behavior of magnetic pillars, we divide our analysis into five sections. (1) Static self-assembly of microparticles of reduced iron. (2) Collective dynamic behavior of magnetic pillars. (3) Object manipulation. (4) Upstream/Downstream locomotion. (5) Independent actuation of two clusters of magnetic pillars.

3.2.1 Static magnetic self-assembly

We begin the study by analyzing the self-assembly of microparticles of reduced iron to create magnetic pillars. The microparticles are magnetized by an external magnetic field generated by coil #9, as depicted in Figure 3.2A. Using the current-to-field map of the system, the magnetic field generated using 1 A through coil #9 is shown for the XY-/YZ- planes, with black arrows representing the magnetic field direction (Figures 3.2B and C). In order to assess the uniformity of the magnetic field, we compute the curvature of the magnetic field at the center of the workspace. Unlike previous studies, which use permanent magnets at varying distances to modify the curvature [90], [133], we investigate the capabilities of an iron-cored electromagnet to create magnetic pillars while maintaining a constant distance from the workspace (25 mm). Considering the magnetic field is cylindri-

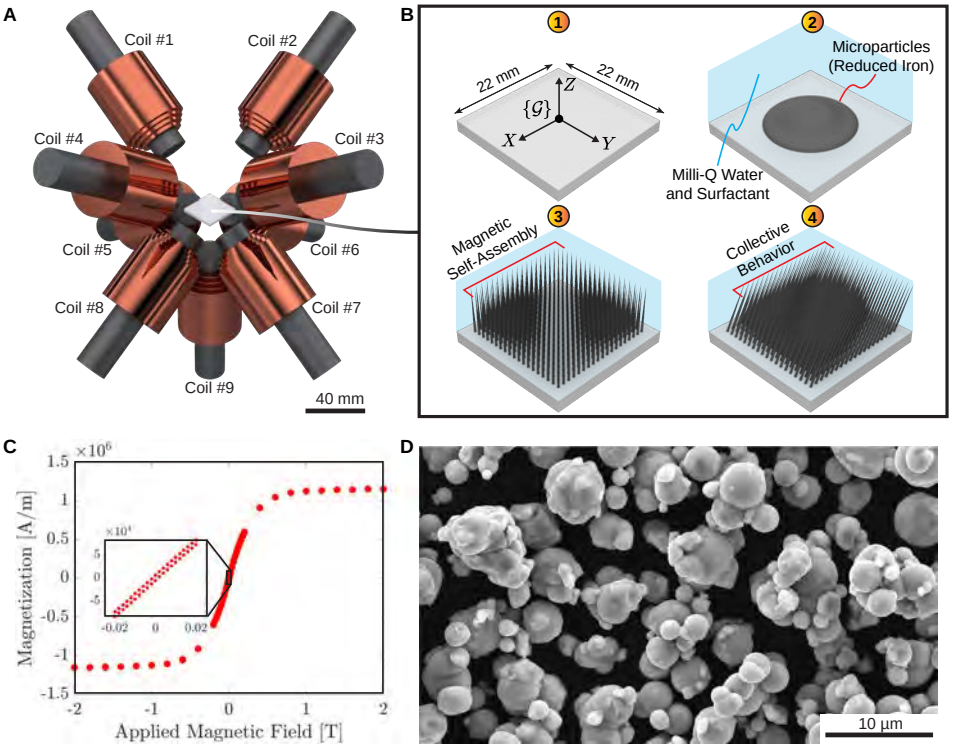


Figure 3.1: Self-assembled magnetic pillars generated from microparticles of reduced iron. (A) Nine-coil electromagnetic actuation system. (B) Generation of self-assembled magnetic pillars and collective behavior. The states of the microparticles of reduced iron are indicated as follows: ①, base of the workspace surrounded the electromagnetic actuation system; ②, magnetic microparticles of reduced iron located within the workspace along with Milli-Q water and surfactant; ③, the coil #9 is activated with a constant current to generate the self-assembled magnetic pillars; ④, the coils #1–8 are activated to generate non-uniform and time-varying magnetic fields, which produce the collective behavior of magnetic pillars. (C) Magnetization curve of reduced iron. (D) Scanning electron microscopy (SEM) of microparticles of reduced iron.

cal symmetric along the coil axis, the curvature along the X and Y-axis exhibit identical values for a static magnetic field. We compute the curvature along the Y-axis $\left(c_Y = -\frac{\mathrm{d}^2|\mathbf{B}(0,0,0)|}{\mathrm{d}Y^2}\right)$ as a function of the magnetic field ($\mathbf{B}(0,0,0)$). Our results demonstrate that the curvature (c_Y) varies linearly with the current of coil #9 and $\mathbf{B}(0,0,0)$ (Figure 3.2D).

By varying the current of coil # 9 ($I_9 = 2$–5 A) and mass of microparticles of reduced iron ($m_{ri} = 10$–40 mg), we estimate the magnetic field at the

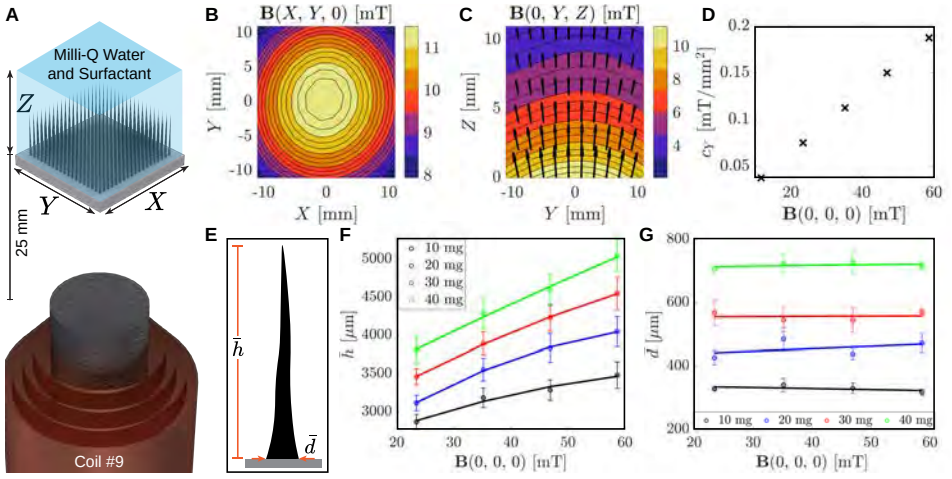


Figure 3.2: Characterization of static magnetic self-assembly of microparticles of reduced iron. (A) Workspace configuration with respect to coil #9. (B) Magnetic field map in XY plane. (C) Magnetic field map in YZ plane. (D) Confining curvature of the magnetic field (c_Y) as a function of the magnetic field at the center of the workspace ($\mathbf{B}(0,0,0)$). (E) Illustration of a magnetic pillar and average geometric parameters ($\bar{h}$ and $\bar{d}$). Experimental characterization of (F) the average height ($\bar{h}$) and (G) base diameter ($\bar{d}$) varying $\mathbf{B}(0,0,0)$ and mass of microparticles of reduced iron.

center of the workspace ($\mathbf{B}(0,0,0)$) and compute the average height ($\bar{h}$) and base diameter ($\bar{d}$) of magnetic pillars (Figure 3.2E). The cameras located at the side and above the workspace permit the acquisition of images, which are subsequently processed to compute $\bar{h}$ and $\bar{d}$, respectively (Geometry of magnetic pillars, Appendix). Figures 3.2F and 3.2G show that $\bar{h}$ increases according to the magnetic field while $\bar{d}$ remains approximately constant. On the other hand, $\bar{h}$ and $\bar{d}$ increase with the mass of reduced iron microparticles within the workspace. Across the tested conditions ($\mathbf{B}(0,0,0) \approx 23$–$59$ mT, $m_{ri} = 10$–40 mg), $\bar{h}$ ranges from approximately 2.9 to 5.0 mm, while $\bar{d}$ remains approximately constant with the magnetic field and increases with mass from approximately 0.33 mm (10 mg) to 0.72 mm (40 mg). It is worth noting that the increase of current through coil #9 is realized abruptly and that the coil is powered off ($I_9 = 0$ A) between measurements. This way, we reduce the influence between adjacent experiments.

3.2.2 Dynamic collective behavior

The study of magnetic self-assembly of microparticles of reduced iron provides valuable insights into the formation of magnetic pillars under non-uniform and static magnetic fields. In this section, we focus on exploring the collective behavior of these magnetic pillars when subjected to non-uniform and time-varying magnetic fields. To this end, we represent all magnetic fields at the center of the workspace ($\mathbf{p}_0 = [0,\, 0,\, 0]^T$) (Figure 3.3A). The magnetic pillars are generated from the static magnetic field created by coil #9 ($\bar{\mathbf{B}}(\mathbf{p}_0, I_9)$) (Figure 3.3A) while coils #1–8 are utilized to create time ($t \in \mathbb{R}^+$) varying magnetic fields ($\tilde{\mathbf{B}}(\mathbf{p}_0, t)$). By considering the spatial configuration of unitary vectors ($\hat{\boldsymbol{\mu}}$ and $\hat{\boldsymbol{\omega}}$), which are perpendicular to the base of the workspace and the oscillation plane, respectively. Prior research has explored precessing and oscillating fields to perform multimodal locomotion of self-assembled magnetic pillars [133], [135], [150]. Drawing inspiration from the previous body of literature, we define two distinct cases for the actuation modalities (Figure 3.3A). The resultant magnetic field the center of the workspace ($\mathbf{B}(\mathbf{p}_0)$) for cases 1 ($\hat{\boldsymbol{\omega}} \parallel \hat{\boldsymbol{\mu}}$) and 2 ($\hat{\boldsymbol{\omega}} \perp \hat{\boldsymbol{\mu}}$) are mathematically defined as follows:

$$\begin{cases} \text{Case 1: } \mathbf{B}(\mathbf{p}_0) = \bar{\mathbf{B}}(\mathbf{p}_0, I_9) + \tilde{\mathbf{B}}_X(\mathbf{p}_0, t) + \tilde{\mathbf{B}}_Y(\mathbf{p}_0, t) \\ \text{Case 2: } \mathbf{B}(\mathbf{p}_0) = \bar{\mathbf{B}}(\mathbf{p}_0, I_9) + \tilde{\mathbf{B}}_X(\mathbf{p}_0, t) + \tilde{\mathbf{B}}_Y(\mathbf{p}_0, t) + \tilde{\mathbf{B}}_Z(\mathbf{p}_0, t), \end{cases} \tag{3.1}$$

where the magnetic fields $\left(\tilde{\mathbf{B}}_X(\mathbf{p}_0, t),\, \tilde{\mathbf{B}}_Y(\mathbf{p}_0, t),\, \text{and}\, \tilde{\mathbf{B}}_Z(\mathbf{p}_0, t)\right)$ are the components of $\tilde{\mathbf{B}}(\mathbf{p}_0, t)$, and are represented by sinusoidal functions with amplitudes (A_X, A_Y, A_Z), frequencies (f_X, f_Y, f_Z), and phases (φ_X, φ_Y, φ_Z), respectively. In this chapter, an actuation modality refers to a prescribed magnetic field configuration and its associated collective response. A functionality refers to a task enabled by these responses, such as object manipulation or locomotion. According to the aforementioned cases and the observed collective behavior generated by the magnetic pillars, we propose the following actuation modalities: convergence, stretching, creep, and homogenization. The actuation modalities are experimentally tested using 30 mg of microparticles of reduced iron and using the parameters presented in Table 3.1 (Figure 3.3B). For providing a metric on the non-uniformity of the magnetic field, each modality is analyzed through the directional curvatures of the magnetic field at the center

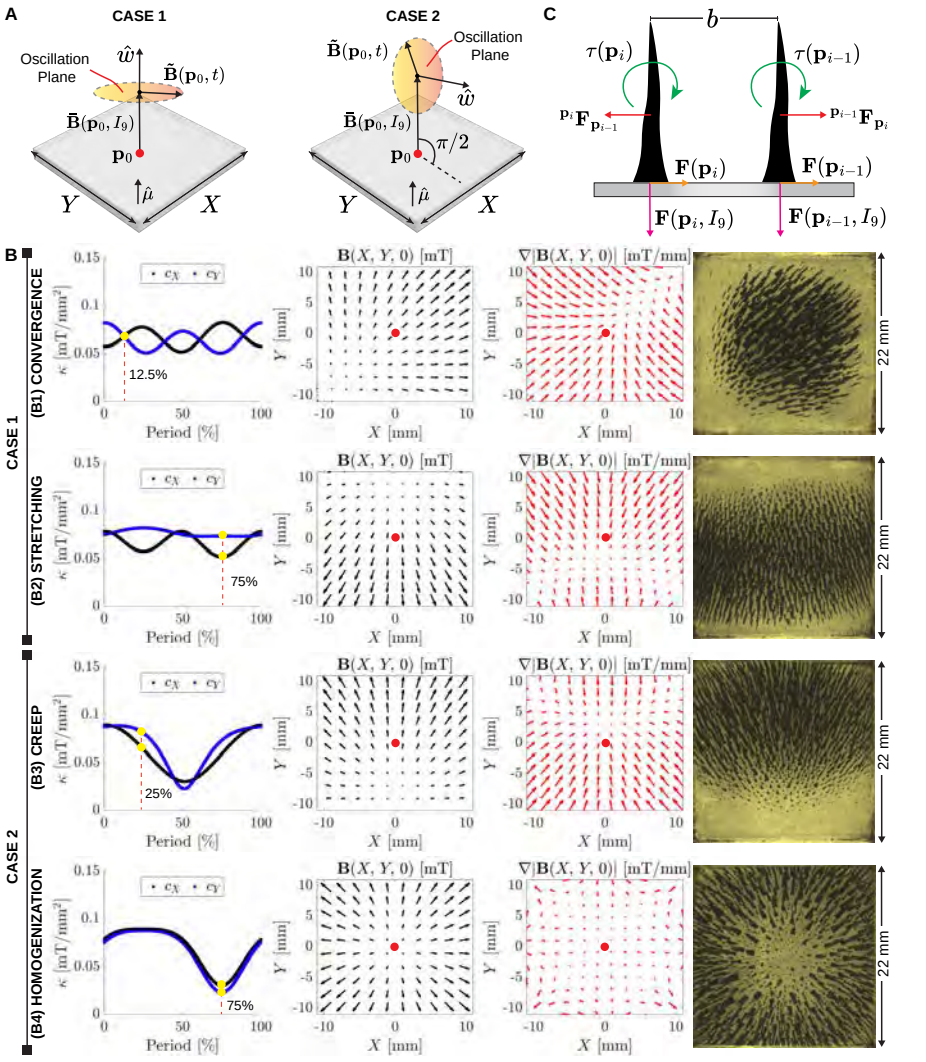


Figure 3.3: Collective behavior of magnetic pillars. (A) Two cases of actuation modalities according to the spatial configuration of unitary vectors ($\hat{\boldsymbol{\mu}}$ and $\hat{\boldsymbol{\omega}}$) perpendicular to the base of the workspace and oscillation plane, respectively. The point ($\mathbf{p}_0 = [0, 0, 0]^T$) is defined to illustrate the components of the magnetic field $\left(\bar{\mathbf{B}}(\mathbf{p}_0, I_9) \text{ and } \tilde{\mathbf{B}}(\mathbf{p}_0, t)\right)$. (B) Four actuation modalities are proposed to generate different collective behaviors of magnetic pillars. The non-uniformity of the magnetic field is analyzed using directional curvatures ($\kappa = [c_X, c_Y]$) at $\mathbf{p}_0$. In addition, the magnetic field ($\mathbf{B}(X, Y, 0)$), gradients ($\nabla|\mathbf{B}(0, 0, 0)|$), and an image frame of the collective behavior of magnetic pillars are provided. The red dots indicate the point ($\mathbf{p}_0$). *Please refer to the accompanying video* (S1 Video, Supplementary information). (C) Illustration of the external ($\mathbf{F}(\mathbf{p}_i)$, $\mathbf{F}(\mathbf{p}_{i-1})$, $\mathbf{F}(\mathbf{p}_i, I_9)$, $\mathbf{F}(\mathbf{p}_{i-1}, I_9)$), internal forces ($^{\mathbf{p}_{i-1}}\mathbf{F}_{\mathbf{p}_i}$ and $^{\mathbf{p}_i}\mathbf{F}_{\mathbf{p}_{i-1}}$), and torques ($\boldsymbol{\tau}(\mathbf{p}_i)$ and $\boldsymbol{\tau}(\mathbf{p}_{i-1})$) applied to adjacent magnetic pillars.

Table 3.1: Actuation modalities for self-assembled magnetic pillars

Modality	I_9 [A]	A_X [mT]	A_Y [mT]	A_Z [mT]	f_X [Hz]	f_Y [Hz]	f_Z [Hz]	φ_X [rad]	φ_Y [rad]	φ_Z [rad]
Convergence	2	10	10	0	1	1	0	0	$\pi/2$	0
Stretching	2	0	10	0	0	1	0	0	0	0
Creep	2	0	8	8	0	1	1	0	0	$\pi/2$
Homogenization	2	0	0	8	0	0	1	0	0	0

of the workspace $\left(\kappa = \left[c_X = -\frac{\mathrm{d}^2|\mathbf{B}_{(\mathbf{0},\mathbf{0},\mathbf{0})}|}{\mathrm{d}X^2},\ c_Y = -\frac{\mathrm{d}^2|\mathbf{B}_{(\mathbf{0},\mathbf{0},\mathbf{0})}|}{\mathrm{d}Y^2}\right]\right)$. Moreover, the magnetic field ($\mathbf{B}(X,Y,0)$), gradient ($\nabla|\mathbf{B}(X,Y,0)|$), and image frame are shown at a specific percentage of the oscillation period (Figure 3.3B).

Prior to discussing each actuation modality, we provide an illustration that depicts the magnetic forces and torques acting on two adjacent pillars (identified by the subscripts "i" and "$i-1$") exposed to a non-uniform magnetic field. We assume that each magnetic pillar is composed of ($N \in \mathbb{N}$) microparticles of reduced iron. The pillars are not permanently bonded to one another or to a common substrate; they form a reconfigurable collective coupled through magnetic interactions. By powering electromagnetic coil #9, we have demonstrated the generation of magnetic pillars. Each pillar behaves as a magnetic dipole since the microparticles of reduced iron become magnetized in response to the external magnetic field. The magnetic gradients generated by powering the coil #9 create forces ($\mathbf{F}(\mathbf{p}_i, I_9)$ and $\mathbf{F}(\mathbf{p}_{i-1}, I_9)$) that are oriented toward the base of the workspace and maintain the shape of the magnetic pillars. Furthermore, each pillar interacts with its adjacent pillar through a repulsive force ($^{\mathbf{p}_{i-1}}\mathbf{F}\mathbf{p}_i = -\,^{\mathbf{p}_i}\mathbf{F}\mathbf{p}_{i-1}$), which keeps the pillars separated by a distance ($b \in \mathbb{R}^+$) (Figure 3.3C). Using coils #1-8, we generate non-uniform and time-varying magnetic fields and gradients. These magnetic fields and gradients exert torques ($\boldsymbol{\tau}(\mathbf{p}_i)$) and ($\boldsymbol{\tau}(\mathbf{p}_{i-1})$) as well as forces ($\mathbf{F}(\mathbf{p}_i)$) and ($\mathbf{F}(\mathbf{p}_{i-1})$) on the magnetic pillars, making them susceptible to tilting and slipping, respectively (Figure 3.3C). It is important to note that for analysis, we are neglecting friction and viscous forces.

To estimate the magnetic loading associated with static self-assembly, we consider coil #9 alone, powered at $I_9 = 2$ A. A representative pillar is approximated as an equivalent solid cone of reduced iron. Using $\bar{h} \approx 2.9$ mm and $\bar{d} \approx 0.33$ mm gives a volume of approximately 8.3×10^{-11} m^3. At the workspace center, located on the electromagnet axis and 25 mm

above it, the static field is 21.1 mT. The measured magnetization curve gives $M \approx 8\times10^4$ A/m (Figure 3.1C), yielding a nominal magnetic moment of approximately 6.6×10^{-6} A m^2. An axial gradient of 1.6 T/m, obtained from the field map and scaled to this current (Figure 3.2C), gives a magnetic force of order 10 μN per pillar toward the supporting surface. This provides a reference under the solid-cone approximation. During dynamic actuation, the additional fields generated by coils #1–8 modify both the local magnetization and field gradients, changing the resulting forces and torques over the actuation cycle.

By understanding the influence of the magnetic field and gradients, we can gain further insights into the collective behavior of magnetic pillars under non-uniform and time-varying magnetic fields. We begin by discussing the actuation modalities corresponding to case 1. The magnetic field oscillates in a parallel plane with respect to the workspace. Thus, the forces ($\mathbf{F}(\mathbf{p}_i, I_9)$) remain constant during a complete period (Figure 3.3C). Moreover, the torques ($\boldsymbol{\tau}(\mathbf{p}_i)$) and forces ($\mathbf{F}(\mathbf{p}_i)$) determine the motion of the magnetic pillar based on the time-varying magnetic fields and gradients, respectively. In particular, the convergence modality exhibits a rotating magnetic field, causing the curvatures along the X and Y-axes to oscillate reciprocally (Figure 3.3(B1)). The magnetic pillars align themselves according to the magnetic field (black arrows), while the gradients (red arrows) generate forces, which tend to gather the magnetic pillars toward the center of the workspace, forming a circumference (S1 Video: 00:07–00:34 s, Supplementary information). The circularity of this circumference can be controlled by adjusting the values of the magnetic field amplitudes (A_X and A_Y). On the other hand, the stretching modality can be considered a subcase of the convergence modality, where the magnetic field along the X-axis is set to zero ($A_X = 0$ mT). As a consequence, the collective of magnetic pillars tends to stretch along the X-axis over time (S1 Video: 00:35–01:01 s, Supplementary information). Typically, the collective can be stretched along different axes by adjusting the values of A_X and A_Y.

For actuation modalities corresponding to case 2, the effective magnetic field along the Z-axis varies according to the amplitude of the oscillating magnetic field along the Z-axis (A_Z). Therefore, we impose the following ratio to maintain the magnetic self-assembly of microparticles of reduced iron: $\frac{A_Z}{|\bar{\mathbf{B}}(\mathbf{p}_0, I_9)|} < 1$. In our experiments, we utilize a maximum ratio (≈ 0.34) such that the magnitude of the static magnetic field predominates over the

oscillating one. Since the effective magnetic field along the Z-axis oscillates over time. The curvatures along the X and Y-axes reach a minimum value when $\bar{\mathbf{B}}(\mathbf{p}_0, I_9)$ and $\tilde{\mathbf{B}}(\mathbf{p}_0, t)$ have opposite directions. In particular, the creep modality uses a rotating magnetic field with components along the Y and Z-axes (A_Y and A_Z) (Figure 3.3(B3)). This way, the magnetic pillars are displaced in response to the resultant magnetic field. (S1 Video, Supplementary information: 01:02–01:26 s). The predefined maximum ratio (≈ 0.34) prevents the magnetic pillars from rotating as their base remains in contact with the base of the workspace. Furthermore, the creep orientation can be modified by introducing a component along the X-axis (A_X) with the same frequency and phase as the one along the Y-axis ($f_X = f_Y$ and $\varphi_X = \varphi_Y$). This actuation modality is subsequently used for experiments involving the motion of magnetic pillars in fluidic tubes. The homogenization modality is a particular case of the creep modality, generating only an oscillating magnetic field along the Z-axis. The simulation and experimental results show that the magnetic pillars tend to move toward the boundaries and the center of the workspace (S1 Video, Supplementary information: 01:27–01:56 s). This collective behavior leads to a reorganization (i.e., homogenization) of magnetic pillars within the workspace. We utilize the homogenization modality to reorganize the magnetic pillars between experiments.

3.2.3 Object manipulation

The dynamic collective behavior of magnetic pillars, achieved through the self-assembly of iron microparticles, presents a concept primarily explored for the assembly/disassembly of various spherical particles (diameter ≤ 1 mm and mass < 1 mg) [133]. However, the challenge remains in achieving two-dimensional and dexterous manipulation of millimeter-sized objects while simultaneously preserving the positional integrity of the collective of magnetic pillars. In this study, we conduct the manipulation of a 2 mm glass bead (mass of 9.3 mg) using magnetic pillars within a workspace containing Milli-Q water and surfactant. The microparticles of reduced iron (20 mg mass) and the bead are positioned within the workspace while powering coil #9 ($\bar{\mathbf{B}}(\mathbf{p}_0, I_9)$ to generate the magnetic pillars. Next, we employ a time-varying magnetic field ($\tilde{\mathbf{B}}(\mathbf{p}_0, t)$) utilizing coils #1–8 to orient the magnetic pillars. The resulting precessing magnetic field is illustrated

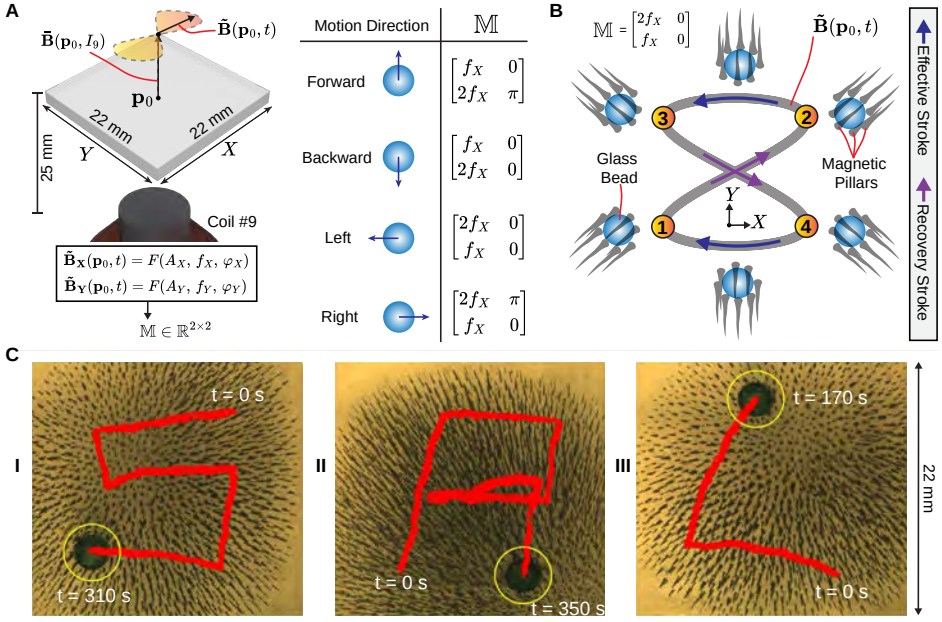


Figure 3.4: Manipulation of a passive object (2 mm glass bead). (A) The components of the magnetic field: Constant magnetic field generated by the coil #9 ($\bar{\mathbf{B}}(\mathbf{p}_0, I_9)$), and oscillating magnetic field $\left(\tilde{\mathbf{B}}(\mathbf{p}_0, t)\right)$ with amplitudes A_X and A_Y along the X and Y-axis, respectively. The matrix ($\mathbb{M} \in \mathbb{R}^{2\times2}$), which encompasses the frequencies (f_X, f_Y) and phases (φ_X, φ_Y), is used to encode the direction of motion of the bead. (B) Illustration of the periodic motion performed by the magnetic pillars to move the 2 mm glass bead towards the left. The precessing magnetic field $\left(\tilde{\mathbf{B}}(\mathbf{p}_0, t)\right)$ describes a Lissajous curve according to the corresponding matrix $\mathbb{M}$. The effective stroke is achieved within the intervals ②→③ and ④→①, whereas the recovery stroke is performed within ①→② and ③→④. (C) Manipulation of a 2 mm glass bead (encircled in yellow). The images show the trajectory (in red) of the glass bead as it describes the alphabet I: "S," II: "R," and III: "L," respectively. The insets show the initial and final time stamps. *Please refer to the accompanying video* (S2 Video, Supplementary information).

in Figure 3.4A and mathematically represented as follows:

$$\mathbf{B}(\mathbf{p}_0) = |\bar{\mathbf{B}}(\mathbf{p}_0, I_9)|\hat{\boldsymbol{k}} + 10\sin(2\pi f_X t + \varphi_X)\hat{\boldsymbol{i}} + 10\sin(2\pi f_Y t + \varphi_Y)\hat{\boldsymbol{j}}\,[\mathrm{mT}], \tag{3.2}$$

where $I_9 = 2$ A and the unitary vectors ($\hat{\boldsymbol{i}}$, $\hat{\boldsymbol{j}}$ and $\hat{\boldsymbol{k}}$) corresponds to the X-/Y-/Z-axis, respectively. The precessing magnetic field ($\tilde{\mathbf{B}}(\mathbf{p}_0, t)$) with components along the X-/Y-axis describes a Lissajous curve depending on the parameters of frequency (f_X and f_Y) and phase (φ_X and φ_Y). We

arrange these parameters as components of a matrix $\left(\mathbb{M} = \begin{bmatrix} f_X & \varphi_X \\ f_Y & \varphi_Y \end{bmatrix}\right)$, which is used to encode the following fundamental motion directions: forward, backward, left, and right (Figure 3.4A). Figure 3.4B depicts the Lissajous curve used to move the bead toward the left direction $\left(\mathbb{M} = \begin{bmatrix} 2\,f_X & 0 \\ f_X & 0 \end{bmatrix}\right)$.

For the analysis, we divide the Lissajous curve into four segments (Figure 3.4B). We experimentally demonstrate that the Lissajous curve permits the relative displacement of the glass bead with respect to the magnetic pillars collective (Motion analysis of the glass bead, Appendix). The intervals ④→① and ②→③ allow for the effective stroke of the bead. Previous research using precessing magnetic fields demonstrates that the Lissajous curve can generate non-reciprocal motion of soft magnetic microparticles [151]. Based on the experimental results depicted in Figure 3.8 (Appendix, p. 62), we demonstrate that the trajectory described by the glass bead can be decomposed into translation and a cyclic motion following the input Lissajous curve. During an actuation cycle, the bead follows the pillars' motion. However, at the end of the cycle, the bead does not return to its initial position, exhibiting a net translation. Since this displacement is always in the same direction relative to the input Lissajous curve, it suffices to change the input signal orientation to select the advancement direction. In the object manipulation experiments, the four motion directions are tested to replicate trajectories that depict the alphabet "S," "R," and "L" (representing the initials of Surgical Robotics Laboratory) (Figure 3.4C).

3.2.4 Upstream/downstream locomotion

Fluid flow can displace magnetic pillars and hinder their controlled motion within confined channels. We first evaluate whether the collective can remain localized under an imposed fluid flow. To this end, we place 10 mg of microparticles of reduced iron inside a glass tube (8 mm inner diameter), connected by one of its ends to a syringe pump. The magnetic pillars are formed by circulating a constant current through coil #9 ($I_9 = 2$ A). Milli-Q water is automatically pumped at the maximum flow rate capacity (100 ml/min) to evaluate the displacement of the magnetic pillars (S3 Video: 00:07–00:40 s, Supplementary information). Our results show that the centroid of magnetic pillars moves approximately 1.4 mm (for a duration of 15 s). Despite the susceptibility of the magnetic pillars to be carried away by

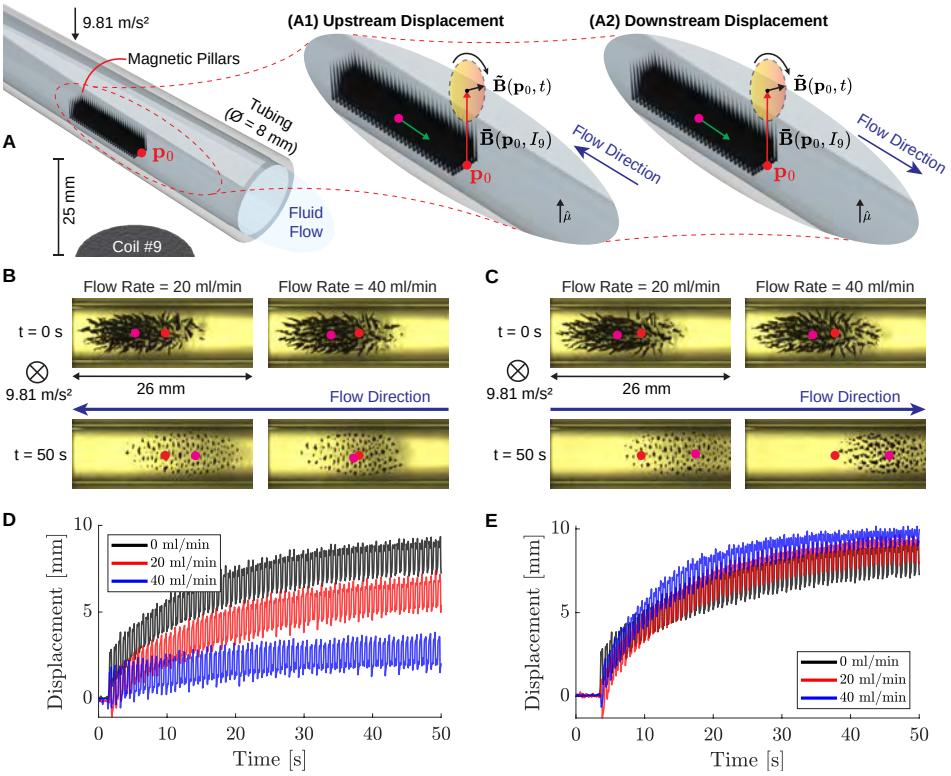


Figure 3.5: Motion of magnetic pillars within a tube transporting Milli-Q water. (A) Magnetic pillars formed from 10 mg of microparticles of reduced iron exposed to a constant magnetic field ($\bar{\mathbf{B}}(\mathbf{p}_0, I_9)$, with $I_9 = 2$ A). The creep modality, which employs a rotating magnetic field ($\tilde{\mathbf{B}}(\mathbf{p}_0, t)$), is utilized to move the pillars upstream (A1) and downstream (A2) the fluid flow. The pink and red dots represent the pillars centroid and center of the workspace ($\mathbf{p}_0$), respectively. Top views of the starting and final frames of magnetic pillars displacing upstream (B) and downstream (C) for 20 ml/min and 40 ml/min flow rates. Upstream (D) and Downstream (E) displacement of the magnetic pillars centroid. The frames corresponding to the times t = 0 s and 50 s show the magnetic pillar states when the electromagnetic system is deactivated and activated, respectively. S3 Video, Supplementary information shows the resistance of the magnetic pillar collective to fluid flow and its upstream and downstream locomotion under magnetic actuation.

the fluid flow, we observe that the collective of pillars withstands the drag forces acting upon them. Furthermore, experiments with 80 ml/min and 60 ml/min show a displacement of less than 0.5 mm for a duration of 15 s.

Following our study, we test the locomotion of magnetic pillars upstream and downstream using the creep modality ($f_Y = f_Z = 1.5$ Hz and $A_Y = A_Z = 8$ mT) within a fluidic tube (Figure 3.5A). The experiments

are carried out for a duration of 50 s (Figures 3.5B and 3.5C). The centroid of the magnetic pillars is tracked while performing periodic motion according to the actuation frequency. The black lines depicted in Figures 3.5D and E represent the displacement in still water (0 ml/min). As the flow rate increases (20 ml/min and 40 ml/min), we observe that the upstream displacement of the centroid decreases by 47.3% and 64.0%, respectively (Figure 3.5D). Conversely, for downstream experiments, the centroid displacement increases with the flow rate by 13.3% and 29.0%, respectively (Figure 3.5E). Our results demonstrate that the magnetic pillars generated using 10 mg of reduced iron can navigate upstream and downstream, utilizing a maximum flow rate of 40 ml/min. Furthermore, the magnetic pillars can structurally withstand a fluid flow of 100 ml/min. It is worth noting that the saturation tendency on the displacement observed in Figures 3.5D and E is due to the gradient generated by coil #9, which attracts the magnetic pillars toward the center of the workspace. In order to reach a more significant displacement, the electromagnetic coil arrangement can be assembled at the end effector of robotic platforms to constantly relocate the magnetic pillars collective [116], [152]. The upstream experiment tests whether magnetic actuation can produce net collective displacement against an imposed fluid flow. Fluid viscosity and pillar dimensions affect hydrodynamic resistance, while confinement and wall contact influence retention and sliding.

3.2.5 Independent actuation of magnetic pillar clusters

The previous experiments are carried out using non-uniform and time-varying magnetic fields, which are the result of imposing a magnetic field at the center of the workspace ($\mathbf{p}_0 = [0,\, 0,\, 0]^T$). Here, we leverage the capabilities of nine iron-cored coils to perform the independent motion of two clusters of magnetic pillars. To this end, we impose two rotating magnetic fields ($\tilde{\mathbf{B}}(\mathbf{p}_1, t)$ and $\tilde{\mathbf{B}}(\mathbf{p}_2, t)$) defined at two points ($\mathbf{p}_1 = [-8,\, 0,\, 0]^T$ mm and $\mathbf{p}_2 = [8,\, 0,\, 0]^T$ mm) within the workspace (Figure 3.6A). The magnetic fields exhibit opposite directions, characterized by amplitudes of 8 mT and frequencies of 1 Hz. The resultant magnetic fields ($\mathbf{B}(\mathbf{p}_1)$ and $\mathbf{B}(\mathbf{p}_2)$) are defined as follows:

$$\begin{cases} \mathbf{B}(\mathbf{p}_1) = |\bar{\mathbf{B}}(\mathbf{p}_1, I_9)|\hat{\boldsymbol{k}} - 8\sin(2\pi t)\hat{\boldsymbol{j}} + 8\cos(2\pi t)\hat{\boldsymbol{k}}\,[\mathrm{mT}] \\ \mathbf{B}(\mathbf{p}_2) = |\bar{\mathbf{B}}(\mathbf{p}_2, I_9)|\hat{\boldsymbol{k}} + 8\sin(2\pi t)\hat{\boldsymbol{j}} + 8\cos(2\pi t)\hat{\boldsymbol{k}}\,[\mathrm{mT}], \end{cases} \tag{3.3}$$

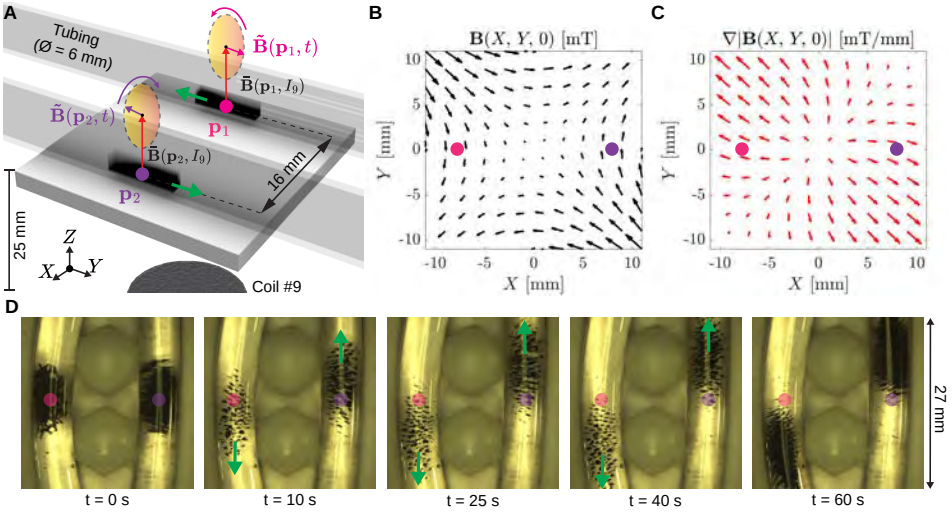


Figure 3.6: (A) Illustration of the independent actuation of two clusters of magnetic pillars. The magnetic pillars are formed from 10 mg of microparticles of reduced iron and the component of the magnetic field ($\bar{\mathbf{B}}(\mathbf{p}_0, I_9)$, with $I_9 = 2$ A). Two points ($\mathbf{p}_1$ and $\mathbf{p}_2$) within the workspace are used to generate two different oscillating magnetic fields $\left(\tilde{\mathbf{B}}(\mathbf{p}_1, t) \text{ and } \tilde{\mathbf{B}}(\mathbf{p}_2, t)\right)$. (B) and (C) show the magnetic field and gradient within the workspace at t = 0.25 s (25 % of the period). The pink and purple dots represent the points $\mathbf{p}_1$ and $\mathbf{p}_2$, respectively. (D) Time frames show the independent motion of two clusters of magnetic pillars. *Please refer to the accompanying video* (S4 Video, Supplementary information).

where $\hat{\boldsymbol{\imath}}$, $\hat{\boldsymbol{\jmath}}$ and $\hat{\boldsymbol{k}}$ are the unitary vectors along the X-/Y-/Z-axis, respectively. Moreover, $|\bar{\mathbf{B}}(\mathbf{p}_1, I_9)| \approx |\bar{\mathbf{B}}(\mathbf{p}_2, I_9)| = 19.3$ mT, since the magnetic field generated by the coil #9 is cylindrical symmetric with respect along the coil axis (Figures 3.2B and 3.2C). Using the current-to-field map of the system, we obtain the magnetic field and gradients at t = 0.25 s, where the pink and purple points represent $\mathbf{p}_1$ and $\mathbf{p}_2$, respectively (Figures 3.6B and 3.6C). For the experiments, two transparent tubes (6 mm inner diameter) are filled with Milli-Q water and 10 mg of microparticles each. The tubes are located within the workspace using two plastic dome nuts (Figure 3.6D). The microparticles of reduced iron are approximately located at the center of each tube. Thereon, the electromagnetic system is activated according to (3.3) as the magnetic pillars move toward opposed directions.

3.3 Conclusions

We introduce non-uniform magnetic fields to explore the collective behavior of self-assembled magnetic pillars formed from microparticles of reduced iron. Our study utilizes an electromagnetic system composed of nine iron-cored coils, which provide field-shaping and spatially selective actuation capabilities within the workspace. We experimentally determine the dimensions of self-assembled magnetic pillars and investigate four different actuation modalities. Through experimental validation, we demonstrate that a precessing magnetic field describing a Lissajous curve can be used for in-plane manipulation of a millimeter-sized glass bead. Furthermore, we examine the performance of magnetic pillars within a fluid-filled tube, providing insights into their ability to withstand and move under varying fluid flow conditions. Lastly, we leverage the potential of the nine-coil electromagnetic system to achieve the independent actuation of two clusters of magnetic pillars. Our results open up new avenues for further exploration and applications of self-assembled magnetic pillars exposed to non-uniform and time-varying magnetic fields.

3.4 Experimental section

Material and Fabrication Details: The magnetic pillars are made of microparticles of reduced iron (12310, Sigma-Aldrich, USA). The microparticles are dispersed in Milli-Q water containing 1 wt% surfactant (Tween 80, Sigma-Aldrich, USA), added to improve wetting and reduce adhesive surface interactions during actuation. The workspace containing microparticles and suspension is a box (base dimensions: 22×22 mm^2) fabricated by laser-cutting (Speedy 300, Trotec Laser, Austria) parts of polymethyl methacrylate (PMMA) sheets (3 mm thickness) and assembling them using transparent glue. For acquiring the magnetization curve, we prepare a sample of microparticles suspended (1:1 mass ratio) in polydimethylsiloxane (PDMS) (Sylgard 184, #101697, UK). The suspension is cured into a cylindrical mold (5 mm diameter and 0.6 mm height) at 70 °C for two hours and placed in the vibrating-sample magnetometer. For object manipulation experiments, a 2 mm diameter glass bead (SFVEBO0020000, RGPBALLS S.R.L, Italy) is employed. In order to facilitate the tracking algorithm, the bead is conveniently stained green using a permanent marker.

Instrumentation: The mass of microparticles of reduced iron utilized in this study is measured on a high-precision scale (SECURA225D-1S, Sartorius Lab Instruments GmbH & Co. KG, Germany). The microparticles are visualized using a scanning electron microscope (JSM-7200F, JEOL, Japan) to reveal further morphological details. In addition, the magnetization curve of microparticles of reduced iron is obtained using a vibrating-sample magnetometer (GMW 3474-140, GMW Associates, USA). Two cameras (FLIR, Wilsonville, USA), positioned above and to the side of the workspace, are equipped with microscope objectives (Optem FUSION, Qioptiq Ltd., UK) to capture high-resolution images (2048 × 2048 pixels) with a pixel size of 17.5 μm. For experiments involving fluid flow, a syringe pump (NE-4000, New Era Pump Systems, USA) generates constant flow rates of Milli-Q water within a transparent tube.

Simulations and Image Processing: The simulations of the magnetic field and gradients are obtained from a current-to-field map [153] that is implemented in MATLAB (version 2023a, MathWorks, USA) for visualization. The algorithms for tracking and computing geometric parameters (average height and diameter) of magnetic pillars are implemented in a custom script of MATLAB. *Please refer to the accompanying text for details* (Tracking of magnetic pillars, Appendix).

Appendix

Geometry of magnetic pillars

We experimentally obtained average values for the height and base diameter of magnetic pillars. The magnetic pillars are generated using coil #9 of a nine-coil electromagnetic system, while videos are recorded from both top and side views (Figure 3.7A). All images are analyzed using a custom script in MATLAB (version 2023a, MathWorks, USA). Images obtained from the side view of the workspace are cropped to obtain an image of length ($L \in \mathbb{N}$) and height ($H \in \mathbb{N}$) in pixels. The cropped image is converted from color to grayscale, and subsequently binarized (Figures 3.7B① and 3.7B②). In the binary image, the position of a pixel along the horizontal axis is identified by the subscript ($j \in \mathbb{N} \cap [1, L]$). The number of black pixels (bp_j) along the jth column is used to determine the height of each column (h_j) as follows:

$$h_j = H - bp_j, \tag{3.4}$$

and is subsequently plotted as a black line (Figure 3.7B③). Furthermore, the root mean square value of h_j (represented as a red dashed line) is multiplied by a pixel to micrometers conversion parameter ($\lambda \in \mathbb{R}^+$) to calculate the average height of magnetic pillars ($\bar{h}$) in micrometers:

$$\bar{h} = \lambda \sqrt{\frac{1}{L} \sum_{j=1}^{L} h_j^2}. \tag{3.5}$$

In order to obtain the average diameter ($\bar{d}$) of magnetic pillars, we analyzed a cropped region measuring 10×10 mm^2 from the images captured by the top camera. Prior to binarizing the images, we enhanced their contrast using morphological top-hat filtering and contrast adjustment (Figure 3.7C①). Subsequently, the binarized images allowed us to identify the number of magnetic pillars ($N_{mp} \in \mathbb{N}$) and their centers of gravity. The ith magnetic pillar has a centroid ($\mathbf{p}_i$) with coordinates along X and Y-axis (xc_i and yc_i, respectively) (Figure 3.7C②). We obtained the projected area ($A_i \in \mathbb{R}^+$) of each magnetic pillar, which is used to calculate the diameter ($\bar{d}_i$) using the following equation:

$$\bar{d}_i = \lambda \sqrt{\frac{4A_i}{\pi}}. \tag{3.6}$$

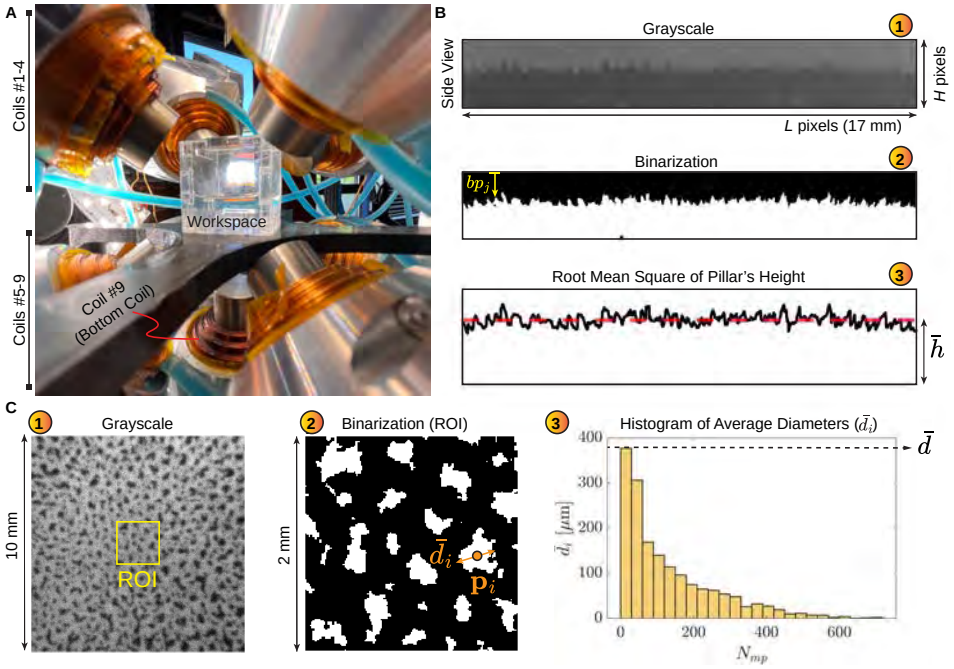


Figure 3.7: (A) Nine-coil electromagnetic system used for experiments with magnetic pillars [92]. (B) Image processing to obtain the average height ($\bar{h}$) of magnetic pillars. The color images are processed as follows: ①, Crop and grayscale conversion; ②, Binarization showing the black pixels (bp_i) along the jth column; ③, The pillar's profile is identified and subsequently extracted as a dark line. The root mean square value of such a line is multiplied by a conversion factor to calculate $\bar{h}$. (C) The procedure to compute the average diameter ($\bar{d}$) of the base of magnetic pillars involves the following steps: ①, Crop and grayscale conversion; ②, Binarization to obtain the average diameter ($\bar{d}_i$) and position ($\mathbf{p}_i$) of each magnetic pillar; ③, Histogram showing the distribution of values of $\bar{d}_i$ according to the number of magnetic pillars (N_{mp}). The value of $\bar{d}$ corresponds to the maximum value depicted in the histogram.

Finally, the values of d_i are plotted in a histogram to obtain the average diameter ($\bar{d}$) of all magnetic pillars (Figure 3.7C③).

Tracking of magnetic pillars

The tracking of magnetic pillars is accomplished by calculating the centroid of the collective. To achieve this, we analyze images obtained from the top view of the workspace using a custom MATLAB script (version 2023a, MathWorks, USA). Following the procedure to obtain the values of $\bar{d}$, we convert the color images to binary and subsequently compute the center of

gravity of each pillar (p_i), which has coordinates along X and Y-axis (xc_i and yc_i, respectively). Moreover, we obtain the projected areas (A_i) of each magnetic pillar (Figure 3.7C②). Using these parameters, we determine the centroid (p_{CM}) of the collective of pillars according to the following equation:

$$p_{CM} = \left[\frac{\sum_{i=1}^{N_{mp}} xc_i A_i}{\sum_{i=1}^{N_{mp}} A_i}, \frac{\sum_{i=1}^{N_{mp}} yc_i A_i}{\sum_{i=1}^{N_{mp}} A_i} \right]. \tag{3.7}$$

Motion analysis of the glass bead

In order to analyze the bead motion, the bead is located in three regions of the workspace (Figure 3.8A). A precessing magnetic field (10 mT amplitude, $I_9 = 2$ A, and $f_X = 1$ Hz) is used to actuate the magnetic pillars formed from 20 mg of reduced iron microparticles. The matrix $\left(\mathbb{M} = \begin{bmatrix} 2\,f_X & 0 \\ f_X & 0 \end{bmatrix} \right)$ encoding the bead motion toward the left direction contains the parameters to generate a magnetic field describing a Lissajous curve. We observe that the trajectory of the glass bead can be decomposed into translation (toward the left direction) and cyclic motion in the shape of a Lissajous curve (Figures 3.8B and C). During an actuation cycle, the magnetic pillars are oriented according to the magnetic field. The glass bead describes a cyclic motion in the shape of a Lissajous curve when interacting with the surrounding pillars. However, at the end of the actuation cycle, a net translation is caused by the non-reciprocal motion between the effective/recovery strokes (Figures 3.8B and C). For the motion analysis experiments, the translation is characterized using the moving average of the bead trajectory (Figure 3.8B). Figure 3.8C shows the cyclic motion described by the bead with respect to the instantaneous moving average position. The asymmetry observed in the Lissajous curves for regions (I and III) is caused by the non-uniform characteristics of the magnetic field within the workspace (S2 Video: 00:42–00:49 s, Supplementary information). This asymmetry gives place to a diagonal motion towards the center of the workspace, as shown in Figure 3.8A and the manipulation experiments (S2 Video: 00:58–01:34 s, Supplementary information).

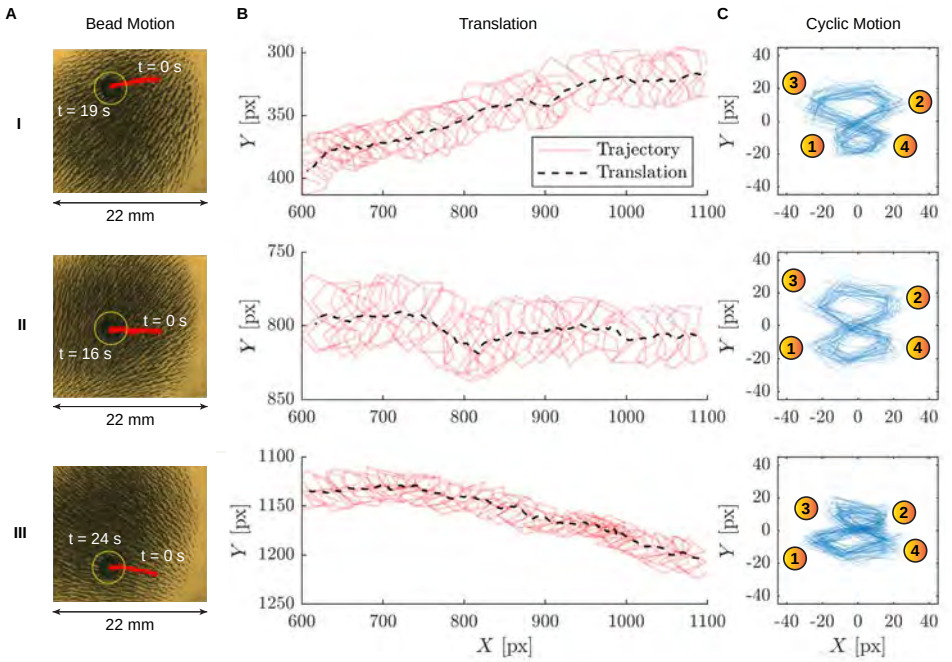


Figure 3.8: Motion analysis of a 2 mm glass bead using 20 mg of reduced iron microparticles. (A) For the analysis, the glass bead (encircled in yellow) is initially located in three regions: I) "Top," II) "Center," and III) "Bottom" within the workspace. The bead trajectory is obtained experimentally and plotted as a red solid line. The trajectory is decomposed into translation and a cyclic motion in the shape of a Lissajous curve. (B) The translation (toward the left) of the bead is computed using a moving average filter. (C) The bead describes a Lissajous curve with respect to its instantaneous moving average position. The effective stroke is achieved within the intervals ②→③ and ④→①, whereas the recovery stroke is performed within ①→② and ③→④.

II

Any colour you like

Part I covered magnetic actuation, which provides the means to act within the microworld via magnetic micro-agents. Fluorescence imaging provides the means to see, distinguish, and interpret these micro-agents as they navigate. A defining feature of fluorescence is the use of color to resolve micro-agents and biological structures. The title of this part, *Any colour you like*, inspired by the 8^{th} track of Pink Floyd's "The Dark Side of the Moon" (1973), reflects this principle. In practice, fluorescence introduces technical constraints in microrobotic experiments. Multicolor imaging often relies on sequential acquisition, which lowers temporal resolution. Biological tissue scatters and absorbs light, limiting visibility with depth. Fluorescence microscopy depends on direct optical access, leaving micro-agents in confined or enclosed regions out of reach.

The next three chapters address these constraints in sequence: **Chapter 4** focuses on speed, using computational reconstruction to improve the temporal resolution of multicolor fluorescence microscopy (**RO.3**). **Chapter 5** focuses on depth, adapting two-photon microscopy to visualize micro-agents through biological tissue (**RO.4**). **Chapter 6** focuses on access, using two-photon fluorescence endomicroscopy to image magnetic micro-agents (**RO.5**). Across these chapters, fluorescence imaging strategies are developed and demonstrated with magnetically actuated micro-agents, linking this part to the actuation established in **Part I**. Together, these studies advance the thesis toward image-guided microrobotics.



CHAPTER 4

Real-time multicolor fluorescence microscopy

The following chapter is adapted from: ***J. J. Huaroto****, Y. Jin, N. Roy, and S. Misra. Real-time multicolor fluorescence microscopy via cross-channel acquisition and deep-learning-based inference, Advanced Intelligent Discovery, e202500176, 2026 [In Press].*
The text, figures, and tables have been adapted for inclusion in this doctoral thesis.

Abstract

Monitoring real-time interactions in microrobotic and biological systems necessitates rapid multicolor fluorescence microscopy to resolve cellular, micro-agent, and environmental dynamics. Sequential acquisition is widely used to capture multiple fluorescence channels while minimizing spectral crosstalk and photobleaching. However, this approach limits imaging speed in proportion to the number of channels, reducing its suitability for capturing micro-agents and cellular interactions. This study introduces a real-time multicolor reconstruction framework that exploits cross-channel inputs (frames containing mixed spectral contributions) to enable simultaneous reconstruction of target fluorescence channels. The framework is evaluated on a custom-built three-channel fluorescence microscope, benchmarking two representative models: a U-Net trained with a pixel-wise reconstruction loss and a pix2pix model that adds adversarial training to the same U-Net architecture. Experimental validation is conducted in a microfluidic environment containing active functionalized structures (Coumarin 6–labeled electrospun magnetic fibers) and passive biological agents (CellTracker Red CMTPX–labeled HeLa cell spheroids), where external magnetic fields actuate the micro-agents to drive interactions with the spheroids. Prediction performance is evaluated in two- and three-channel settings, yielding high-fidelity reconstructions at 13.9 ms inference time. The proposed approach can increase the effective frame rate for three-color channels by up to 83%, enabling high-throughput multicolor imaging.

4.1 Introduction

Multicolor fluorescence microscopy is a fundamental tool in modern bioimaging, enabling the simultaneous visualization of multiple biological structures through spectrally distinct fluorophores [154], [155]. This capability is increasingly valuable in medical microrobotics and related fields, where functional micro-agents interact with living tissues [156], deliver therapeutics [157], detect toxins [158], [159], or perform precision biopsies within complex biological environments [69], [160]. Visualizing the spatiotemporal dynamics of such micro-agents, often involving multiple fluorophore-labeled agents, requires high spectral specificity and real-time imaging to capture rapid events such as binding, internalization, or mechanical manipulation [45]. Applications such as targeted cancer therapy, localized drug delivery, and minimally invasive interventions can benefit from multicolor imaging, enabling simultaneous monitoring of micro-agent motion, cellular responses, and environmental markers [161]–[163]. However, achieving high temporal and spectral resolution for microrobotic systems interacting with biological samples is challenging and demands real-time and spectrally-resolved imaging [164]–[166].

Fluorescence acquisition speed is constrained by the exposure required to collect sufficient signal, detector readout and data transfer, and synchronization of excitation and detection. Shortening exposure reduces the number of detected photons, while increasing illumination to compensate can accelerate photobleaching and, in living specimens, phototoxicity. Multicolor acquisition introduces an additional timing constraint when channels are recorded sequentially.

Multicolor fluorescence systems typically balance spectral specificity against acquisition time in four ways: (1) Sequential time-multiplexing alternates excitation and detection paths to acquire each channel separately [93]. This minimizes crosstalk but reduces the effective frame rate and risks temporal misregistration in rapidly moving scenes [167]. (2) Hyperspectral microscopy and Fourier transform imaging spectroscopy (FTIS) resolve a per-pixel spectrum and separate fluorophores by spectral unmixing using measured libraries [168], [169]. In FTIS, the interferogram of each pixel is recorded by stepping the optical path difference, and its spectrum is recovered via inverse Fourier transform with phase/apodization corrections [170], [171]. These approaches typically require spectral calibration and

are computationally demanding, which can constrain real-time use [172]–[174]. (3) Snapshot/compressive spectral imaging acquires one or a few coded measurements and reconstructs a spatial–spectral datacube (or band images) by solving an inverse problem—classically via iterative, sparsity-regularized solvers. This trades spatial/spectral resolution for speed and can be sensitive to motion and solver artifacts. (4) Optical multiplexing without scanning assigns spectral identity to engineered point spread function (PSF) shapes for computational classification [175]. Performance is sensitive to PSF morphology—which varies with depth, aberrations, and emitter density/crowding—making it less robust in dynamic, extended, or scattering scenes. Another optical-multiplexing route is simultaneous multichannel acquisition (e.g., beam splitters/multi-sensors), which demands precise inter-channel registration and crosstalk calibration for software correction [176].

Beyond acquisition strategies, deep learning enables reconstruction of images and spectra by learning relationships between measured data and desired outputs [177]. AutoUnmix separates mixed multichannel fluorescence images into fluorophore-specific outputs and then remixes these outputs to reproduce the measured inputs, allowing the network to learn both spectral separation and mixing [95].

Generative adversarial networks (GANs) train two networks together: a generator produces reconstructed images, while a discriminator learns to distinguish generated images from reference images. This additional training objective encourages reconstructions with image characteristics resembling the reference data. GAN-based approaches have been applied to cross-modality super-resolution and reconstruction of optically sectioned images from wide-field measurements [96], [178]. Task-assisted GANs additionally use a biological analysis task, such as segmentation, to guide reconstruction toward features relevant to that task [179]. In pix2pix, the PatchGAN discriminator evaluates local image patches, encouraging reconstruction of local structure and texture [180].

Other approaches exploit information encoded in the optical measurements. The point spread function (PSF), the image formed by a point emitter, varies with wavelength; neural networks can use these differences to classify emitter colors and help design optical elements that improve color discrimination [181]. In snapshot hyperspectral confocal microscopy, neural networks reconstruct wavelength-resolved images from optically coded

measurements [182]. SpecGAN uses adversarial training to denoise single-molecule fluorescence spectra, reducing the photon collection needed for spectral analysis [183]. Filter-free fluorescence microscopy instead learns digital spectral filtering to recover fluorescence channels from images containing both fluorescence and scattered excitation light [184].

Despite these advances, the studies discussed above do not establish real-time fluorescence channel reconstruction during magnetic actuation of micro-agents interacting with biological samples. This setting involves changing agent configurations and interactions that must be resolved across fluorescence channels. Furthermore, several approaches rely on specialized optical platforms, motivating evaluation of learned reconstruction using a sequential multicolor microscope.

This study presents a real-time multicolor reconstruction framework that simultaneously predicts target fluorescence channels from cross-channel inputs (i.e., frames containing mixed spectral contributions). During deployment, reconstruction reduces the number of sequential acquisitions required for multicolor imaging, shortening acquisition time and reducing excitation exposures while preserving channel-specific fidelity and temporal coherence. We benchmark the framework on a custom-built three-channel fluorescence microscope using two representative models under matched settings: a supervised U-Net and a pix2pix model with an identical U-Net generator and a PatchGAN discriminator. Validation is performed on a microfluidic platform under magnetic manipulation, comprising Coumarin 6–labeled electrospun magnetic fibers (active micro-agents) interacting with CellTracker Red CMTPX–labeled HeLa spheroids (passive agents). In this setting, the framework supports spatial analysis of spheroid position and micro-agent orientation, while maintaining performance on unseen sequences and under reduced-excitation conditions. Overall, the proposed strategy provides a practical and scalable route to real-time multicolor fluorescence imaging in dynamic microsystems.

4.2 Results and discussions

The results are organized to introduce and evaluate the proposed framework for real-time multicolor reconstruction. We first outline the cross-channel acquisition scheme and the two benchmarking models (U-Net and pix2pix), then motivate real-time constraints with a dynamic micro-agent–spheroid

assay under magnetic manipulation. We then quantify the structural informativeness of the cross-channel inputs relative to each target channel using a gradient-normalized cross-correlation metric. Reconstruction fidelity and latency are assessed with quantitative metrics and visual comparisons. We further examine performance under reduced excitation, analyze fluorescence efflux over time, and probe spatial accuracy with a tracking-based analysis. We extend the workflow from two to three channels by incorporating an auxiliary background-fluorescence measurement. Finally, we test our approach on morphology-matched spheroids labeled with different fluorescent dyes.

4.2.1 Cross-channel acquisition and deep-learning-based inference

In multicolor fluorescence microscopy, achieving spectral separation between fluorescence channels requires careful selection of labels that can be independently excited by tunable or discrete wavelengths. Each fluorescent label emits spectrally filtered fluorescence upon excitation and is directed to one or more detectors (e.g., cameras or photomultipliers) for image formation. To minimize spectral crosstalk and cumulative phototoxicity, channels are typically acquired sequentially using synchronized excitation sources and either a shared detector with tunable filters or multiple source–detector pairs. However, this sequential strategy can be limited in real-time multicolor fluorescence microscopy, as the effective frame rate decreases with the number of channels, and timing becomes more demanding as throughput increases. Figure 4.1A illustrates this conventional strategy, where staggered timing underscores the sequential nature of acquisition and each frame corresponds to a matched excitation–emission pair.

We introduce a cross-channel acquisition strategy coupled with deep-learning–based reconstruction. Instead of acquiring each fluorescence channel separately, cross-channel frames are captured using crossed excitation/emission paths (Figure 4.1B). This way, based on the fluorophore spectra and filter sets, the acquired images contain a mixed but informative contribution from the target channel. A deep-learning model then uses this mixed input to reconstruct the target channels simultaneously in real time. This reduces the number of exposures per acquisition cycle, increases the effective sampling rate, and maintains channel specificity through learned

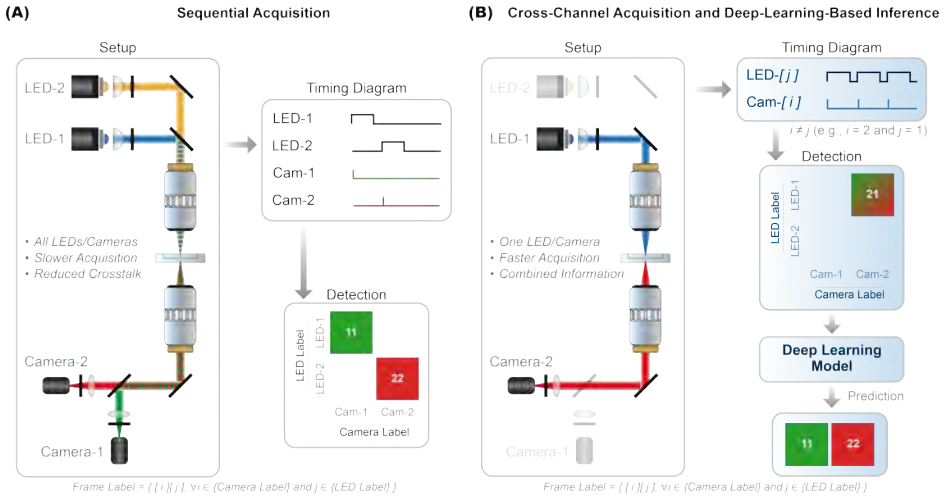


Figure 4.1: Conceptual overview and comparison of sequential multicolor fluorescence acquisition and the proposed framework. **(A)** Sequential acquisition: each fluorescence channel is acquired independently using matching excitation–detection pairs, requiring multiple LED-camera cycles to obtain multicolor images with reduced crosstalk. **(B)** A predefined cross-channel excitation–detection combination captures mixed information used by a deep learning model (U-Net or pix2pix) to predict the fluorescence channels in real-time.

cross-channel mappings. Model selection is guided by the paired image-to-image reconstruction task, the need to preserve spatial detail, and the opportunity to compare training objectives while keeping the prediction architecture unchanged. U-Net [185] provides the baseline: its encoder extracts image features, while its decoder reconstructs the output image. Skip connections pass features directly from the encoder to corresponding decoder stages, helping retain spatial information. Here, U-Net predicts fluorescence intensities and is trained with an L1 loss that penalizes absolute pixel-wise differences from the target images.

Pix2pix [180] uses the same U-Net as its generator and adds a second network, the PatchGAN discriminator, during training. This discriminator evaluates local patches of the reconstructed or ground-truth images together with their corresponding input, making the model conditional on the acquired cross-channel frame. The adversarial loss encourages local image structure resembling the training targets and complements the L1 reconstruction loss. Comparing these models therefore assesses the contribution of adversarial training. Only the generator is needed during infer-

ence, so the discriminator adds no computation during deployment. U-Net and PatchGAN architectures are detailed in Figure 4.9 (Appendix, p. 95). Training uses paired data consisting of the cross-channel frame (input) and ground-truth target channels obtained from sequential acquisitions. Pre- and post-processing, as well as key hyperparameters, are kept identical across models to ensure a fair comparison (details in the Experimental Section). At deployment, U-Net and pix2pix generator models are exported and compiled with Torch-TensorRT into a unified pipeline, with identical input/output and batching paths.

4.2.2 Real-time imaging of micro-agent-spheroid interactions

The dynamic interaction between magnetic micro-agents and biological targets presents a complex imaging scenario requiring high temporal and accurate spectral channel separation. Sequential fluorescence acquisition, while minimizing spectral crosstalk, is inherently limited by temporal resolution and risks spatial drift or misalignment across channels due to object motion during the acquisition process. In this study, Coumarin 6-labeled electrospun magnetic fibers serve as micro-agents, magnetically actuated to interact with CellTracker Red CMTPX-labeled HeLa cell spheroids (Figure 4.2A). Under external magnetic fields, the micro-agents exhibit controlled translational and angular motion, enabling physical contact, manipulation, and displacement of spheroids within the microfluidic environment. While these interactions can lead to partial spatial overlap at the interface between agents and spheroids, the system does not involve true fluorescence co-localization within the same diffraction-limited volume, as the fluorophores label distinct physical entities.

Fluorescence channels for micro-agents (M) and spheroids (C) are defined by specific LED–camera configurations designed to selectively excite and capture channel-specific information from each agent (Figure 4.2B). Overlap arises primarily from emission tail spillover between detection channels and cross-excitation of the fluorophores, due to partial spectral overlap in their excitation and emission spectra. Although excitation and emission filters (details can be found in the Experimental Section) are employed to suppress this crosstalk, residual spectral mixing and optical scattering persist, particularly under off-diagonal LED–camera combinations. These conditions result in cross-channel frames containing mixed yet struc-

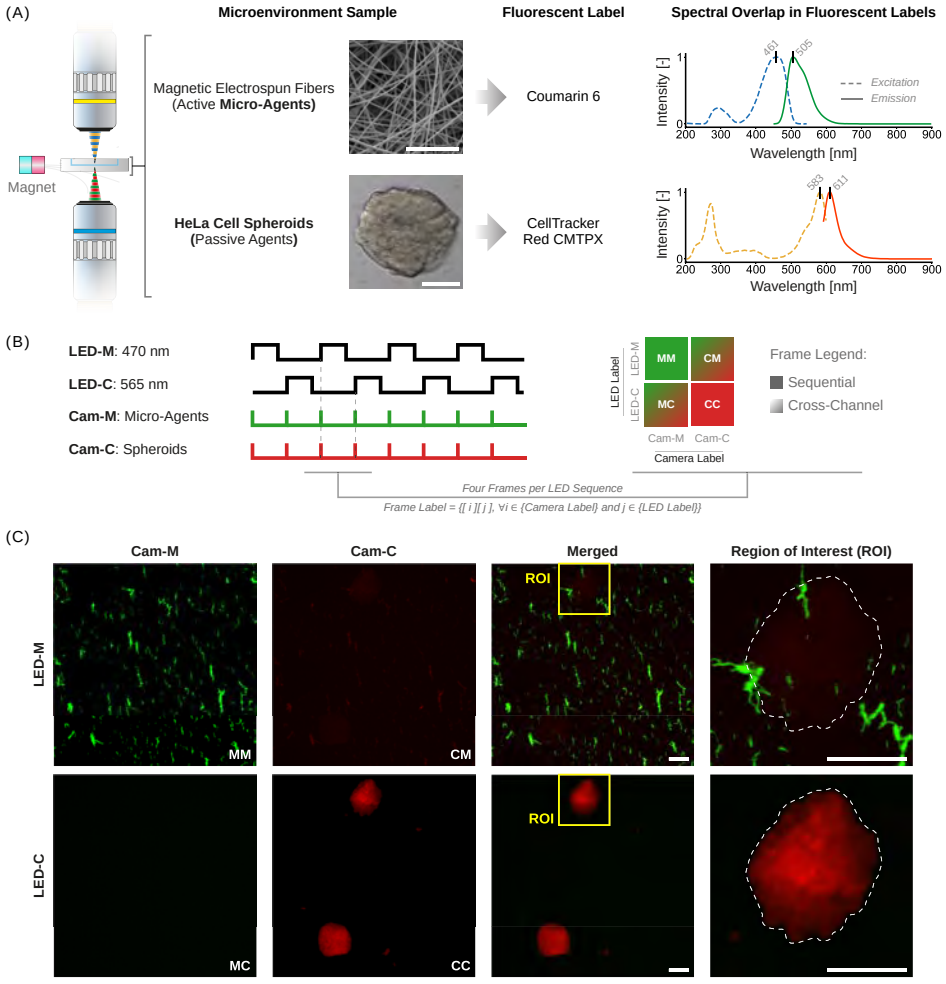


Figure 4.2: Experimental system and acquisition design for multicolor fluorescence imaging of microrobotic and cellular microenvironments. **(A)** Schematic of the microfluidic sample environment containing magnetic micro-agents (made of electrospun fibers labeled with Coumarin 6) and HeLa cell spheroids (passive agents, labeled with CellTracker Red CMTPX), alongside fluorescence excitation and emission spectra of each label. The spectra were measured experimentally, with numbers indicating the excitation and emission peaks of each label. The emission of Coumarin 6 extends beyond 600 nm into the emission range of CMTPX, and the excitation spectrum of CMTPX extends below 500 nm into the excitation range of Coumarin 6. Excitation and emission filters narrow these ranges but cannot fully remove the overlap, particularly as the number of channels increases. **(B)** Timing diagram of LED excitation and camera detection for each fluorescence label, illustrating sequential and cross-channel acquisition frames. Frame labels denote excitation–detection pairings for micro-agents (M) and HeLa cell spheroids (C). **(C)** Example fluorescence images acquired under sequential and cross-channel excitation–detection combinations, shown by camera and LED pairing. Scale bars: 100 µm.

turally informative fluorescence signals.

In the context of the proposed framework, these cross-channel frames serve as inputs for reconstructing the target fluorescence channels. To acquire sequential and cross-channel frames, all cameras are hardware-triggered on every LED pulse (Figure 4.2B), producing four frames per LED sequence. Frames with matched excitation/detection (LED-M→Cam-M and LED-C→Cam-C) form the sequential frames, denoted MM and CC. The non-matched pairs (LED-M→Cam-C and LED-C→Cam-M) are the cross-channel frames, denoted CM and MC. Figure 4.2C shows representative sequential and cross-channel frames capturing micro-agent–spheroid interactions. The cross-channel frames embed mixed spectral and spatial features, providing the basis for computational reconstruction of target fluorescence channels.

4.2.3 Channel reconstruction assessment

To evaluate the feasibility of reconstructing the sequential fluorescence channels (i.e., ground truth) from cross-channel inputs, we quantified their structural overlap using gradient-normalized cross-correlation (G-NCC). This metric captures the correlation between the spatial gradient fields, making it suitable for microscopy, where morphology, edges, and fine details are of paramount relevance. G-NCC emphasizes image structure by comparing spatial intensity gradients. Figure 4.3A outlines the analysis workflow. At each percentile threshold, the cross-channel input is masked by setting intensities at or below the corresponding percentile of its positive pixel intensities to zero. Sobel gradient-magnitude maps are then calculated for the masked input and the unmasked target frame. Their normalized cross-correlation is computed over all image pixels. The largest absolute correlation across the tested thresholds is retained for each input–target pair, yielding a score between 0 and 1 (metric definition in Section 4.4). This score identifies the strongest structural correspondence obtained across the threshold sweep and serves as a diagnostic of shared structural information. Figure 4.3B shows that CM has substantially higher structural overlap with MM than with CC, indicating strong morphological cues from the micro-agent channel. For both ground truths (MM and CC), CM also yields higher structural overlap compared to MC. This asymmetry highlights a directional bias in cross-channel information, driven by the specific

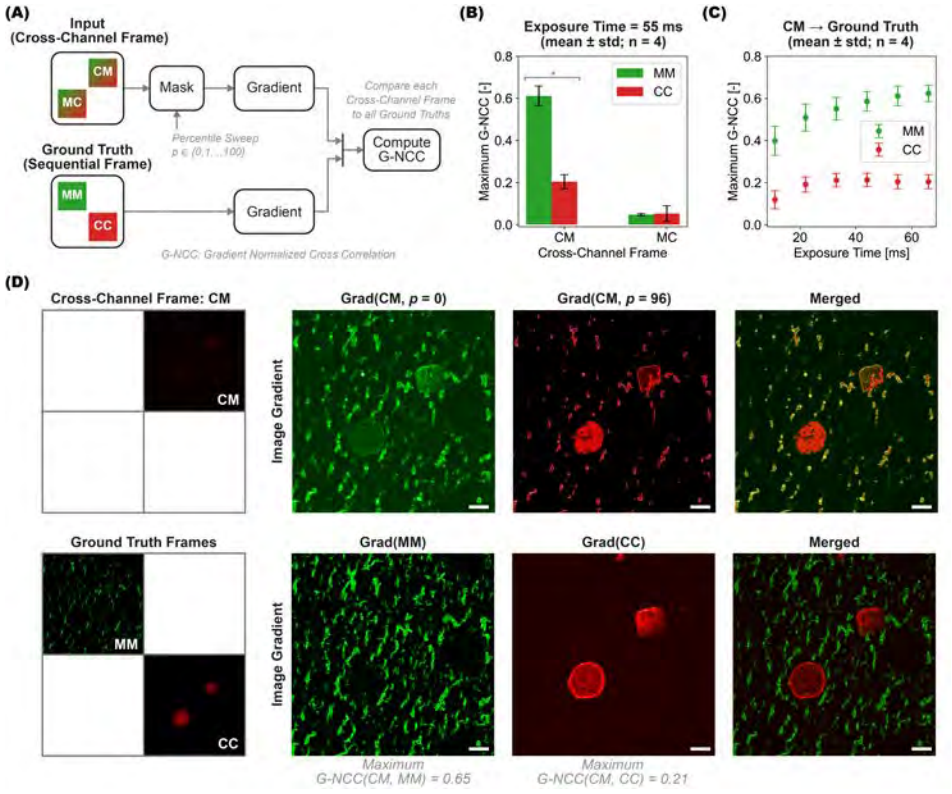


Figure 4.3: Gradient-based cross-channel analysis for evaluating channel reconstruction. **(A)** Workflow diagram: gradients are computed from cross-channel input frames and sequential ground truth frames, followed by gradient-normalized cross-correlation (G-NCC) between input and ground truth gradients. **(B)** Bar plot of maximum G-NCC values across all cross-channel frames (mean ± SD, n = 4) at 55 ms exposure. **(C)** Dependence of maximum G-NCC values on exposure time (mean ± SD, n = 4) for CM input frame against each ground truth channel. **(D)** Example analysis for cross-channel frame CM: gradient images of CM input (top row) and ground truth channels MM and CC (bottom row), with corresponding maximum G-NCC values. Gradient visualizations are contrast-enhanced by applying a luminance bias toward the upper dynamic range using a linear-light overlay transformation. Scale bars: 100 µm

excitation–emission characteristics of the fluorophores and the configuration of spectral filters. Although the acquisition geometry appears symmetric, the resulting structural content is not, due to factors such as unequal emission tails, filter leakage, and differential brightness. This asymmetry suggests that cross-channel selection should be guided by acquisition balance and the actual information content captured under each configuration.

Figure 4.3C presents a systematic evaluation of G-NCC as a function of exposure time, using CM as the input for reconstructing the target fluorescence channels. For CM–MM, the mean maximum absolute G-NCC increases from approximately 0.40 at 11 ms to 0.51 at 22 ms and continues to increase at longer exposures. For CM–CC, it increases from approximately 0.12 to 0.19 between 11 and 22 ms and remains approximately 0.20–0.21 from 33 ms onward. Although 33 ms provides higher structural correspondence, it increases exposure time by 50% compared with 22 ms. We therefore select 22 ms for training and deployment as a compromise between acquisition speed and retaining structural cues corresponding to both target channels. The G-NCC framework enables a pre-training diagnostic to evaluate channel informativeness and guide model design. In different imaging systems employing automated filter wheels or tunable optics, similar cross-channel relationships can be characterized in advance. It is worth noting that the model learns the mapping defined by the supervision it receives. Consequently, sufficient separation in the target channels is essential at the training stage, as strongly mixed targets do not provide the supervisory structure required to learn or enforce channel-separated outputs.

4.2.4 Evaluation

The models are trained on 3000 paired frames (6000 after augmentation) from 12 video sequences. An additional 750 pairs from three sequences are reserved for validation and early stopping. Reconstruction performance is subsequently assessed on a separate test dataset (750 frames) that is excluded from training and early stopping. We compare U-Net against pix2pix (U-Net generator and PatchGAN discriminator) predictions, both trained using the same L_1 loss weight. Thereby, any performance gap isolates the effect of the adversarial term used in pix2pix. In both cases, CM serves as the input to predict MM (micro-agents) and CC (spheroids) channels. Figure 4.4A shows one representative frame, including the input, ground truth, and model predictions for MM and CC channels. Quantitative analysis is performed using structural similarity index (SSIM), peak signal-to-noise ratio (PSNR), and contrast similarity (GCS) between ground truth and predictions (Figure 4.4B). Our results show consistent reconstruction capabilities as reflected by SSIM (CM→CC >0.95; CM→MM

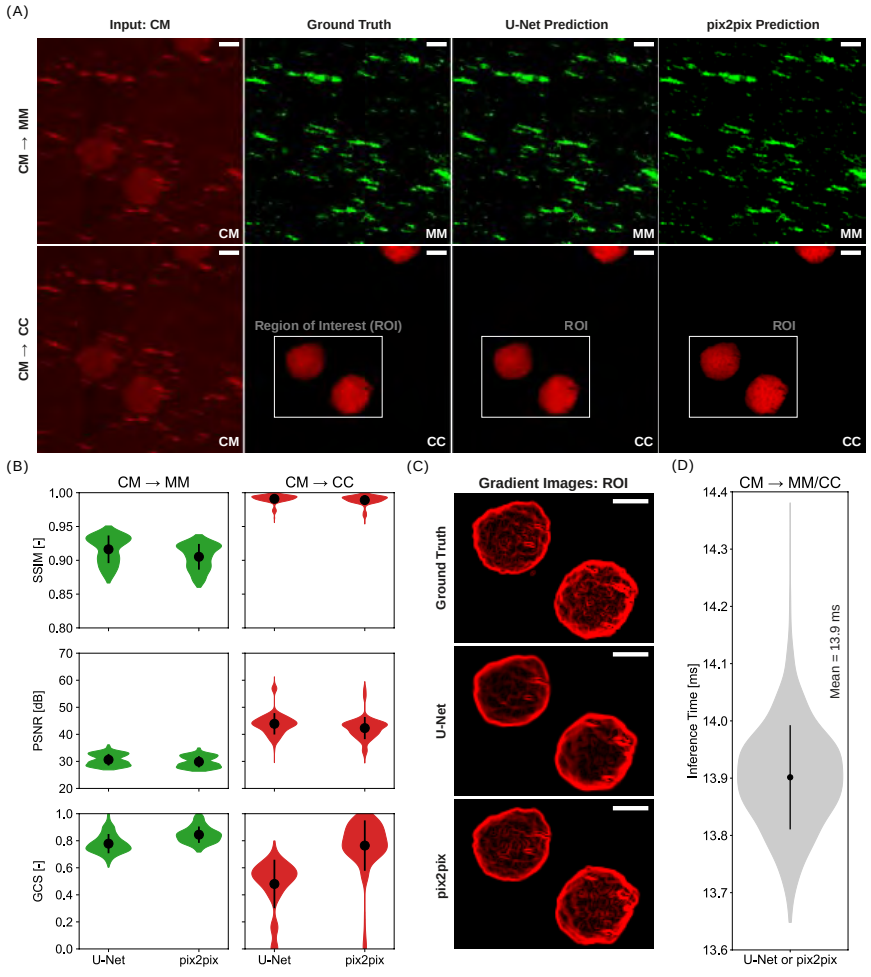


Figure 4.4: Framework performance using U-Net and pix2pix architectures. **(A)** Representative frame reconstructions for each target channel (MM: micro-agents; CC: spheroids) from a single CM input (cross-channel frame). Columns show input, ground truth, and predictions. Gamma correction ($\gamma = 0.5$) is applied to the input CM to improve the visualization. **(B)** Quantitative evaluation of structural similarity index (SSIM), peak signal-to-noise ratio (PSNR), and contrast similarity (GCS) across 750 frames. Violin plots show distribution, mean ($\cdot$), and standard deviation (vertical black line). **(C)** Gradient images of regions of interest (ROIs) presented in panel (A), comparing ground truth and model predictions. **(D)** Inference time distribution of U-Net and pix2pix over 750 frames, representing simultaneous reconstruction of both MM and CC channels. Because pix2pix uses a U-Net generator, the inference time is effectively identical for both models (shared violin; mean $\approx$ 13.9 ms). Scale bars: 100 µm

>0.87) and PSNR (>25 dB for both models) values across models. In comparison to U-Net, pix2pix yields higher GCS values on CC predictions without a significant reduction of SSIM and PSNR. This suggests that the adversarial term primarily improves perceptual/texture contrast while preserving intensity-based fidelity. For MM, differences are minimal as micro-agent morphology presents lower intrinsic texture (i.e., more edge-dominated) relative to CC. Figure 4.4C illustrates the texture differences using gradient images of a region of interest in channel CC. Consistent with these observations, Figure 4.11 (Appendix, p. 98) shows that even the introduction of a small adversarial weight (λ_{adv}) systematically increases GCS while leaving SSIM and PSNR virtually unchanged. The inference time distribution is identical for the two models (i.e., mean ≈13.9 ms) because pix2pix uses a U-Net generator (Figure 4.4D). This low-latency performance supports real-time deployment at standard video frame rates, enabling live reconstruction of magnetically actuated micro-agents interacting with biological targets in microfluidic environments.

The framework's robustness under limited excitation is evaluated across four irradiance levels. We tested U-Net and pix2pix by progressively dimming LED-M and LED-C in tandem (Figures 4.13A and B, Appendix, p. 101), from the training settings of 62.5 and 13.5 mW cm^{-2} down to 18.9 and 3.8 mW cm^{-2}, respectively. With a fixed L_1 weight ($\lambda_1 = 100$) and $\lambda_{\text{adv}} = 0.05$ for pix2pix, both models produced stable MM and CC reconstructions across the full range, including irradiances outside training (Figure 4.13C, Appendix, p. 101). We further assessed real-time performance on an independent dataset acquired at 30.7 and 6.5 mW cm^{-2} for LED-M and LED-C (Video S1), where the framework maintained high reconstruction accuracy without retraining, indicating generalization to dimmer conditions.

Following the variable-irradiance test, we evaluate the framework's capability to track a natural fluorescence decay due to dye efflux. This setting isolates temporal intensity changes from illumination effects while tracking the fluorescence change of a HeLa cell spheroid labeled with CellTracker Red CMTPX. Figure 4.5A shows a time-lapse sequence of ground truth and U-Net/pix2pix merged predictions. The predictions for micro-agents (green) and spheroid (red) channels qualitatively preserve structural integrity. Moreover, Figure 4.5B shows that normalized fluorescence change ($\Delta F/F_0$) in the spheroid channel closely follows the monotonic ground truth

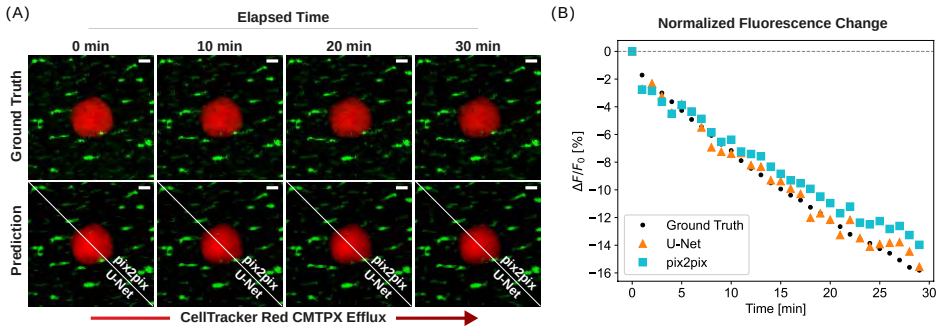


Figure 4.5: Temporal fluorescence decay and model tracking of dye efflux. **(A)** Time-lapse fields of view at 0, 10, 20, and 30 minutes showing a HeLa cell spheroid labeled with CellTracker Red CMTPX within an aqueous solution containing micro-agents (green). Top: Ground Truth; bottom: Merged predictions using U-Net and pix2pix. The gradual loss of red intensity reflects CMTPX efflux. **(B)** Normalized fluorescence change ($\Delta F/F_0$) over time, computed on a centered 128×128 pixels region of interest with F_0 taken at $t = 0$ min. Each 1-minute time point represents the average of three consecutive acquisitions. Predictions closely follow the Ground Truth (black circles), capturing the monotonic decay dynamics across the full 30-minute sequence. Scale bars: 50 µm.

trend across the tested models. Root mean square errors are reported for U-Net: 0.58% and pix2pix: 1.55%. Notably, the models track the trend and slope of the fluorescence decay $F(t)$ over time while minimizing the excitation dose on the spheroid. In practice, cross-channel acquisition reduces direct excitation of the spheroid dye, limiting the illumination dose. Coumarin 6 is incorporated into the polystyrene micro-agents, and sample preparation includes removal of residual free dye before combining the labeled populations. These steps reduce free-dye carryover, although passive dye release from the fixed spheroids may still contribute to the observed fluorescence decay. Such release does not necessarily imply appreciable dye transfer to the micro-agents.

4.2.5 Fluorescence-guided real-time tracking

To assess the framework's suitability for real-time applications, we evaluate its spatial accuracy on dynamic fluorescence sequences using U-Net and pix2pix (Video S2, Supporting Information). Figure 4.6A shows frame-by-frame comparisons between ground truth and pix2pix predictions for the MM and CC channels across representative time stamps. Colored markers indicate spheroid centroids for direct prediction–ground truth comparison.

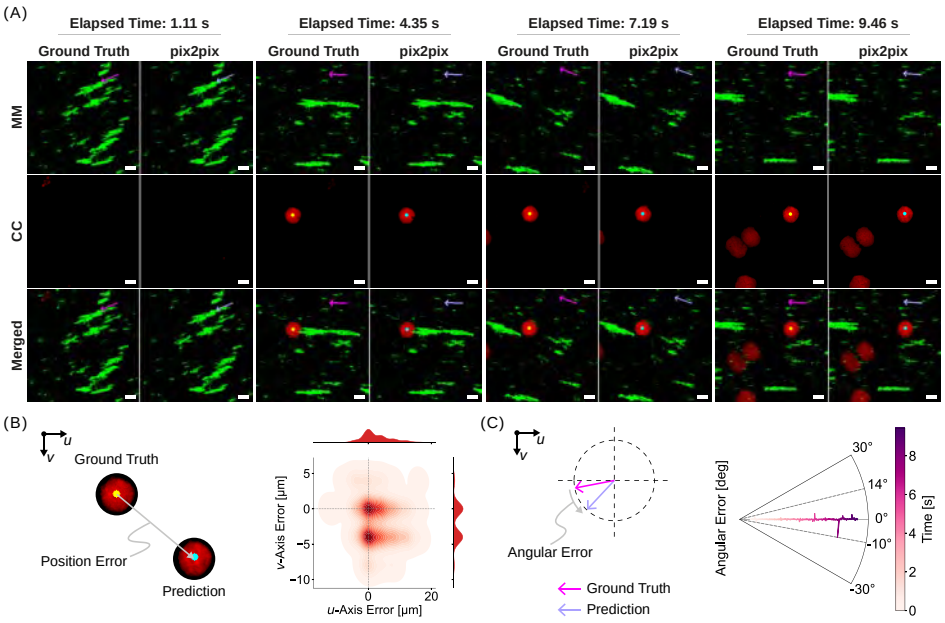


Figure 4.6: Assessment of spatial accuracy on unseen frames. **(A)** Frame-by-frame comparison of ground truth and pix2pix predicted fluorescence channels for micro-agents (MM, green) and HeLa cells (CC, red) at selected time points. The merged view illustrates channel overlays, showing preserved structure and spatial consistency in predicted frames. Colored markers indicate the detected positions of spheroids in the ground truth (yellow) and predictions (cyan), while arrows show the orientation of magnetic micro-agents in the ground truth (magenta) and predictions (pink), enabling error quantification in a tracking-like test scenario. **(B)** Left: schematic illustration of spheroid position error as the vector displacement between predicted and ground truth centers. Right: joint histogram of 2D localization errors along the frame axes (u and v) across test frames (n = 350), with marginal distributions highlighting error spread. **(C)** Left: schematic of angular error between predicted and ground truth orientations of micro-agent. Right: polar plot showing angular error (in degrees) as a function of elapsed time, color-coded temporally. Dashed lines indicate the maximum and minimum deviations observed during the sequence. Scale bars: 100 µm. (Video S2, Supporting Information)

Positional errors along frame axes (u and v) are shown in Figure 4.6B, demonstrating subcellular-scale localization accuracy. Figure 4.6C shows angular error in micro-agent orientation, confirming directional consistency across the sequence. Root-mean-square errors for spheroid position and micro-agent orientation using U-Net and pix2pix are presented in Table 4.1. Independent of the models used, the input channel (CM) is acquired in 22 ms, and the inference of MM and CC takes ≈13.9 ms. This way, the effective dual color frame rate increased by 22% with respect to fully sequential dual-

Table 4.1: Aggregate root-mean-square (RMS) errors for spheroid radial localization and micro-agents orientation across models.

Error Metric	U-Net	pix2pix
Spheroid position — radial RMS [µm]	5.79	6.15
Micro-agents orientation — RMS [deg]	1.53	1.05

color acquisition at 44 ms. It is worth noting that for tracking applications, precise position and orientation matter more than texture realism. U-Net is less computationally demanding and less prone to non-convergence than pix2pix, while still providing accurate centroid and pose estimates. When visual fidelity and realism are critical, pix2pix is preferable.

4.2.6 Three-color fluorescence microscopy

Building on the real-time two-channel results, we extend the framework to three-color fluorescence microscopy. We add a third channel (LED-B/Camera-B) and introduce indocyanine green (ICG), which labels the microfluidic channel and the surrounding medium, providing context beyond the primary agents (Figure 4.7A). Although ICG is spectrally separated from Coumarin 6 and CMTPX, the BB images contain spatial contrast associated with the micro-agents and spheroids. BB-based reconstruction, therefore, evaluates whether a separately trained model can predict the visible target channels from these indirect structural cues.

We evaluate two input configurations for three-channel operation: (1) CM→(MM, CC), using an auxiliary BB frame acquired sequentially for contextual visualization only; and (2) BB→(MM, CC) to test how informative BB is as an alternative input (Figures 4.7B and C). For CM-based reconstruction, CM and BB are acquired sequentially while MM/CC inference overlaps BB exposure, yielding 44 ms per three-color frame (50% higher frame rate relative to fully sequential acquisition at 66 ms). In contrast, BB-based reconstruction requires only 36 ms per three-color frame (83% higher frame rate relative to fully sequential). Video S3 shows CM- and BB-based reconstructions using U-Net and pix2pix. Predictions at two timestamps with pix2pix are shown in Figure 4.7D, demonstrating three-channel fluorescence imaging. Overall, pix2pix reconstructions are consistent, as reflected by the SSIM values (Figure 4.7E). Mean SSIM and

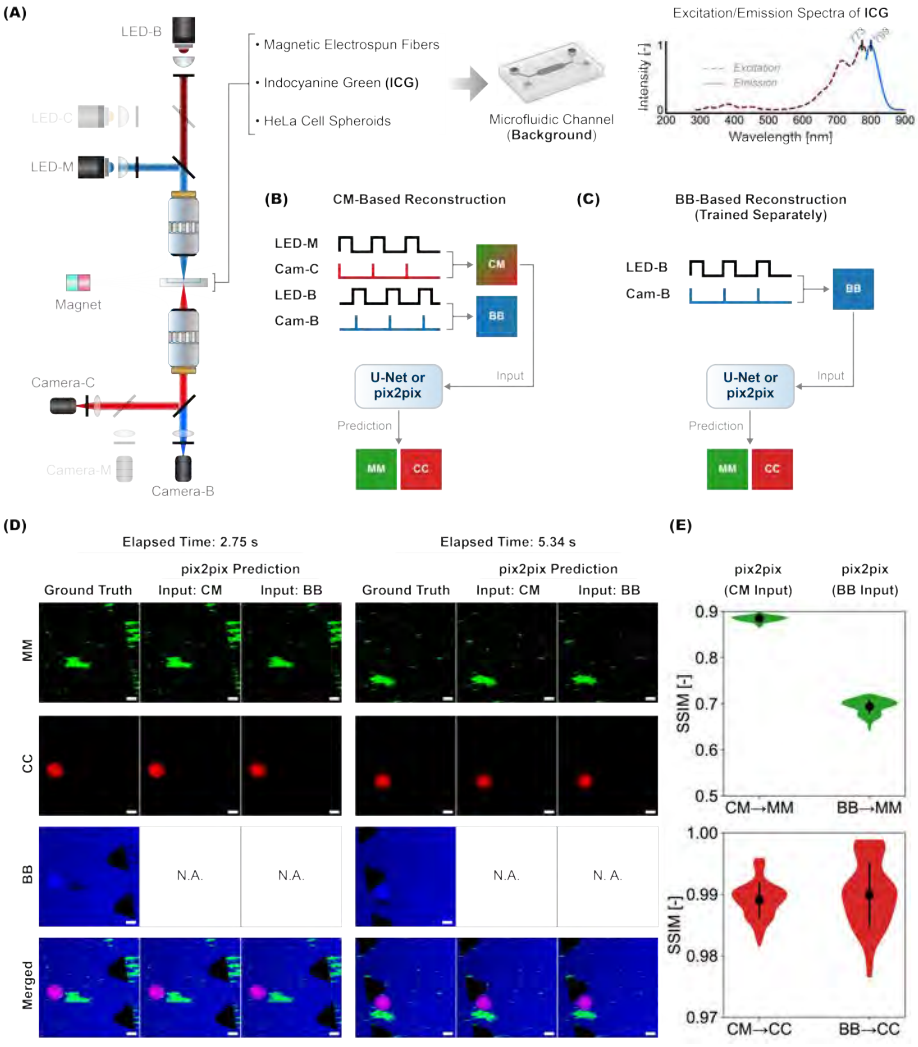


Figure 4.7: Real-time inference within a three-channel fluorescence microscopy workflow. **(A)** Fluorescence imaging setup used to acquire the framework input frame (CM: LED-M/Cam-C). An additional acquisition (BB: LED-B/Cam-B) captures indocyanine green (ICG) fluorescence from the surrounding medium, providing contextual information on the microfluidic environment. Right: excitation and emission spectra of ICG. **(B)** CM-based reconstruction of MM and CC channel frames. The BB frames are acquired sequentially for visualization but are not used during inference. Inference is performed in parallel with BB acquisition. **(C)** BB-based reconstruction of MM and CC. This configuration evaluates the informativeness of BB as an alternative reconstruction source. **(D)** Representative predictions from both models compared to ground truth MM and CC frames. **(E)** Structural similarity index (SSIM) comparison for MM and CC reconstructions using CM or BB as model input (n = 350 test patches). Scale bars: 100 µm. (Video S3, Supporting Information)

Table 4.2: Target channels (MM and CC) reconstruction performance across inputs (CM and BB) and models in a three-channel microscopy workflow.

Metric (mean)	Input: CM				Input: BB			
	MM		CC		MM		CC	
	U-Net	pix2pix	U-Net	pix2pix	U-Net	pix2pix	U-Net	pix2pix
SSIM [-]	0.89	0.88	0.98	0.98	0.72	0.69	0.98	0.98
PSNR [dB]	29.69	29.26	37.04	37.83	23.32	22.83	37.49	39.21

PSNR values for U-Net and pix2pix are reported in Table 4.2. CM-based reconstruction achieves higher similarity in MM, likely because BB frames do not carry the same fine-grained information for MM as they do for CC. From an image-formation standpoint, the lower fidelity of BB→MM reconstruction is consistent with reliance on indirect structural cues, potentially arising from scattering by iron-oxide–doped fibers and gradual ICG uptake by spheroids. These cues are weaker, geometry-dependent, and biased toward low spatial frequencies, rendering the recovery of MM's high-frequency features ill-posed.

In both proposed input configurations, the framework runs in real-time with comparable inference latency (13.9 ms for two output channels) as the deployment pipeline is identical across models and inputs. Although BB is a feasible alternative input, ICG's lower photostability and higher susceptibility to photobleaching than the other labels can reduce quality during extended imaging [45], [74]. Thus, under these settings, BB is most useful as a contextual channel and for exploratory reconstructions, while CM-based input is preferred when maximizing MM fidelity and robustness is the priority.

Following the three-channel workflow, we next consider the portability of the framework to new dye sets and microscope architectures. Because the proposed approach relies on informative cross-channel signals, successful deployment requires coarse awareness of cross-channel coupling and accurate channel registration to ensure that the acquired inputs encode recoverable information. As the number of channels increases, acquisition of paired training data becomes the primary bottleneck, particularly for frame-synchronous schemes using a single detector or filter turret, where switching speed limits throughput.

Within these constraints, several practical strategies can be employed,

alone or in combination. (1) Clean, per-channel targets can be acquired on stationary samples to establish ground truth under representative optical conditions. (2) During continuous cross-channel acquisition, occasional fully separated target frames can be interleaved and registered to nearby frames to provide sparse supervision. (3) Clean targets can be forward-mixed using empirically measured cross-channel responses to synthesize cross-channel inputs matched to deployment conditions.

4.2.7 Performance with morphology-matched spheroids

When morphology differs across fluorescence channels, the proposed framework can utilize shape and texture cues alongside cross-channel intensity information to separate target channels. In such settings, reconstruction is typically robust to moderate noise and clutter. Here, we instead consider a morphology-matched regime in which shape-based discrimination is minimized, and reconstruction relies primarily on the intensity information contained in the cross-channel input.

To this end, we evaluate the framework on HeLa cell spheroids stained with two spectrally distinct dyes (green CMFDA and red CMTPX). In this configuration, the two channels share nearly identical morphology, making relative intensity differences the main source of discriminative information. U-Net and pix2pix reconstruct the target channels with minimal false merging or cross-contamination (Figure 4.8A and Video S4). Quantitatively, full-frame structural similarity index metric (SSIM) values are ≥ 0.97 for both channels (MM and CC) (Figure 4.8B), indicating reliable intensity-based separation under morphology-matched conditions.

To probe the framework's behavior under controlled intensity imbalance, we construct a synthetic evaluation scenario based on an empirically fitted cross-channel map (Figure 4.8C). Intensity imbalance is introduced by scaling the target channels using a parameter (β). The resulting scaled targets (MM′ and CC′) are then combined through the cross-channel map to generate a synthetic cross-channel input frame (CM′ = aMM′ + bCC′ + c). This synthetic input is processed by a pix2pix model trained on MM, CC, and CM data (Figure 4.8D), allowing assessment of reconstruction behavior outside the training intensity distribution.

Reconstruction accuracy quantified by masked SSIM (details in the Experimental Section) shows a non-monotonic dependence on β, with MM′

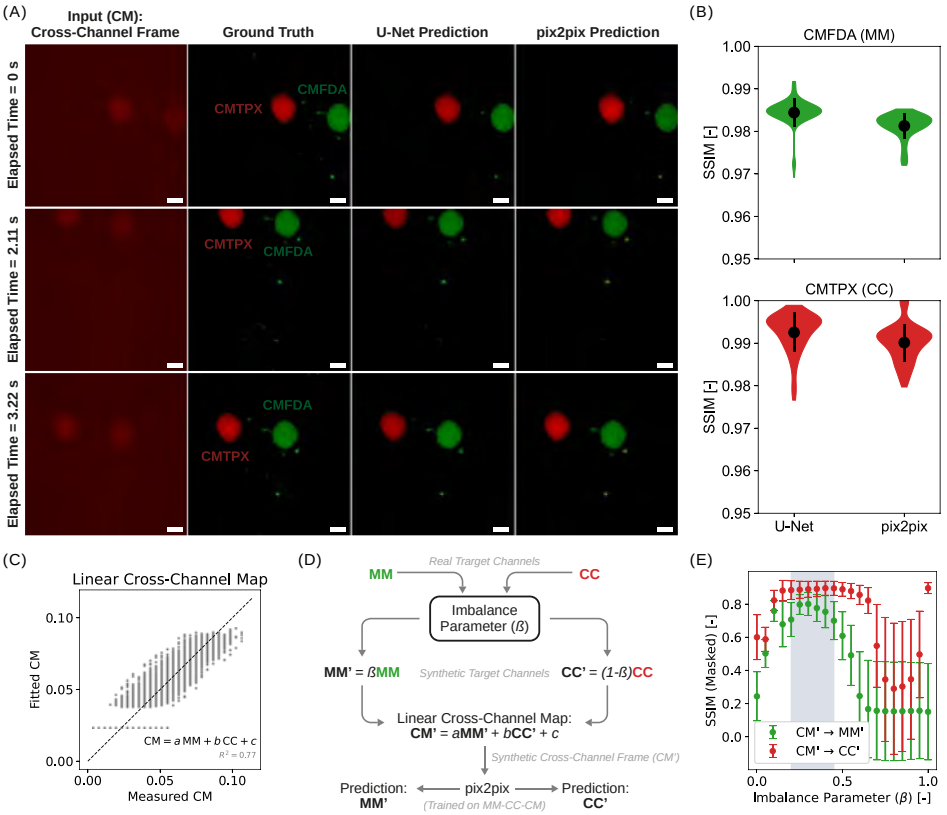


Figure 4.8: Inference under similar morphology with intensity-based discrimination. **(A)** Spheroid samples are stained with two different dyes (green CMFDA and red CMTPX). Left to right: cross-channel input frame, ground truth, and model predictions at three representative frames. Despite morphology-matched spheroids, both models successfully recover distinct channels based on the intensity differences shown in input frames. **(B)** Structural similarity index metric (SSIM) distributions for CMFDA (MM) and CMTPX (CC) reconstructions using U-Net and pix2pix (n = 116). Dots denote means and bars standard deviations. Scale bars: 100 µm. (Video S4, Supporting Information). **C)** Linear cross-channel map fitted from real tri-channel measurements (MM, CC, CM), relating the measured cross-channel intensity (CM) to a linear combination of the corresponding target channels. D) Schematic of the synthetic imbalance framework. Real target channels (MM, CC) are scaled using an imbalance parameter (β) to generate synthetic target channels (MM′ and CC′), which are combined via the empirical cross-channel map to form a synthetic cross-channel frame (CM′). A pix2pix model trained on real MM, CC, and CM data is then used to predict MM′ and CC′ from CM′. E) Masked SSIM between pix2pix predictions and synthetic targets as a function of the imbalance parameter (β). Dots and error bars indicate mean values and standard deviations across samples, respectively. The grey shaded region highlights the empirically identified well-conditioned operating regime.

and CC′ peaking within a well-conditioned regime ($\beta \approx 0.2$–0.45) (Figure 4.8E). Across all β, CC′ is reconstructed more robustly than MM′, reflecting the CC-dominant mixture statistics present in the measured training data. Representative reconstructions and ROI-averaged scatter plots illustrating this transition are shown in Figures 4.14A and B (Appendix, p. 102). As β approaches ~ 0.52, the relative contributions of MM′ and CC′ to CM′ become comparable ($a\beta \approx b(1-\beta) \Leftrightarrow \beta = \frac{b}{a+b} \approx 0.52$), leading to a gradual loss of reconstruction fidelity for both channels. This transition is accompanied by an increasing spatial redistribution of the predicted signal, as quantified in Figure 4.14C (Appendix, p. 102).

Notably, this transition is continuous, reflecting a gradual loss of identifiability as relative signal contributions depart from the training distribution. This behavior is consistent with an intensity-based inversion constrained by empirically learned relationships between the input and target signals. In practice, fluorescence channel reconstruction is further limited when the target channel contributions to the cross-channel frames approach the background offset captured by the constant term (c) in the empirical map. As either $a\beta$MM or $b(1-\beta)$CC becomes comparable to this offset, the corresponding signal is no longer reliably encoded in CM′, defining a practical operating regime governed by relative signal balance and absolute information level.

From a hardware perspective, incomplete spectral separation is a recognized and often unavoidable limitation in several established fluorescence imaging modalities. In live-cell multicolor imaging, spectral overlap between fluorescent proteins and organic dyes is common, particularly under high-speed acquisition, where sequential excitation or filter switching is impractical [186]. Similar constraints arise in Förster resonance energy transfer experiments, where donor bleed-through and acceptor cross-excitation must be explicitly modeled due to unavoidable crosstalk [187]. Reduced-excitation and low-phototoxicity imaging accentuate crosstalk effects by operating close to the noise floor [155]. In such regimes, crosstalk is tolerated as a trade-off for temporal resolution or signal efficiency, motivating computational strategies that exploit informative cross-channel coupling.

4.3 Conclusions

This study introduces a real-time, deep learning–based framework for multicolor fluorescence microscopy that uses cross-channel acquisition to reduce reliance on fully sequential channel capture. The framework is evaluated with two real-time inference architectures (U-Net and pix2pix), enabling high-fidelity imaging of dynamic microsystems while preserving spectral specificity and structural detail. Our approach increases the multicolor frame rate by 22% in two-color mode and up to 83% in three-color mode, relative to fully sequential acquisition. The framework covers two- and three-color micro-agent–spheroid imaging, reduced-excitation imaging, normalized fluorescence change due to dye efflux, real-time tracking, and inference under morphology-matched scenarios. These results highlight the ability of cross-channel learning to recover missing target fluorescence channels when informative correlations are present. Future work will extend the framework to higher channel counts and fully parallel multi-channel inference, while accounting for conditioning limits imposed by cross-channel coupling and signal imbalance. Incorporating label-free contrast mechanisms or multimodal imaging modalities could further broaden applicability, from high-content screening to *in vivo* imaging, where rapid, multiplexed acquisition is critical.

4.4 Experimental section

Cell culture and spheroid preparation: HeLa cells are cultured in Dulbecco's modified Eagle's medium (11–965-092, Fisher Scientific Ltd., Canada), supplemented with 10% fetal bovine serum (F7524–500ML, Sigma-Aldrich, USA), and 1% penicillin-streptomycin (15–140-122, Thermo Fisher Scientific Inc., USA). During the culture period, the cells are maintained at 37°C in a humidified atmosphere containing 5% carbon dioxide. In the 2D cell culture, the medium is changed every 48 hours. When cells reach 80% confluency, the cells are trypsinized, counted, and resuspended in cell culture medium at a concentration of 2×10^6 cells/ml. For spheroid preparation, 0.2 mL of cell suspension is placed on top of an agarose mold containing 1500 microwells with a depth and a diameter of 200 µm. This results in spheroids which, on average, include approximately 270 cells. Solutions of 10 µM CellTracker Red CMTPX and Green CMFDA are prepared in

a serum-free medium and subsequently incubated for 30 minutes with the spheroids, which have been compacted for 3 days under cultivation conditions. Afterward, the working solutions are removed, and the culture medium is added again. HeLa cell spheroids stained with CMTPX and CMFDA are fixed for 15 minutes with 4% formaldehyde (F8775–25ML, Sigma-Aldrich, USA) at room temperature for long-term storage. This is followed by washing twice with Dulbecco's phosphate-buffered saline.

Preparation of magnetic micro-agents: Magnetic Electrospun fibers are fabricated using the electrospinning technique. The two polymer solutions for electrospinning consist of polystyrene pellets (430102–1KG, Sigma-Aldrich, USA) as a carrier polymer, Coumarin 6 (442631–1G, Sigma-Aldrich, USA) and Nile Red (72485–1G, Sigma-Aldrich, USA) as hydrophobic fluorophores, iron oxide (Fe_3O_4) nanoparticles (637106–25G, Sigma-Aldrich, USA) as a magnetic material, and anhydrous N, N-Dimethylformamide (DMF) as a solvent (227056–1L, Sigma-Aldrich, USA). The polymer solutions are prepared using a 45.0% (29.8% polystyrene, 15% Fe_3O_4, and 0.2% Coumarin 6) weight-to-volume ratio in DMF. Each polymer solution is homogenized by stirring for 24 hours using a vertical roller (LLG-uniRoller 6, LLG-Labware, Germany). For electrospinning, the polymer solution is placed in a plastic syringe and connected through Teflon tubing to an 18-gauge blunt-tip needle (TS18SS-15, Adhesive Dispensing Ltd., UK). Each solution (0.04 mL) is electrospun at once using an accelerating voltage of 14 kV, a feed rate of 2.5 mL/h, and a needle tip-to-collector distance of 16 cm. Randomly oriented fiber meshes are collected on grounded aluminum foil at 22°C and 30% humidity and dried at room temperature for 12 hours to remove the solvent residue. Deposited fiber meshes are cut into 2-3 mm pieces using a scalpel and then immersed in a glass vial containing 1% (volume/volume) Tween 80 (P4780-100ML, Sigma-Aldrich, USA) in Milli-Q water. Fluorescent and magnetic electrospun fibers are obtained by grinding the fibers using a sonicator (model 2510, Branson, USA) for 2 hours. Finally, the resulting micro-agents are magnetically collected at the bottom of the vial using a permanent magnet, allowing for the removal of the fluorescent supernatant, which is then replaced with 4 mL of fresh Milli-Q water containing 1% Tween 80.

Microenvironment sample: For two-channel experiments, 7 µL each of micro-agent solution and HeLa spheroid suspension are used. An additional 7 µL of indocyanine green (ICG) solution (250 mg/mL in phosphate-

buffered saline) is included for three-channel experiments, maintaining a 1:1:1 volumetric ratio. The microfluidic channels are fabricated using a standard soft lithography process [188]. Negative molds of microfluidic channels (height ≈187 µm) are prepared on a silicon wafer in the cleanroom using SU-8 photoresist. A mixture of 10:1 Sylgard 184 Polydimethylsiloxane (PDMS) and the curing agent is poured onto the wafer and cured in the oven at 70°C overnight. The cured PDMS layer is gently removed from the wafer, and inlet and outlet ports are punched. Finally, the microfluidic channels are obtained by bonding the PDMS layer to a microscope slide using plasma oxidation.

Excitation and emission spectra: Excitation and emission spectra of fluorescent labels are measured using a spectrofluorometer (FP-8300, Jasco, Japan) in the range of 200 nm and 900 nm with a 1 nm data interval. For spectrum analysis, 2.5 µM indocyanine green (I2633–25MG, Sigma-Aldrich, USA) solution is prepared by dissolving 1.5 µg indocyanine green in 700 µL fetal bovine serum (16000044, Thermo Fisher Scientific, USA). The solution is placed in a water bath at 37 °C for 2 hours to bind indocyanine green to proteins in the culture medium [189]. A 10 mM stock solution of CellTracker Red CMTPX (Thermo Fisher Scientific, USA) is prepared by dissolving 50 µg of dye in 7.29 µL dimethyl sulfoxide (D2650-100ML, Sigma-Aldrich, USA). The stock solution is then diluted 1:1000 in serum-free medium to obtain a 10 µM working solution. A solution of 4 µg of Coumarin 6 (442631–1G, Sigma-Aldrich, USA) is prepared in 700 µL dimethylformamide (227056–1L, Sigma-Aldrich, USA). All fluorescent solutions are placed in different quartz cuvettes (CV10Q700F, Thorlabs, USA) for analysis.

Multicolor fluorescence microscope: All experiments presented in this study are carried out using a custom-built multicolor fluorescence microscope [74]. The microscope consists of excitation and emission units. The excitation unit generates discrete light beams with the center wavelengths of 470 nm, 565 nm, and 780 nm for sharp excitation of the fluorophores using three individual narrow-spectrum light-emitting diodes (LEDs) (M470L3, M565L3, M780LP1, Thorlabs, USA). LEDs are collimated using 20 mm focal length aspheric condenser lenses (ACL2520U-A, ACL2520U-B, Thorlabs, USA) and coupled with filters (ET470/40x, ET572/35x, ET775/50x, Chroma, USA) to select the excitation wavelengths. Three discrete and collimated light beams are combined using two dichroic mirrors (T660lpxrxt,

T510lpxrxt, Chroma, USA) for the excitation of the fluorophores using a single optical path. The incoming light is focused and then collimated using bi-convex and plano-convex lenses. Images of the LED chips are obtained on the front focal plane of the plano-convex lens. A protective silver mirror (PF10–03–P01, Thorlabs, USA) directs the collimated light. A 10× long working distance objective lens (Plan Apo, Mitutoyo, Japan) is employed to focus the excitation light on the sample. The objective is placed so that its back focal plane intersects with the image plane of the LED chips. Emitted light from fluorophores is collected using a 5× long working distance objective (Plan Apo, Mitutoyo, Japan) and transmitted toward the emission unit by a protective silver mirror (PF20–03–P01, Thorlabs, USA). The emission unit separates the emitted fluorescence light into spectral components for individual image formation of microfluidic channels, HeLa cells, and micro-beads using two dichroic mirrors (DMLP567L and DMLP805L, Thorlabs, USA). Individual fluorescence light beams are directed onto tube lenses (ITL200, Thorlabs, USA) to form images onto complementary metal-oxide-semiconductor (CMOS) cameras (CS135MUN, DCC3240N, Thorlabs, USA). Emission filters (ET845/55m, ET623/60m, ET520/40m, Chroma, USA) are placed before the cameras to block excitation light and select fluorescence wavelengths.

Dataset acquisition and preprocessing: We employed hardware triggering to enable the simultaneous acquisition of sequential and cross-channel fluorescence frames. Two programmable signal generators (33510B, Keysight Inc., USA) are used in lock mode to ensure synchronization among signal outputs. For two-channel experiments, one generator controlled the sequential LED excitation, while the other provided synchronized triggers to the cameras. For three-channel experiments, one generator is connected to a demultiplexer integrated circuit (74HC4052, Texas Instruments, USA) to drive three independent LED channels [74]. The second generator is used to send simultaneous trigger pulses to all cameras. All cameras are set to 0 gain to ensure consistent image acquisition conditions. The generated signals are validated using a high-resolution four-channel oscilloscope (DSOX3024A, Keysight Inc., USA). We mitigate camera-floor bias in the ground-truth channels via intensity thresholding applied before augmentation and training; cross-channel inputs are kept raw.

Model training and deployment: For training, fluorescence images acquired at 22 ms exposure and native resolution 1024 × 1024 are resized to

256 × 256. Each resized frame is split into four non-overlapping 128 × 128 tiles, which are spatially shuffled to increase variability. Models are trained on both the full resized frames and the shuffled-tile variants; random gamma jitter is applied only to the tile variants, while raw resized frames are left unchanged (Figure 4.10, Appendix, p. 97). The dataset is split 4:1 into training and validation. In total, 3750 paired images (input–output) are extracted from 15 continuous video sequences spanning five distinct samples that include different spheroid sizes/morphologies and diverse micro-agent actuation/aggregation patterns (Table 4.3, Appendix, p. 96). Three sequences (750 pairs) are reserved for validation; the remaining 3000 pairs are doubled to 6000 via the tile-shuffle augmentation for training.

We evaluate the proposed framework with two architectures: a plain U-Net and a pix2pix model (U-Net generator with a PatchGAN discriminator). Training is performed on an NVIDIA RTX A6000 GPU (48 GB VRAM), using 45 GB of system RAM and an 8-core CPU, with batch size 16 and learning rate 1×10^{-4}. Early stopping monitors the mean SSIM on the validation set (750 images) with a patience of six epochs and a minimum improvement threshold of 5×10^{-4}. A detailed list of training parameters is provided in Table 4.4 (Appendix, p. 99).

The U-Net is optimized purely with an L_1 reconstruction loss:

$$\mathcal{L}_{\text{U-Net}} \;=\; \lambda_1 \left\| \mathbf{y} - G(\mathbf{x}) \right\|_1, \tag{4.1}$$

with $\lambda_1 = 100$, where G maps the cross-channel input $\mathbf{x}$ to a predicted output $\hat{\mathbf{y}} = G(\mathbf{x})$, which is compared against the ground-truth target y.

For pix2pix training, the discriminator D distinguishes real pairs $(\mathbf{x}, \mathbf{y})$ from fake pairs $(\mathbf{x}, G(\mathbf{x}))$ and minimizes

$$\mathcal{L}_D = -\mathbb{E}_{\mathbf{x},\mathbf{y}}[\log D(\mathbf{x}, \mathbf{y})] - \mathbb{E}_{\mathbf{x}}\big[\log\big(1 - D(\mathbf{x}, G(\mathbf{x}))\big)\big]\,. \tag{4.2}$$

The generator uses a non-saturating adversarial objective and $\mathcal{L}_{\text{U-Net}}$:

$$\mathcal{L}_G = \lambda_{\text{adv}}\, \mathbb{E}_{\mathbf{x}}[-\log D(\mathbf{x}, G(\mathbf{x}))] + \lambda_1 \left\| \mathbf{y} - G(\mathbf{x}) \right\|_1, \tag{4.3}$$

with $\lambda_1 = 100$ and $\lambda_{\text{adv}} \in \{0.05, 0.1, 0.2, 0.4, 1.0\}$. For comparison, the U-Net corresponds to the $\lambda_{\text{adv}} = 0$ case but is trained separately with $\mathcal{L}_{\text{U-Net}}$. All trainings are stable, with smoothly decreasing generator losses and steadily improving validation SSIM until early stopping (Figure 4.12, Appendix, p. 100).

For the morphology-matched spheroids labeled with red CMTPX and green CMFDA, we curated new datasets containing 1268 paired images for training and 317 for validation and early stopping. Augmentations are applied as described in Figure 4.10 (Appendix, p. 97), resulting in a total training dataset of 2536 paired frames.

For deployment, the independently trained generators (Input Channel → MM/CC) are wrapped into a single PyTorch module that fans out a shared input and returns both outputs concurrently. The composite model is compiled with Torch-TensorRT at FP16 for an input of $1 \times 1 \times 256 \times 256$. Inference runs on the RTX A6000, and latency is measured over the validation set with CUDA synchronization. Please refer to the GitHub repository (https://github.com/JuanJJHS/Cross-Channel-Acquisition-and-Deep-Learning-Based-Inference) for the scripts used for preprocessing, augmentation, and training.

Brightfield and scanning electron microscopy: Brightfield images are acquired using an inverted microscope (Axiovert A1, Carl Zeiss AG, Germany) for morphological inspection of HeLa cell spheroids. Scanning electron microscopy (SEM) is performed using a JSM-7200F (JEOL, Japan) to visualize the morphology of magnetic electrospun fibers at 450× magnification, 7.3 mm working distance and an accelerating voltage of 5 kV.

Irradiance measurements: LED irradiance per channel is measured using a photodiode sensor (S130VC, Thorlabs, USA) connected to a digital power meter console (PM100D, Thorlabs, USA). Reported values are averaged over 10 consecutive measurements to ensure accuracy and repeatability.

Quantitative metrics: All metrics are computed on native grayscale images (no histogram matching). When regions of interest (ROIs) are used, the side length and location are reported in the figure captions. Let y denote the ground-truth image and $\hat{y}$ the predicted image, both quantized to $L = 255$ gray levels. Unless noted, all metrics are computed over all N pixels in the image, where i indexes pixel positions.

- Gradient-normalized cross-correlation (G-NCC): This metric compares spatial intensity changes rather than absolute brightness. A percentile sweep of input intensities evaluates structural correspondence while progressively retaining brighter input features. G-NCC

is computed as:

$$\mathrm{G{-}NCC}_p(g,\hat{g}_p) = \frac{\sum_{i=1}^{N}(g_i-\bar{g})(\hat{g}_{p,i}-\bar{\hat{g}}_p)}{\sqrt{\sum_{i=1}^{N}(g_i-\bar{g})^2}\sqrt{\sum_{i=1}^{N}(\hat{g}_{p,i}-\bar{\hat{g}}_p)^2}},$$

where g is the Sobel gradient-magnitude map of the unmasked target image, and $\hat{g}_p$ is the Sobel gradient-magnitude map of the input after intensity thresholding at percentile p. Thresholds are calculated from positive input intensities, with intensities at or below each threshold set to zero. The quantities $\bar{g}$ and $\bar{\hat{g}}_p$ denote the means of the respective gradient maps over all N image pixels. If either map has a standard deviation below 10^{-6}, the correlation is assigned zero. The final score is:

$$\mathrm{maxG{-}NCC} = \max_p \left|\mathrm{G{-}NCC}_p(g,\hat{g}_p)\right|,$$

which ranges from 0 to 1.

- Structural similarity index metric (SSIM): This metric correlates with perceived quality by jointly assessing luminance, contrast, and structure. We compute SSIM using the following equation:

$$\mathrm{SSIM}(y,\hat{y}) = \frac{(2\mu_y\mu_{\hat{y}}+C_1)(2\sigma_{y\hat{y}}+C_2)}{(\mu_y^2+\mu_{\hat{y}}^2+C_1)(\sigma_y^2+\sigma_{\hat{y}}^2+C_2)},$$

with local means $\mu_y, \mu_{\hat{y}}$, variances $\sigma_y^2, \sigma_{\hat{y}}^2$, and covariance $\sigma_{y\hat{y}}$ computed using a Gaussian 11×11 window. The constants $C_1 = (K_1L)^2$, $C_2 = (K_2L)^2$ with $K_1 = 0.01$, $K_2 = 0.03$, $L = 255$. These values follow the standard SSIM formulation and help stabilize the metric when local means or variances are close to zero.

- Peak signal-to-noise ratio (PSNR): This standard interpretable error metric in dB complements SSIM by emphasizing absolute, pixel-wise fidelity. PSNR is defined as follows:

$$\mathrm{PSNR}(y,\hat{y}) = 10\log_{10}\left(\frac{255^2}{\mathrm{MSE}(y,\hat{y})}\right),\ \mathrm{MSE}(y,\hat{y}) = \frac{1}{N}\sum_i (y_i-\hat{y}_i)^2.$$

- GLCM-based contrast similarity (GCS): This metric complements SSIM and PSNR, providing micro-texture similarity and perceptual

realism. Let $P_{ij}(z)$ be the normalized gray-level co-occurrence matrix (GLCM) of image z computed with offset distance d=1 pixel and angle 0°, 256 gray levels, symmetric counting, and normalization $\sum_{i,j} P_{ij}(z)$=1. GLCM contrast is computed as follows:

$$C(z) = \sum_{i,j} (i-j)^2 \, P_{ij}(z).$$

We compare contrast via:

$$\mathrm{GCS}(y, \hat{y}) = \max\left(0,\ 1 - \frac{|\, C(\hat{y}) - C(y) \,|}{C(y) + \varepsilon}\right),$$

where $\varepsilon = 10^{-6}$. GCS $\in [0, 1]$; 1 indicates perfect contrast match.

- Normalized fluorescence change ($\Delta F/F_0$): This is a dimensionless measure used in fluorescence imaging to track relative intensity dynamics independent of absolute gain. For a region containing N pixels (full frame or an ROI), let:

$$F(t) = \frac{1}{N} \sum_{i \in R} z_i(t),$$

where $z_i(t)$ is the grayscale intensity at time t. We compute the normalized fluorescence change as follows:

$$\frac{\Delta F}{F_0}(t) = \frac{F(t) - F_0}{F_0} \times 100\ \%,$$

where the baseline F_0 is the fluorescence intensity reference.

Cross-channel map and intensity imbalance analysis: We estimated a linear cross-channel map using measured target channels (MM and CC) and their corresponding cross-channel frames (CM). The model is fitted using 116 paired frames acquired under identical imaging conditions. A linear least-squares regression is performed to estimate the average coupling between channels, yielding the following relationship: CM = a MM+b CC+ c, with fitted coefficients a = 0.1241, b = 0.1334, and a constant offset c = 0.02327, which accounts for background signal and residual noise. This empirical model is subsequently used to generate synthetic cross-channel

inputs for controlled evaluation. Synthetic target channels are obtained by globally scaling the measured images using an imbalance parameter β, such that $\mathrm{MM}' = \beta\,\mathrm{MM}$ and $\mathrm{CC}' = (1-\beta)\,\mathrm{CC}$. The corresponding synthetic cross-channel frame is then computed as $\mathrm{CM}' = a\,\mathrm{MM}' + b\,\mathrm{CC}' + c$. These synthetic inputs are used exclusively for evaluation and are not included during model training.

Reconstruction accuracy under intensity imbalance is quantified using a masked structural similarity index metric (SSIM). Regions of interest (ROIs) are defined from the measured ground truth target channels by percentile thresholding to exclude background-dominated regions. Specifically, for measured target channels, binary ROI masks are defined as

$$\mathcal{R}_{\mathrm{MM}}(i) = \begin{cases} 1, & \mathrm{MM}(i) \geq P_{98}(\mathrm{MM}) \\ 0, & \text{otherwise} \end{cases}, \quad \mathcal{R}_{\mathrm{CC}}(i) = \begin{cases} 1, & \mathrm{CC}(i) \geq P_{98}(\mathrm{CC}) \\ 0, & \text{otherwise} \end{cases}, \tag{4.4}$$

where i indexes pixels and $P_{98}(\cdot)$ denotes the 98th percentile of pixel intensities. The resulting ROI masks are computed once from the measured channels and applied identically to the corresponding synthetic targets $(\mathrm{MM}', \mathrm{CC}')$ and their predictions prior to metric computation within the ROI.

To quantify the redistribution of predicted signal between channel-specific regions, a signal leakage ratio (ρ) is computed. For the predicted MM' ($\widehat{\mathrm{MM}'}$), this ratio is defined as

$$\rho_{\mathrm{MM}} = \frac{\left\langle \widehat{\mathrm{MM}'} \cdot \mathcal{R}_{\mathrm{CC}} \right\rangle}{\left\langle \widehat{\mathrm{MM}'} \cdot \mathcal{R}_{\mathrm{MM}} \right\rangle}, \tag{4.5}$$

whereas for the predicted CC' ($\widehat{\mathrm{CC}'}$) it is defined as

$$\rho_{\mathrm{CC}} = \frac{\left\langle \widehat{\mathrm{CC}'} \cdot \mathcal{R}_{\mathrm{MM}} \right\rangle}{\left\langle \widehat{\mathrm{CC}'} \cdot \mathcal{R}_{\mathrm{CC}} \right\rangle}. \tag{4.6}$$

Here, $\langle \cdot \rangle$ denotes the mean over pixels within the ROI. This ratio provides a direct and directional measure of cross-channel signal leakage in the predicted outputs as a function of the imposed intensity imbalance.

Appendix

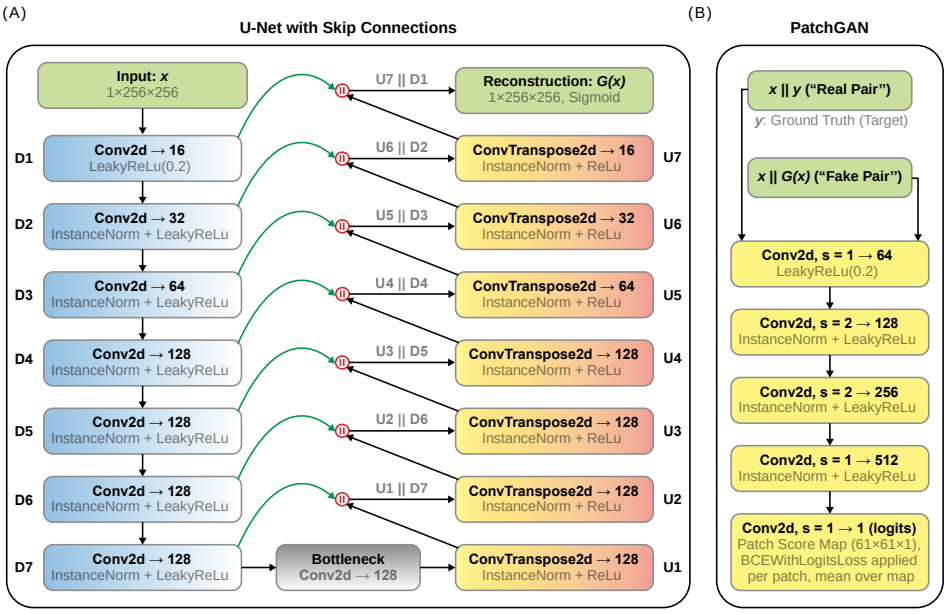


Figure 4.9: Architectures used in the real-time reconstruction framework. **(A)** U-Net with a stem (first encoder block), six further encoder blocks, a bottleneck, seven decoder blocks, and a final transposed convolution that produces a $1 \times 256 \times 256$ reconstruction ($G(x)$) from input cross-channel frame (x). To maintain pixel-level registration between the input and the reconstruction, all two-dimensional convolutions (Conv2d) and transposed convolutions (ConvTranspose2d) use a kernel (k=4), stride (s=1), and padding (p=1) (reflect padding for Conv2d). The U-Net architecture features skip connections, which are channel-wise concatenations: $U2 \leftarrow [U1 \,\|\, D7]$, $U3 \leftarrow [U2 \,\|\, D6]$, …, Final $\leftarrow [U7 \,\|\, D1]$. **(B)** PatchGAN inputs are concatenated pairs—real ($[x \,\|\, y]$) and fake ($[x \,\|\, G(x)]$). With strides (s = 1, 2, 2, 1, 1), it outputs a patch logit map $61 \times 61 \times 1$. Binary cross-entropy with logits is computed element-wise and averaged over patches within each mini-batch.

Table 4.3: Acquisition settings per dataset used for training and validation. All sequences were recorded at 1024×1024 with 0 dB camera gain and 22 ms exposure time. "FOV Motion" indicates stage-driven field of view motion during acquisition.

Dataset	LED–M (mW/cm^2)	LED–C (mW/cm^2)	Frames	Sample	#Spheroids	FOV Motion	Magnetic actuation	Observations
D01	62.5	13.5	250	S01	1	yes	unidirectional	No relative translation / rotation of spheroid.
D02	62.5	13.5	250	S01	0	yes	unidirectional	-
D03	62.5	13.5	250	S01	3	yes	multi-orient	One spheroid partially outside the FOV
D04	62.5	13.5	250	S01	5	yes	multi-orient	Spheroids have irregular shape; different fluorescence intensities
D05	62.5	13.5	250	S02	2	yes	multi-orient	Spheroid rotation
D06	62.5	13.5	250	S02	1	yes	multi-orient	Spheroid translation
D07	62.5	13.5	250	S03	1	yes	unidirectional	Spheroid has irregular shape
D08	62.5	13.5	250	S03	1	yes	multi-orient	Spheroid has irregular shape; translation
D09	62.5	13.5	250	S03	1	yes	multi-orient	Spheroid translation due to micro-agent interaction
D10	62.5	13.5	250	S04	1	yes	unidirectional	Spheroid translation and rotation
D11	62.5	13.5	250	S04	1	yes	unidirectional	Spheroid translation
D12	62.5	13.5	250	S04	2	yes	unidirectional	Spheroids partially outside the FOV
D13	62.5	13.5	250	S04	2	yes	multi-orient	Spheroids show different fluorescence intensity; translation
D14	62.5	13.5	250	S05	2	yes	multi-orient	Spheroids show different fluorescence intensity; translation and rotation
D15	62.5	13.5	250	S05	1	yes	unidirectional	Spheroid translation and rotation

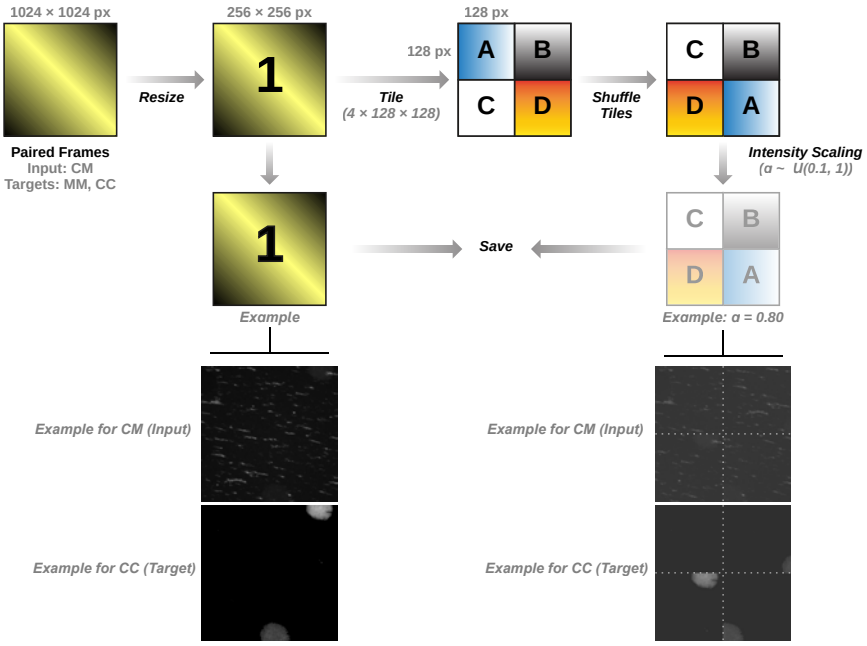


Figure 4.10: Data augmentation used to train U-Net and pix2pix. From each paired frame set—co-registered images of the same field of view consisting of the cross-channel input (CM) and its targets (MM, CC)—we generate two training samples. (1) Resized-only: resize to 256×256 pixels. (2) Tiled–shuffled: take the resized frame, split into four 128×128 tiles, randomly permute their order (re-sampled for each source frame), and scale by $\alpha \sim \mathcal{U}(0.1, 1.0)$. The same α is applied to the input and its paired target to preserve correspondence. Both outputs (resized-only and tiled–shuffled) are stored and used for training. For intensity scaling notation, "$\sim$" means "is drawn from", and $\mathcal{U}(a, b)$ denotes the continuous uniform distribution on $[a, b]$.

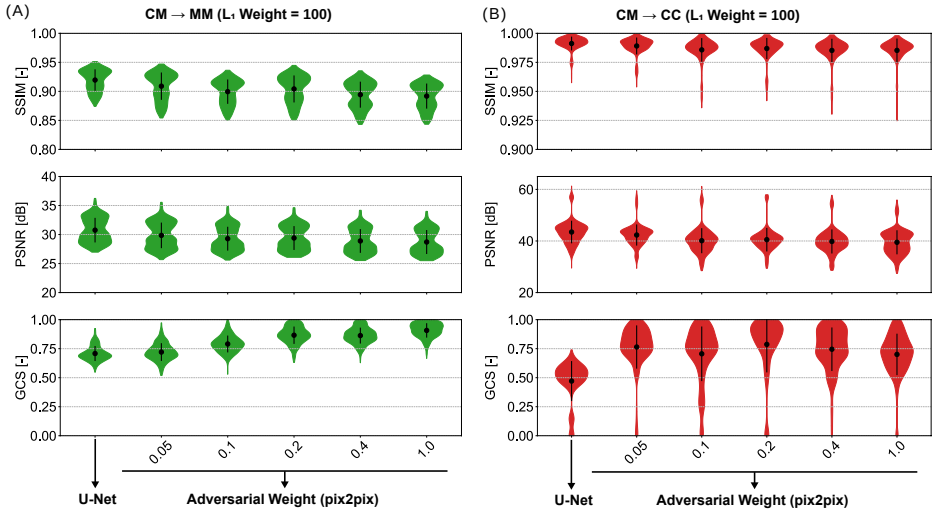


Figure 4.11: Effect of adversarial weight on reconstruction quality. Violin plots of structural similarity index metric (SSIM), peak signal-to-noise ratio (PSNR), and contrast similarity (GCS) for **(A)** CM→MM and **(B)** CM→CC. All models use an L_1 loss with a reference weight of 100. pix2pix model adds an adversarial loss weight ($\lambda_{\text{adv}} \in \{0.05, 0.1, 0.2, 0.4, 1.0\}$). The U-Net baseline (leftmost) corresponds to $\lambda_{\text{adv}} = 0$. Increasing λ_{adv} improves the texture reconstruction fidelity and slightly reduces the SSIM and PSNR. In channel CC, this improvement is more notorious even at small adversarial weights as the spheroids contain more texture features compared to the micro-agent channel (MM). All pix2pix reconstructions presented in this study used λ_{adv} = 0.05, selected as a trade-off between GCS, PSNR, and SSIM. Violin envelopes show the score distribution for the 3 sequences used for validation (750 paired frames). Black dots and bars are the mean ± standard deviation.

Table 4.4: General training hyperparameters used for training U-Net and pix2pix models.

Parameter	**Setting**
Optimizer	Adam
Learning rate	1×10^{-4}
Adam betas	(0.5, 0.999)
Batch size	16
Precision	Mixed precision (AMP)
Max. epochs	50
Early stopping	patience = 6, $\Delta_{\text{min}} = 5 \times 10^{-4}$
DataLoader workers	8
Output activation	Sigmoid
Update ratio (Generator:Discriminator)	1 : 1
Normalization	InstanceNorm2d
Patch size	256×256

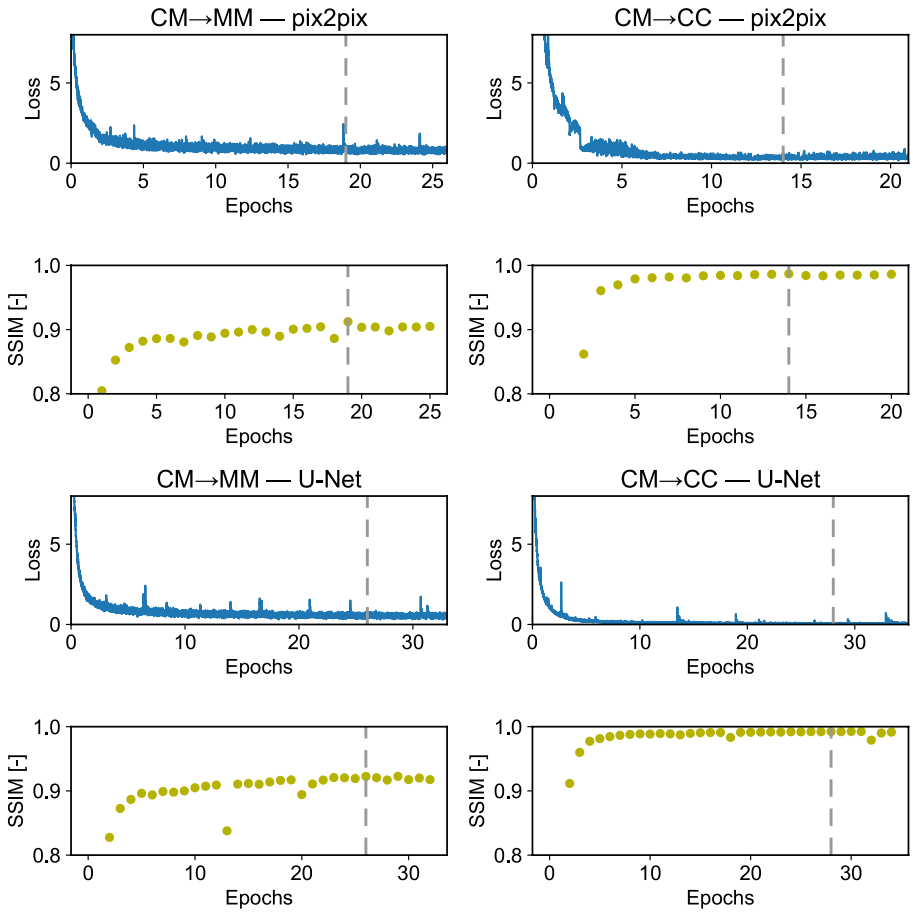


Figure 4.12: Training and validation performance for micro-agent (CM→MM) and spheroid models (CM→CC) using U-Net (λ_{adv}=0) and pix2pix (λ_{adv}=0.05) configurations. The first and third rows show generator loss curves—weighted sum of L_1 loss (λ_1=100) and adversarial loss (λ_{adv})—plotted across training epochs. The second and fourth rows show the corresponding validation SSIM curves used for early stopping. Vertical dashed gray lines mark the selected early-stopping checkpoints. Loss spikes reflect mini-batch variability and the inherent adversarial dynamics under mixed precision.

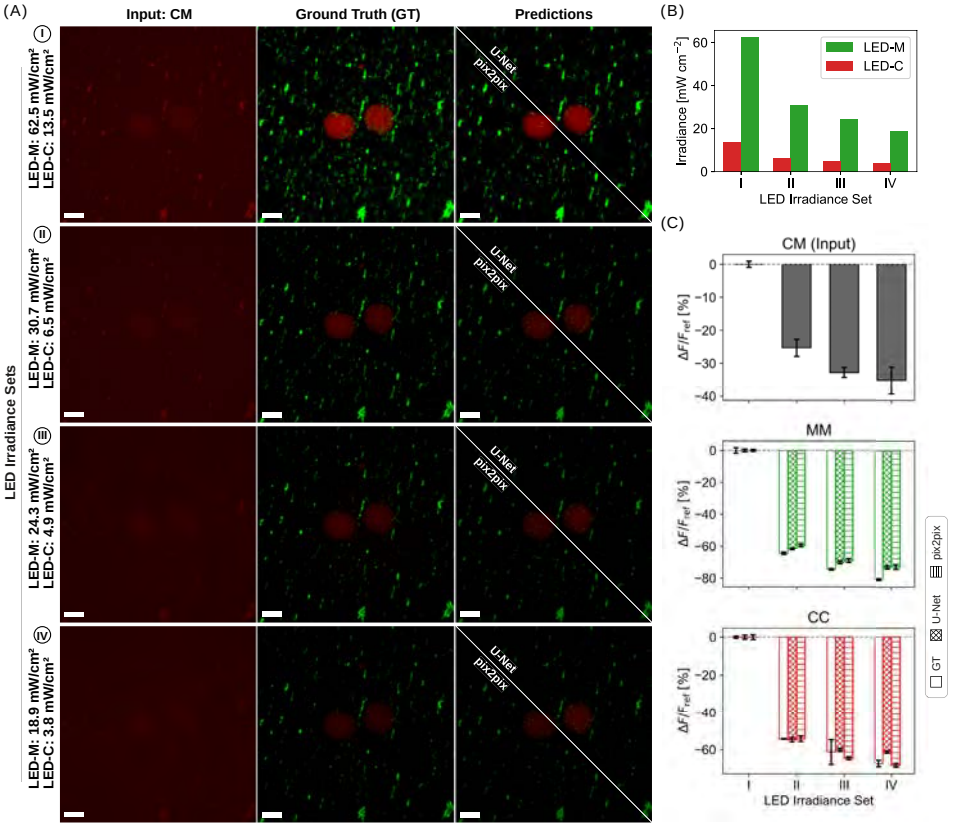


Figure 4.13: Fluorescence channel reconstructions under progressive LED dimming. **(A)** Representative CM input frames, ground truth, and composed reconstructions for MM (micro-agents) and CC (spheroids) at four irradiance sets (I–IV). Gamma correction ($\gamma = 0.5$) is applied to input frames to improve visualization. Scale bars: 100 µm. **(B)** LED irradiance for sets I–IV, showing tandem dimming. **(C)** Relative fluorescence change ($\Delta F/F_{ref}$) for CM, MM , and CC frames.Using U-Net ($\lambda_1 = 100$, $\lambda_{\text{adv}} = 0$) and pix2pix ($\lambda_1 = 100$, $\lambda_{\text{adv}} = 0.05$), we accurately reconstruct MM and CC and track per-channel $\Delta F/F_0$ across irradiance levels.

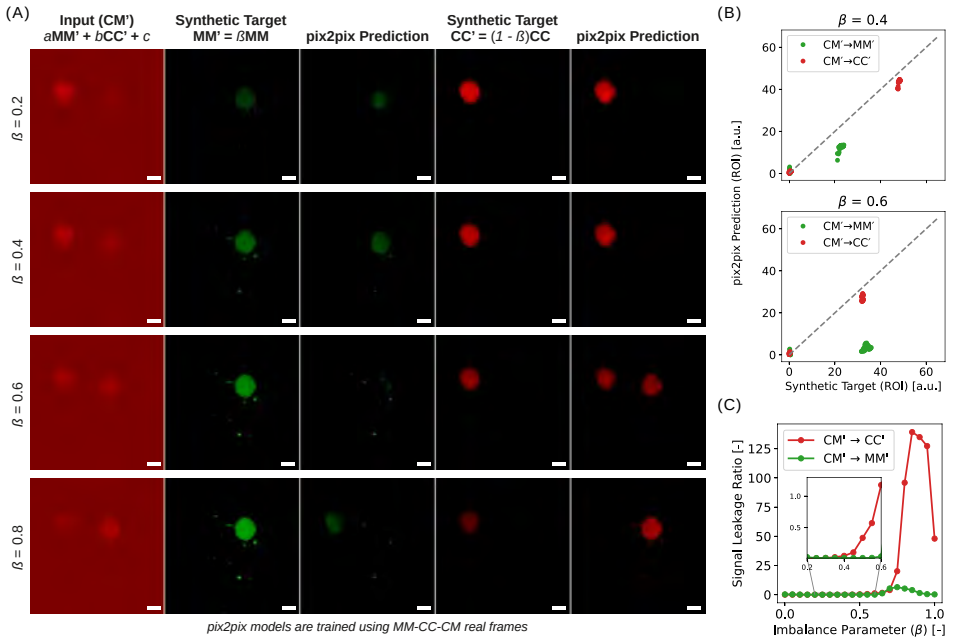


Figure 4.14: Intensity imbalance analysis using synthetic cross-channel inputs. **(A)** Representative synthetic cross-channel inputs (CM′), corresponding synthetic target channels (MM′ and CC′), and pix2pix predictions for increasing intensity imbalance (β). Scale bars: 100 µm. **(B)** Scatter plots of region-of-interest (ROI)–averaged intensities comparing pix2pix predictions with corresponding synthetic targets for representative β values. **(C)** Signal leakage ratio as a function of β, quantifying redistribution of predicted signal into the opposite channel's region. Ratios remain near zero in the well-conditioned regime ($\beta = 0.2$–0.45) and increase sharply across the transition regime ($\beta = 0.52$), indicating a progressive loss of identifiability as the intensity mixture becomes ill-conditioned.

CHAPTER 5

Two-photon microscopy for microrobotics

The following chapter is adapted from: ***J. J. Huaroto****, L. Capuano, M. Kaya, I. Hlukhau, F. Assayag, S. Mohanty, G.-w. Römer, and S. Misra. Two-photon microscopy for microrobotics: Visualization of micro-agents below fixed tissue, PLoS ONE, vol. 18, no. 8, pp. e0289725, 2023.*
The text and figures have been adapted for inclusion in this doctoral thesis.

Abstract

Optical microscopy is frequently used to visualize microrobotic agents (i.e., micro-agents) and physical surroundings with a relatively high spatial and temporal resolution. However, the limited penetration depth of optical microscopy techniques used in microrobotics (in the order of 100 µm) reduces the capability of visualizing micro-agents through biological tissue. Two-photon microscopy is a technique that exploits the principle of two-photon absorption, permitting live tissue imaging with sub-micron resolution and optical penetration depths (over 500 µm). The two-photon absorption principle has been widely applied to fabricate sub-millimeter-scale components via direct laser writing (DLW). Yet, its use as an imaging tool for microrobotics remains unexplored in the state-of-the-art. This study introduces and reports on two-photon microscopy as an alternative technique for visualizing micro-agents through biological tissue. In order to validate two-photon image acquisition for microrobotics, two types of micro-agents are fabricated and employed: (1) electrospun fibers stained with an exogenous fluorophore and (2) bio-inspired structure printed with autofluorescent resin via DLW. The experiments are devised and conducted to obtain three-dimensional reconstructions of both micro-agents, perform a qualitative study of laser-tissue interaction, and visualize micro-agents along with tissue using second-harmonic generation. We experimentally demonstrate

*J. J. Huaroto and L. Capuano contributed equally to this work.

two-photon microscopy of micro-agents through formalin-fixed tissue with a maximum penetration depth of 800 µm and continuous imaging of magnetic electrospun fibers with one frame per second acquisition rate (in a field of view of 135 × 135 µm^2). Our results show that two-photon microscopy can be an alternative imaging technique for microrobotics by enabling visualization of micro-agents under *in vitro* and *ex ovo* conditions. Furthermore, bridging the gap between two-photon microscopy and the microrobotics field has the potential to facilitate *in vivo* visualization of micro-agents.

5.1 Introduction

The field of microrobotics has the potential to revolutionize the traditional way of performing surgery by steering microrobotic agents within confined anatomical structures [190], [191]. Microrobotic agents (i.e., micro-agents) are the means to achieve tasks such as drug delivery, biopsy, and micro-assembly of biological samples [12], [192]. Typically, these miniaturized agents are responsive to external stimuli (e.g., magnetic fields [29], acoustic waves [193], and light [32], [33], [194]) and necessitate sensing/detection strategies for navigation and feedback. The development of novel techniques for visualization of micro-agents holds importance to translate the microrobotics field to the clinics and expand the application domains to clinically-relevant scenarios [192], [195], [196]. Visualization or imaging is required in microrobotics because the traditional sensors cannot be attached to the micro-agents due to size limitations. Thus, imaging modalities are used as external sensors to validate the functionalities and provide feedback. The literature on imaging techniques for microrobotics identifies three essential components towards visualization of micro-agents under *in vivo* and *in vitro* conditions. (1) Visualize micro-agents and physical surroundings [45]. (2) Achieve relatively high spatio-temporal resolution and penetration depth [197]. (3) Reduce the risk of side effects on patients/clinicians [21].

Current imaging techniques for the application domains of microrobotics partially undertake all three essential components. Ionizing techniques (e.g., X-ray computerized tomography [40], positron emission tomography [41], fluoroscopy [198], and single-photon emission computerized tomography [199]) have been proved for visualization of micro-agents towards *in vivo* applications. Nevertheless, the risk of side effects on patients and clin-

icians encourages the development of non-ionizing imaging techniques for microrobotics. Optical imaging [45], [79], [200], ultrasound [42], magnetic resonance imaging [43], photoacoustic imaging [44], [196], and magnetic particle imaging [201] are non-ionizing techniques used for visualization of micro-agents and physical surroundings. Optical imaging techniques such as bright field, confocal, and fluorescence microscopy offer a relatively high spatio-temporal resolution compared to other non-ionizing imaging techniques [21]. Yet, the limited optical penetration depth, scattering, and background noise reduce the capability of visualization micro-agents through biological tissue [74], [79]. Among non-ionizing techniques, photoacoustic imaging (i.e., microscopy and tomography) is a hybrid technique applicable to the field of microrobotics, addressing the limited penetration depth commonly encountered in optical microscopy techniques. For example, photoacoustic microscopy enables imaging of micro-agents underneath shallow tissue regions ($<\sim$ 1 mm) with a relatively high spatial resolution (3.2 µm) [194]. Photoacoustic tomography can overcome the penetration depth of photoacoustic microscopy. However, there exists a trade-off between spatial resolution and penetration depth. The spatial resolution achieved by photoacoustic tomography is typically in the order of 100 µm, which can hinder the detailed visualization of micro-agent morphology and intricacies [21], [195], [196]. Furthermore, the distortion of wavefronts caused by the non-uniform speed of sound in biological tissues can significantly impact the imaging performance under *in vivo* conditions [202].

An appealing remedy to overcome the shortcomings of optical microscopy techniques in microrobotics is two-photon microscopy [21], [70]. This non-ionizing fluorescence technique uses a near-infrared femtosecond pulsed laser to generate two-photon absorption, allowing for visualization of biological tissue with penetration depths over 500 µm [203], [204]. Two-photon excitation produces fluorescence at the characteristic emission wavelengths of the fluorophore, generally matching those obtained with one-photon excitation [76]. Thus, although near-infrared light is used for excitation, the emitted fluorescence must still travel through the tissue at visible wavelengths. Absorption and scattering therefore affect both excitation delivery and fluorescence collection. Two-photon excitation can also generate tissue autofluorescence, while second-harmonic generation provides a distinct nonlinear mechanism for stain-free contrast [205].

The spatial and temporal resolutions achieved through two-photon mi-

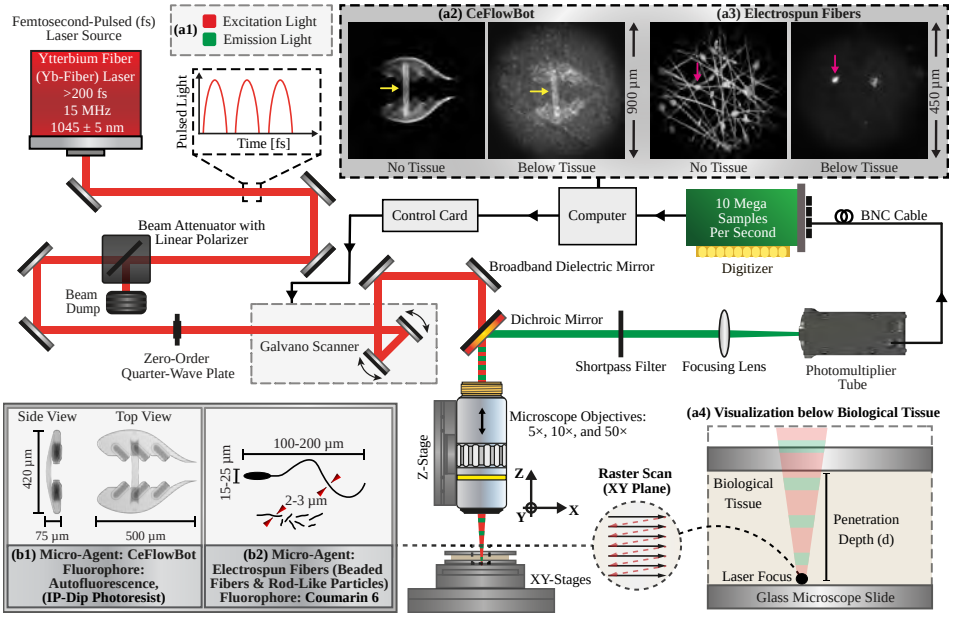


Figure 5.1: Schematic showing the optical layout of the two-photon microscope developed for visualization of micro-agents along with biological tissue. (a1) The microscope utilizes a femtosecond laser for excitation light generation while the emission light is delivered to a photomultiplier. The following micro-agents are located below formalin-fixed tissue and visualized through it: (a2) a bio-inspired structure called CeFlowBot, and (a3) electrospun fibers. The colored arrows indicate structural morphologies of the micro-agents that are visible through biological tissue. (a4) Illustration of the imaging geometry, with the micro-agents positioned beneath a fixed-tissue layer relative to the microscope objective. Here, the penetration depth (d) refers to the nominal thickness of the overlying tissue layer. The static through-tissue experiments use nominal depths ranging from 250 to 800 μm. (b1)-(b2) Schematic representation of the fabricated fluorescent micro-agents.

croscopy are in the order of sub-microns and 26.4 frames per second (in the field of view of 1490 × 128 pixels), respectively [197]. Although two-photon absorption has found applications for fabricating sub-millimeter size components via direct laser writing (DLW) (e.g., micro-agents [104], miniaturized optical lenses [206], and metamaterials [207]), its use in microrobotics for visualizing miniaturized agents through biological tissue remains unexplored in the literature.

This study investigates two-photon microscopy for visualizing micro-agents through biological tissue. In the fixed-tissue experiments, the tissue layer is positioned between the microscope objective and the micro-agents.

Two types of fluorescent micro-agents are fabricated and used for visualization. (1) A bio-inspired structure (called CeFlowBot) printed with an autofluorescent resin (IP-Dip resin) via DLW [104]. (2) Electrospun fibers (i.e., beaded fibers and rod-like particles) stained with an exogenous fluorophore (coumarin 6) [45]. The biological tissues used throughout the study are prepared from rat organs and White Leghorn chick embryos according to protocols for bio-products and the Dutch animal care guidelines. The rat organs are fixed to preserve cells and tissue morphology long-term. An overview of the microscope, micro-agent types, and through-tissue imaging geometry is shown in Fig 5.1. The remainder of this study presents and discusses five experimental protocols. (1) The spectrum analysis of the fluorescent micro-agents. (2) Two-/Three-dimensional visualization of micro-agents. (3) Qualitative study of laser-tissue interaction. (4) Visualization of micro-agents through fixed tissue. (5) Continuous visualization and magnetic actuation of electrospun fibers.

5.2 Results

5.2.1 Spectrum analysis of fluorescent micro-agents

The first step in two-photon microscopy of fluorescent micro-agents is the spectrum analysis of fluorophores used for staining or fabricating micro-agents. The spectrum analysis of fluorophores provides the excitation and emission wavelength limits for fluorescence imaging. Fig 5.2(a1) shows the spectrum analysis of coumarin 6 (exogenous) used to stain electrospun fibers (i.e., beaded fibers and rod-like particles). Coumarin 6 exhibits normalized fluorescence intensity peaks (excitation/emission) of 461 nm and 505 nm, respectively. For validating the spectrum analysis of coumarin 6, electrospun fibers are imaged using a custom-built fluorescence microscope [74] with excitation light wavelengths (450–490 nm) (Fig 5.2(a2) and (a3)).

The second fluorophore used in this study is a photoresist (IP-Dip) in the form of an autofluorescent resin widely used for fabricating sub-millimeter components for microrobotics via DLW [208]. Previous studies on excitation/emission spectra of IP-Dip resin provide the emission spectrum for a limited range of wavelengths [209], [210]. Here, we present the ultraviolet and visible spectra of IP-Dip resin at varying excitation and emission wavelengths (Fig 5.2(b1)-(b3)). The IP-Dip resin shows normal-

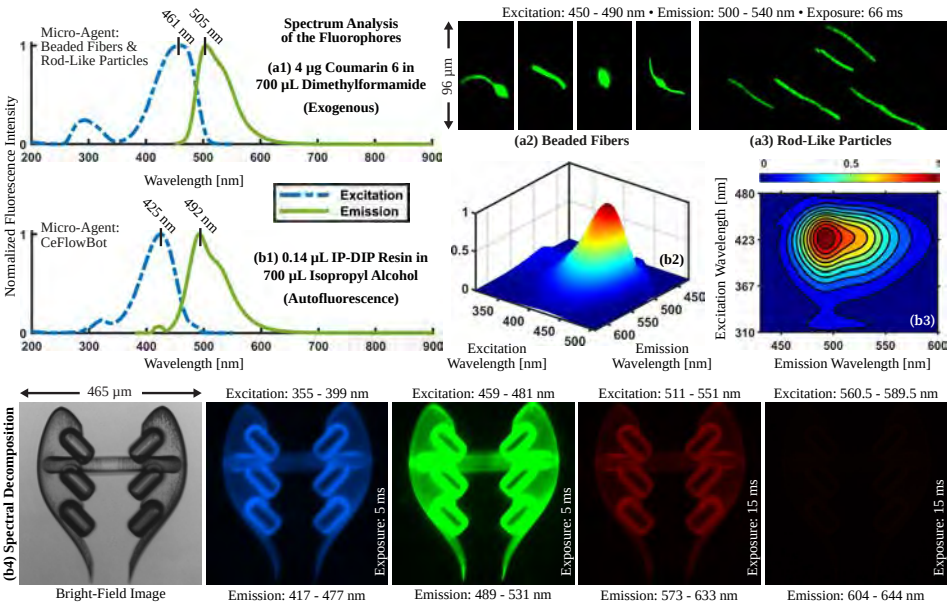


Figure 5.2: Spectrum analysis of fluorophores. (a1) Coumarin 6 (exogenous) (442631-1G, Sigma-Aldrich, USA) and (b1) IP-Dip resin (autofluorescence) (IP-Dip, Nanoscribe GmbH, Germany). Fluorescence microscopy of electrospun fibers with the following types of morphology: (a2) beaded fibers and (a3) rod-like particles. (b2)-(b3) 3D and contour plots showing the spectrum of IP-Dip resin at varying excitation and emission wavelengths. (b4) Spectral decomposition of CeFlowBot (made from IP-Dip resin) using a fluorescence microscope (EVOS FL, Life Technologies, USA).

ized fluorescence intensity peaks (excitation/emission) of 425 nm and 492 nm, respectively. In order to validate the spectrum analysis of IP-Dip, we perform the spectral decomposition of CeFlowBot using a commercial fluorescence microscope (EVOS FL, Life Technologies, USA). The spectral decomposition permits the identification of the excitation light wavelengths for fluorescence imaging. Fig 5.2(b4) shows that excitation light in the wavelength range (355–551 nm) can generate fluorescence image acquisition with exposure durations of 5 ms and 15 ms.

5.2.2 Two-photon microscopy of micro-agents

The spectrum analysis and spectral decomposition of fluorescent micro-agents determine the wavelength limits of excitation/emission light for fluorescence image acquisition. However, it is often difficult to predict the

two-photon excitation spectra from one-photon data because of the different quantum mechanical backgrounds [211]. In order to experimentally validate two-photon microscopy of fluorescent micro-agents characterized by one-photon excitation/emission spectra, we set the photomultiplier at maximum gain. The laser power percentage (LPP) is gradually increased until image formation is obtained. Our results show that a minimum of 10% LPP (6 mW average power at 15 MHz repetition rate) is required for visualization of the structural morphologies of micro-agents. Fig 5.1(a2) and (a3) show two-photon image acquisition of both micro-agents using 20% LPP (35 mW average power).

Two-photon microscopy can be applied for three-dimensional visualization of biological tissue [204]. Here, we test two-photon microscopy to enable three-dimensional visualization of micro-agents by conducting Z-stacking experiments (Fig 5.3(a1) and (b1)). The beaded fiber and a scaled version of CeFlowBot (scale factor of 0.5) are imaged with 50× and 10× microscope objectives and spacing steps of 1 µm and 5 µm, respectively. The Z-stacking images, which are obtained using 20% LPP, are analyzed using 3D slicer software for three-dimensional reconstructions (Fig 5.3(a2) and (b2), respectively) [212]. Furthermore, scanning electron microscopy of both micro-agents is included to validate the three-dimensional reconstructions and provide further morphology details (Fig 5.3(a3) and (b3)). Two-photon microscopy is experimentally validated for two-/three-dimensional visualization of fluorescent micro-agents. Yet, experiments involving biological tissue require further analysis regarding laser-tissue interaction to reduce the risk of side effects under *in vitro* and *in vivo* conditions.

5.2.3 Laser-tissue interaction

Visualization of micro-agents through biological tissue using a near-infrared femtosecond pulsed laser holds the risk of tissue damage by laser ablation and cellular necrosis under live imaging conditions [213]. Here, we present a qualitative study of laser-tissue interaction to assess visible ablation at the tested laser power levels. Current studies on two-photon microscopy suggest average laser powers in the order of 100 mW (at 80 MHz and pulse width from 1 fs to 10 ns) to avoid optical breakdown [214]. Here, we analyze the tissue damage by laser ablation generated by our femtosecond pulsed laser (15 MHz repetition rate and 230 fs pulse width). Fig 5.3(c) shows the

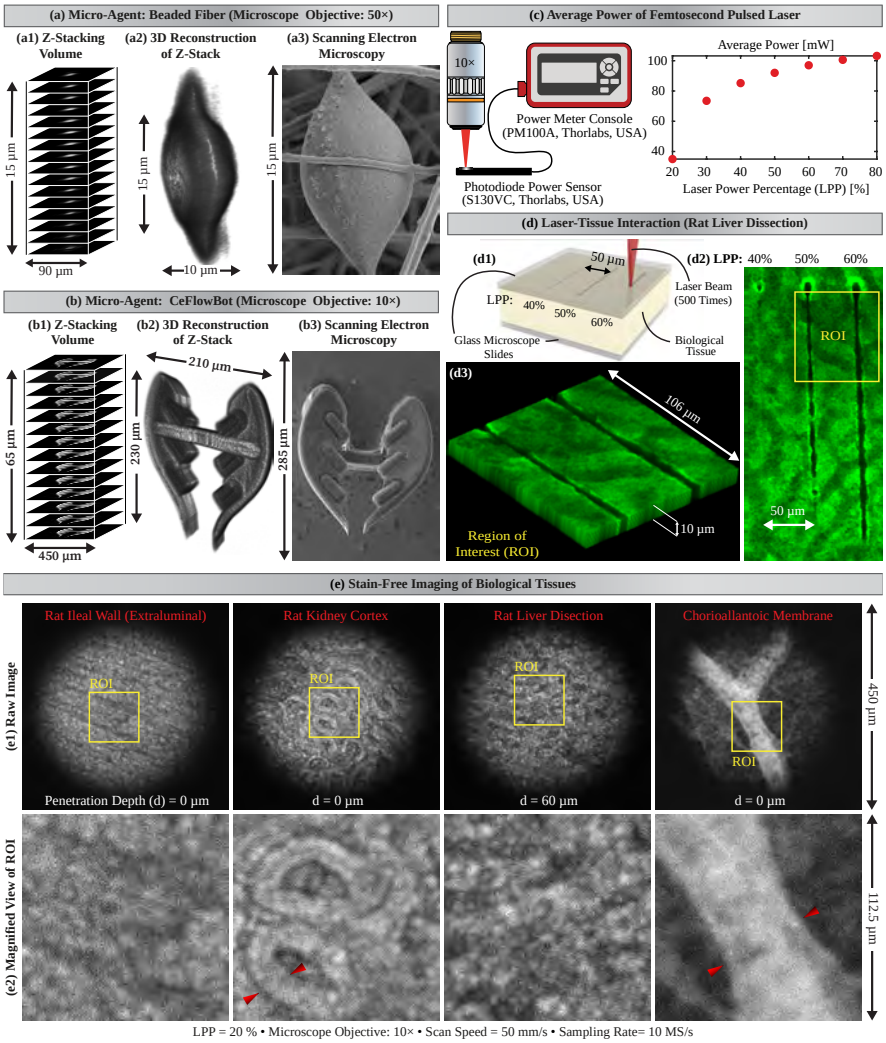


Figure 5.3: Z-stacking, 3D reconstruction, and scanning electron microscopy of micro-agents. (a1)-(a3) beaded fiber and (b1)-(b3) a scaled version of the bio-inspired structure (CeFlowBot), respectively. (c) Average power of femtosecond pulsed laser (pulse width of ∼ 230 fs and repetition rate of 15 MHz) at the focus of the laser beam. (d1) Illustration of the laser-tissue interaction using three laser power percentages (LPPs): 40%, 50%, and 60% with the corresponding average powers of 85 mW, 92 mW, and 97 mW, respectively. (d2) Confocal microscopy of laser-affected tissue (rat liver dissection). (d3) Z-stacking of a region of interest (ROI) containing laser-affected tissue corresponding to 50% and 60% LPP. (e1) Raw images acquired from stain-free imaging of formalin-fixed rat tissues and *ex ovo* chorioallantoic membrane using second-harmonic generation. (e2) Magnified view of the region of interest within the raw image. The red arrows indicate renal collecting tubules and vasculatures containing erythrocytes in rat kidney cortex and *ex ovo* chorioallantoic membrane, respectively.

average power of the femtosecond pulsed laser by varying the laser power percentage (LPP).

The tissue damage by laser ablation is a photo-thermal effect that depends on the optical properties of tissue (e.g., absorption and reduced scattering coefficient) [215]. We use a formalin-fixed tissue (rat liver dissection) for laser ablation experiments. Three different LPPs (LPP = 40%, 50%, 60%) are employed with a spacing of 50 µm between lines to analyze the tissue damage by laser ablation (Fig 5.3(d1)). The laser-affected tissue is imaged using a confocal microscope for analysis. A visual inspection shows that 40% of LPP does not generate tissue damage by laser ablation compared to 50% and 60% LPPs (Fig 5.3(d2)). Based on these observations, an LPP $\leq$ 40% (85 mW average power) was adopted for the subsequent imaging experiments. Fig 5.3(d3) shows the Z-stacking (10 µm depth) within a region of interest containing laser-affected tissue corresponding to 50% and 60% LPP. It is worth noting that there is an increase in the absorption and reduced scattering coefficients of tissue after formalin fixation [216]. Thus, further experiments on laser-tissue interaction are required to validate our microscope in clinically-relevant scenarios.

In order to test the microscope under *ex vivo* and *ex ovo* conditions, four biological tissues are visualized using a stain-free approach and 20% LPP (35 mW average power) (Fig 5.3(e)). Stain-free imaging of biological tissue includes autofluorescence and second-harmonic generation according to excitation/emission spectra of proteins or cells in biological tissue [205]. Fig 5.3(e1) shows the micrographs of fixed tissues and *ex ovo* chorioallantoic membrane containing erythrocytes within the vasculatures. Two-photon microscopy of biological tissue is tested using the maximum gain of the multiplier and gradually decreasing the value of LPP from 40% to 5%. Our results show that using an LPP $\leq$ 10% (6 mW average power) does not trigger the fluorescence intensity required for image formation.

5.2.4 Visualization of micro-agents through biological tissue

The spectrum analysis of fluorescent micro-agents and the qualitative study of laser-tissue interaction pave the way for the visualization of micro-agents along with biological tissue. The two-photon microscope used in this study has a single channel for fluorescence acquisition. Thus, the visualization of micro-agent and tissue relies upon the difference between the intensity

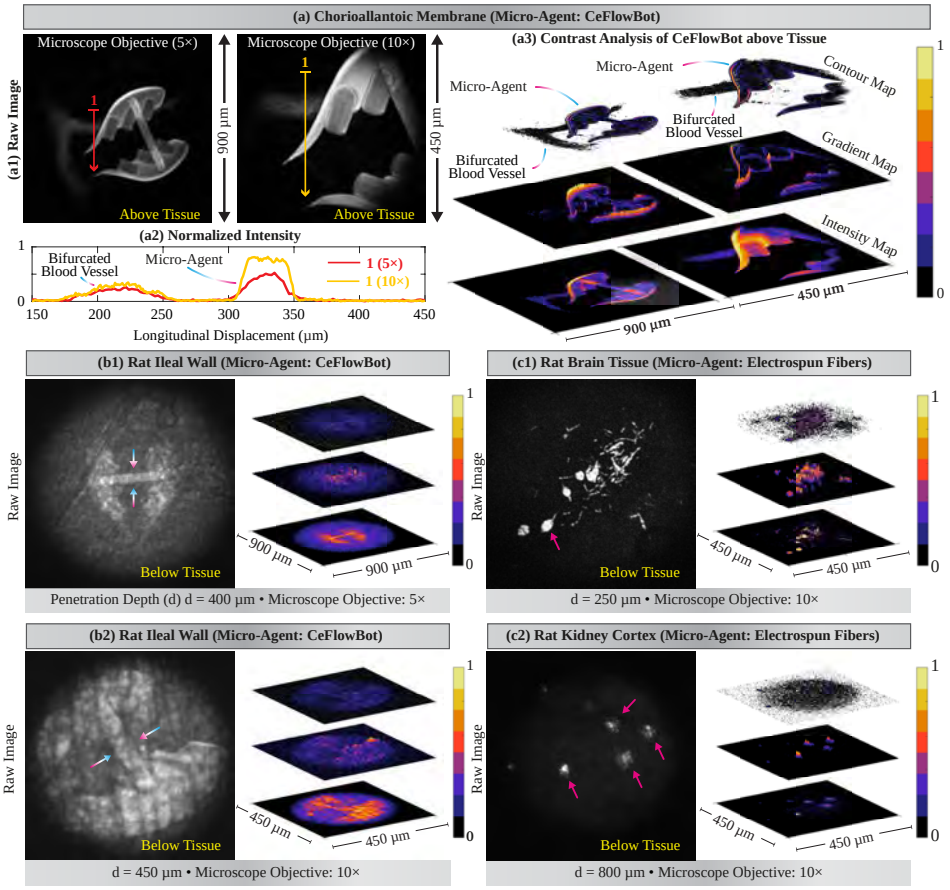


Figure 5.4: Contrast analysis of the two-photon microscopy images containing micro-agents and biological tissue. (a) Two-photon microscopy of CeFlowBot placed above a bifurcated vessel containing erythrocytes from *ex ovo* chorioallantoic membrane. (a1) Raw images acquired with 5× and 10× microscope objectives. (a2) Normalized fluorescence intensity of micro-agent and a bifurcated blood vessel along a longitudinal line. (a3) Contrast analysis to identify CeFlowBot and a bifurcated blood vessel. Two-photon microscopy and contrast analysis of CeFlowBot placed below a layer of rat ileal wall (fixed) using 5× (b1) and 10× (b2) microscope objectives. Two-photon microscopy and contrast analysis of electrospun fibers placed below a layer of rat brain tissue (fixed) (c1) and rat kidney cortex (fixed) (c2). The colored arrows indicate structural morphologies that are visible through fixed tissue.

of fluorescence signals. Contrast analysis provides information about the micro-agent and physical surroundings by extracting contour, gradient, and intensity maps from the acquired images (Fig 5.4). The CeFlowBot is initially imaged above an *ex ovo* chorioallantoic membrane to illustrate our method (Fig 5.4(a)). Two microscope objectives (5× and 10×) are utilized to modify the resolution and analyze the influence of the depth of field on the generation of fluorescence emission light (Fig 5.4(a1)). We observe that using the 10× microscope objective increases the image resolution, allowing for visualization of CeFlowBot morphology. Fig 5.4(a2) shows the normalized fluorescence intensity of CeFlowBot and *ex ovo* chorioallantoic membrane along a longitudinal line. The depth of field of the 10× microscope objective (3.5 µm) compared to the 5× microscope objective (14 µm) allows for more localized excitation of CeFlowBot, resulting in increased fluorescence emission light generation (Fig 5.4(a2)). Contrast analysis allows for the identification of CeFlowBot and bifurcated blood vessel (containing erythrocytes) from the *ex ovo* chorioallantoic membrane (Fig 5.4(a3)).

Experiments to visualize CeFlowBot through the rat ileal wall (fixed) are carried out with a maximum laser power percentage (LPP) of 40% to reduce the risk of tissue damage and demonstrate the potential of two-photon microscopy towards *ex vivo* and *in vivo* applications. Fig 5.4(b1) and (b2) show the visualization of CeFlowBot through the rat ileal wall using 5× and 10× microscope objectives. Our results reveal the structural morphology of CeFlowBot and provide visualization of the physical surroundings (e.g., muscularis propria) with penetration depths over 400 µm. Electrospun fibers are also imaged through formalin-fixed rat brain tissue and kidney cortex (Fig 5.4(c1) and (c2)). The sample for visualization of electrospun fibers through rat brain tissue is prepared for imaging with a maximum penetration depth of 250 µm. Fig 5.4(c1) shows a detailed visualization of electrospun fibers (i.e., beaded fibers and rod-like particles) morphology. For imaging experiments of electrospun fibers along with rat kidney cortex, the samples are prepared with a maximum penetration depth of 800 µm. Fig 5.4(c2) shows two-photon microscopy and contrast analysis of electrospun fibers imaged through a layer of rat kidney cortex. The fundamental morphology of electrospun fibers remains discernible through both tissue layers.

Published spectra of fresh rat tissues show higher reduced scattering in brain tissue than in heart and kidney tissues over 450–700 nm [217]. Tis-

sue absorption is characterized by the absorption length ($\ell_a(\lambda) = 1/\mu_a(\lambda)$), where μ_a is the absorption coefficient. For example, fresh rat kidney tissue exhibits an absorption coefficient of approximately 2.5 mm^{-1} near 550 nm, corresponding to an absorption length of approximately 0.4 mm [217]. Broader spectral measurements are available for human brain tissues over 360–1100 nm [218]. Absorption length accounts for absorption alone; achievable imaging depth also depends on scattering and signal collection.

The images acquired from electrospun fibers through fixed tissue do not reveal further information about the physical surroundings because the fluorescence intensity of electrospun fibers is higher compared to the autofluorescence and second-harmonic generation in biological tissue. An appealing approach to overcome the challenges of using a single photomultiplier tube is to incorporate additional dichroic mirrors along with photomultiplier tubes for color-coded visualization [204].

5.2.5 Continuous visualization of magnetic electrospun fibers

Static image acquisition of micro-agents through formalin-fixed tissue is the first step to bridging the gap between two-photon microscopy and microrobotics. However, the application domains of microrobotics require continuous imaging tools to localize micro-agents and verify their functionality. Here, we use two-photon microscopy for image acquisition of magnetic electrospun fibers at one frame per second in the field of view of 135 × 135 μm^2 (Fig 5.5). A solution containing magnetic electrospun fibers is perfused into a microfluidic channel with a height of 187 µm made from polydimethylsiloxane (PDMS) [45]. Thereon, an electromagnetic coil is utilized for actuating the magnetic fibers (Fig 5.5(a)). In order to elucidate continuous imaging of micro-agents, we devise two experiments for motion analysis using Lucas-Kanade optical flow as vector fields [219], [220]. The first experiment shows two magnetic electrospun fibers (micro-agent 1 and 2) within a microfluidic channel (Fig 5.5(b)). The micro-agents are oriented and pulled according to the magnetic field and gradients. During the experiment, we show the attachment of both micro-agents due to electrostatic interaction. Electrostatic interactions are caused by residual charges embedded within the surface or volume of the electrospun fibers [221]. The micro-agents are detached once the magnetic field turns from a negative to a positive value, demonstrating the visualization of micro-agent

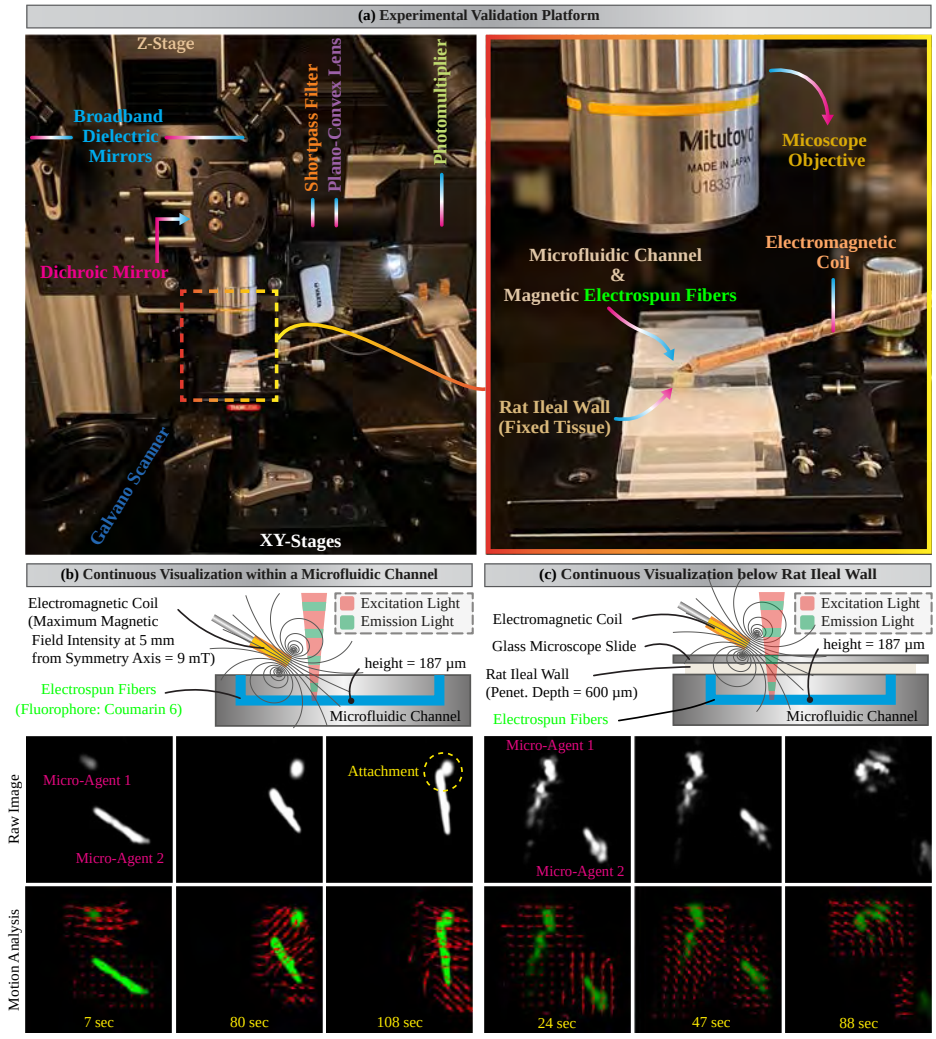


Figure 5.5: Actuation, continuous visualization, and motion analysis of magnetic electrospun fibers. (a) Experimental validation platform for two-photon image acquisition of micro-agents through biological tissue. (b) Visualization of magnetic electrospun fibers within a microfluidic channel using 10% laser power percentage (LPP) (6 mW average power). (c) Visualization of magnetic electrospun fibers through fixed tissue (rat ileal wall) using 40% LPP (85 mW average power). The experiments are carried out with a 10× microscope objective, a scanning speed of 50 mm/s, and a sampling rate of 10 MS/s. The vector field colored in red represents the motion analysis. The continuous image acquisition experiments are shown in Video S1 (Supporting information).

functionalities via two-photon microscopy.

The second experiment is carried out by placing fixed tissue (rat ileal wall 600 µm thick) on top of the microfluidic channel and covering it with a glass microscope slide (Fig 5.5(c)). The results of this experiment uphold continuous imaging and actuation of two magnetic electrospun fibers through formalin-fixed tissue. In particular, fixed tissue is a dispersive medium showing increments of reduced scattering coefficient compared to fresh tissue [216]. Therefore, visualization of electrospun fibers through tissue requires a higher laser power percentage (LPP = 40%) for image formation compared to the previous experiment without tissue (LPP = 10%). Despite the increase in scattering, our results permit us to identify the morphology of electrospun fibers while providing continuous image acquisition for detection and visual tracking of micro-agents through biological tissue. The experiments are performed with an LPP $\leq$ 40% to reduce the risks of tissue damage by laser ablation.

One of the challenges observed in the experiments is the frame acquisition rate (1 fps), which imposes a limitation on the analysis of micro-agents with high dynamics. Previous *in vivo* studies have demonstrated that micro-agents can move at relatively low velocities ($<$ 10 µm/s) under magnetic guidance [195], [222]. Drawing upon this comprehension, our two-photon microscope holds the potential for effective *in vivo* visualization. Furthermore, the incorporation of optical and optomechanical technologies, such as polygonal mirrors and resonant scanners coupled with optical fibers, can improve the scan rate of our two-photon microscope and enable real-time imaging [197], [223].

5.3 Conclusion

This chapter demonstrates two-photon microscopy of autofluorescent CeFlowBot structures and fluorescent electrospun fibers, including 3D reconstruction and visualization through formalin-fixed rat tissues. Static imaging reveals micro-agent morphology through nominal tissue thicknesses of 250 μm for brain tissue, 400–450 μm for the ileal wall, and 800 μm for kidney cortex. Continuous imaging during magnetic actuation is demonstrated through a nominal ileal-wall thickness of 600 μm at one frame per second over a field of view of 135 $\times$ 135 μm^2. The continuous-imaging demonstrations use average laser powers of 6 mW without overlying tissue

and 85 mW through the tissue layer. The qualitative laser–tissue interaction study identifies visible ablation in fixed liver tissue at average powers of 92 and 97 mW, whereas no visible ablation is observed at 85 mW under the tested scanning conditions. These observations are specific to the tested specimen and exposure conditions. The results establish the feasibility of combining magnetic actuation with continuous two-photon observation through fixed tissue. The acquisition rate of one frame per second limits observation of rapid dynamics, while single-channel detection limits separation of micro-agent fluorescence from weaker tissue signals.

5.4 Experimental section

Experimental validation platform: The two-photon microscope used to visualize micro-agents and biological tissue is shown in Fig 5.1. This microscope uses a Ytterbium fiber (Yb-fiber) femtosecond pulsed laser (Y-Fi, KMLabs, USA) as an excitation light source to generate fluorescence emission light from the samples (Fig 5.1(a1)). The laser beam is characterized by ultra-short pulses ($>$ 200 fs) with a repetition rate of 15 MHz and a center wavelength (λ) of 1045 nm. The energy of the laser pulses is modulated using a beam power attenuator (Ultrafast, Altechna, Lithuania), which also generates a linear polarized beam. Next, a zero-order quarter-wave plate (WPQSM05-1030, Thorlabs, USA) creates a circularly polarized beam for image contrast enhancement [224]. Three infinity-corrected microscope objectives (M Plan Apo, Mitutoyo, Japan) with different magnifications (5×, 10×, and 50× magnification) are used to focus the beam and collect the emission light from three fields of view (900 × 900 µm^2, 450 × 450 µm^2, and 90 × 90 µm^2, respectively). An XY-stage (ALS130-150, Aerotech, USA) with a positioning resolution of 100 nm holds and moves the sample on the plane. A linear stage (ATS100, Aerotech, USA) with a positioning resolution of 500 nm is employed to manipulate the microscope objective along the Z-axis and adjust the focal plane. In order to perform a raster scan, a control card (RTC4, SCANLAB GmbH, Germany) is used to rotate the mirrors of a Galvano scanner (IntelliScan14, SCANLAB GmbH, Germany) and steer the laser beam. Next, the laser beam is oriented through the microscope objective and focused on the sample for excitation. Fig 5.1(a4) shows the samples used in the experiments, in which micro-agents are placed below a layer of biological tissue. The excitation

light (laser beam) delivered by the microscope objective is dispersed due to the optical components, stretching the pulse length. The pulse length is measured (∼ 230 fs) after the excitation light passes through the microscope objective using an autocorrelator (pulseCheck, APE Angewandte Physik und Elektronik GmbH, Germany). The emission light generated by the sample passes back through the microscope objective and is reflected by the dichroic mirror (DMLP805, Thorlabs, USA) in the wavelength range of 400–785 nm. The reflected emission light passes through a short pass filter (FESH0750, Thorlabs, USA) (transmission range of 400–740 nm) and a focusing lens (LA1509-A, Thorlabs, USA) before being collected with a photomultiplier tube (PMT1001/m, Thorlabs, USA) for image formation (Fig 5.1(a2) and (a3)). For magnetic actuation of magnetic electrospun fibers, a needle-shaped electromagnetic coil is fabricated and employed [225]. The electromagnetic coil can generate 9 mT and 3.5 T/m at 5 mm from the tip axis by powering the coil at 1 A with a power source (E36313A, Keysight, USA).

Fluorescence data acquisition: The fluorescence data is acquired synchronously while steering the laser beam (50 mm/s scanning speed) with the Galvano scanner (IntelliScan14, SCANLAB GmbH, Germany). The voltage signal produced by the photomultiplier tube (PMT1001/m, Thorlabs, USA) in response to the varying fluorescent light is digitized using a data acquisition card (ATS 9146, Alazartech, Canada) that allows for the acquisition and transmission of data simultaneously (10 MS/s sampling rate). The data is acquired in dark room conditions to avoid direct light contamination. The data obtained in each raster scan cycle (Fig 5.1) is converted into a gray-scale image for analysis. Since the two-photon microscope has a single photomultiplier channel, 16-bit gray images (over 65000 shades) are used for analyzing micro-agents along with the tissue.

Image analysis: The gray-scale images (raw images) acquired from the two-photon microscope are analyzed offline through a MATLAB (version R2022b, MathWorks, USA) custom script. Since the two-photon microscope has a single photomultiplier channel, the analysis of micro-agents along with biological tissue relies on the difference in fluorescence intensities. We implement a contrast analysis based on contour, gradient, and intensity maps normalized to the corresponding maximum values. Although the microscope has a single photomultiplier channel, the three maps provide information about the micro-agents and surroundings. For continuous

visualization of magnetic electrospun fibers, we acquired and stored the images using an acquisition rate of 1 frame per second in a field of view of 135 $\times$ 135 µm^2. Thereon, the motion analysis is carried out offline using the Lucas-Kanade optical flow method [219]. The results of motion analysis are expressed as vector fields, which provide information on the motion of magnetic electrospun fibers [45], [220].

Fabrication of micro-agents: The CeFlowBot is fabricated from an autofluorescent photoresist (IP-Dip, Nanoscribe GmbH, Germany) via dip-in laser lithography (DiLL) using a 25$\times$ microscope objective (0.8 numerical aperture) (Fig 5.1(b1)) [104]. The CeFlowBot samples are micro-printed on a glass substrate coated with Indium-tin oxide using a laser lithography system (Photonic Professional GT2, Nanoscribe GmbH, Germany) in Galvano scanning mode with a laser power of 25 mW, a scanning speed of 4×10^4 µm/s, and slicing/hatching distances equal to 1 µm. The 3D printed structure is developed in cleaning solvent (RER 600) for 25 min and rinsed in isopropyl alcohol for 5 min. Thereon, the substrate containing CeFlowBot samples is baked in a hot plate (150 °C) for 15 min to remove the photoresist residues.

Electrospun fibers (i.e., beaded fibers and rod-like particles) are fabricated using the electrospinning technique (Fig 5.1(b2)) [45]. The polymer solution for electrospinning consists of polystyrene pellets (430102-1KG, Sigma-Aldrich, USA) as a carrier polymer, coumarin 6 (442631-1G, Sigma-Aldrich, USA) as a hydrophobic fluorophore, iron oxide (Fe_3O_4) nanoparticles (637106-25G, Sigma-Aldrich, USA) as a magnetic material, and anhydrous N, N-Dimethylformamide (DMF) as a solvent (227056-1L, Sigma-Aldrich, USA). For beaded fibers (fluorescent micro-agents), a polymer solution is prepared using 30.0% (29.8% polystyrene and 0.2% coumarin 6) weight-to-volume ratio in DMF. For rod-like particles (fluorescent and magnetic micro-agents), the polymer solution is 45.0% (29.8% polystyrene, 15% Fe_3O_4, and 0.2% coumarin 6) weight-to-volume ratio in DMF. Each polymer solution is homogenized by stirring for 12 hours using a vertical roller (LLG-uniRoller 6, LLG-Labware, Germany). Each solution (0.04 mL) is electrospun at once using an accelerating voltage of 14 kV, a feed rate of 2.5 mL/h, and a needle tip-to-collector distance of 16 cm. Randomly oriented fiber meshes are collected on a grounded aluminum foil at 24 °C and 22% humidity and dried at room temperature for 12 hours to remove the solvent residue. Fluorescent and magnetic electrospun fibers are obtained by grind-

ing the fibers using a sonicator (model 2510, Branson, USA) for 2 hours. Magnetic electrospun fibers are prepared for continuous image acquisition using 1% (volume/volume) Tween 80 (P4780-100ML, Sigma-Aldrich, USA) in Milli-Q water.

Scanning electron microscopy of micro-agents: A scanning electron microscope (JSM-7200F, JEOL, Japan) is utilized to obtain micrographs, which provide visual information about the morphology of the micro-agents. The microscopy parameters for imaging micro-agents (i.e., beaded fiber and CeFlowBot) include magnification, working distance, and acceleration voltage. The micrograph of beaded fiber is acquired using 6000× magnification, 9.2 mm working distance, and 5 kV acceleration voltage (Fig 5.3(a3)). For the micrograph of CeFlowBot, we use 150× magnification, 4 mm working distance, and 15 kV acceleration voltage (Fig 5.3(b3)).

Spectrum analysis of fluorophores: The spectrum analysis of the fluorophores utilized in the micro-agents is performed using a spectrofluorometer (FP-8300, Jasco, Japan). The exogenous fluorophore is prepared for analysis using a solution of 4 µg of coumarin 6 (442631-1G, Sigma-Aldrich, USA) in 700 µL dimethylformamide (227056-1L, Sigma-Aldrich, USA) [45]. The autofluorescent resin is prepared for analysis using a solution of 0.14 µL of IP-Dip resin (IP-Dip, Nanoscribe GmbH, Germany) and 700 µL of Isopropyl alcohol (20842.312, VWR International, USA). Both solutions are transferred into separate quartz cuvettes (CV10Q700F, Thorlabs, USA) for spectrofluorometry using wavelength intervals of 1 nm.

Tissue preparation: The rat tissues used in the experiments are taken post-mortem from outbred albino naïve female rats (RjHan: WI, Janvier Labs, France). Organs and biological samples are prepared and disposed of according to the Cat.1 directive for animal bio-products. The rat organs are fixed using a 10% buffered formalin solution (Formalin 10% Qpath Ref: 11699404 from VWR) overnight. Thereon, the organs are immersed in 100% ethanol for 24h and finally stored dry at 4 °C. The rat tissues are accurately sliced with a scalpel and placed between two glass microscope slides for flattening the surface.

For static imaging, spacers of known thickness are placed between the glass microscope slides. For continuous imaging, the tissue is placed over the microfluidic channel containing the micro-agents and compressed beneath a glass slide, with spacers positioned between the slide and the channel. In both configurations, the penetration depth (d) reported in the

figures and supplementary videos denotes the nominal thickness of the overlying tissue layer estimated using these spacers. For static imaging, micro-agents rest on the supporting glass substrate, and the focal plane is positioned within their fluorescent structures. The focus-to-glass distance therefore ranges from approximately zero to the axial thickness of the agent: up to 75 μm for the standard-size CeFlowBot lying flat, and up to the bead diameter (15–25 μm) for the bead regions of the electrospun fibers. For optical sections acquired within tissue itself, d is instead estimated from axial stage displacement relative to optically identified surface features (Figure 5.3(e1)).

The *ex ovo* chorioallantoic membranes are obtained from incubating White Leghorn chick embryos at 38 °C and 65% humidity throughout the culturing process [45]. At the embryonic day of development (EDD) 10, the egg contents are cracked into 60 mm cell culture Petri dishes for imaging. According to the Dutch animal care guidelines, Institutional Animal Care and Use Committee (IACUC) approval for chicken embryo experimentation is not necessary unless hatching is expected. Moreover, only experiments with chick embryos of development EDD14 and older need IACUC approval. The embryos used in this study are all in the early stages of embryo development (EDD10). Fertilized chicken eggs used in this study are purchased from approved poultry egg farms in the Netherlands.

Tissue damage by laser ablation: The laser beam is focused on the fixed tissue (rat liver dissection). Thereon, a Galvano scanner (IntelliScan 14, SCANLAB GmbH, Germany) steers the laser beam along a straight line of 400 µm five hundred times at 50 mm/s. The laser-affected tissue is imaged using a confocal microscope (Zeiss LSM 880, Carl Zeiss AG, Germany) with a 20× microscope objective (LD Plan-Neofluar, Carl Zeiss AG, Germany). The average power of the femtosecond pulsed laser is characterized by the laser power percentage (LPP), which is modulated by a beam attenuator (Ultrafast, Altechna, Lithuania). A photodiode power sensor (S130VC, Thorlabs, USA) measures the average laser power at the focal plane of a 10× microscope objective (M Plan Apo, Mitutoyo, Japan).

CHAPTER 6

Two-photon endomicroscopy for image-guided magnetic microrobotics

The following chapter is adapted from: ***J. J. Huaroto****, G.-w. Römer, Ivo M. Vellekoop, and S. Misra. Two-photon endomicroscopy for image-guided magnetic micro-agents, Small, vol. 22, no. 56, pp. e75051, 2026.*
The text, figures, and table have been adapted for inclusion in this doctoral thesis.

Abstract

Magnetic microrobotics holds promise for minimally invasive biomedical applications, yet imaging in this field still relies predominantly on external modalities. Endoscopic imaging offers an alternative route for in situ visualization and micro-agent guidance, but its use in microrobotics has so far remained limited to standard endoscopic modalities. This study demonstrates two-photon endomicroscopy (TPE) for real-time fluorescence imaging of magnetically actuated micro-agents. Dynamic experiments under rotating magnetic fields support motion analysis across multiple actuation frequencies. In addition, dual-color imaging enables analysis of mixed magnetic and non-magnetic micro-agent populations labeled with distinct fluorescent dyes. Imaging through biological tissue shows that magnetic micro-agents remain detectable through a 140 µm rat mammary gland tissue layer. The feasibility of image-guided re-centering of a HeLa cell spheroid within the TPE field of view is also shown, compensating for displacement induced by the magnetic micro-agents. These results extend TPE from passive observation to active image-guided functionality in microrobotic systems.

6.1 Introduction

The need for precise interventions within confined anatomical regions has driven the development of microrobotics for minimally invasive diagnosis and therapy [14], [191], [226], [227]. Engineered micro-agents have been explored as carriers for drugs, cells, and genes in applications ranging from targeted chemotherapy to reproductive medicine [4], [161], [228], [229]. However, their successful therapeutic deployment requires reliable navigation through complex physiological environments, such as the digestive, circulatory, and reproductive systems [230]. Magnetic [29], acoustic [231], and optical fields [37] provide powerful strategies for remote micro-agent actuation. Yet, in vivo controlled guidance depends on imaging modalities capable of providing real-time and informative feedback during actuation [21].

Among actuation strategies, magnetism is particularly attractive because time-varying magnetic fields and gradients enable diverse steering and locomotion modes [232], [233]. In many minimally invasive scenarios, magnetically actuated micro-agents are intended to operate near a target site for tasks such as localized therapeutic delivery and interaction with biological samples [13], [98], [234], [235]. In this setting, in situ visualization becomes a valuable complementary modality for monitoring micro-agent position, proximity to biological structures, and their interactions.

From the imaging perspective, most reported approaches in microrobotics rely on external systems based on established modalities such as X-ray computed tomography [40], positron emission tomography [41], fluoroscopy [198], single-photon emission computed tomography [199], ultrasound (US) [236], photoacoustic imaging (PAI) [195], magnetic resonance imaging [237], optical coherence tomography (OCT) [200], and magnetic particle imaging [238]. While these techniques enable non-invasive visualization, they typically involve trade-offs among spatial resolution, temporal resolution, and penetration depth that limit their effectiveness for precise micro-agent tracking and guidance [21].

Endoscopic imaging offers an alternative route by moving the imaging modality closer to the site of interest and enabling in situ visualization [85], [98], [239]. Endoscopic modalities span a wide range of spatial-resolution and imaging-depth trade-offs. Fluorescence endomicroscopy and OCT provide high spatial resolution at shallow imaging depths, whereas

endoscopic US and PAI enable deeper imaging with comparatively lower spatial resolution. These capabilities support clinical applications such as tissue inspection, cancer detection, mucosal screening, and deep-tissue imaging [83], [97], [202], [240], [241]. These systems are primarily optimized for tissue assessment, where motion is often intrinsic, slowly varying, or manageable through averaging, motion correction, and post-processing. Microrobotics introduces a different operating regime, in which imaging targets are micrometer-scale, move under external actuation, and require real-time feedback for guidance [14]. Despite the rapid development of clinical endoscopic imaging, microrobotic applications have so far relied on standard endoscopes [98]. In this context, fluorescence endomicroscopy is particularly attractive because fluorescent labeling can provide contrast for distinguishing micro-agents from surrounding biological structures. However, fluorescence-based endomicroscopy remains underdeveloped for tracking and guiding magnetically actuated micro-agents.

Two-photon endomicroscopy (TPE) extends fluorescence endoscopy by exploiting nonlinear absorption to achieve intrinsically localized excitation, thereby limiting out-of-focus signals and reducing background fluorescence in scattering tissue [70], [242], [243]. Fiber-based TPE probes have advanced rapidly in recent years for applications such as in vivo tissue imaging and neural activity imaging, establishing their potential as compact, high-resolution imaging tools for minimally invasive use [81], [99], [100]. For example, Kim et al. demonstrated in vivo tissue imaging using a TPE probe with a diameter of 2.6 mm, operating at five frames per second with lateral and axial resolutions of 0.70 and 7.6 μm, respectively [244]. More recently, Liu et al. developed a focus-tunable fiberscope with a distal diameter of 2.4 mm, a field of view 350 μm in diameter, and an axial focus-tuning range of 400 μm, demonstrated for in vivo neural imaging [245]. In parallel, two-photon microscopy has enabled in vivo visualization during acoustic navigation and continuous imaging of magnetic micro-agents through biological tissue [46], [246]. These developments position two-photon imaging as a promising modality for microrobotics, while leaving open the use of TPE for in situ imaging and guidance of magnetically-actuated micro-agents. In this setting, image guidance can benefit from real-time, dual-color fluorescence imaging to distinguish labeled micro-agents from biological structures and observe their interactions during actuation. Furthermore, because these interactions unfold within a limited imaging field, active repositioning is also

important for maintaining micro-agents and biological structures in view throughout actuation.

To investigate these capabilities, this study demonstrates two-photon endomicroscopy (TPE) for real-time fluorescence imaging of magnetically actuated micro-agents. The presented approach supports dual-color visualization and motion analysis of differently labeled micro-agents, imaging through biological tissue, and image-guided re-centering of a biological structure. Figure 6.1(A) depicts the proposed TPE system concept for visualizing magnetic micro-agents and other fluorescently labeled structures during actuation. Figure 6.1(B) shows the corresponding experimental implementation, in which a fiber-based TPE probe provides distal imaging and a permanent magnet drives actuation. The magnetic micro-agents used here are discrete fragments produced by sonication of Coumarin 6-labeled electrospun precursor fibers containing Fe_3O_4 nanoparticles (Figure 6.1(C)). Representative dual-color TPE images of magnetic micro-agents interacting with a HeLa cell spheroid, used here as a 3D cellular model, are shown in Figure 6.1(D).

6.2 Results and discussions

This section presents the TPE system and the main experimental results used to assess its performance for real-time fluorescence imaging of magnetic micro-agents. Section 6.2.1 provides a concise overview of the TPE system and its key operating characteristics, while Section 6.2.2 characterizes the fluorescent and magnetic properties of the electrospun precursor fibers used to generate the micro-agents. Sections 6.2.3–6.2.5 demonstrate TPE for motion analysis under magnetic actuation, imaging through biological tissue, and image-guided re-centering of a biological structure. Further details of the TPE probe, magnetic micro-agents, and experimental procedures are provided in Section 6.4.

6.2.1 Endomicroscopy system

The TPE system enables real-time fluorescence imaging and supports two spectral detection channels (Figure 6.2(A)). A femtosecond pulsed laser centered at 900 nm is delivered through a double-clad fiber to the distal probe, and the generated fluorescence is collected through the same optical

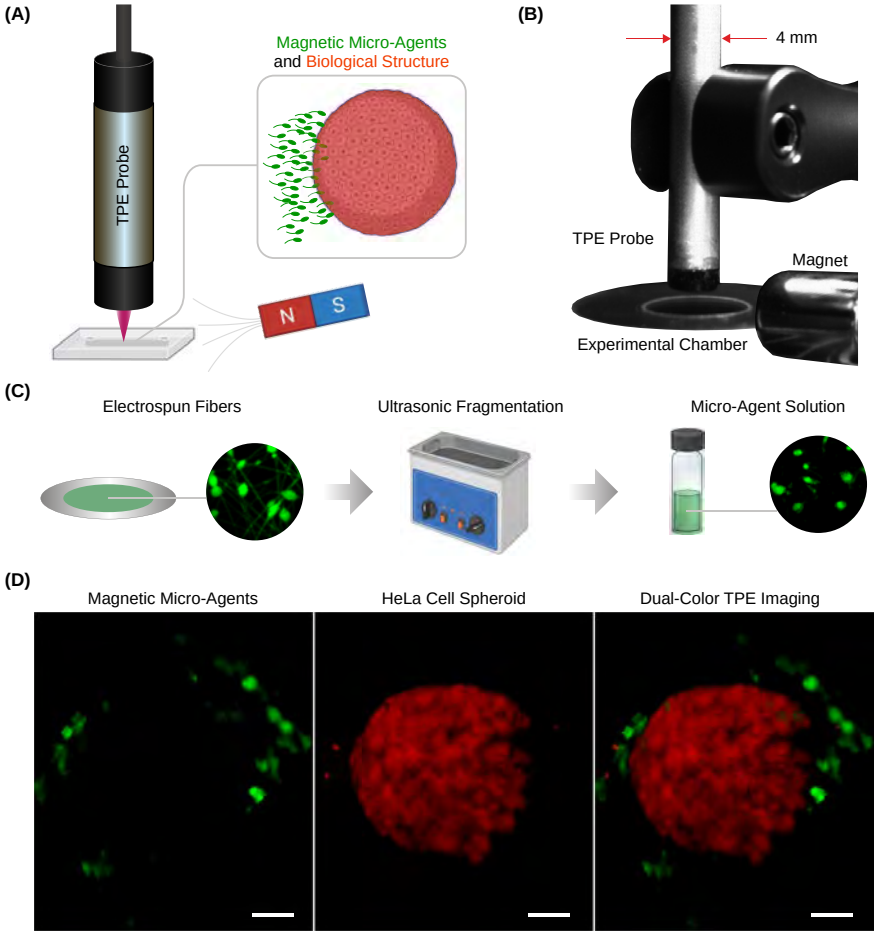


Figure 6.1: Two-photon endomicroscopy (TPE) system for imaging of magnetic micro-agents and biological structures. **(A)** Conceptual schematic of the experimental approach. A fiber-based TPE probe enables fluorescence imaging of magnetic micro-agents (green) and a fluorescently labeled biological structure (red), while external magnetic fields remotely actuate the micro-agents. **(B)** Experimental implementation showing the distal TPE probe positioned adjacent to a permanent magnet used to generate magnetic fields for micro-agent actuation. **(C)** Fabrication workflow of fluorescent magnetic micro-agents. Electrospun precursor fibers are fragmented by ultrasonication to generate an aqueous suspension of micro-agents. **(D)** Representative two-photon endomicroscopy images showing magnetic micro-agents (green), a HeLa cell spheroid used here as a 3D cellular model (red), and the merged dual-color TPE image. Scale bars = 50 µm.

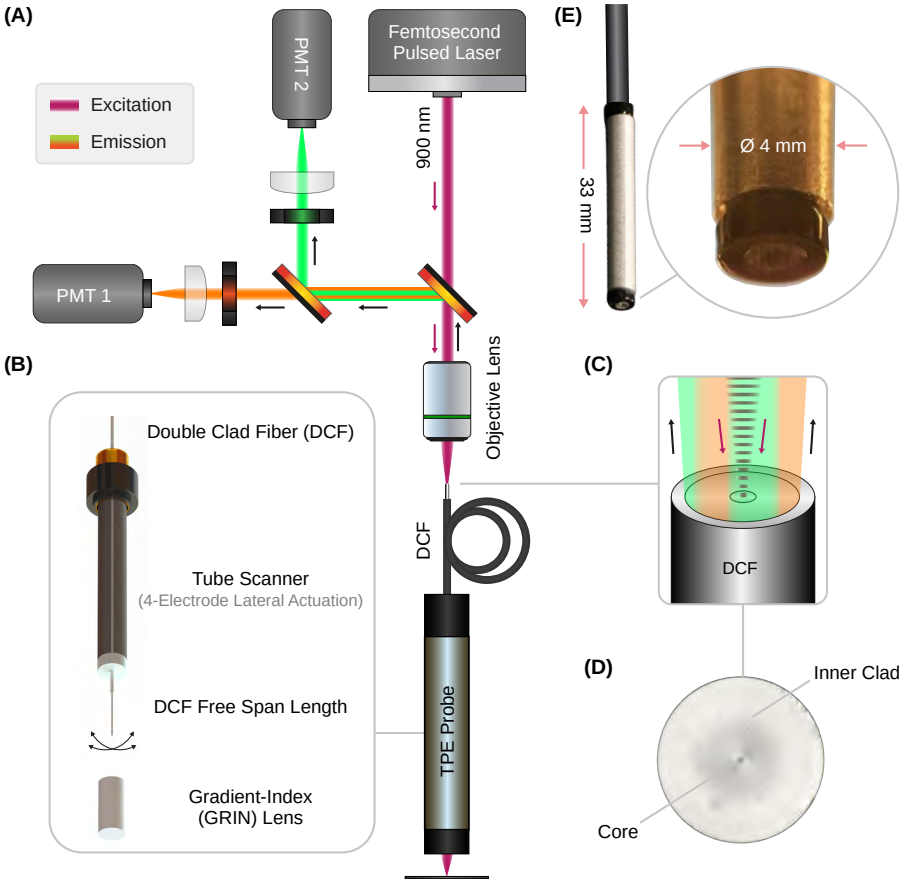


Figure 6.2: Optical configuration and probe architecture of the two-photon endomicroscopy (TPE) system. **(A)** Optical layout of the TPE system. Femtosecond laser excitation at 900 nm is coupled into a double-clad fiber (DCF) through the objective lens and delivered to the distal probe. Fluorescence generated at the sample is collected through the same fiber and separated into two spectral detection channels using dichroic optics and photomultiplier tubes (PMT1 and PMT2) for dual-color imaging. **(B)** Distal probe architecture showing the four-electrode piezoelectric tube scanner, free-span DCF length, and gradient-index (GRIN) lens. Two-dimensional lateral scanning is achieved by oscillatory actuation of the assembled DCF–tube scanner, while the GRIN lens focuses the excitation beam into the sample. **(C)** Schematic of the double-clad fiber operating principle. Excitation light propagates through the fiber core, while fluorescence emission is collected through the inner clad. **(D)** Microscopy image of the double-clad fiber cross-section showing the core and inner clad. **(E)** Photograph of the fabricated TPE probe, showing a distal tip diameter of approximately 4 mm and a rigid length of 33 mm.

pathway and separated into two spectral channels for dual-color imaging.

The distal probe combines a piezoelectric tube scanner, a double-clad fiber (DCF), and a GRIN lens (Figure 6.2(B)). Lateral scanning is produced by oscillatory actuation of the assembled DCF–tube scanner, while the GRIN lens focuses the excitation beam into the sample and collects the emitted fluorescence. The DCF geometry and operating principle are illustrated in Figures 6.2(C) and (D), and a photograph of the fabricated distal probe is shown in Figure 6.2(E).

Figure 6.3(A) summarizes the distal optical configuration of the DCF–GRIN lens assembly, including the DCF tip–GRIN lens gap (l_0), the effective numerical aperture, and the focused beam diameter. Physical-optics simulations are used to guide the selection of l_0 for efficient two-photon excitation. While the full simulation analysis spans $l_0 = 1.0$–4.5 mm (Figure 6.9, Appendix, p. 155), the final probe design is selected within $l_0 = 2.5$–3.0 mm range to balance centered focusing performance with off-axis beam propagation during scanning. The selected configuration is excited by a laser source centered at 900 nm with a measured bandwidth of 9 nm (Figure 6.3(B)). Under these conditions, the probe delivers a focused distal spot with a lateral full width at half maximum of approximately 2.1 µm (Figure 6.3(C)), and beam propagation measurements support an effective numerical aperture of approximately 0.26 in air (Figure 6.3(D)).

The scanning characteristics of the assembled probe are then obtained experimentally to identify the operating conditions and usable scan extent (Figure 6.10, Appendix, p. 158). The responses along the two lateral axes show resonance peaks near 810 Hz, consistent with the finite-element analysis of a DCF free length of 11.5 mm (Figure 6.11, Appendix, p. 159). Operation near this resonance yields relatively large scan amplitudes at drive voltages below the tube scanner limit of 200 V. For stable operation, the orthogonal electrodes are driven at 825 and 820 Hz with corresponding peak-to-peak voltages of 147.4 V and 122.5 V, generating a Lissajous scan with robust spatial coverage across the scanned region. Under these conditions, the scan achieves lateral extents of 232 and 316 µm along the two axes at a 5 Hz image rate.

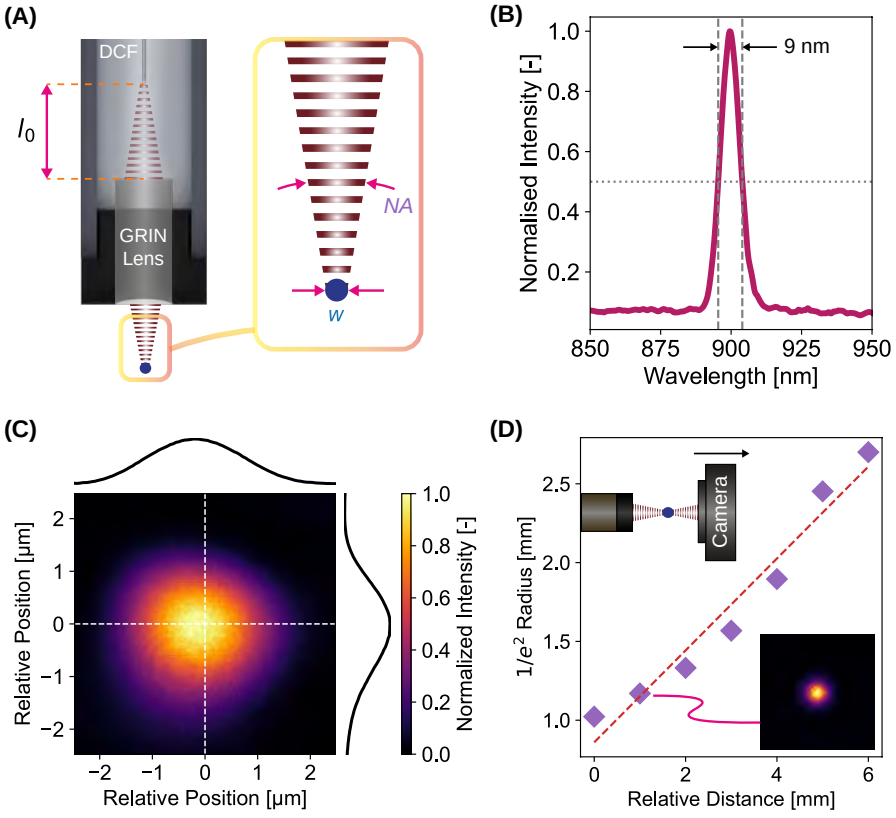


Figure 6.3: Optical characterization of the two-photon endomicroscopy probe. **(A)** Schematic of probe geometry showing the fiber-to-lens gap (l_0), focal spot size (w) and effective numerical aperture (NA). **(B)** Normalized laser emission spectrum centered at 900 nm, showing a 9 nm spectral bandwidth. **(C)** Lateral intensity profile at the focal plane used to estimate the probe point-spread function. The measured focal spot has a full width at half maximum of approximately 2.1 µm. **(D)** Beam propagation measurements showing the evolution of the $1/e^2$ beam radius with axial distance from the probe tip. The dashed line indicates a linear fit used to estimate beam divergence. The inset shows a representative beam profile at one axial position. The fitted slope corresponds to an effective numerical aperture of approximately 0.26 in air.

6.2.2 Engineering and characterization of electrospun precursor fibers

Having established the optical and scanning performance of the TPE probe, the system is next used to characterize electrospun precursor fibers that later serve as the source material for magnetic micro-agents generated by ultrasonic fragmentation. The fibers are electrospun from polystyrene (PS) solutions in dimethylformamide (DMF) containing fluorescent dyes and magnetic nanoparticles, while the polymer concentration is varied to produce either straight or beaded morphologies (Figure 6.4(A)); detailed fabrication parameters are provided in Section 6.4. Coumarin 6 (C6) and Nile Red (NR) are selected as fluorescent dyes because both generate detectable two-photon fluorescence under 900 nm excitation and provide partially separated spectral signatures for dual-channel imaging.

Electrospun fibers labeled with increasing dye loading (0.2–1.6 wt%) are shown in Figure 6.4(B). For C6-labeled fibers, Channel 1 captures the dominant fluorescence signal, while Channel 2 shows partial crosstalk due to spectral overlap. In contrast, NR-labeled fibers emit predominantly in Channel 2 with negligible signal in Channel 1. Fluorescence intensity is quantified using the 95th percentile (P95) intensity. For C6, the signal increases approximately linearly over the investigated concentration range in both channels, indicating efficient dye incorporation with minimal self-quenching. For NR, the signal also increases with dye loading, but the trend becomes sub-linear at higher concentrations, suggesting concentration-dependent quenching or aggregation within the polymer matrix. Based on these trends, the highest investigated dye loading (1.6 wt%) is selected for both C6 and NR in the subsequent analyses. The observed spectral overlap, particularly for C6, further motivates the later use of spectral unmixing for improved channel separation.

Morphology is further tuned to produce either straight fibers or fibers containing localized bead structures (Figure 6.4(A)). Representative two-photon fluorescence images of straight and beaded fibers labeled with C6 and NR are shown in Figure 6.4(C). Beaded fibers exhibit localized regions of increased fluorescence intensity for both dyes, consistent with dye accumulation within bead structures. Quantitative analysis confirms higher P95 fluorescence values for beaded fibers than for straight fibers (Figure 6.4(D)), reflecting the increased local fluorescent volume within bead regions. To

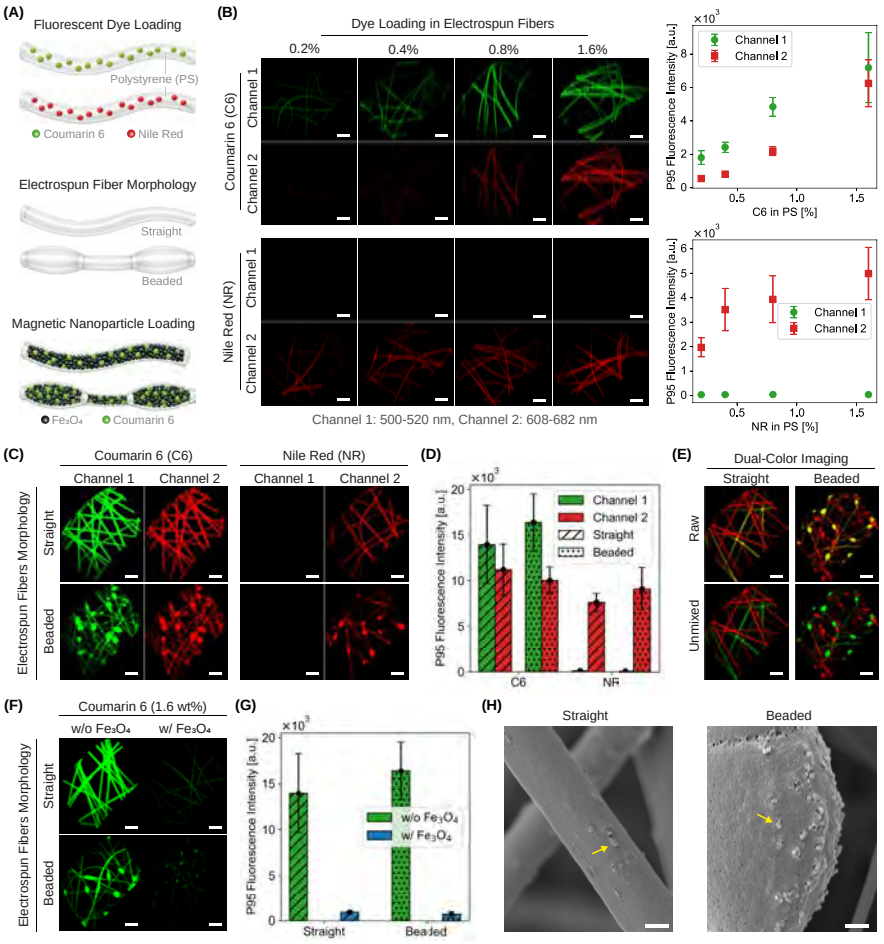


Figure 6.4: Engineering and optical characterization of electrospun precursor fibers used to generate magnetic micro-agents. **(A)** Conceptual illustration of electrospun fiber engineering showing fluorescent dye incorporation (Coumarin 6 and Nile Red), controllable fiber morphology (straight and beaded), and magnetic nanoparticle loading. **(B)** Fluorescence imaging of electrospun fibers with increasing dye loading in polystyrene (PS) (0.2–1.6%), imaged in the two detection channels (Channel 1, Channel 2). Top: Coumarin 6 (C6) fibers; bottom: Nile Red (NR) fibers. Corresponding plots show the 95th percentile (P95) fluorescence intensity versus dye concentration for each channel. **(C)** Straight and beaded fibers labeled with C6 or NR, illustrating morphology-dependent fluorescence patterns. **(D)**Quantification of fluorescence intensity across dyes and morphologies. **(E)** Dual-color imaging of fibers labeled with both dyes, showing raw and spectrally unmixed reconstructions for straight and beaded morphologies. **(F)** Fibers containing magnetic nanoparticles (Fe_3O_4) compared with non-magnetic fibers. **(G)** Quantification of fluorescence intensity for fibers with and without Fe_3O_4. **(H)** Scanning electron microscopy (SEM) images of straight and beaded fibers showing embedded magnetic nanoparticles (yellow arrows). All quantitative fluorescence data in panels (B), (D), and (G) are presented as mean ± SD across four FOVs ($n = 4$). Scale bars = 50 µm (fluorescence) and 1 µm (SEM).

improve spectral separation between the two fluorescent dyes, linear spectral unmixing is applied to the dual-color images (Figure 6.4(E)). Unmixing reduces C6 leakage into Channel 2 while preserving NR signal integrity, enabling clearer discrimination of spatially overlapping fluorescence signals.

Magnetic functionality is introduced by incorporating Fe_3O_4 nanoparticles into the electrospinning solution while maintaining the overall solids concentration. Coumarin 6 is selected as the fluorescent dye for magnetic fibers because it provides a more stable two-photon fluorescence response than Nile Red. Representative two-photon images of fibers with and without Fe_3O_4 are shown in Figure 6.4(F). The incorporation of magnetic nanoparticles reduces fluorescence intensity (Figure 6.4(G)), which is attributed to the partial replacement of the fluorescent polymer by nanoparticles, along with additional optical absorption and scattering introduced by Fe_3O_4. Scanning electron microscopy images confirm the presence of embedded nanoparticles within both straight and beaded fibers while preserving the overall fiber morphology (Figure 6.4(H)).

6.2.3 Real-time two-photon endomicroscopy of magnetic micro-agents

Having established fluorescent labeling and magnetic loading of the precursor fibers, this section evaluates the ability of TPE to support reliable real-time motion extraction from magnetically actuated micro-agents. The analysis first considers Fe_3O_4-loaded magnetic micro-agents labeled with Coumarin 6 (C6). In these single-population experiments, the micro-agents are derived from beaded electrospun fibers, suspended in a fluid-filled chamber (75 µm in height), and actuated using a rotating permanent magnet positioned near the distal probe. Morphological analysis of magnetic micro-agents yielded median long- and short-axis dimensions of 18.1 µm (IQR: 14.9–19.6 µm) and 13.5 µm (IQR: 10.7–15.3 µm), respectively, with a median aspect ratio of 1.3 (IQR: 1.2–1.5), indicating a predominantly elongated morphology (Figure 6.13, Appendix, p. 161).

Magnetic actuation is generated using a diametrically magnetized permanent magnet mounted on a DC motor (Figure 6.5(A)). Magnet rotation produces a time-varying magnetic field at the sample location, driving the reorientation and motion of the magnetic micro-agents. The corresponding magnetic field trajectory at the workspace is shown in Figure 6.5(B),

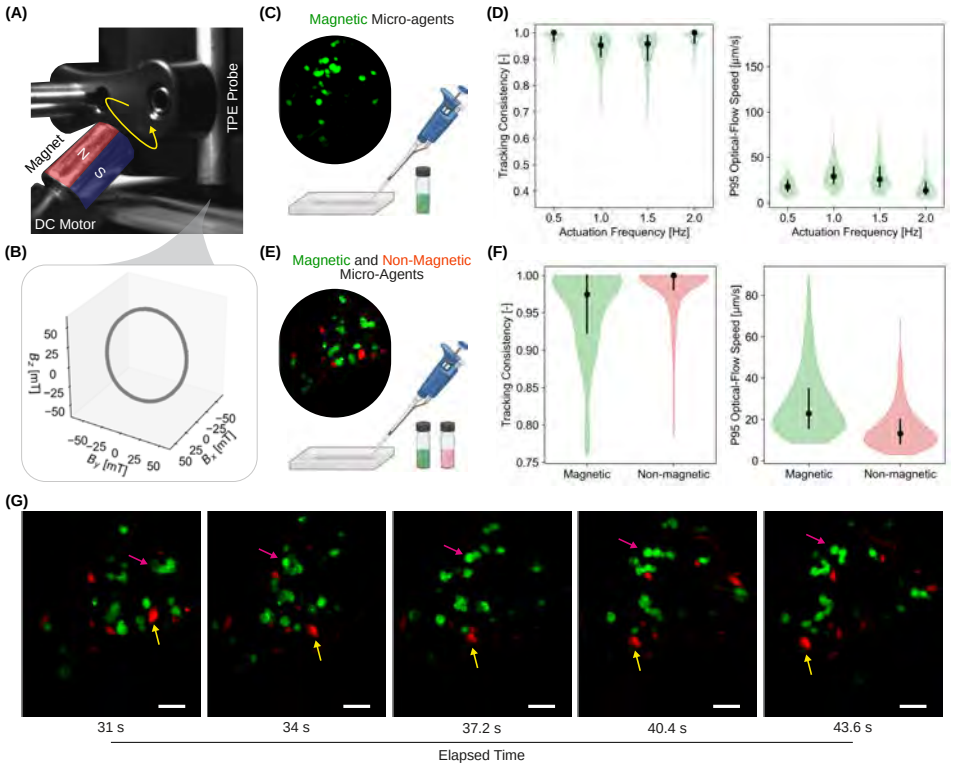


Figure 6.5: Magnetic actuation and dynamic motion analysis of fluorescent micro-agents. **(A)** Experimental configuration for magnetic actuation of micro-agents using a rotating permanent magnet mounted on a DC motor positioned near the distal TPE probe. **(B)** Magnetic field trajectory generated by the rotating magnet, illustrating the rotating magnetic field used for micro-agent actuation. **(C)** Representative two-photon image of magnetic micro-agents (Coumarin 6, green) during actuation experiments. **(D)** Motion analysis for magnetic micro-agents across actuation frequencies (0.5–2 Hz). Violin plots show the per-frame tracking consistency (left) and P95 optical-flow speed (right) at each frequency, with 350 per-frame values per distribution; the marked point and bar give the median and interquartile range. **(E)** Representative dual-color two-photon image of magnetic (Coumarin 6-labeled, green) and non-magnetic (Nile Red-labeled, red) micro-agents. **(F)** Motion analysis for the dual-color experiment, in which magnetic (Coumarin 6, green) and non-magnetic (Nile Red, red) agents are actuated together at 1 Hz. Violin plots show the per-frame tracking consistency (left) and P95 optical-flow speed (right) for each population (250 frames each; median and interquartile range marked). **(G)** Representative time-lapse sequence illustrating the motion of micro-agents under magnetic actuation. Arrows indicate selected agents across frames. Scale bars = 50 µm. The complete dynamic sequences are provided in Video S1.

where the field rotates in a plane with a magnitude of approximately 43–63 mT over each cycle. From these measurements and the magnet specifications, the field gradient at the workspace is estimated to be on the order of 20 $\mathrm{T\,m^{-1}}$, varying over each rotation cycle. In this rotating-field regime, the comparison of the magnetic torque scale with the gradient-force contribution over a characteristic micro-agent length indicates that torque-driven reorientation dominates by approximately two orders of magnitude (details in Appendix, p. 160). Figure 6.14 (Appendix, p. 162) shows the experimental motor voltage-to-frequency mapping used to tune the actuation frequency. Figure 6.15 (Appendix, p. 163) shows the measured temporal evolution of the magnetic field components and magnitude in the workspace. The actuation frequency is varied through the motor driving voltage, enabling experiments in the 0.5–2 Hz range.

A representative TPE image of fluorescent magnetic micro-agents, together with a schematic of the sample preparation, is shown in Figure 6.5(C). Micro-agent motion is quantified from the acquired image sequences using optical-flow analysis. Consistent with the reduced fluorescence intensity observed after Fe_3O_4 incorporation (Section 6.2.2), the excitation power is increased to 65 mW in the dynamic experiments to maintain a sufficient signal-to-noise ratio for reliable motion estimation.

Tracking consistency is quantified using a metric based on forward–backward optical-flow agreement to assess the reliability of motion extraction from the acquired TPE sequences under magnetic actuation (details in Section 6.4). Mean tracking consistency remains high (> 0.9) across the tested actuation frequencies (Figure 6.5(D), left), indicating stable feature tracking and consistent image quality during dynamic operation. The corresponding P95 optical-flow speed distributions (Figure 6.5(D), right) show a non-monotonic dependence on actuation frequency. The median speed reaches 29.2 $\mu\mathrm{m\,s^{-1}}$ at 1.0 Hz (IQR: 21.2–38.9 $\mu\mathrm{m\,s^{-1}}$) and decreases to 13.3 $\mu\mathrm{m\,s^{-1}}$ at 2.0 Hz (IQR: 9.1–21.7 $\mu\mathrm{m\,s^{-1}}$). This roll-off at higher frequency is consistent with the agents no longer following the rotating field in phase, indicating a frequency-limited response under the tested conditions [232]. The broad distributions at each frequency further reflect heterogeneous, interaction-mediated motion across the sample, consistent with local contacts and mechanical constraints within the chamber.

The analysis is then extended to mixed samples containing Fe_3O_4-loaded magnetic and Fe_3O_4-free non-magnetic micro-agents, labeled with

Coumarin 6 and Nile Red, respectively. Dual color TPE is used to assess channel specificity and population-specific motion analysis. The experiments are performed at 1 Hz, selected from the actuation sweep presented in Figure 6.5(D, right). A representative dual-color TPE image and the corresponding preparation schematic are shown in Figure 6.5(E), where both populations can be distinguished. Quantitative analysis of the dual-channel sequences shows high tracking consistency for both magnetic and non-magnetic agents (Figure 6.5(F), left). The same image sequences show that, although magnetic agents respond directly to the rotating magnetic field, nearby non-magnetic agents also undergo displacement, likely due to local contact interactions and fluid-mediated coupling within the chamber. Representative time-lapse frames illustrating these interactions are shown in Figure 6.5(G), where arrows identify selected magnetic and non-magnetic agents across frames.

6.2.4 Micro-agent detection through biological tissue

To evaluate TPE performance under attenuated imaging conditions, magnetic micro-agents are imaged through excised rat mammary gland tissue. Because Fe_3O_4 incorporation reduces fluorescence intensity (Section 6.2.2), this experiment uses the magnetic agents as a stringent test of detectability through tissue. In this configuration, the tissue sample is placed in contact with the micro-agents, while the TPE probe is positioned above the tissue surface, such that fluorescence from the agents is detected through the scattering layer (Figure 6.6(A)). The tissue thickness in these experiments is approximately 140 µm (details in Section 6.4).

The experimental implementation of this configuration is shown in Figure 6.6(B). A separate white-light endoscopic camera attached to the TPE scanner is used to guide probe positioning relative to the tissue sample (Figure 6.6(C)). Video S2 shows the corresponding workflow, including surface positioning, axial scanning to identify the focal plane, and the excitation-power sweep used for imaging through tissue.

Representative TPE fluorescence images acquired through the tissue layer at different excitation powers are shown in Figure 6.6(D). Despite the attenuation introduced by the tissue, fluorescent magnetic micro-agents remain detectable beneath the scattering interface, and the image intensity increases with excitation power while preserving spatial localization. The

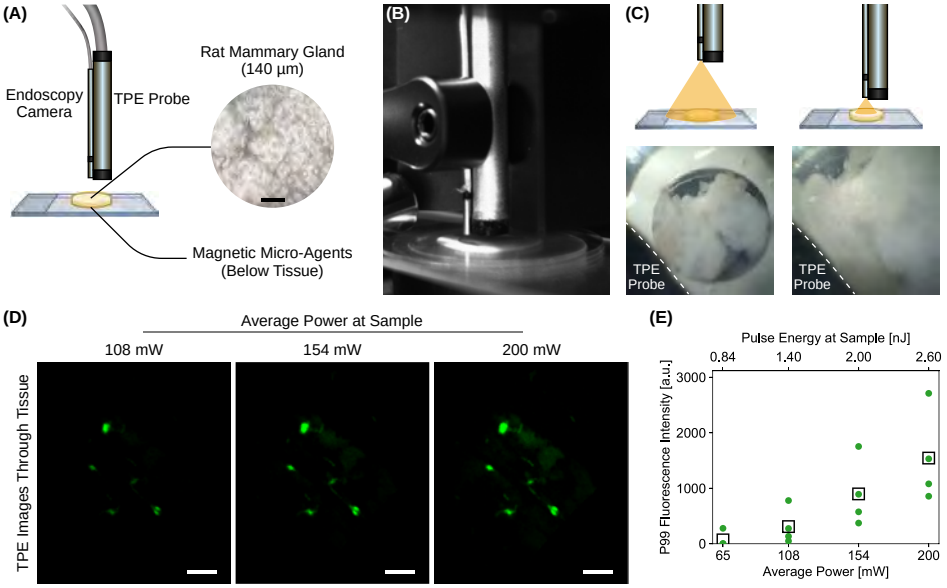


Figure 6.6: Two-photon endomicroscopy (TPE) imaging of Coumarin 6-labeled magnetic micro-agents through biological tissue. **(A)** Conceptual schematic of the imaging configuration showing the TPE probe positioned above a rat mammary gland tissue sample (140 µm thickness), with fluorescent magnetic micro-agents located beneath the tissue layer. An auxiliary endoscopic camera is positioned for surface visualization and probe alignment during the experiment. The inset shows a microscopy image of the rat tissue sample. Scale bar = 100 µm. **(B)** Experimental implementation of the imaging setup showing the distal TPE probe and endoscopic camera positioned above the tissue sample. **(C)** Representative endoscopic camera views illustrating probe positioning relative to the tissue sample during imaging experiments. The complete workflow is provided in Video S2. **(D)** TPE fluorescence images of magnetic micro-agents acquired through the tissue layer at different average laser powers at the sample with a constant repetition rate (77 MHz). Scale bars = 50 µm. **(E)** Quantification of the 99th percentile (P99) fluorescence intensity as a function of average power at the sample, with the corresponding pulse energy on the top axis. Each measurement is averaged over 10 consecutive frames; individual measurements from four independent sample preparations (n = 4) are plotted as green circles, and squares denote the mean at each power level.

corresponding fluorescence intensity, quantified using the 99th percentile (P99) metric, increases with the average power delivered at the sample (Figure 6.6(E)), confirming the visual trend observed in the images.

Because through-tissue imaging requires increased excitation power, illumination-induced effects are assessed using a stationary-beam control on Rhodamine B-stained mammary gland tissue (Figure 6.16, Appendix, p. 164). The excitation beam is parked near the center of the tissue surface

for 3 min at 240 mW, exceeding both the highest power used in the imaging experiments and the typical local exposure duration during scanning. Under these conditions, no visible change in tissue morphology is observed in the images, while the fluorescence intensity within the exposed region decreases by approximately 9.5% (Figure 6.16(B)–(D), Appendix, p. 164).

To place this exposure in quantitative context, the onset of femtosecond laser ablation is commonly expressed as a fluence threshold, which depends on the tissue type and irradiation conditions [247]. The estimated per-pulse fluence at the TPE probe focus is approximately 0.05 J cm^{-2} at the highest imaging power and 0.06 J cm^{-2} during the 240-mW stationary-beam control (calculation detailed in Section 6.4). These values are more than one order of magnitude below the reported 0.7 J cm^{-2} material-removal threshold for bone [248] and below the 4.3 J cm^{-2} minimal-visible-lesion threshold reported for corneal neovascular tissue [249]. The fluence comparison and stationary-beam control indicate no detectable gross structural alteration or ablation under the fixed-tissue conditions used. This analysis specifically addresses structural damage and ablation. Photochemical phototoxicity and cumulative heating in viable tissue occur through distinct mechanisms at substantially lower exposures and are not quantified in this study.

Imaging micro-agents beneath a tissue layer represents the intended operating regime of TPE, in which the endomicroscopic probe is positioned locally near a target site. Conventional fiber-scanning TPE systems have demonstrated useful imaging depths on the order of 100–200 µm [81], [250], [251]. Recent probe designs have extended the accessible imaging depth, with enhanced fluorescence collection enabling two-photon imaging to 300 µm in excised tissue and integrated focus tuning providing an axial imaging range of 400 µm over a 350 µm diameter field of view [245], [252]. In practice, actual penetration in tissue remains dependent on tissue attenuation, distal focusing geometry, and excitation and fluorescence collection efficiency [81].

Because Fe_3O_4 incorporation reduces the emission fluorescence of the precursor fibers (Section 6.2.2), the practical detection depth of magnetic micro-agents is expected toward the shallower end of the 100–200 µm regime typical of compact fiber-scanning systems. Engineered micro-agents with enhanced fluorescence contrast, together with improved detection sensitivity, could extend the accessible depth. In the present experiment, mag-

netic micro-agents remain detectable through a 140 µm fixed mammary gland layer, consistent with the practical depth regime of conventional fiber-scanning TPE. The fixed-tissue configuration provides a controlled model for evaluating tissue-induced attenuation while retaining aspects of tissue morphology and spatial heterogeneity. The absence of perfusion and physiological motion allows attenuation from the preserved tissue layer to be assessed independently, while these physiological processes remain relevant under in vivo conditions.

Within the broader landscape of deep-tissue imaging, TPE occupies a local, near-target regime, distinct from external modalities that provide greater penetration and spatial coverage. Clinical ultrasound provides label-free, real-time structural imaging at centimeter-scale depths, with resolution and penetration determined by the acoustic frequency and imaging geometry [236], [253]. PACT converts absorbed pulsed optical energy into acoustic waves detected by ultrasound transducers and has demonstrated whole-body small-animal and human breast imaging, including breast visualization at depths up to 4 cm [254]–[256]. MPI directly detects the nonlinear magnetic response of superparamagnetic tracers and is not subject to signal attenuation by intervening tissue [238], [257]. These capabilities define complementary spatial regimes. External modalities support deep-tissue visualization and organ-scale localization, whereas TPE, through endoscopic access, provides high-resolution imaging of a localized tissue volume.

At the local, near-target scale, TPE is most directly compared with endoscopy and endomicroscopy modalities. For example, wide-field fluorescence endoscopy provides real-time, surface-weighted fluorescence visualization but lacks depth-resolved optical sectioning [258]. Confocal endomicroscopy provides cellular-scale fluorescence optical sectioning over superficial depths and a submillimeter field of view [259]. Endoscopic OCT provides label-free, depth-resolved structural imaging over millimeter-scale depths, but does not provide fluorescence-specific discrimination [260]. Photoacoustic endoscopy reaches greater, millimeter-scale depths (1–3 mm) than TPE and can separate absorbers by their absorption spectra. However, this contrast is not fluorophore-specific and is obtained at coarser spatial resolution [261]. Relative to these modalities, TPE combines nonlinear optical sectioning with micron-scale, fluorophore-specific multicolor contrast for distinguishing labeled micro-agents from adjacent labeled bio-

logical structures. These modalities, together with representative external deep-tissue systems, are compared in Table 6.1 (Appendix, p. 165) across resolution, imaging depth, field of view, and other imaging parameters.

6.2.5 Image-guided re-centering of a HeLa cell spheroid during micro-agent interaction

Beyond motion analysis and imaging through biological tissue, image feedback can also support active re-centering during magnetic micro-agent interaction. Maintaining a biological structure within the imaging field of view becomes important when contact with magnetic micro-agents induces lateral displacement. Here, two-photon endomicroscopy (TPE) is used to demonstrate the feasibility of image-guided lateral re-centering of a HeLa cell spheroid during magnetic micro-agent interaction.

Image-guided re-centering is implemented through active probe repositioning to maintain the spheroid near the center of the TPE field of view. The experimental configuration shown in Figure 6.7(A) combines translational magnetic actuation with motorized stage correction. Magnetic micro-agents and a spheroid with a diameter of approximately 200 µm are placed in a chamber of 190 µm height, and spheroid motion is monitored in the lateral image plane. In contrast to the rotation-based actuation experiments described in Section 6.2.3, a handheld permanent magnet is used to generate directional magnetic forces that drive the translation of the magnetic micro-agents. As the agents interact mechanically with the spheroid boundary and induce lateral displacement within the chamber, motorized linear stages reposition the imaging probe along the x and y directions to maintain the spheroid near the center of the image.

The spheroid position is estimated in real time by segmenting its visible region within the TPE field of view and computing the centroid of the resulting mask. The distance between this centroid and a predefined target position defines the image-derived error utilized as the control variable. Figure 6.7(B, top) shows the corresponding image-derived error over time. To limit stage oscillations while maintaining centering accuracy, inner and outer deadbands are applied. When the error exceeds the outer deadband (20.0 µm), stage correction is triggered; correction stops once the error returns within the inner deadband (13.3 µm). The corresponding stage displacements along the x and y axes are shown in Figure 6.7(B, bottom).

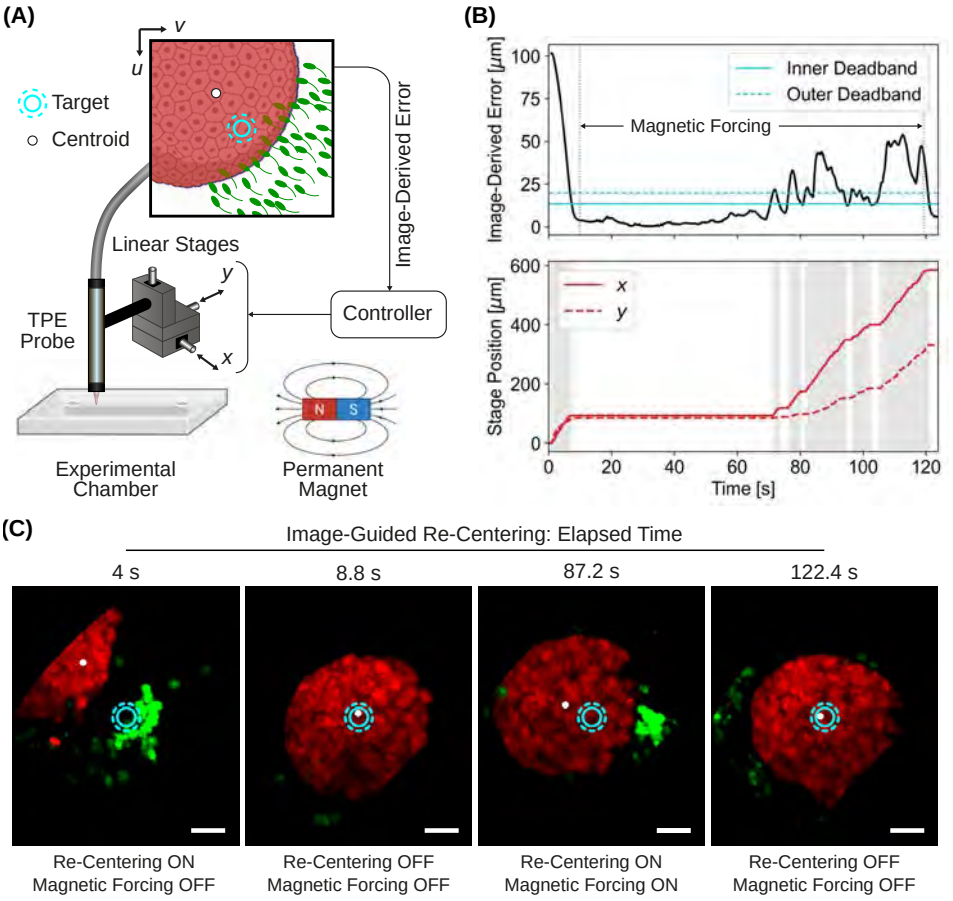


Figure 6.7: Image-guided re-centering using two-photon endomicroscopy feedback. (A) Schematic of the image-based feedback control system. The centroid of the target spheroid (Rhodamine B-labeled, red) is extracted from the TPE image and compared with a predefined target location in the field of view. A controller uses the resulting image-derived error to command motorized linear stages that adjust the probe position relative to the sample while magnetic micro-agents (Coumarin 6-labeled, green) induce target displacement. (B) Re-centering performance. Top: image-derived error relative to the target location, with the inner and outer deadband thresholds indicated. Magnetic forcing is applied intermittently from t = 10.0 to 119.0 s. Bottom: corresponding relative stage positions along the x and y directions. The grey regions indicate periods during which stage correction is active. (C) Representative dual-color TPE frames acquired during the re-centering experiment at different elapsed times. The cyan marker indicates the target location, and the white dot represents the detected spheroid centroid. Magnetic micro-agents (green) displace the spheroid through direct mechanical pushing, while closed-loop control restores its image position within the inner deadband. Scale bars: 50 µm. The complete dynamic sequence is provided in Video S3.

Because the magnetic forcing is applied manually with a handheld permanent magnet, the induced spheroid displacements occur intermittently and with variable magnitudes and directions. Re-centering performance is therefore evaluated event-wise, using excursions beyond the outer deadband as perturbation events. Following the onset of magnetic forcing ($t = 10.0$ s), seven perturbation events are detected within the analyzed actuation sequence. Each event is followed by a return of the image-derived error to the inner deadband, with a median recovery time of 6.0 s (IQR: 3.9–11.7 s). During magnetic forcing, the largest tracked error excursion followed by recovery is approximately 54 µm. Over the analyzed sequence, the relative stage positions span 585 and 331 µm along the x and y axes, respectively (Figure 6.7(B)).

Representative dual-color TPE frames at selected time points are shown in Figure 6.7(C), illustrating the progressive re-centering of the spheroid. Magnetic micro-agents (green) accumulate near the spheroid boundary, and the spheroid is displaced through direct mechanical pushing. These results demonstrate image-guided re-centering of a HeLa cell spheroid while preserving dual-color visualization of the interacting magnetic micro-agents.

Previous studies on photoacoustic- and ultrasound-guided microrobotic systems have demonstrated navigation over larger imaging regions and at greater tissue depths [44], [262]. In comparison, the present TPE approach provides local, high-resolution fluorescence feedback near the micro-agent–target interaction site, but with a smaller field of view and limited penetration depth. Accordingly, the TPE-guided re-centering demonstrated here represents a near-target feedback strategy complementary to modalities intended for wider-range navigation.

6.3 Conclusions and future work

This study demonstrates a two-photon endomicroscopy (TPE) system for real-time fluorescence imaging of magnetically actuated micro-agents. The TPE system enables image-based motion analysis, while dual-color imaging expands its capability to distinguish mixed micro-agent populations labeled with distinct fluorescent dyes. Magnetic micro-agents remain detectable through a 140µm fixed mammary gland tissue layer. Real-time visual feedback further supports a feasibility demonstration of image-guided re-centering, keeping a displaced HeLa cell spheroid within the field of view

during magnetic micro-agent interaction. These results extend TPE from passive observation to active image-guided functionality in microrobotic systems. Future work will extend imaging to living tissue, where heterogeneity, perfusion, and physiological motion become relevant. Additionally, a new fabrication approach for the magnetic micro-agents will be explored to lower the excitation power required for imaging. Further directions include multimodal imaging, reproducible magnetic perturbations for systematic evaluation of closed-loop re-centering, and advanced control strategies for coordinated guidance of multiple micro-agents. Such developments can further expand the role of endomicroscopy in minimally invasive microrobotic interventions.

6.4 Experimental section

Two-photon endomicroscopy system: The TPE system employs a wavelength-tunable femtosecond pulsed laser (Cronus 2P, Light Conversion, Lithuania) operating at 900 nm with a spectral bandwidth of 9 nm. The laser delivers pulses of 160 fs duration at a repetition rate of 77 MHz with a beam diameter of approximately 3 mm. Pulse chirp is adjusted using the internal compressor to compensate for dispersion introduced by downstream optical components.

The excitation beam is coupled into the core of a 0.65 m double-clad fiber (DCF) (IXF-2CF-PAS-4-130-0.14, iXblue, France) using an infinity-corrected microscope objective (EC Epiplan-NEOFLUAR 20×/0.5 HD, Leica Microsystems GmbH, Germany). The DCF is routed concentrically through a lead–zirconate–titanate (PZT) tube scanner (PIC255, PI Ceramic GmbH, Germany), enabling lateral scanning of the fiber tip.

The fiber is supported within the scanner using two custom adapters fabricated from IP-S photoresin (Nanoscribe GmbH, Germany) via dip-in laser lithography (Photonic Professional GT2, 10×/0.3 NA objective). The adapters are bonded to the PZT tube using cyanoacrylate adhesive (Loctite 401, Henkel AG & Co. KGaA, Germany). The DCF ends are cleaved prior to assembly and bonded to the adapters using UV-curable optical adhesive (NOA68, Norland Products, USA). A protective fiber jacket terminates at the proximal adapter and is fixed using cyanoacrylate adhesive to provide mechanical stability while allowing the distal fiber segment to oscillate freely.

The PZT–DCF assembly is housed within an aluminum probe body using a laser-cut acrylic support (Speedy 400, Trotec Laser GmbH, Austria). At the distal end of the probe, a gradient-index (GRIN) lens (#64-538, Edmund Optics Inc., USA) is mounted in a dedicated acrylic holder. The holder is bonded to the probe housing using cyanoacrylate adhesive, while the GRIN lens is fixed using optical adhesive (NOA63, Norland Products, USA) to ensure stable optical alignment. The axial spacing between the fiber tip and GRIN lens is adjusted using a digital caliper (500-196-30, Mitutoyo Corp., Japan).

During imaging, excitation light emerging from the DCF core is focused onto the sample by the distal GRIN lens. Fluorescence generated at the focal region is collected by the inner cladding of the DCF and relayed back through the proximal objective to the detection optics. The returning emission is separated into two spectral channels using dichroic mirrors (DMLP805 and DMLP605R, Thorlabs, USA) and bandpass filters (HQ510/20m and ET645/75m, Chroma, USA), corresponding to wavelength ranges of 500–520 nm (channel 1) and 608–682 nm (channel 2). The filtered signals are focused by collection lenses (AC254-150-A-ML, Thorlabs, USA) onto photomultiplier tubes (PMT1001/M and PMT2101/M, Thorlabs, USA). A summary of the transmission curves for dichroic mirrors and bandpass filters is presented in Figure 6.8 (Appendix, p. 154).

Scanning and image formation: Lateral scanning of the distal fiber tip is achieved by driving the four electrodes of the PZT tube scanner using a voltage amplifier (TD250-INV, PiezoDrive, USA) controlled by a function generator (33510B, Keysight, USA). The 10-MHz reference clock generated by the function generator is shared with a two-channel high-speed digitizer (ATS-9146, AlazarTech, Canada), ensuring a common timing base for both waveform generation and acquisition. In addition, a hardware trigger derived from the function generator is used to initiate digitizer acquisition, providing deterministic synchronization between the scanner drive signals and fluorescence detection in two spectral channels.

Fluorescence signals from the two photomultipliers are digitized at 16-bit resolution and 10 MS^{-1} sampling rate using the synchronized digitizer. The digitizer is operated with full analog bandwidth (no bandwidth limiting enabled). Image formation is performed online in real time (5 fps) using pre-calibrated lookup tables that map the instantaneous fiber-tip position to the acquired waveform samples. Because Lissajous scanning produces a

non-uniform dwell-time distribution across the valid scanned region, image intensities are normalized by the local sampling density during reconstruction. For the 300 × 343 px reconstruction grid enclosing the scan trace, the median dwell time across valid pixels is 2.6 µs, with a 5th–95th percentile range of 1.1–8.6 µs at 5 fps and 10 MS^{-1} sampling rate. The lookup tables are generated from measurements obtained with a lateral beam-position sensor (PDP90A, Thorlabs, USA) placed downstream of the probe. The calibration signals are acquired using the same digitizer and timing configuration as used during imaging, ensuring consistent temporal registration. During image formation, the non-uniform pixel sampling inherent to the Lissajous scan is compensated by normalizing the accumulated signal by the corresponding dwell time at each valid pixel. During routine operation, the acquisition bandwidth results in a sustained data throughput of approximately 40 MB s^{-1}.

Micro-agent fabrication: Electrospun fluorescent fibers are first fabricated and subsequently fragmented via ultrasonic treatment into discrete, micrometer-scale fiber fragments, referred to here as micro-agents. The term is used operationally: these agents are functionalized only for magnetic actuation and fluorescence imaging. Micro-agents prepared without iron oxide (Fe_3O_4) nanoparticles are designated non-magnetic and are not directly actuated by the applied magnetic field, whereas those incorporating Fe_3O_4 are designated magnetic. Polystyrene (PS) pellets (430102–1KG, Sigma-Aldrich, USA) are used as the carrier polymer and dissolved in anhydrous N,N-dimethylformamide (DMF) (227056–1L, Sigma-Aldrich, USA). For fluorescence labeling, Coumarin 6 (442631–1G, Sigma-Aldrich, USA) or Nile Red (72485, Sigma-Aldrich, USA) is incorporated into the polymer solution.

For non-magnetic fibers used in fluorescence characterization experiments, PS solutions with total polymer concentrations of 28 wt% and 45 wt% in DMF are prepared. The dye concentration is varied according to the desired loading and expressed relative to the PS mass fraction. Each solution is homogenized by stirring for 24 h using a roller mixer (LLG-uniRoller 6, LLG-Labware, Germany).

Electrospinning is performed by loading the polymer solution into a plastic syringe connected through Teflon tubing to an 18-gauge blunt-tip needle (TS18SS-15, Adhesive Dispensing Ltd., UK). A voltage of 14 kV is applied between the needle and a grounded collector, with a feed rate

of 2.5 mL h^{-1} and a tip-to-collector distance of 16 cm. Randomly oriented fiber meshes are collected on grounded aluminum foil under ambient conditions (20°C, 30% relative humidity) and dried at room temperature for 12 h to remove residual solvent.

For magnetic fiber fabrication, Fe_3O_4 nanoparticles (637106–25G, Sigma-Aldrich, USA) are incorporated into the electrospinning solution. The total solids concentration is maintained at either 28 wt% or 45 wt%, while PS and Fe_3O_4 are mixed at a mass ratio of 2:1. Thus, Fe_3O_4 partially replaces PS relative to the corresponding non-magnetic formulation while the total solids concentration remains constant. Coumarin 6 is used as the fluorescent dye for magnetic fibers at a concentration of 1.6 wt% relative to the total solids.

To generate micro-agents, the deposited fiber meshes are cut into 2–3 mm pieces and transferred to a glass vial containing 1% (v/v) Tween 80 (P4780-100ML, Sigma-Aldrich, USA) in Milli-Q water. The fibers are fragmented using an ultrasonic bath (Model 2510, Branson, USA) for 2 h, producing discrete fluorescent micro-agents. Non-magnetic micro-agents are allowed to sediment naturally for approximately 2 h, whereas magnetic micro-agents are collected using a permanent magnet. In both cases, the supernatant is removed and replaced with fresh Milli-Q water containing 1% Tween 80.

Dispersion compensation and optical power measurements: Group delay dispersion (GDD) precompensation is adjusted using the internal compressor of the femtosecond laser (Cronus 2P, Light Conversion, Lithuania) to optimize pulse delivery at the distal probe tip. For this characterization, straight electrospun fluorescent fibers are used as test samples. The dispersion setting is varied from no precompensation (0 fs^2) to the maximum negative value available from the integrated compressor (−20000 fs^2). For each dispersion setting, 10 consecutive fluorescence images are acquired at 16-bit depth, and fluorescence intensity statistics are computed from the resulting image sequences (Figure 6.12(A,B), Appendix, p. 160). To validate the dispersion settings used during imaging experiments, second-harmonic generation (SHG) signals are measured using a microscope-slide peak-power sensor (NS170C, Thorlabs, USA) (Figure 6.12(C), Appendix, p. 160).

The average excitation power delivered at the probe output is measured using a silicon photodiode sensor (S130C, Thorlabs, USA). Both sensors are

connected to the same power meter console (PM400, Thorlabs, USA), and all measurements are averaged over 100 samples for each experimental condition. During electrospun fiber characterization, the average excitation power at the sample plane is maintained at 16 mW. For dynamic imaging experiments, the average power is increased to 65 mW to maintain a sufficient fluorescence signal for motion analysis and image-guided recentering experiments.

Rat tissue sample: The rat mammary gland used in this study is collected post-mortem from outbred albino naïve female rats (RjHan: WI, Janvier Labs, France). Organs and biological samples are prepared and disposed of according to the Cat.1 directive for animal bio-products. The organs are fixed overnight in a 10% buffered formalin solution (Formalin 10%, Qpath Ref: 11699404, VWR). Subsequently, the tissues are immersed in 100% ethanol for 24 h and then stored at 4 °C. The fixed mammary gland is carefully sliced with a scalpel and placed between two coverslips for surface flattening, together with a custom spacer made of plastic film with double-sided medical-grade adhesive (ARcare® 90106NB, Adhesives Research, Inc., USA). The spacer, approximately 140 µm thick, is fabricated by laser cutting (Speedy 400, Trotec Laser GmbH, Austria), forming a ring with an 8 mm inner diameter. To enable imaging through rat tissue, 2 µL of micro-agent solution is deposited within the inner ring and allowed to dry at ambient temperature before placing the rat tissue on top. Finally, 2 µL of Dulbecco's phosphate-buffered saline is added to maintain a humid environment during the experiments.

Estimation of focal fluence: The peak per-pulse fluence (F_{peak}) is estimated from the average excitation power (P_{avg}), laser repetition rate (f_{rep}), and the measured lateral focal-spot intensity profile. The lateral profile shown in Figure 6.3(C) is used to estimate the probe point-spread function and gives a focal-spot full width at half maximum (d_{FWHM}) of approximately 2.1 µm. Using the Gaussian representation of this measured profile, the corresponding $1/e^2$ intensity radius (w_0) is

$$w_0 = \frac{d_{\text{FWHM}}}{\sqrt{2\ln 2}} \approx 1.78\ \mu m. \tag{6.1}$$

The pulse energy (E_{p}) and peak per-pulse fluence are calculated as

$$E_{\text{p}} = \frac{P_{\text{avg}}}{f_{\text{rep}}}, \qquad F_{\text{peak}} = \frac{2E_{\text{p}}}{\pi w_0^2}, \tag{6.2}$$

where $f_{rep} = 77$ MHz. The 16-mW average power used for electrospun-fiber characterization corresponds to a pulse energy of approximately 0.21 nJ and a peak per-pulse fluence of 0.0042 J cm^{-2}. The 65-mW average power used for the dynamic-imaging and image-guided re-centering experiments corresponds to approximately 0.84 nJ and 0.017 J cm^{-2}, respectively. The 200-mW maximum used for through-tissue imaging corresponds to approximately 2.60 nJ and 0.052 J cm^{-2}, while the 240-mW stationary-beam control corresponds to approximately 3.12 nJ and 0.062 J cm^{-2}.

Auxiliary endoscopic imaging: A camera (V1000LH, Misumi Electronics Corp., Japan) is used to visualize the tissue surface during tissue imaging experiments. The camera is positioned adjacent to the TPE probe and provides wide-field views of the tissue surface for probe alignment and positioning.

Cell culture and spheroid preparation: HeLa cells are cultured in Dulbecco's Modified Eagle Medium (11–965-092, Fisher Scientific Ltd., Canada) supplemented with 10% fetal bovine serum (F7524–500ML, Sigma-Aldrich, USA) and 1% penicillin–streptomycin (15–140-122, Thermo Fisher Scientific Inc., USA). Cells are maintained at 37 °C in a humidified incubator with 5% CO_2.

For spheroid formation, cells are trypsinized at approximately 80% confluency, counted, and resuspended in culture medium at a concentration of 2×10^6 cells mL^{-1}. A volume of 0.2 mL of the suspension is seeded onto an agarose microwell mold containing 1500 wells with a diameter and depth of 200 µm. Cells self-aggregate within the microwells and form compact spheroids after approximately 3 days of incubation.

Prior to imaging experiments, spheroids are stained using a 1 mM Rhodamine B solution prepared in phosphate-buffered saline to enhance fluorescence contrast. The stained spheroids are subsequently rinsed with fresh buffer and fixed for 15 min in 4% formaldehyde (F8775–25ML, Sigma-Aldrich, USA) at room temperature. After fixation, the spheroids are washed twice with Dulbecco's phosphate-buffered saline before being introduced into the experimental chamber for image-guided re-centering experiments.

Spectrum analysis: The emission spectra of fluorescent dyes used for micro-agent fabrication are acquired using a spectrofluorometer (FP-8300, Jasco, Japan) with a 1 nm data interval. For Coumarin 6 and Nile Red sample preparation, we dissolve 1.5 µg dye in 700 µL of dimethylformamide

(DMF) (227056–1L, Sigma-Aldrich, USA). Both solutions are blended for two hours using a roller mixer (LLG-uniRoller 6, LLG-Labware, Germany). For analysis, the blends are placed in quartz glass cuvettes (CV10Q700F, Thorlabs, USA). The emission plots are presented in Figure 6.8 (Appendix). These spectra are used as an initial reference for dye selection and TPE system design. The corresponding fluorescence performance is evaluated experimentally under two-photon excitation (Section 6.2.2).

Tissue staining: To enable fluorescence visualization of the tissue surface and evaluate potential illumination-induced structural changes, rat mammary gland samples are stained with 2 µL of a 1 mM Rhodamine B solution prepared in phosphate-buffered saline.

Magnetic actuation: Magnetic actuation is implemented using permanent magnets to generate rotating or translational magnetic fields at the sample location. For rotational actuation experiments, a diametrically magnetized NdFeB ring magnet (R06.8×03×10GD-40SH, Article No. 9963-6098, HKCM Engineering GmbH, Germany) is mechanically coupled to a DC gearmotor (2358, Pololu Corp., USA). The motor is powered using a programmable power supply (E36313A, Keysight Technologies, USA), allowing control of the magnet rotation frequency. The magnetic field at the sample workspace was characterized with a high precision three-axis teslameter probe (3MH3A-500MT, Senis AG, Baar, Switzerland). A dipole-based estimate of the corresponding field gradient is provided in the Supporting Information. For image-guided re-centering experiments, a handheld neodymium–iron–boron (NdFeB) permanent magnet (S-45-30-N, Supermagnete, Germany) is used to generate directional magnetic forces on the micro-agents.

Statistical Analysis: For fluorescence-characterization experiments, each field-of-view (FOV) value is obtained by averaging four consecutive frames acquired at 5 fps (technical repeats used to reduce frame-to-frame noise, not independent observations), unless a different number is stated in the caption. Group data for these experiments are reported as mean ± standard deviation across the stated unit, which is the number of FOVs for fiber characterization and the number of independent sample preparations for the through-tissue quantification (n specified per figure). Morphology and re-centering results are reported as the median and interquartile range (IQR), over individual micro-agents (n = 56) from 10 independent frames and over perturbation events within a single actuation sequence (n = 7), respectively.

Optical-flow speed and tracking consistency are reported as distributions of per-frame values over the actuation phase, summarized by the median and IQR. These values come from consecutive frames of a single continuous recording and are therefore not treated as independent measurements.

Magnetic Micro-Agent Morphology Analysis: Magnetic micro-agents are segmented from the C6 fluorescence channel after Gaussian smoothing using Otsu-derived threshold. Small image artifacts are removed, and touching objects are separated using watershed segmentation. All detected regions are subsequently inspected manually to retain individual micro-agents and exclude fiber remnants, unresolved agglomerates, and poorly segmented objects. The long and short axes and projected area are obtained from each accepted segmented region, and the aspect ratio is calculated as the long axis divided by the short axis. Measurements are converted to physical units using an image scale of 1.11 µm pixel^{-1}.

Optical flow–based motion analysis: Micro-agent motion is quantified using feature-based optical-flow analysis implemented in Python with OpenCV. Image sequences acquired during magnetic actuation are processed frame by frame to estimate local displacement vectors between consecutive frames using the pyramidal Lucas–Kanade method [263]. Feature points are detected with the Shi–Tomasi corner detector [264] and tracked between consecutive frames to estimate local displacement vectors.

Two quantitative metrics are computed from the optical-flow analysis: the optical-flow speed and the tracking consistency. The optical-flow speed is defined as the 95th percentile of the displacement-magnitude distribution for each frame, providing a robust descriptor of the upper range of observed motion. Pixel displacements are converted to physical units using the spatial calibration of the imaging system and multiplied by the frame rate (5 fps) to obtain speeds in µm s^{-1}. Tracking consistency is used to assess motion-estimation reliability through a forward–backward consistency check. Feature positions tracked forward between consecutive frames are subsequently tracked backward to the original frame, and the Euclidean distance between the original and reconstructed positions is computed. Vectors with forward–backward error below 1 pixel are considered consistent, and tracking consistency is defined as the fraction of consistent vectors within each frame. All metrics are computed during the actuation phase and summarized across frames using the median and interquartile range for each actuation frequency.

Image-guided re-centering and stage actuation: Image-guided re-centering is implemented through closed-loop visual servo control using DC servo motor actuators (Z812B, Thorlabs, USA) to reposition the imaging probe along the x and y directions. Each actuator is driven by a T-Cube DC servo controller (TDC001, Thorlabs, USA). The controllers are mounted on a T-Cube controller hub (TCH002, Thorlabs, USA), which provides power distribution and a USB interface for simultaneous control through a single connection to the host computer. Stage motion is commanded through the Kinesis control interface with a maximum velocity of 0.05 mm s^{-1} and an acceleration of 0.5 mm s^{-2} to ensure smooth probe motion during imaging.

The spheroid position is estimated directly from the TPE image stream by segmenting the spheroid fluorescence signal in each frame after Gaussian smoothing, intensity thresholding, and morphological filtering. The centroid of the largest segmented region is used to compute the image-derived error relative to a predefined target location at the center of the field of view. The image-derived error (e_x, e_y) is converted into stage commands using a proportional control law

$$\Delta x = -K_p e_x p, \qquad \Delta y = -K_p e_y p,$$

where p is the effective pixel size (0.35 µm $pixel^{-1}$) and K_p is the proportional gain. To reduce oscillatory corrections, a hysteresis-based deadband strategy is applied: stage motion is triggered only when the error exceeds an outer deadband and stops once it returns within an inner deadband.

Optical beam characterization: The focal spot size of the TPE probe is measured using an auxiliary optical imaging setup. The emitted beam is imaged directly onto a CMOS camera (acA2040-90um, Basler AG, Germany) using a finite-corrected microscope objective (100×, Mitutoyo 375-053, Mitutoyo Corp., Japan). A neutral density filter (NE10A-B, Thorlabs, USA) is placed in the optical path to attenuate the beam during these measurements. To estimate the effective numerical aperture of the probe, beam propagation measurements are performed using the same camera with the bare sensor exposed to the beam.

Experimental chamber fabrication: Experimental imaging chambers are fabricated using standard glass microscope slides as the base substrate. Circular chambers with an 8 mm diameter are created by laser cutting adhesive spacer films using a CO_2 laser system (Speedy 400, Trotec Laser GmbH, Austria). Two spacer materials are used depending on the experi-

ment. A transfer adhesive film (3M 9969, 3M, USA) providing a chamber height of approximately 75 µm is used for magnetic micro-agent dynamic analysis. For spheroid re-centering experiments, a thicker medical-grade adhesive spacer (ARcare® 90106NB, Adhesives Research Inc., USA) with a thickness of approximately 190 µm is used to accommodate the larger sample volume. The adhesive spacers are applied onto the glass slide to define the chamber boundary, and the chambers are sealed using a glass coverslip placed on top of the spacer to enclose the sample.

Numerical simulations: Numerical simulations are performed to support the design and characterization of the scanning probe and optical focusing performance. The mechanical behavior of the fiber scanner inside the piezoelectric tube actuator is analyzed using finite-element simulations in COMSOL Multiphysics (COMSOL AB, Sweden). The simulations are used to estimate the resonance behavior and lateral displacement of the oscillating fiber under sinusoidal excitation.

Optical propagation and distal focusing are analyzed in OpticStudio (Zemax LLC, USA) using physical-optics simulations. The model includes the double-clad fiber output and the gradient-index (GRIN) lens, and examines both centered and decentered input conditions to evaluate beam propagation, focal spot size, and the effective numerical aperture at the sample plane.

Linear Spectral Unmixing: Linear spectral unmixing is used to reduce fluorescence crosstalk between the two detection channels. The measured intensity in Channel 2 (I_2) is assumed to contain the desired Channel 2 signal ($I_{2,\text{true}}$) and a contribution from the measured Channel 1 intensity (I_1): $I_2 = I_{2,\text{true}} + \alpha I_1$, where the crosstalk coefficient (α) describes how much of the Channel 1 signal is detected in Channel 2.

For each imaging configuration, the crosstalk coefficient (α) is determined using a single-color control acquired with the same sample composition, excitation power, and detector settings as the corresponding dual-color experiment. After background subtraction, the coefficient is calculated as

$$\alpha = \frac{\sum_{p\in\Omega} I_{1,p} I_{2,p}}{\sum_{p\in\Omega} I_{1,p}^2},$$

where the pixel position (p) identifies the same location in both channels,

the calibration mask (Ω) contains fluorescent and non-saturated pixels, and the pixel intensities in Channels 1 and 2 are denoted by $I_{1,p}$ and $I_{2,p}$, respectively.

Each calibration uses eight fields of view ($n = 8$). Four consecutive frames are acquired at 5 fps in each field of view to reduce frame-to-frame noise. The coefficient is calculated for every frame, after which the median of the four values is used for that field of view. The median across the eight fields of view is then used as the crosstalk coefficient for the corresponding experiment. The corrected Channel 2 intensity ($I_{2,\mathrm{corr}}$) is calculated as $I_{2,\mathrm{corr}} = \max\left(I_2 - \alpha I_1,\, 0\right)$, with negative values set to zero. The dual-population and re-centering experiments use the same Coumarin 6-labeled magnetic micro-agents under matched excitation power and detector settings, so the coefficient $\alpha = 2.15$ determined for the dual-population experiment is applied directly to the re-centering experiment. The differing Channel 2 species (Nile Red for the non-magnetic agents, Rhodamine B for the spheroid) does not affect α, since neither contributes to Channel 1 leakage. A value greater than one reflects the different detector responses and gains of the two channels. Single-color Nile Red and Rhodamine B controls show no measurable crosstalk into Channel 1, so no correction is applied in the reverse direction.

Appendix

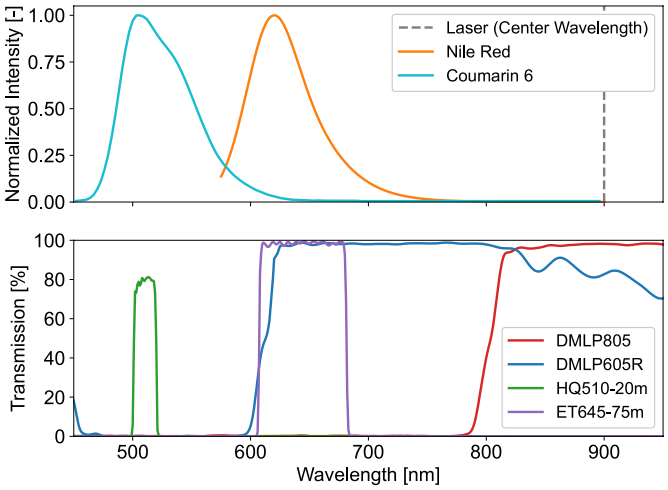


Figure 6.8: Spectral reference for dye selection and channel separation in the TPE system. Top panel: Normalized one-photon emission spectra of Coumarin 6 and Nile Red acquired using a spectrofluorometer. The dashed vertical line marks the 900 nm excitation wavelength used in the microscopy system and is shown only as a reference to the TPE excitation source. Spectra are normalized to their respective maxima for visualization. Bottom panel: Transmission spectra of the dichroic mirrors (DMLP805, DMLP605R) and bandpass filters (HQ510-20m, ET645-75m) used in the excitation and detection paths. These plots summarize the spectral rationale used for dye selection and nominal channel separation.

Optical design of the distal assembly

The distal optical response of the probe is analyzed using physical-optics simulations (Zemax LLC, USA) of the double-clad fiber (DCF) coupled to the GRIN lens. The main geometric control parameter is the axial spacing (l_0) between the DCF tip and the GRIN lens, which determines the beam expansion before entering the lens and, therefore, the distal focusing condition (Figure 6.9(A)).

For the centered case, the distal focusing condition is characterized by the beam width (w) and the working distance (z). As shown in Figure 6.9(B,C), increasing l_0 produces a monotonic decrease in z, whereas w shows a local minimum within the analyzed range around $l_0 = 3.5$–4.0 mm. This indicates that increasing l_0 initially improves the centered focus, but

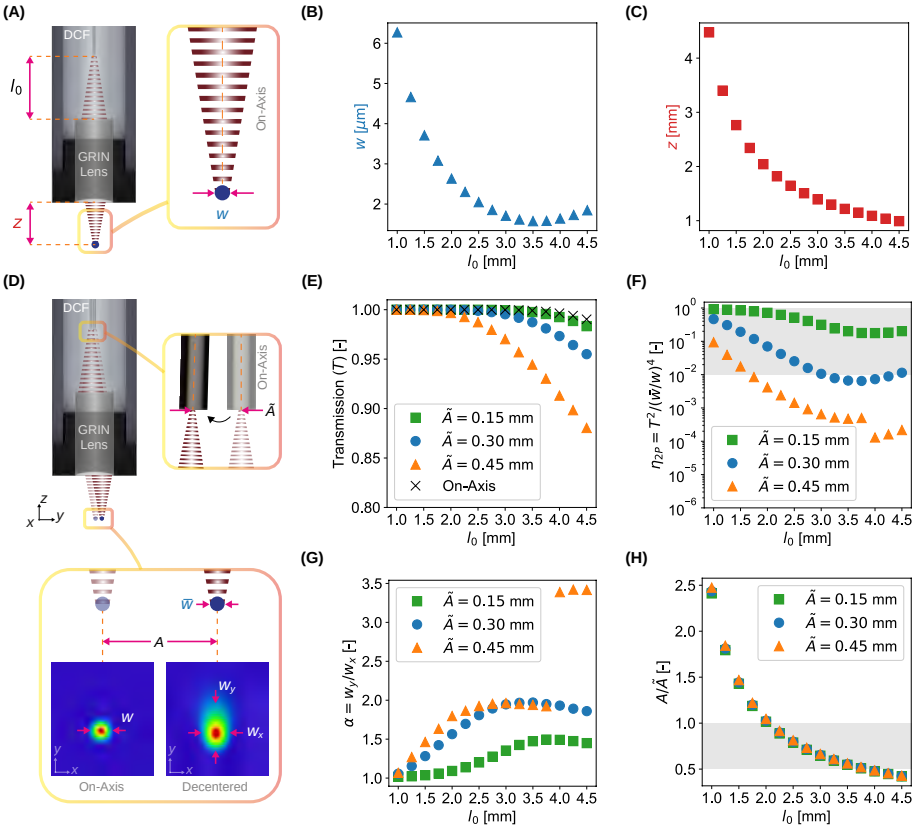


Figure 6.9: Optical beam propagation and off-axis beam behavior in the TPE probe. **(A)** Schematic of the centered optical configuration. The GRIN lens focuses light exiting the double-clad fiber (DCF). The axial fiber-to-lens offset (l_0) determines the focusing geometry, while the beam width and working distance characterize the distal focusing condition. **(B)** Simulated centered beam width (w) as a function of l_0. **(C)** Working distance (z) versus l_0. **(D)** Schematic of the decentered case. A lateral input decenter ($\tilde{A}$) is used to emulate off-axis beam positions during DCF scanning, producing a distal optical displacement (A). The decentered spot is characterized by different widths along the x/y-axes (w_x and w_y) with average width ($\bar{w}$). **(E)** Normalized transmission (T) versus l_0 for different imposed decenters, including the centered case as reference. **(F)** Relative two-photon excitation proxy ($\eta_{2P} = T^2/(\bar{w}/w)^4$) versus l_0. The shaded region indicates the reference range $10^{-2} \leq \eta_{2P} \leq 1$. **(G)** Beam anisotropy ($\alpha = w_y/w_x$) versus l_0. **(H)** Scan transfer ratio ($A/\tilde{A}$) versus l_0. The shaded region indicates the reference range $0.5 \leq A/\tilde{A} \leq 1$.

beyond this range, the spot no longer becomes narrower. As later shown in Figure 6.9(E), this regime is associated with a progressive loss of on-axis transmission.

To evaluate off-axis performance, a lateral input decenter ($\tilde{A}$) is imposed at the DCF side, producing a distal optical displacement (A) and an off-axis focal spot with axis-dependent widths (w_x and w_y) (Figure 6.9(D)). The average off-axis width is defined as $\bar{w} = (w_x + w_y)/2$. Figure 6.9(E) shows that the normalized transmission (T) already decreases in the on-axis case as l_0 increases, and that this reduction becomes more pronounced for larger imposed decenters. This behavior is consistent with a progressively larger fraction of the beam approaching the GRIN boundary at larger l_0, which penalizes off-axis transmission more strongly.

To summarize the off-axis implications for two-photon operation, a relative two-photon excitation proxy is defined as

$$\eta_{2P} = \frac{T^2}{(\bar{w}/w)^4}.$$

This quantity combines delivered power and focal broadening into a compact proxy for relative off-axis two-photon excitation efficiency. As shown in Figure 6.9(F), η_{2P} decreases with increasing l_0 and with larger imposed decenters, indicating that stronger off-axis penalties accompany a narrower on-axis spot. The shaded region in Figure 6.9(F) marks the selected reference range $10^{-2} \leq \eta_{2P} \leq 1$, corresponding to the retention of 1% to 100% of the on-axis excitation proxy. This range is used as a practical design reference to avoid configurations with severe off-axis degradation.

Beam anisotropy is quantified by $\alpha = w_y/w_x$, which captures off-axis spot distortion. Figure 6.9(G) shows that α increases with both l_0 and $\tilde{A}$, indicating progressively stronger elongation of the focal spot. The abrupt deviation observed for the largest imposed decenter ($\tilde{A} = 0.45$ mm) near $l_0 = 4$ mm is consistent with strong clipping at the GRIN boundary, which also explains the discontinuity visible in η_{2P} in Figure 6.9(F).

The scan-transfer ratio ($A/\tilde{A}$) describes how proximal beam motion is converted into distal optical displacement and is therefore directly related to the accessible scanned field of view. As shown in Figure 6.9(H), $A/\tilde{A}$ decreases with increasing l_0, indicating reduced scan transfer at larger fiber-to-lens offsets. The shaded region in Figure 6.9(H) marks the selected reference range $0.5 \leq A/\tilde{A} \leq 1$, which is used as a design criterion to retain

at least half of the imposed proximal scan amplitude at the distal field.

Taken together, these simulations show that the distal optical design is not selected by optimizing a single on-axis metric. Although the centered beam width w continues to decrease up to larger l_0, this is accompanied by progressively stronger off-axis penalties in transmission, η_{2P}, beam anisotropy, and scan-amplitude ratio. The selected range of approximately $l_0 = 2.5$–3.0 mm is therefore chosen as a design compromise, where the centered spot remains sufficiently narrow, and the off-axis metrics still satisfy the selected reference criteria for excitation efficiency and scan amplitude.

Scanning characterization

The oscillatory scanning behavior of the assembled probe, including the GRIN focusing optics, is experimentally characterized to determine the operating conditions used for imaging. Sinusoidal voltages are applied to the orthogonal electrode pairs of the PZT tube, producing lateral oscillations of the fiber tip along the x and y directions. The corresponding driving signals are

$$V_x(t) = 0.5V_{ppx}\sin(2\pi f_x t), \qquad V_y(t) = 0.5V_{ppy}\sin(2\pi f_y t),$$

where V_{ppx} and V_{ppy} denote the peak-to-peak driving voltages, and f_x and f_y are the driving frequencies.

The scanning range is first measured as a function of driving frequency at a fixed peak-to-peak voltage of 25 V. As shown in Figure 6.10(C), the scanner responses along both lateral axes exhibit resonance peaks near 810 Hz. These results are consistent with the cantilever resonance predicted by the mechanical analysis in Figure 6.11 for free fiber lengths (l_f) around the assembled value of 11.5 mm. For imaging operation, frequencies within the 820–840 Hz interval are selected, where the response remains stable and approximately linear.

Within this frequency range, the scanning range increases approximately linearly with the applied peak-to-peak voltage along both axes (Figure 6.10(D)). The slopes of the voltage–displacement response are extracted for different operating frequencies to quantify the achievable scan extent (Figure 6.10(E)).

Lissajous scanning trajectories are generated by selecting pairs of driving frequencies (f_x, f_y) with slightly different values. The selection proce-

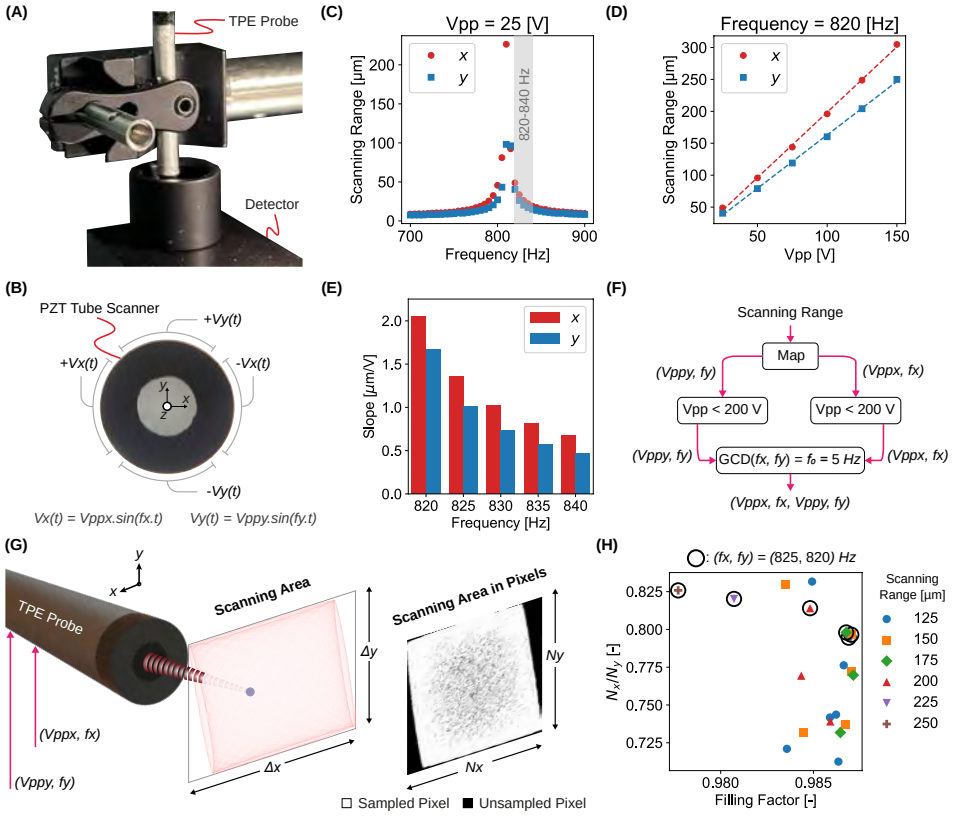


Figure 6.10: Oscillation and scanning characterization of the two-photon endomicroscopy (TPE) probe. **(A)** Experimental setup used to measure the fiber oscillations and scanning trajectory. **(B)** Cross-section of the PZT tube scanner showing the electrode configuration and sinusoidal driving voltages $V_x(t)$ and $V_y(t)$. **(C)** Scanning range as a function of driving frequency at $V_{pp} = 25$ V. The scanner exhibits a resonance near ∼810 Hz; the 820–840 Hz interval is selected for further analysis due to its approximately linear response. **(D)** Scanning range versus peak-to-peak voltage V_{pp} at $f = 820$ Hz for both x and y axes. **(E)** Slopes of the scanning range–voltage relationship within the 820–840 Hz interval. **(F)** Workflow for selecting pairs of driving frequencies (f_x, f_y) that achieve the desired scanning range while maintaining $V_{pp} <$ 200 V. The greatest common divisor of (f_x, f_y) defines the Lissajous scanning frequency $f_0 =$ 5 Hz. **(G)** Mapping of the Lissajous scanning trajectory to the pixel grid. N_x is fixed, while N_y is determined by the ratio $\Delta x/\Delta y$. **(H)** Scanning anisotropy versus filling factor for valid frequency pairs at scanning ranges between 125 and 250 μm with N_x=300 pixels. The pair $(f_x, f_y) = (825, 820)$ Hz (encircled) remains valid across the entire range.

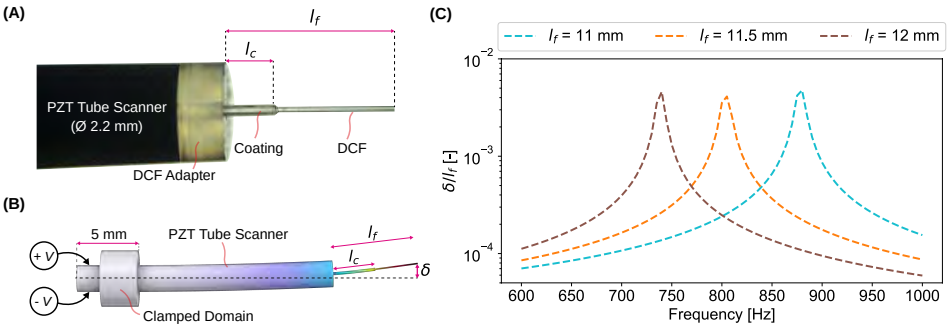


Figure 6.11: Resonant response of the PZT tube scanner as a function of free fiber length. **(A)** Photograph of the probe assembly showing the PZT tube scanner (outer diameter 2.2 mm), DCF adapter, coated fiber section, and double-clad fiber (DCF). The coating length (l_c) and free fiber length (l_f) are indicated. **(B)** Schematic representation of the PZT tube scanner operating as a cantilever. The clamped domain spans 5 mm, while the free fiber section (l_f) extends beyond the tube. Differential voltage applied to the PZT electrodes produces a lateral tip deflection δ. The coating length is defined as $l_c = 0.1 l_f$. **(C)** Simulated frequency response of the normalized tip deflection (δ/l_f) for three representative free lengths (l_f = 11.0, 11.5, and 12.5 mm). Increasing l_f shifts the resonant response toward lower frequencies, consistent with cantilever behavior.

dure is summarized in Figure 6.10(F): candidate frequency pairs are constrained by the scanner voltage limit ($V_{pp} < 200$ V) and chosen such that their greatest common divisor satisfies $\gcd(f_x, f_y) = f_0$. Here, $f_0 = 5$ Hz is used as the fundamental scan frequency, providing a practical compromise between image rate and spatial coverage. The resulting trajectories are mapped to the image grid to evaluate pixel coverage and sampling behavior (Figure 6.10(G)). The filling factor and scanning anisotropy are computed for all valid frequency pairs within the selected operating range (Figure 6.10(H)).

Based on this analysis, the frequency pair $(f_x, f_y) = (825, 820)$ Hz is selected as it is a valid pair throughout the entire analyzed scanning range (125–250 µm). For the final operating condition, we use the corresponding peak-to-peak driving voltages of $V_{pp,x} = 147.4$ V and $V_{pp,y} = 122.5$ V. This configuration leads to a Lissajous scan with 232 and 316 µm along the two scanning axes. The reported field of view corresponds to the lateral extent of the Lissajous scan trace, with valid image pixels defined by the lookup table.

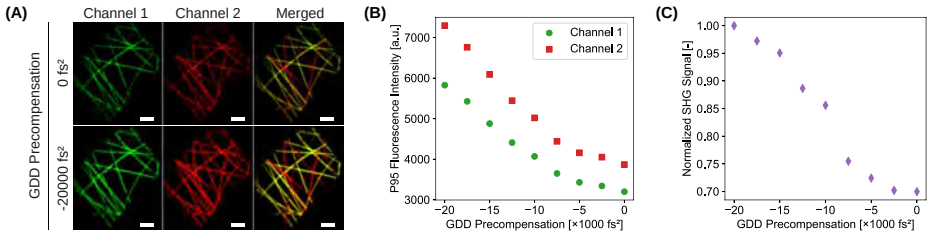


Figure 6.12: Effect of dispersion precompensation on nonlinear signal generation. **(A)** Two-color fluorescence images acquired without dispersion precompensation (0 fs^2) and with optimized precompensation (-20000 fs^2). Channel 1 (green) and Channel 2 (red) correspond to two spectrally separated fluorescence signals, and the merged images illustrate their spatial overlap. Improved signal brightness is observed when dispersion is compensated. Scale bars = 50 µm. **(B)** 95th percentile (P95) fluorescence intensity for both channels as a function of applied group delay dispersion (GDD) precompensation. Increasing negative GDD enhances the detected fluorescence signal, indicating improved pulse compression at the sample. **(C)** Normalized second-harmonic generation (SHG) signal as a function of GDD precompensation. The SHG response confirms that dispersion compensation increases peak pulse intensity, consistent with more efficient nonlinear excitation.

6

Magnetic field gradient estimate

The field gradient at the workspace was estimated from the measured rotating field and the manufacturer specifications of the ring magnet (remanence $B_r = 1.24$ T; outer diameter $D_\mathrm{o} = 6.8$ mm, inner diameter $D_\mathrm{i} = 3.0$ mm, height $h = 10$ mm). Approximating the magnet as a point dipole, its moment is

$$m = \frac{B_r V}{\mu_0} \approx 0.29 \text{ A m}^2, \text{ with } \quad \mathrm{V} = \frac{\pi}{4}\left(\mathrm{D_o^2} - \mathrm{D_i^2}\right)\mathrm{h}. \tag{6.3}$$

The field of the dipole at position $\mathbf{r}$ is

$$\mathbf{B}(\mathbf{r}) = \frac{\mu_0}{4\pi r^3}\left[\,3(\mathbf{m}\cdot\hat{\mathbf{r}})\,\hat{\mathbf{r}} - \mathbf{m}\,\right]. \tag{6.4}$$

As the diametrically magnetized magnet rotates, the field at the workspace traces a planar ellipse whose minor semi-axis amplitude A_min fixes the magnet–workspace distance,

$$A_\mathrm{min} = \frac{\mu_0 m}{4\pi r^3} \quad \Longrightarrow \quad r = \left(\frac{\mu_0 m}{4\pi A_\mathrm{min}}\right)^{1/3} \approx 9 \text{ mm}. \tag{6.5}$$

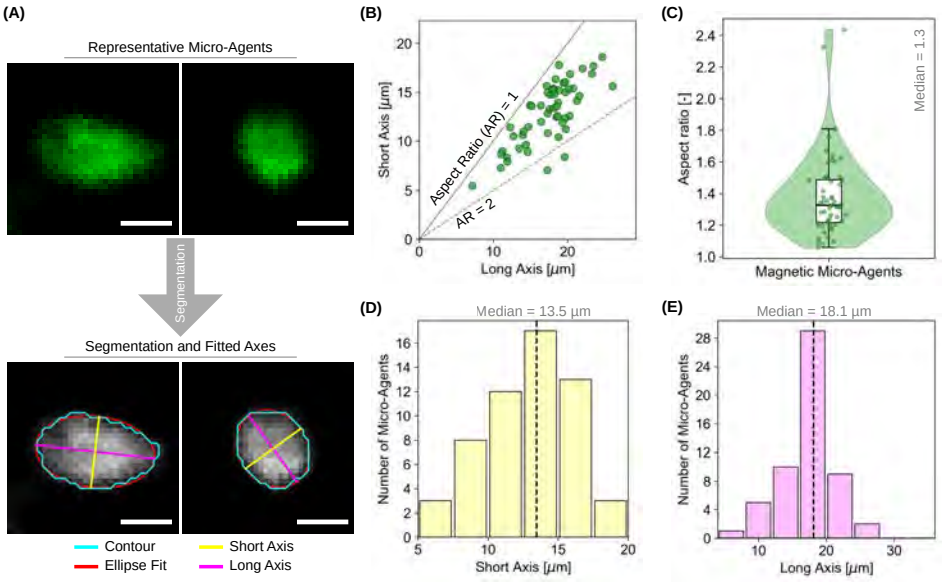


Figure 6.13: Size and morphology of magnetic micro-agents. **(A)** Representative two-photon images of magnetic micro-agents and the corresponding segmentation and ellipse fitting used to determine their dimensions. Cyan, red, magenta, and yellow indicate the detected contour, fitted ellipse, long axis, and short axis, respectively. Scale bars: 10 µm. **(B)** Short-axis dimension plotted against the long-axis dimension for individual micro-agents. The solid and dashed diagonal lines indicate aspect ratios of 1 and 2, respectively. **(C)** Distribution of the measured aspect ratios, showing individual observations and an embedded box plot. **(D,E)** Distributions of the short- and long-axis dimensions, respectively. Dashed vertical lines indicate the corresponding medians. Measurements comprise 56 individual micro-agents segmented across 10 distinct frames.

Because the dipole field scales as r^{-3}, the corresponding gradient scales as r^{-4}, giving a representative magnitude

$$|\nabla \mathbf{B}| \sim \frac{3\,|\mathbf{B}|}{r} \sim 20\ \mathrm{T\,m^{-1}}, \tag{6.6}$$

which, because the field rotates, varies over each actuation cycle. As the recovered distance is comparable to the magnet dimensions, the point-dipole model provides an order-of-magnitude estimate value. In this rotating-field regime, micro-agent motion is governed primarily by magnetic torque ($\mathbf{m} \times \mathbf{B}$). To compare the magnetic torque scale with the gradient-force contribution over the micro-agent size, a characteristic length is defined as the arithmetic mean of the median short and long micro-agent axis dimen-

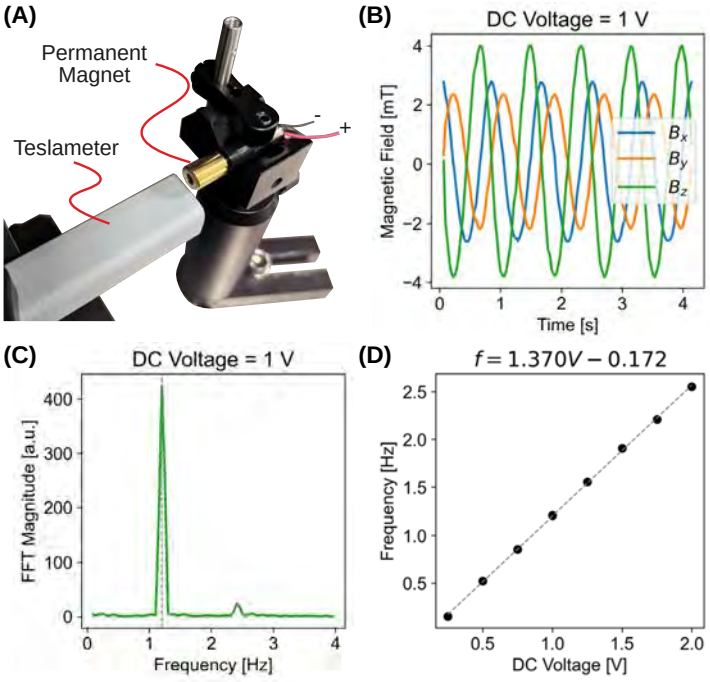


Figure 6.14: Magnetic field characterization and voltage-to-frequency mapping for micro-agent actuation. **(A)** Experimental setup used to measure the magnetic field generated by the rotating permanent magnet. A teslameter probe is positioned near the actuation region to record the time-varying magnetic field components. **(B)** Temporal evolution of the magnetic field components (B_x, B_y, B_z) measured at a DC voltage of 1 V applied to the motor. The oscillatory behavior arises from the rotation of the permanent magnet. **(C)** Fast Fourier transform (FFT) of the measured magnetic field signal, showing the dominant frequency component associated with magnet rotation. **(D)** Rotation frequency as a function of the applied DC voltage. The dashed line indicates a linear fit ($f = 1.370V$ - 0.172), showing linear control of the actuation frequency through the motor driving voltage.

sions ($L \approx 16\ \mu$m) (Figure 6.13(D)–(E)). Using this characteristic length, the ratio between the torque scale and the gradient-force contribution over the micro-agent size is $\frac{|\mathbf{B}|}{L|\nabla\mathbf{B}|} \approx 10^2$, indicating that torque-driven reorientation, not gradient pulling, dominates the actuation.

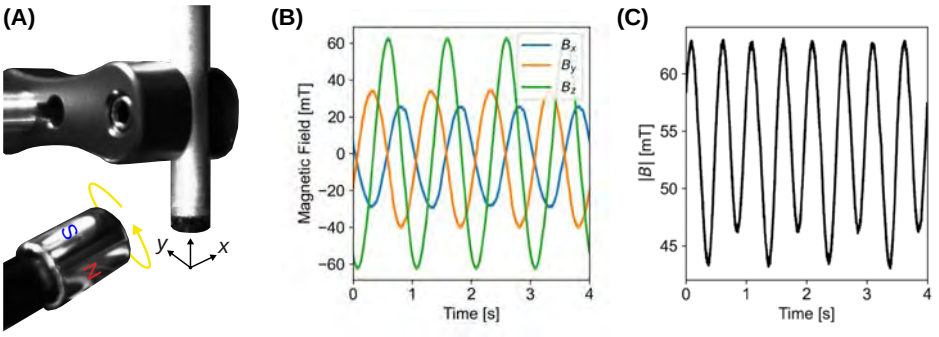


Figure 6.15: Rotating magnetic field generation for micro-agent actuation. **(A)** Experimental configuration showing the rotating permanent magnet used to generate a time-varying magnetic field at the workspace. The rotation axis and coordinate system are indicated as yellow and black arrows, respectively. **(B)** Measured temporal evolution of the magnetic field components (B_x, B_y, B_z) during magnet rotation, illustrating the periodic variation of the vector field. **(C)** Corresponding magnitude of the magnetic field ($|B|$) as a function of time, demonstrating the oscillatory field strength experienced at the measurement location.

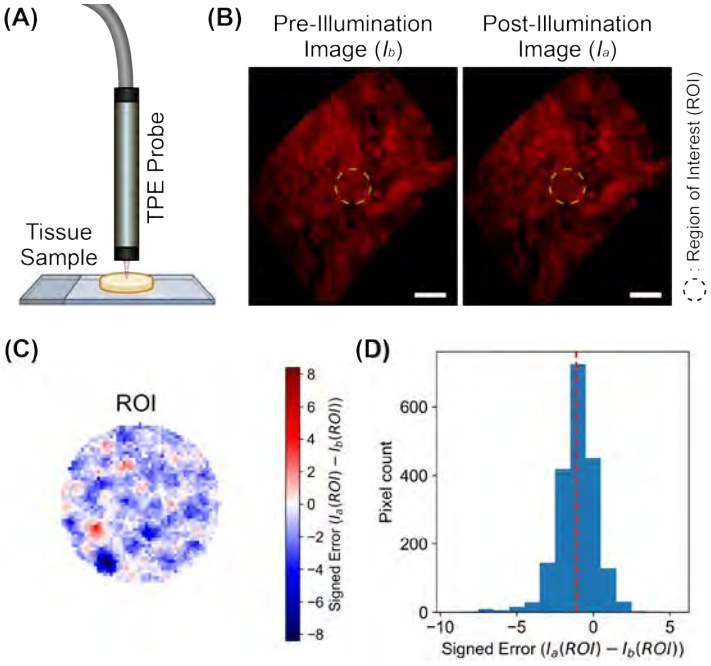


Figure 6.16: Evaluation of illumination-induced effects during stationary beam exposure. **(A)** Schematic of the experimental configuration used to assess potential illumination-induced changes. The TPE probe is positioned above the surface of a Rhodamine B–stained mammary gland tissue sample, and the excitation beam (240 mW average power, 77 MHz repetition rate) is parked at the tissue surface for 3 min, exceeding the highest imaging power used in this study (200 mW). **(B)** Representative pre-illumination image (I_b) and post-illumination image (I_a) acquired before and after stationary beam exposure. A circular region of interest (ROI, 50 px diameter) centered at the beam location is used for the quantitative analysis. For each condition, 10 frames are recorded and averaged to reduce frame-to-frame fluctuations. Scale bars = 50 µm. **(C)** Mean signed error map within the ROI, computed as I_a(ROI) - I_b(ROI). **(D)** Histogram of pixel-wise signed intensity differences within the ROI. The dashed red line indicates the mean of the distribution (-1.11 on a 0–255 scale), corresponding to a 9.5% decrease in mean intensity relative to the pre-illumination value

Table 6.1: Representative performance of external and local imaging modalities relevant to micro-agents.

Modality	Distal diameter	Spatial resolution	Useful depth	FOV	Temporal resolution	Contrast	Label-free	Depth sectioning[e]	Ref.
Clinical B-mode ultrasound	–	∼0.1–1 mm	Several cm to > 10 cm	cm-scale	Tens of fps	Acoustic backscatter	Yes	Echo delay	[253], [265] [236], [266]
Photoacoustic computed tomography	–	125–255 μm in-plane	cm-scale (up to 4 cm)	∼3.9–4.8 cm in-plane	10–50 Hz (2D)	Optical absorption (spectral)[d]	Yes	Acoustic arrival time	[254], [255] [202], [256]
Magnetic particle imaging (MPI)	–	∼1–5 mm	No tissue attenuation[a]	cm-scale	Tens of volumes s^{-1}	Magnetic tracer	No	Magnetic spatial encoding	[238], [257]
Local endoscopic/endomicroscopic imaging									
Photoacoustic endoscopy	∼0.8–3.2 mm[f]	Lat.: ∼10–300 μm Axial: ∼30–60 μm	∼1–3 mm (tissue-dependent)	mm-scale (360° scan)	∼2–50 fps	Optical absorption (spectral)[d]	Yes	Acoustic time-of-flight	[261], [267]
Wide-field fluorescence endoscopy	Platform-dependent	Working-distance dependent	Surface	mm–cm	Video-rate	Fluorescence (multicolor)	Possible[b]	None	[83], [258] [268]
Confocal endomicroscopy	∼0.9–2.7 mm	Lat.: ∼0.7–3.5 μm Axial: ∼3–15 μm	∼40–250 μm	∼240–700 μm	∼8–12 fps	Fluorescence/ reflectance	Possible[b]	Confocal pinhole rejection	[259], [269] [268]
Endoscopic optical coherence tomography	∼0.9–3.2 mm	Lat.: ∼20–40 μm Axial: ∼5–15 μm	∼1–2 mm	mm-scale (360° scan)	∼40–200 fps	Interferometric backscatter	Yes	Coherence gating	[260], [270] [200]
Two-photon endomicroscopy (TPE)	∼2.4–5.8 mm	Lat.: ∼0.6–3.1 μm Axial: ∼3–10 μm	∼100–200 μm 300 μm[c]	∼80–750 μm	∼0.7–26 fps	Nonlinear fluorescence (multicolor)	Possible[b]	Nonlinear focal excitation	[244], [250], [251] [81], [197], [271] [99], [100], [272] [252], [273], [274] [245]

[a] MPI signal is not attenuated by intervening tissue, although spatial resolution, sensitivity, and accessible volume remain dependent on tracer properties and scanner geometry.

[b] "Possible" denotes that endogenous fluorescence or reflectance can generate contrast without an administered agent. Target-specific molecular contrast generally requires an exogenous agent.

[c] The 300 μm TPE result was demonstrated using enhanced fluorescence collection. Compact fiber-scanning systems in scattering tissue more commonly operate over approximately 100–200 μm. The reported 400 μm focus-tuning range is an addressable axial range rather than a measured tissue-penetration depth and is therefore not listed as useful depth.

[d] Spectral optoacoustic discrimination requires sufficiently distinct absorption spectra and multispectral acquisition; it is not directly equivalent to fluorophore-channel separation.

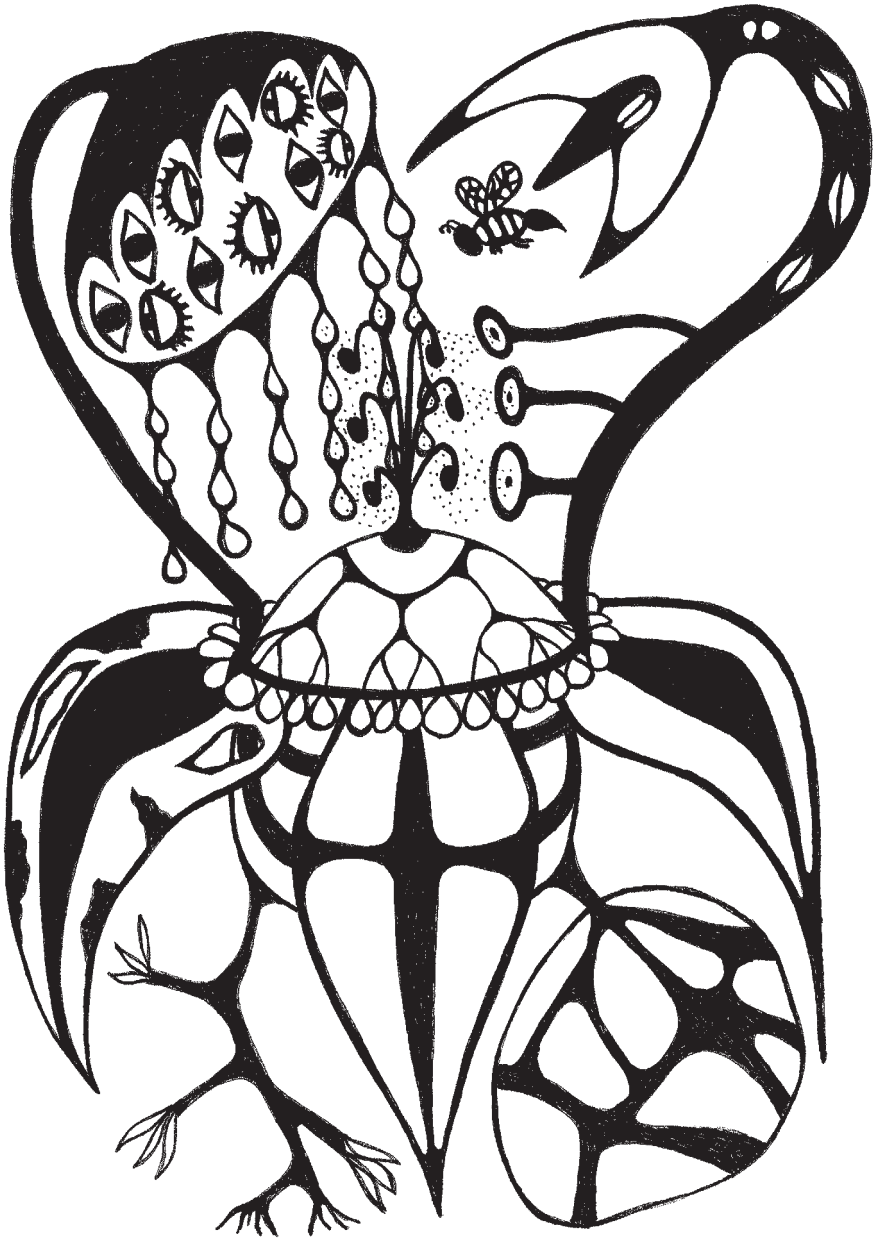
[e] Depth sectioning denotes the mechanism used to assign signal to depth or restrict contributions from out-of-focus regions. Confocal imaging filters out-of-focus fluorescence at detection, whereas TPE limits its generation through nonlinear focal excitation.

[f] The photoacoustic-endoscopy diameter range refers to compact catheter or working-channel probes. Larger capsule- and MEMS-based prototypes are not included in this table.

III

The end of the beginning

This final part discusses the combination of the two capabilities developed in the preceding parts: magnetic actuation to exert contactless forces and torques, and fluorescence imaging to visualize micro-agents and biological structures with specificity. **Chapter 7** revisits the contributions of **Chapters 2–6** and the connections between them, tracing the integration toward image-guided microrobotics. **Chapter 8** then reflects on the challenges that remain for operation in living, dynamic, and heterogeneous environments, and the future directions toward biomedical practice. The title of this part, *The end of the beginning*, inspired by the God Is an Astronaut debut album of the same name (2002), reflects the nature of this work: not an endpoint, but the foundation for the journey ahead. The thesis demonstrates the integration of magnetic actuation and fluorescence imaging under controlled conditions and reveals the challenges that remain for operation in living, dynamic, and heterogeneous environments. The thesis closes by outlining future directions toward biomedical practice.



CHAPTER 7

Discussion and conclusions

This doctoral thesis developed magnetic actuation and fluorescence imaging strategies toward image-guided microrobotics in biologically relevant environments. This chapter brings together the resulting contributions and examines what the studies add relative to earlier work at the Surgical Robotics Laboratory and prior literature in the field of microrobotics. The discussion is organized by chapter because individual studies contribute to more than one research objective (RO). The following sections revisit **Chapters 2–6**, discussing their main findings, scope, limitations, and connections to the ROs.

Chapter 2: Miniaturized electromagnets for local actuation

As the first study of *Invisible touch*, **Chapter 2** introduced MagNeed, a localized actuation system based on three positionable needle-shaped electromagnets. Their arrangement around a target region defines a compact workspace. Field characterization yielded a magnetic field gradient of 3.5 T/m at 5 mm from the needle axis at 1 A. At the adopted operating limit of 0.75 A, each needle consumed approximately 0.5 W, and its surface temperature remained below 42 °C during the 480 s thermal tests. In the trapping experiment at a water flow rate of 100 mL/min, a single needle retained a 1 mm magnetic bead while consuming 8 mW, compared with 2827 mW for the external nine-coil system. This power comparison is specific to the tested configurations and trapping conditions.

The contribution of this chapter is the development and experimental validation of a configurable system for localized magnetic actuation, combining needle-shaped electromagnets, near-field modeling, and reconstruction of source poses. The MILiMAC system previously developed at the Surgical Robotics Laboratory integrated three miniaturized electromagnets into a flexible catheter [85]. MagNeed uses separate needle-shaped

sources whose positions and orientations can be selected around the target region and reconstructed using a 3D camera. Earlier electromagnetic needles demonstrated selective and cooperative manipulation of magnetic microparticles [86], [87]. MagNeed extends the experimental investigation to localized trapping and actuation within a fluid-filled tube under flow. The experimental characterization establishes the magnetic, thermal, and trapping performance of this implementation under the tested conditions.

This chapter contributes to **RO.1** by developing and characterizing a configurable magnetic actuation strategy for compact workspaces. Demonstrations with a 1 mm magnetic bead establish feasibility at the millimeter scale. The accompanying force estimates provide a basis for interpreting the observed trapping and localized actuation behavior. Extension to smaller agents requires assessing how their volume and magnetization affect the available magnetic force. Micro-agent motion also depends on the balance between magnetic force, hydrodynamic drag, and forces arising from interactions with nearby surfaces. Localized actuation is subsequently demonstrated with magnetic electrospun micro-agents in **Chapter 5**, where a needle-shaped electromagnet is used during two-photon imaging. The emphasis on placing magnetic sources close to the target also connects this work to **Chapter 6**, where permanent-magnet actuation is positioned near the endomicroscopy probe.

Chapter 3: Collective behavior of magnetic microparticles

Chapter 3 concluded *Invisible touch* by extending the actuation perspective from individual agents to magnetic microparticle collectives. Experiments were performed using BatMag, the nine-coil electromagnetic system previously developed at the Surgical Robotics Laboratory for independent control of individual microrobots [92]. Reduced iron microparticles measuring 1–5 μm were assembled into millimeter-scale pillars using a static magnetic field generated by the base electromagnet. Across the tested conditions, the average pillar height ranged from approximately 2.9 to 5.0 mm, and the average base diameter ranged from approximately 0.33 to 0.72 mm. Pillar height increased with both field magnitude and particle mass, while the base diameter remained approximately constant with field magnitude

and increased with particle mass.

After pillar formation, the remaining eight electromagnets generated additional nonuniform and time-varying fields for actuation. Varying the field configuration enabled four actuation modalities: convergence, stretching, creep, and homogenization. These respectively gathered, elongated, translated, and redistributed the pillars. For object manipulation, precessing fields following Lissajous patterns drove collective pillar motion, enabling two-dimensional manipulation of a 2 mm glass bead with a mass of 9.3 mg. Spatially selective fields also translated two separated pillar clusters in opposite directions. Flow experiments were performed in a water-filled tube with an inner diameter of 8 mm. A pillar collective formed from 10 mg of reduced iron moved upstream and downstream at tested flow rates up to 40 mL/min. At 100 mL/min, the pillars remained assembled, with a centroid displacement of approximately 1.4 mm over 15 s. These flow experiments complement the single-bead trapping and actuation demonstrations in **Chapter 2**.

Building on earlier demonstrations of tentacle- and carpet-like magnetic swarms [133], this chapter develops and experimentally demonstrates actuation strategies based on programmed spatial variations in the magnetic field. Here, BatMag's field-shaping capabilities are extended to the formation, reorganization, and spatially selective motion of self-assembled pillar collectives. These findings contribute to **RO.2** by characterizing collective responses under nonuniform and time-varying magnetic fields. The collective perspective connects this chapter to **Chapters 4 and 6**, where fluorescence imaging is used to observe groups of magnetic micro-agents and distinguish agent populations during actuation.

Chapter 4: Real-time multicolor fluorescence microscopy

Chapter 4 opened *Any colour you like* by addressing the temporal cost of sequential multicolor fluorescence acquisition. Acquiring channels separately helps to reduce spectral crosstalk, but it lowers the effective multicolor frame rate as the number of channels increases. This chapter developed a framework combining cross-channel acquisition with deep-learning-based inference to predict separate fluorescence images from frames con-

taining mixed signals. U-Net and pix2pix were compared under matched conditions using magnetic micro-agents interacting with HeLa cell spheroids in a microfluidic platform.

For two-color imaging, the framework used a single frame containing mixed fluorescence from the Coumarin 6-labeled micro-agents and CMTPX-labeled spheroids to reconstruct their separate channels. This replaced two sequential acquisitions with one acquisition followed by inference. Reconstruction of both target channels required approximately 13.9 ms on the tested hardware. With a 22 ms input exposure, the effective two-color frame rate increased by 22% relative to fully sequential acquisition. Comparisons with directly acquired reference channels yielded aggregate root-mean-square errors below 6.2 μm for spheroid localization and below 1.6° for micro-agent orientation. These results demonstrate that the reconstructed images retain information relevant to observing position and orientation during actuation.

For three-color imaging, indocyanine green (ICG) was added to the surrounding medium to provide an additional near-infrared fluorescence channel for visualizing the microfluidic environment. Combining this separately acquired channel with the reconstructed micro-agent and spheroid channels increased the effective frame rate by 50% relative to fully sequential acquisition. Although ICG is spectrally separated from Coumarin 6 and CMTPX, the ICG images also contained spatial contrast associated with the micro-agents and spheroids. This contrast may arise from variations in ICG distribution and from absorption or scattering of its fluorescence by these structures, without requiring spectral overlap with their visible labels. An alternative workflow used a separately trained model to predict the visible channels from these indirect structural cues. This achieved an 83% increase in effective frame rate relative to fully sequential acquisition, with lower reconstruction fidelity for the micro-agent channel.

The contribution of this chapter is the development and experimental validation of an acquisition-and-inference workflow that reduces the number of sequential measurements required for multicolor observation. Earlier studies demonstrated deep-learning-based spectral unmixing and filter-free fluorescence reconstruction [95], [184]. Within the Surgical Robotics Laboratory, prior work established serial and real-time multicolor imaging of micro-agents and biological structures [45], [74]. This chapter extends that imaging approach through continuous prediction of target channels from re-

duced acquisitions, evaluated through both image reconstruction and tracking performance. Tests with morphology-matched spheroids and controlled intensity imbalance further examined the information supporting reconstruction and its limitations. The results from this chapter contribute to **RO.3** by increasing the effective frame rate of multicolor fluorescence imaging under the tested conditions. Reconstruction depends on informative input signals and training data representative of the imaging conditions. The observation of groups of magnetic micro-agents connects this chapter to the collective perspective of **Chapter 3**, while multicolor visualization during actuation continues in **Chapter 6** through dual-color endomicroscopy.

Chapter 5: Two-photon microscopy for microrobotics

Chapter 5 continued *Any colour you like* by investigating two-photon microscopy for visualizing micro-agents through biological tissue. Two agent types were studied: fluorescent electrospun fibers prepared following earlier work at the Surgical Robotics Laboratory [45], and CeFlowBot structures fabricated from autofluorescent resin following the design of Mohanty *et al.* [104]. The study characterized their fluorescence and demonstrated optical sectioning and three-dimensional reconstruction of both agent types.

Two-photon imaging used a pulsed laser operating at 1045 nm with a repetition rate of 15 MHz. The excitation wavelength lies near the short-wavelength end of the second near-infrared (NIR-II) spectral range, where reduced scattering relative to visible wavelengths can favor light propagation through tissue [243]. This benefits the delivery of excitation light to the fluorescent structures. However, the system collected fluorescence within 400–740 nm, so the returning emission remained subject to absorption and scattering at visible wavelengths. Imaging depth, therefore, depends on tissue attenuation along both the excitation and emission paths.

Static imaging revealed CeFlowBot morphology through fixed rat ileal-wall layers with nominal thicknesses of 400–450 μm. Electrospun fibers were visualized through nominal thicknesses of 250 μm of brain tissue and 800 μm of kidney cortex. The nominal thicknesses of the overlying tissue layers were estimated using spacers during sample preparation. Magnetic electrospun micro-agents were also actuated using a needle-shaped elec-

tromagnet developed in **Chapter 2**. Continuous observation through a nominal 600 μm ileal-wall layer was demonstrated at one frame per second over a field of view of 135 $\times$ 135 μm^2. These demonstrations used average laser powers of 6 mW without overlying tissue and 85 mW through the tissue layer. A separate qualitative laser–tissue interaction study used the same laser to examine visible ablation in fixed rat liver. No visible ablation was observed at an average power of 85 mW, while ablation was observed at 92 mW and 97 mW under the tested scanning conditions. These observations are specific to the specimen and exposure protocol.

The contribution of this chapter is the experimental establishment of two-photon visualization of these micro-agent types through fixed tissue, including continuous observation during magnetic actuation. This chapter also extends the optical investigation of existing micro-agent designs at the Surgical Robotics Laboratory to scattering tissue layers and contributes to **RO.4**. The needle-shaped electromagnet also builds on the localized actuation strategy developed for **RO.1**. Acquisition at one frame per second limits observation of rapid dynamics, while single-channel detection limits spectral separation of agent fluorescence from weaker tissue signals. The benchtop configuration also limits optical access to confined anatomical regions, motivating the probe-based imaging system developed in **Chapter 6**.

Chapter 6: Two-photon endomicroscopy for image-guided magnetic microrobotics

Chapter 6 concluded *Any colour you like* by developing two-photon endomicroscopy for observing magnetically actuated micro-agents and their interactions with biological structures. The endomicroscopy system extends the benchtop imaging approach used in **Chapter 5** to a fiber-optic probe that delivers excitation light and collects fluorescence near the micro-agents.

The probe combined a piezoelectric fiber scanner, a double-clad fiber, and a gradient-index (GRIN) lens. Using excitation at 900 nm with a repetition rate of 77 MHz, the system acquired simultaneous dual-color images at five frames per second over a field of view of 232 $\times$ 316 μm^2. Optical characterization yielded a focused-spot lateral full width at half

maximum of approximately 2.1 μm. Characterization of the electrospun precursor fibers further showed how dye loading and fiber morphology influenced fluorescence intensity, while incorporating magnetic nanoparticles reduced the fluorescence signal. These results identified an optical cost of introducing magnetic functionality into the agents. The acquired images supported motion analysis during magnetic actuation at frequencies of 0.5–2 Hz. Two-photon absorption enabled the excitation of the selected fluorophores at a single near-infrared wavelength, while simultaneous detection in two spectral channels avoided sequential acquisition of the two colors. This enabled magnetic and nonmagnetic micro-agent populations to be distinguished and their motion to be analyzed separately within the same workspace.

Magnetic micro-agents also remained detectable through a nominal 140 μm fixed rat mammary gland tissue layer at average excitation powers up to 200 mW. The endomicroscopy system used a laser operating at 900 nm and 77 MHz, whereas the benchtop microscope in **Chapter 5** used a different laser operating at 1045 nm and 15 MHz. Consequently, the 200 mW used here corresponds to approximately 2.6 nJ per pulse, compared with approximately 5.7 nJ at the 85 mW used in **Chapter 5**. Despite the higher average power, the endomicroscopy system delivered lower energy per pulse. However, neither quantity alone provides a transferable tissue-damage criterion. Formal comparison requires accounting for wavelength, pulse duration at the sample, focusing geometry, and scanning exposure.

Beyond passive observation, TPE images provided feedback for closed-loop probe repositioning during micro-agent–spheroid interaction. A manually positioned permanent magnet actuated the micro-agents, which displaced a HeLa cell spheroid. The image-derived spheroid position was compared with a predefined target position, and motorized stages automatically adjusted the probe to re-center the spheroid within the field of view. In the analyzed sequence, all seven detected perturbation events were followed by a return of the image-derived position error within the 13.3 μm inner deadband. The median recovery time was 6.0 s, with an interquartile range of 3.9–11.7 s. Consistent with the framework introduced in **Chapter 1**, this demonstration implements image-guided microrobotics through closed-loop adjustment of the imaging system during magnetic micro-agent operation.

The contribution of **Chapter 6** is the development and experimental validation of a probe-based imaging and feedback platform for magnetic

microrobotics. Building on established fiber-scanning and multicolor TPE approaches [244], [273], the work extends their use to micro-agent motion analysis and image-guided probe repositioning. Relative to earlier fluorescence imaging at the Surgical Robotics Laboratory [45], [46], it brings these functions into a compact probe-based architecture. These results address **RO.5** by combining magnetic actuation and two-photon fluorescence endomicroscopy for image-guided microrobotics. Through-tissue detection and feedback-guided re-centering were evaluated in separate experiments. Combined operation through biological tissue remains to be established.

CHAPTER 8

Outlook

The studies in this thesis establish a foundation for image-guided microrobotics in biologically relevant environments. However, further progress is required in the individual components and in their coordination among actuation, imaging, and feedback control under conditions closer to realistic deployment. From this perspective, this chapter outlines a roadmap toward biological and clinical use. The roadmap begins with the transition from the controlled samples used in this thesis to living and perfused biological environments (Section 8.1). Subsequent steps strengthen guidance through multimodal imaging (Section 8.2), instruments integrating delivery, imaging, and actuation (Section 8.3), and closed-loop control across scales (Section 8.4). The final stage connects guidance with therapeutic function and outlines a staged path toward clinical use (Section 8.5).

8.1 Toward living biological environments

One of the next steps is to move from controlled biological samples toward living and perfused environments. The fixed tissues, microfluidic channels, and cell spheroids used in this thesis provide reproducible conditions. However, such conditions simplify several features that are central to realistic biological settings. Perfused or vascularized models introduce flow, tissue heterogeneity, sample motion, and evolving boundaries, all of which affect micro-agent transport and image quality [275]. Moving toward *in vivo* studies requires evaluation of biological responses, including cell viability, tissue integrity, and the effects of micro-agent exposure, optical illumination, and magnetic actuation over time [13].

Vascularized models can provide an intermediate step between the controlled platforms used here and *in vivo* studies. In addition, the image-guided microrobotics concept can be tested under conditions where the environment actively perturbs both the micro-agents and the imaging signal [276]. Increasing biological realism helps assess the robustness of actuation

and imaging strategies in living, dynamic, and heterogeneous environments.

8.2 Multimodal imaging

Fluorescence imaging provides high sensitivity and spectral separation for identifying labeled micro-agents and biological structures. However, guidance under *in vivo* conditions may also depend on structural and spatial information that fluorescence does not directly provide. Tissue boundaries, anatomical landmarks, flow paths, and regions outside the optical field of view can all influence micro-agent deployment and guidance. This motivates combining fluorescence with complementary imaging channels selected depending on the guidance problem. Structural methods, such as optical coherence tomography [277], could help define tissue boundaries, while photoacoustic imaging [278] could extend visualization deeper into scattering tissue. Nonlinear optical approaches, including second- and third-harmonic generation, coherent anti-Stokes Raman scattering, and stimulated Raman scattering, could add label-free structural or chemical contrast [204], [279], [280]. Wavefront shaping offers another route by compensating for scattering-induced distortions, which could become relevant when guidance depends on optical access through heterogeneous tissue [281]–[284]. Several of these contrast and correction strategies have already been explored in nonlinear endomicroscopy and fiber-probe platforms, making them relevant for future multimodal microrobotic guidance [285]–[288]. Multimodal imaging becomes valuable when each modality contributes a distinct layer of information needed for guidance.

8.3 Toward endomicrorobotic instruments

The actuation and imaging strategies developed in this thesis point toward a common direction: bringing control and visualization closer to the region where micro-agents operate. MagNeed showed that magnetic fields can be generated locally near a confined workspace, while the two-photon endomicroscopy probe demonstrated that imaging can be miniaturized and brought close to that region. A natural next step is therefore to co-design these capabilities within a probe-based platform that also supports micro-agent delivery [13], [98]. In this context, an endomicrorobotic instrument

can be understood as a system that provides local access, micro-agent deployment, imaging, and actuation within the same operational workspace.

An endomicrorobotic instrument, however, requires more than just placing components side by side. The actuation workspace must overlap with the imaging field of view, the actuation source must remain thermally and mechanically compatible with the surrounding tissue, and the probe geometry must preserve imaging performance while allowing access to a region of interest. Arrays of the needle-shaped electromagnets developed in **Chapter 2** could be investigated for localized collective actuation using the field-shaping strategies of **Chapter 3**. This integration is subject to several constraints: heat must be dissipated close to tissue, neighboring sources couple magnetically, and the attainable fields and gradients depend on source dimensions and allowable currents. The number and arrangement of sources are also constrained by the space available around the target region and the routing of electrical connections, while the combined magnetic response of the array requires calibration.

The endomicroscopy probe developed in this thesis has a distal diameter of approximately 4 mm and a rigid length of 33 mm, set by the piezoelectric tube scanner, the GRIN lens, and the free fiber length required for resonant scanning. Smaller probe formats have been demonstrated for TPE, including a distal diameter of 2.4 mm [245], while commercial white-light videoendoscopes such as Iriscope have nominal probe diameters of 1.3 mm [289]. The 4 mm diameter of the present probe therefore reflects its current implementation rather than a fundamental size requirement of TPE. For this prototype, laparoscopic access through nominal 5 mm trocars is a potential route, for inspection of peritoneal tissue. Flexible endoscopic access through tortuous anatomy may require smaller scanners and shorter rigid sections, together with integration into steerable catheters or endoscope working channels suited to the target anatomy. Mechanical suitability for a specific anatomical access route, including shaft bending stiffness, allowable curvature, and steering requirements, remains to be evaluated.

If a working channel is included for micro-agent delivery, its outlet must also be aligned with the imaging and actuation workspaces. In such a system, imaging, actuation, and delivery become coupled functions. This concept can bring image-guided microrobotics closer to operation in confined biological environments, where micro-agents must be delivered, visualized, and actuated within a shared local workspace.

8.4 Multiscale closed-loop control

The closed-loop capability demonstrated in **Chapter 6** represents an initial step toward control strategies that use imaging as an active feedback signal. In this demonstration, two-photon endomicroscopy provided feedback to keep a HeLa cell spheroid within the field of view while magnetically actuated micro-agents interacted with and displaced it. Future systems will require control at multiple scales: positioning the probe relative to a region of interest, maintaining micro-agents and biological structures within the field of view, and coordinating micro-agent motion during local interactions [136], [290], [291].

Such control requires more than image acquisition alone. Visual feedback must be combined with actuation models, state estimation, and controllers that can adapt to flow, tissue motion, and changing micro-agent configurations [292]. Coordinated guidance of multiple agents, autonomous recovery when micro-agents or biological structures leave the field of view, and task-level control of micro-agent–cell interactions remain open challenges. The imaging and actuation framework developed in this thesis provides a starting point for this transition in dynamic biological environments.

8.5 Clinical relevance

The long-term biomedical relevance of image-guided microrobotics depends on connecting micro-agent guidance with defined biological or therapeutic functions. The micro-agents used in this thesis were functionalized for magnetic actuation and fluorescence visualization, making them suitable for studying motion, imaging, interaction, and feedback control. However, these agents were not designed for therapeutic applications. Micro-agents used in this thesis did not carry drug payloads nor release active compounds, and did not produce a defined biological effect.

Future work would benefit from micro-agents designed for therapeutic functions [161]. Drug-loaded fibers, biodegradable carriers, or stimuli-responsive materials could enable localized release in response to external stimuli such as light or heat, or to local biological conditions such as pH or enzymatic activity [22], [157], [293], [294]. Fluorescence imaging could localize the micro-agents and verify their accumulation, retention,

activation, and interaction with the surrounding tissue. A clinical path for image-guided microrobotics is likely to be staged. The imaging probe could first be evaluated on its own, for example, label-free imaging of tissue during laparoscopic procedures, where its dimensions are already compatible with standard access routes (Section 8.3). Magnetic actuation and micro-agents would follow once their biocompatibility, the optical and thermal safety of the imaging, and the behavior of micro-agents in perfused tissue are established in preclinical models. Each stage requires evaluation under the applicable medical device regulations before first use in patients. This direction shifts microrobotics from controlled motion toward purposeful intervention. In that sense, the path forward is toward microrobots that can reach targeted sites within the body and deliver treatment under image guidance. For this thesis, such a path marks not the end of the journey but the end of the beginning.

References

[1] T. Ji and D. S. Kohane, "Nanoscale systems for local drug delivery," *Nano today*, vol. 28, p. 100765, 2019.

[2] M. T. Manzari, Y. Shamay, H. Kiguchi, N. Rosen, M. Scaltriti, and D. A. Heller, "Targeted drug delivery strategies for precision medicines," *Nature Reviews Materials*, vol. 6, no. 4, pp. 351–370, 2021.

[3] S. Pallatt, A. Shibili, S. Nambidi, S. M. Jain, A. Banerjee, and S. Pathak, "Microrobots in colorectal cancer diagnosis: Advancements and applications," in *Colorectal Cancer Diagnosis*. CRC Press, 2025, pp. 183–200.

[4] R. Nauber, S. R. Goudu, M. Goeckenjan, M. Bornhäuser, C. Ribeiro, and M. Medina-Sánchez, "Medical microrobots in reproductive medicine from the bench to the clinic," *Nature Communications*, vol. 14, no. 1, p. 728, 2023.

[5] M. F. Deering, "The limits of human vision," in *2nd international immersive projection technology workshop*, vol. 2, no. 1, 1998.

[6] H. Lee and I. J. Rhyu, "Antonie van leeuwenhoek and the dawn of microscopic observation: a narrative review from delft's lens to the modern microscope," *Applied Microscopy*, vol. 56, no. 1, p. 3, 2026.

[7] T. G. Rochow and P. A. Tucker, *Introduction to microscopy by means of light, electrons, X rays, or acoustics*. Springer Science & Business Media, 1994.

[8] P. W. Hawkes and J. C. Spence, *Science of microscopy*. Springer, 2007, vol. 1.

[9] C. Eggeling, "Advances in bioimaging—challenges and potentials," *Journal of Physics D: Applied Physics*, vol. 51, no. 4, p. 040201, 2018.

[10] D. B. Schmolze, C. Standley, K. E. Fogarty, and A. H. Fischer, "Advances in microscopy techniques," *Archives of pathology & laboratory medicine*, vol. 135, no. 2, pp. 255–263, 2011.

[11] Y. Bellouard, "Microrobotics," in *Methods and applications*. CRC-Press, 2010.

[12] M. Sitti, H. Ceylan, W. Hu, J. Giltinan, M. Turan, S. Yim, and E. Diller, "Biomedical applications of untethered mobile milli/microrobots," *Proceedings of the IEEE*, vol. 103, no. 2, pp. 205–224, 2015.

[13] V. Iacovacci, E. Diller, D. Ahmed, and A. Menciassi, "Medical microrobots," *Annual Review of Biomedical Engineering*, vol. 26, no. 1, pp. 561–591, 2024.

[14] X. Ju, C. Chen, C. M. Oral, S. Sevim, R. Golestanian, M. Sun, N. Bouzari, X. Lin, M. Urso, J. S. Nam *et al.*, "Technology roadmap of micro/nanorobots," *ACS nano*, vol. 19, no. 27, pp. 24 174–24 334, 2025.

[15] I. Asimov, *Fantastic voyage: A novel*. Bantam, 2011.

[16] E. Kolb, *Inner space/outer space*. University of Chicago Press, 1986.

[17] R. Feynman, "There's plenty of room at the bottom," in *Feynman and computation*. CRC Press, 2018, pp. 63–76.

[18] M. Ye, Y. Zhou, H. Zhao, Z. Wang, B. J. Nelson, and X. Wang, "A review of soft microrobots: Material, fabrication, and actuation," *Advanced Intelligent Systems*, vol. 5, no. 11, p. 2300311, 2023.

[19] F. Soto, J. Wang, R. Ahmed, and U. Demirci, "Medical micro/nanorobots in precision medicine," *Advanced science*, vol. 7, no. 21, p. 2002203, 2020.

[20] H. Hussein, A. Damdam, L. Ren, Y. Obeid Charrouf, J. Challita, M. Zwain, and H. Fariborzi, "Actuation of mobile microbots: a review," *Advanced Intelligent Systems*, vol. 5, no. 9, p. 2300168, 2023.

[21] A. Aziz, S. Pane, V. Iacovacci, N. Koukourakis, J. Czarske, A. Menciassi, M. Medina-Sánchez, and O. G. Schmidt, "Medical imaging of microrobots: Toward in vivo applications," *ACS Nano*, vol. 14, no. 9, pp. 10 865–10 893, 2020.

[22] B. J. Nelson and S. Pané, "Delivering drugs with microrobots," *Science*, vol. 382, no. 6675, pp. 1120–1122, 2023.

[23] A. Pedram and H. Nejat Pishkenari, "Smart micro/nano-robotic systems for gene delivery," *Current gene therapy*, vol. 17, no. 2, pp. 73–79, 2017.

[24] M. Tian, M. Keshavarz, A. A. Demircali, B. Han, and G.-Z. Yang, "Localized microrobotic delivery of enzyme-responsive hydrogel-immobilized therapeutics to suppress triple-negative breast cancer," *Small*, vol. 21, no. 18, p. 2408813, 2025.

[25] L. Xie, J. Liu, Z. Yang, H. Chen, Y. Wang, X. Du, Y. Fu, P. Song, and J. Yu, "Microrobotic swarms for cancer therapy," *Research*, vol. 8, p. 0686, 2025.

[26] Y. Wang, D. Jin, X. Liu, L. Lin, H. Cao, Z. Guo, X. Sun, X. Yan, Q. Wang, J. Guo *et al.*, "Magnetic microrobot with drilling-sensing dual functionality for targeted biopsy of deep-seated tracheal microlesions," *Advanced Materials*, vol. 38, no. 2, p. e14664, 2026.

[27] F. M. Yurtsever and M. Pumera, "Translational application of biomedical microrobots in female reproductive system," *ACS Nano Medicine*, 2026.

[28] J. J. Abbott, E. Diller, and A. J. Petruska, "Magnetic methods in robotics," *Annu. Rev. Control Robot. Auton. Syst.*, vol. 3, no. 1, pp. 57–90, 2020.

[29] L. Wang, Z. Meng, Y. Chen, and Y. Zheng, "Engineering magnetic micro/nanorobots for versatile biomedical applications," *Advanced Intelligent Systems*, vol. 3, no. 7, p. 2000267, 2021.

[30] A. Aghakhani, O. Yasa, P. Wrede, and M. Sitti, "Acoustically powered surface-slipping mobile microrobots," *Proceedings of the National Academy of Sciences*, vol. 117, no. 7, pp. 3469–3477, 2020.

[31] S. Mohanty, Y.-H. Lin, A. Paul, M. R. van den Broek, T. Segers, and S. Misra, "Acoustically actuated flow in microrobots powered by axisymmetric resonant bubbles," *Advanced Intelligent Systems*, vol. 6, no. 1, p. 2300465, 2024.

[32] A.-I. Bunea and J. Glückstad, "Strategies for optical trapping in biological samples: Aiming at microrobotic surgeons," *Laser & Photonics Reviews*, vol. 13, no. 4, p. 1800227, 2019.

[33] S. Zhang, F. Nan, and S. L. Neale, "Light-driven microrobots: mechanisms and applications," *Field-Driven Micro and Nanorobots for Biology and Medicine*, pp. 91–111, 2022.

[34] D. Park, S. J. Park, S. Cho, Y. Lee, Y. K. Lee, J.-J. Min, B. J. Park, S. Y. Ko, J.-O. Park, and S. Park, "Motility analysis of bacteria-based microrobot (bacteriobot) using chemical gradient microchamber," *Biotechnology and Bioengineering*, vol. 111, no. 1, pp. 134–143, 2014.

[35] Z. Xiao, M. Voigtmann, and J. Simmchen, "Biomimetic chemotactic motion of self-assembling doublet microrobots," *Advanced Intelligent Systems*, vol. 7, no. 10, p. 2400839, 2025.

[36] P. Harder, N. İyisan, C. Wang, F. Kohler, I. Neb, H. Lahm, M. Dreßen, M. Krane, H. Dietz, and B. Özkale, "A laser-driven microrobot for thermal stimulation of single cells," *Advanced Healthcare Materials*, vol. 12, no. 26, p. 2300904, 2023.

[37] A.-I. Bunea, D. Martella, S. Nocentini, C. Parmeggiani, R. Taboryski, and D. S. Wiersma, "Light-powered microrobots: challenges and opportunities for hard and soft responsive microswimmers," *Advanced Intelligent Systems*, vol. 3, no. 4, p. 2000256, 2021.

[38] K. Han, C. W. Shields IV, and O. D. Velev, "Engineering of self-propelling microbots and microdevices powered by magnetic and electric fields," *Advanced Functional Materials*, vol. 28, no. 25, p. 1705953, 2018.

[39] F. Katzmeier and F. C. Simmel, "Microrobots powered by concentration polarization electrophoresis (cpep)," *Nature Communications*, vol. 14, no. 1, p. 6247, 2023.

[40] G. Go, A. Yoo, K. T. Nguyen, M. Nan, B. A. Darmawan, S. Zheng, B. Kang, C.-S. Kim, D. Bang, S. Lee *et al.*, "Multifunctional microrobot with real-time visualization and magnetic resonance imaging for chemoembolization therapy of liver cancer," *Science Advances*, vol. 8, no. 46, p. eabq8545, 2022.

[41] D. Vilela, U. Cossío, J. Parmar, A. M. Martínez-Villacorta, V. Gómez-Vallejo, J. Llop, and S. Sánchez, "Medical imaging for the tracking of micromotors," *ACS nano*, vol. 12, no. 2, pp. 1220–1227, 2018.

[42] S. Pane, V. Iacovacci, E. Sinibaldi, and A. Menciassi, "Real-time imaging and tracking of microrobots in tissues using ultrasound phase analysis," *Applied Physics Letters*, vol. 118, no. 1, p. 014102, 2021.

[43] S. Martel, O. Felfoul, J.-B. Mathieu, A. Chanu, S. Tamaz, M. Mohammadi, M. Mankiewicz, and N. Tabatabaei, "Mri-based medical nanorobotic platform for the control of magnetic nanoparticles and flagellated bacteria for target interventions in human capillaries," *The International Journal of Robotics Research*, vol. 28, no. 9, pp. 1169–1182, 2009.

[44] Z. Wu, L. Li, Y. Yang, P. Hu, Y. Li, S.-Y. Yang, L. V. Wang, and W. Gao, "A microrobotic system guided by photoacoustic computed tomography for targeted navigation in intestines in vivo," *Science Robotics*, vol. 4, no. 32, p. eaax0613, 2019.

[45] M. Kaya, F. Stein, P. Padmanaban, Z. Zhang, J. Rouwkema, I. S. Khalil, and S. Misra, "Visualization of micro-agents and surroundings by real-time multicolor fluorescence microscopy," *Scientific Reports*, vol. 12, no. 1, p. 13375, 2022.

[46] J. J. Huaroto, L. Capuano, M. Kaya, I. Hlukhau, F. Assayag, S. Mohanty, G.-w. Römer, and S. Misra, "Two-photon microscopy for microrobotics: Visualization of micro-agents below fixed tissue," *PLoS ONE*, vol. 18, no. 8, p. e0289725, 2023.

[47] T. Xu, J. Yu, X. Yan, H. Choi, and L. Zhang, "Magnetic actuation based motion control for microrobots: An overview," *Micromachines*, vol. 6, no. 9, pp. 1346–1364, 2015.

[48] B. Herman, *Fluorescence microscopy*. Garland Science, 2020.

[49] D. J. Griffiths, *Introduction to electrodynamics*. Cambridge University Press, 2023.

[50] M. Sauer, J. Hofkens, and J. Enderlein, *Handbook of fluorescence spectroscopy and imaging: from ensemble to single molecules*. John Wiley & Sons, 2010.

[51] M. Sitti and D. S. Wiersma, "Pros and cons: Magnetic versus optical microrobots," *Advanced Materials*, vol. 32, no. 20, p. 1906766, 2020.

[52] A. J. Petruska, J. Edelmann, and B. J. Nelson, "Model-based calibration for magnetic manipulation," *IEEE Trans. Magn.*, vol. 53, no. 7, pp. 1–6, 2017.

[53] W. Wei, L. Yang, X. Zhang, G. Ling, and P. Zhang, "Combining soft and hard properties: Synergistic innovation of magnetic hydrogel microrobots in precision medicine," *Small*, vol. 22, no. 21, p. e14867, 2026.

[54] A. J. Petruska and B. J. Nelson, "Minimum bounds on the number of electromagnets required for remote magnetic manipulation," *IEEE Trans. Robot.*, vol. 31, no. 3, pp. 714–722, 2015.

[55] L.-J. W. Ligtenberg, N. C. Rabou, C. Goulas, W. C. Duinmeijer, F. R. Halfwerk, J. Arens, R. Lomme, V. Magdanz, A. Klingner, E. A. Klein Rot *et al.*, "Ex vivo validation of magnetically actuated intravascular untethered robots in a clinical setting," *Communications Engineering*, vol. 3, no. 1, p. 68, 2024.

[56] Z. Zhang, B. Lin, A. Klingner, G. Feng, Y. Liao, J. Guo, W. Xue, F. Li, W. Geng, S. Misra, and I. S.M.Khalil, "Study on worst-case gradient forces on untethered magnetic devices using two synchronized rotating magnetic dipoles," *IEEE Magnetics Letters*, vol. 17, pp. 1–5, 2026.

[57] C. Heunis, J. Sikorski, and S. Misra, "Flexible instruments for endovascular interventions: Improved magnetic steering, actuation, and image-guided surgical instruments," *IEEE Robotics & Automation Magazine*, vol. 25, no. 3, pp. 71–82, 2018.

[58] R. Chen, D. Folio, and A. Ferreira, "Analysis and comparison of electromagnetic microrobotic platforms for biomedical applications," *Appl. Sci.*, vol. 12, no. 1, p. 456, 2022.

[59] J. J. Abbott, K. E. Peyer, M. Cosentino Lagomarsino, L. Zhang, L. Dong, I. K. Kaliakatsos, and B. J. Nelson, "How should microrobots swim?" *The International Journal of Robotics Research*, vol. 28, no. 11–12, pp. 1434–1447, 2009.

[60] O. Cugat, J. Delamare, and G. Reyne, "Magnetic micro-actuators and systems (MAGMAS)," *IEEE Transactions on Magnetics*, vol. 39, no. 6, pp. 3607–3612, 2003.

[61] D. Jin and L. Zhang, "Collective behaviors of magnetic active matter: Recent progress toward reconfigurable, adaptive, and multifunctional swarming micro/nanorobots," *Accounts of Chemical Research*, vol. 55, no. 1, pp. 98–109, 2021.

[62] G. Gardi, S. Ceron, W. Wang, K. Petersen, and M. Sitti, "Microrobot collectives with reconfigurable morphologies, behaviors, and functions," *Nature Communications*, vol. 13, no. 1, p. 2239, 2022.

[63] H. Xie, M. Sun, X. Fan, Z. Lin, W. Chen, L. Wang, L. Dong, and Q. He, "Reconfigurable magnetic microrobot swarm: Multimode transformation, locomotion, and manipulation," *Science Robotics*, vol. 4, no. 28, p. eaav8006, 2019.

[64] X. Dong and M. Sitti, "Controlling two-dimensional collective formation and cooperative behavior of magnetic microrobot swarms," *The International Journal of Robotics Research*, vol. 39, no. 5, pp. 617–638, 2020.

[65] D. Ahmed, A. Sukhov, D. Hauri, D. Rodrigue, G. Maranta, J. Harting, and B. J. Nelson, "Bioinspired acousto-magnetic microswarm robots with upstream motility," *Nature Machine Intelligence*, vol. 3, no. 2, pp. 116–124, 2021.

[66] J. W. Lichtman and J.-A. Conchello, "Fluorescence microscopy," *Nature methods*, vol. 2, no. 12, pp. 910–919, 2005.

[67] A. Hawe, M. Sutter, and W. Jiskoot, "Extrinsic fluorescent dyes as tools for protein characterization," *Pharmaceutical research*, vol. 25, no. 7, pp. 1487–1499, 2008.

[68] R. A. Velapoldi and H. H. Tønnesen, "Corrected emission spectra and quantum yields for a series of fluorescent compounds in the visible spectral region," *Journal of fluorescence*, vol. 14, pp. 465–472, 2004.

[69] M. Yang, X. Guo, F. Mou, and J. Guan, "Lighting up micro-/nanorobots with fluorescence," *Chemical Reviews*, vol. 123, no. 7, pp. 3944–3975, 2022.

[70] F. Helmchen and W. Denk, "Deep tissue two-photon microscopy," *Nature Methods*, vol. 2, no. 12, pp. 932–940, 2005.

[71] J. J. Field, R. Carriles, K. E. Sheetz, E. V. Chandler, E. E. Hoover, S. E. Tillo, T. E. Hughes, A. W. Sylvester, D. Kleinfeld, and J. A. Squier, "Optimizing the fluorescent yield in two-photon laser scanning microscopy with dispersion compensation," *Optics Express*, vol. 18, no. 13, pp. 13 661–13 672, 2010.

[72] P. Luu, S. E. Fraser, and F. Schneider, "More than double the fun with two-photon excitation microscopy," *Communications Biology*, vol. 7, no. 1, p. 364, 2024.

[73] M. Müller, J. Squier, and G. Brakenhoff, "Measurement of femtosecond pulses in the focal point of a high-numerical-aperture lens by two-photon absorption," *Optics Letters*, vol. 20, no. 9, pp. 1038–1040, 1995.

[74] M. Kaya, F. Stein, J. Rouwkema, I. S. Khalil, and S. Misra, "Serial imaging of micro-agents and cancer cell spheroids in a microfluidic channel using multicolor fluorescence microscopy," *PLoS ONE*, vol. 16, no. 6, p. e0253222, 2021.

[75] N. Keshava, "A survey of spectral unmixing algorithms," *Lincoln laboratory journal*, vol. 14, no. 1, pp. 55–78, 2003.

[76] C. Xu and W. W. Webb, "Measurement of two-photon excitation cross sections of molecular fluorophores with data from 690 to 1050

nm," *Journal of the Optical Society of America B*, vol. 13, no. 3, pp. 481–491, 1996.

[77] M. Zhou, M. P. Gomes, A. Elgersma, H. I. Korkmaz, B. K. Boekema, and M. L. Groot, "Multiscale investigation of collagen structure in human skin and gel matrices using polarization resolved second harmonic generation microscopy," *Scientific Reports*, vol. 15, no. 1, p. 20025, 2025.

[78] O. I. Kolenc and K. P. Quinn, "Evaluating cell metabolism through autofluorescence imaging of nad(p)h and fad," *Antioxidants & redox signaling*, vol. 30, no. 6, pp. 875–889, 2019.

[79] E. B. Steager, M. Selman Sakar, C. Magee, M. Kennedy, A. Cowley, and V. Kumar, "Automated biomanipulation of single cells using magnetic microrobots," *The International Journal of Robotics Research*, vol. 32, no. 3, pp. 346–359, 2013.

[80] P. S.-P. Thong, M. Olivo, S. S. Tandjung, M. M. Movania, F. Lin, K. Qian, H.-S. Seah, and K.-C. Soo, "Review of confocal fluorescence endomicroscopy for cancer detection," *IEEE Journal of Selected Topics in Quantum Electronics*, vol. 18, no. 4, pp. 1355–1366, 2011.

[81] V. Kučikas, M. P. Werner, T. Schmitz-Rode, F. Louradour, and M. A. M. J. van Zandvoort, "Two-photon endoscopy: State of the art and perspectives," *Molecular Imaging and Biology*, vol. 25, no. 1, pp. 3–17, 2023.

[82] N. D. Pilonis, W. Januszewicz, and M. di Pietro, "Confocal laser endomicroscopy in gastro-intestinal endoscopy: technical aspects and clinical applications," *Translational gastroenterology and hepatology*, vol. 7, p. 7, 2022.

[83] J. A. Stibbe, P. Hoogland, F. B. Achterberg, D. R. Holman, R. S. Sojwal, J. Burggraaf, A. L. Vahrmeijer, W. B. Nagengast, and S. Rogalla, "Highlighting the undetectable—fluorescence molecular imaging in gastrointestinal endoscopy," *Molecular Imaging and Biology*, vol. 25, no. 1, pp. 18–35, 2023.

[84] B. D. Matthews, D. A. LaVan, D. R. Overby, J. Karavitis, and D. E. Ingber, "Electromagnetic needles with submicron pole tip radii for nanomanipulation of biomolecules and living cells," *Appl. Phys. Lett.*, vol. 85, no. 14, pp. 2968–2970, 2004.

[85] J. Sikorski, S. Mohanty, and S. Misra, "MILiMAC: Flexible catheter with miniaturized electromagnets as a small-footprint system for microrobotic tasks," *IEEE Robot. Autom. Lett.*, vol. 5, no. 4, pp. 5260–5267, 2020.

[86] J.-A. Seon, Z. Cenev, and Q. Zhou, "Automatic noncontact extraction and independent manipulation of magnetic particles using electromagnetic needle," *IEEE/ASME Trans. Mechatron.*, vol. 25, no. 2, pp. 931–941, 2019.

[87] O. Işıtman, H. Bettahar, and Q. Zhou, "Non-contact cooperative manipulation of magnetic microparticles using two robotic electromagnetic needles," *IEEE Robot. Autom. Lett.*, vol. 7, no. 2, pp. 1605–1611, 2021.

[88] J. V. Timonen, M. Latikka, L. Leibler, R. H. Ras, and O. Ikkala, "Switchable static and dynamic self-assembly of magnetic droplets on superhydrophobic surfaces," *Science*, vol. 341, no. 6143, pp. 253–257, 2013.

[89] Q. Wang, L. Yang, B. Wang, E. Yu, J. Yu, and L. Zhang, "Collective behavior of reconfigurable magnetic droplets via dynamic self-assembly," *ACS Applied Materials & Interfaces*, vol. 11, no. 1, pp. 1630–1637, 2018.

[90] K. Ni and Z. Wang, "Recent progress on the development of magnetically-responsive micropillars: Actuation, fabrication, and applications," *Advanced Functional Materials*, vol. 33, no. 14, p. 2213350, 2023.

[91] E. Diller, J. Giltinan, P. Jena, and M. Sitti, "Three dimensional independent control of multiple magnetic microrobots," in *Proceedings of the 2013 IEEE International Conference on Robotics and Automation*. IEEE, 2013, pp. 2576–2581.

[92] F. Ongaro, S. Pane, S. Scheggi, and S. Misra, "Design of an electromagnetic setup for independent three-dimensional control of pairs of identical and nonidentical microrobots," *IEEE Trans. Robot.*, vol. 35, no. 1, pp. 174–183, 2019.

[93] C. M. Browning, S. Mayes, S. A. Mayes, T. C. Rich, and S. J. Leavesley, "Microscopy is better in color: development of a streamlined spectral light path for real-time multiplex fluorescence microscopy," *Biomedical Optics Express*, vol. 13, no. 7, pp. 3751–3772, 2022.

[94] W.-Y. Oh, S. Yun, B. Vakoc, M. Shishkov, A. Desjardins, B. Park, J. De Boer, G. Tearney, and B. Bouma, "High-speed polarization sensitive optical frequency domain imaging with frequency multiplexing," *Optics express*, vol. 16, no. 2, pp. 1096–1103, 2008.

[95] Y. Jiang, H. Sha, S. Liu, P. Qin, and Y. Zhang, "Autounmix: an autoencoder-based spectral unmixing method for multi-color fluorescence microscopy imaging," *Biomedical Optics Express*, vol. 14, no. 9, pp. 4814–4827, 2023.

[96] H. Wang, Y. Rivenson, Y. Jin, Z. Wei, R. Gao, H. Günaydın, L. A. Bentolila, C. Kural, and A. Ozcan, "Deep learning enables cross-modality super-resolution in fluorescence microscopy," *Nature methods*, vol. 16, no. 1, pp. 103–110, 2019.

[97] N. Masoumi, H. Rivaz, I. Hacihaliloglu, M. O. Ahmad, I. Reinertsen, and Y. Xiao, "The big bang of deep learning in ultrasound-guided surgery: a review," *IEEE Transactions on Ultrasonics, Ferroelectrics, and Frequency Control*, 2023.

[98] B. Wang, K. F. Chan, K. Yuan, Q. Wang, X. Xia, L. Yang, H. Ko, Y.-X. J. Wang, J. J. Y. Sung, P. W. Y. Chiu *et al.*, "Endoscopy-assisted magnetic navigation of biohybrid soft microrobots with rapid endoluminal delivery and imaging," *Sci. Robot.*, vol. 6, no. 52, p. eabd2813, 2021.

[99] A. Li, H. Guan, H.-C. Park, Y. Yue, D. Chen, W. Liang, M.-J. Li, H. Lu, and X. Li, "Twist-free ultralight two-photon fiberscope enabling neuroimaging on freely rotating/walking mice," *Optica*, vol. 8, no. 6, pp. 870–879, 2021.

[100] W. Liang, D. Chen, H. Guan, H.-C. Park, K. Li, A. Li, M.-J. Li, I. Gannot, and X. Li, "Label-free metabolic imaging in vivo by two-photon fluorescence lifetime endomicroscopy," *ACS Photonics*, vol. 9, no. 12, pp. 4017–4029, 2022.

[101] S. Ornes, "Inner workings: Medical microrobots have potential in surgery, therapy, imaging, and diagnostics," *Proc. Natl. Acad. Sci.*, vol. 114, no. 47, pp. 12 356–12 358, 2017.

[102] B. Sun, G. Wood, and S. Miyashita, "Milestones for autonomous in vivo microrobots in medical applications," *Surgery*, vol. 169, no. 4, pp. 755–758, 2021.

[103] O. Erin, X. Liu, J. Ge, J. Opfermann, Y. Barnoy, L. O. Mair, J. U. Kang, W. Gensheimer, I. N. Weinberg, Y. Diaz-Mercado *et al.*, "Overcoming the force limitations of magnetic robotic surgery: Magnetic pulse actuated collisions for tissue-penetrating-needle for tetherless interventions," *Adv. Intell. Syst.*, vol. 4, no. 6, p. 2200072, 2022.

[104] S. Mohanty, A. Paul, P. M. Matos, J. Zhang, J. Sikorski, and S. Misra, "CeFlowBot: A biomimetic flow-driven microrobot that navigates under magneto-acoustic fields," *Small*, vol. 18, no. 9, p. 2105829, 2022.

[105] F. N. Piñan Basualdo, A. Bolopion, M. Gauthier, and P. Lambert, "A microrobotic platform actuated by thermocapillary flows for manipulation at the air-water interface," *Sci. Robot.*, vol. 6, no. 52, p. eabd3557, 2021.

[106] S. Lee, J.-Y. Kim, J. Kim, A. K. Hoshiar, J. Park, S. Lee, J. Kim, S. Pané, B. J. Nelson, and H. Choi, "A needle-type microrobot for targeted drug delivery by affixing to a microtissue," *Adv. Healthc. Mater.*, vol. 9, no. 7, p. 1901697, 2020.

[107] G. Z. Lum, Z. Ye, X. Dong, H. Marvi, O. Erin, W. Hu, and M. Sitti, "Shape-programmable magnetic soft matter," *Proc. Natl. Acad. Sci.*, vol. 113, no. 41, pp. E6007–E6015, 2016.

[108] E. Diller, J. Giltinan, G. Z. Lum, Z. Ye, and M. Sitti, "Six-degree-of-freedom magnetic actuation for wireless microrobotics," *Int. J. Robot. Res.*, vol. 35, no. 1-3, pp. 114–128, 2016.

[109] Q. Wang, L. Yang, and L. Zhang, "Micromanipulation using reconfigurable self-assembled magnetic droplets with needle guidance," *IEEE Trans. Autom. Sci. Eng.*, vol. 19, no. 2, pp. 759–771, 2021.

[110] H. Lee, A. Purdon, and R. Westervelt, "Manipulation of biological cells using a microelectromagnet matrix," *Appl. Phys. Lett.*, vol. 85, no. 6, pp. 1063–1065, 2004.

[111] B. Panigrahi, C.-H. Lu, N. Ghayal, and C.-Y. Chen, "Sperm activation through orbital and self-axis revolutions using an artificial cilia embedded serpentine microfluidic platform," *Sci. Rep.*, vol. 8, no. 1, pp. 1–9, 2018.

[112] Q. Jin, Y. Yang, J. A. Jackson, C. Yoon, and D. H. Gracias, "Untethered single cell grippers for active biopsy," *Nano Lett.*, vol. 20, no. 7, pp. 5383–5390, 2020.

[113] M. Richter, V. K. Venkiteswaran, and S. Misra, "Multi-point orientation control of discretely-magnetized continuum manipulators," *IEEE Robot. Autom. Lett.*, vol. 6, no. 2, pp. 3607–3614, 2021.

[114] M. P. Kummer, J. J. Abbott, B. E. Kratochvil, R. Borer, A. Sengul, and B. J. Nelson, "Octomag: An electromagnetic system for 5-dof wireless micromanipulation," *IEEE Trans. Robot.*, vol. 26, no. 6, pp. 1006–1017, 2010.

[115] F. Niu, J. Li, W. Ma, J. Yang, and D. Sun, "Development of an enhanced electromagnetic actuation system with enlarged workspace," *IEEE/ASME Trans. Mechatron.*, vol. 22, no. 5, pp. 2265–2276, 2017.

[116] L. Yang, X. Du, E. Yu, D. Jin, and L. Zhang, "Deltamag: An electromagnetic manipulation system with parallel mobile coils," in *Proceedings of the 2019 International Conference on Robotics and Automation (ICRA)*. IEEE, 2019, pp. 9814–9820.

[117] B. V. Johnson, N. Esantsi, and D. J. Cappelleri, "Design of the μMAZE platform and microrobots for independent control and micromanipulation tasks," *IEEE Robot. Autom. Lett.*, vol. 5, no. 4, pp. 5677–5684, 2020.

[118] Y. Xiang, J. Miller, V. Sica, and D. A. LaVan, "Optimization of force produced by electromagnet needles acting on superparamagnetic microparticles," *Appl. Phys. Lett.*, vol. 92, no. 12, p. 124104, 2008.

[119] J. Sikorski, C. M. Heunis, F. Franco, and S. Misra, "The ARMM system: An optimized mobile electromagnetic coil for non-linear actuation of flexible surgical instruments," *IEEE Trans. Magn.*, vol. 55, no. 9, pp. 1–9, 2019.

[120] S. A. Sapareto and W. C. Dewey, "Thermal dose determination in cancer therapy," *International Journal of Radiation Oncology, Biology, Physics*, vol. 10, no. 6, pp. 787–800, 1984.

[121] International Electrotechnical Commission, "IEC 60601-1:2005+AMD1:2012 Medical electrical equipment – Part 1: General requirements for basic safety and essential performance," 2012.

[122] F. Suligoj, C. M. Heunis, J. Sikorski, and S. Misra, "RobUSt–an autonomous robotic ultrasound system for medical imaging," *IEEE Access*, vol. 9, pp. 67 456–67 465, 2021.

[123] G. M. Whitesides and B. Grzybowski, "Self-assembly at all scales," *Science*, vol. 295, no. 5564, pp. 2418–2421, 2002.

[124] T. Vicsek and A. Zafeiris, "Collective motion," *Physics Reports*, vol. 517, no. 3-4, pp. 71–140, 2012.

[125] A. Okubo, "Dynamical aspects of animal grouping: swarms, schools, flocks, and herds," *Advances in Biophysics*, vol. 22, pp. 1–94, 1986.

[126] J. L. Deneubourg, S. Aron, S. Goss, J. Pasteels, and G. Duerinck, "Random behaviour, amplification processes and number of participants: how they contribute to the foraging properties of ants," *Physica D: Nonlinear Phenomena*, vol. 22, no. 1-3, pp. 176–186, 1986.

[127] H. Mori, "Transport, collective motion, and brownian motion," *Progress of Theoretical Physics*, vol. 33, no. 3, pp. 423–455, 1965.

[128] V. Liljeström, C. Chen, P. Dommersnes, J. O. Fossum, and A. H. Gröschel, "Active structuring of colloids through field-driven self-assembly," *Current Opinion in Colloid & Interface Science*, vol. 40, pp. 25–41, 2019.

[129] M. Rubenstein, C. Ahler, and R. Nagpal, "Kilobot: A low cost scalable robot system for collective behaviors," in *in Proceedings of IEEE International Conference on Robotics and Automation*. IEEE, 2012, pp. 3293–3298.

[130] J. Werfel, K. Petersen, and R. Nagpal, "Designing collective behavior in a termite-inspired robot construction team," *Science*, vol. 343, no. 6172, pp. 754–758, 2014.

[131] J. Elgeti, R. G. Winkler, and G. Gompper, "Physics of microswimmers—single particle motion and collective behavior: a review," *Reports on Progress in Physics*, vol. 78, no. 5, p. 056601, 2015.

[132] S. Yang, Q. Wang, D. Jin, X. Du, and L. Zhang, "Probing fast transformation of magnetic colloidal microswarms in complex fluids," *ACS Nano*, vol. 16, no. 11, pp. 19 025–19 037, 2022.

[133] Z. Xu and Q. Xu, "Collective behaviors of magnetic microparticle swarms: From dexterous tentacles to reconfigurable carpets," *ACS Nano*, vol. 16, no. 9, pp. 13 728–13 739, 2022.

[134] L. Yang, J. Yu, S. Yang, B. Wang, B. J. Nelson, and L. Zhang, "A survey on swarm microrobotics," *IEEE Transactions on Robotics*, vol. 38, no. 3, pp. 1531–1551, 2021.

[135] Z. Xu, Z. Wu, M. Yuan, H. Chen, W. Ge, and Q. Xu, "Multiple cilia-like swarms enable efficient microrobot deployment and execution," *Cell Reports Physical Science*, vol. 4, no. 3, p. 101329, 2023.

[136] Q. Zhou, V. Sariola, K. Latifi, and V. Liimatainen, "Controlling the motion of multiple objects on a chladni plate," *Nature communications*, vol. 7, no. 1, p. 12764, 2016.

[137] W. Liu, H. Gao, K. Liu, D. Lei, K. Pei, and G. Hu, "A review on particle assembly in standing wave acoustic field," *Journal of Nanoparticle Research*, vol. 24, no. 4, p. 81, 2022.

[138] D. Hu, Y. Wang, J. Liu, Y. Mao, X. Chang, and Y. Zhu, "Light-driven sequential shape transformation of block copolymer particles through three-dimensional confined self-assembly," *Nanoscale*, vol. 14, no. 17, pp. 6291–6298, 2022.

[139] J. H. Kim, S. M. Kang, B. J. Lee, H. Ko, W.-G. Bae, K. Y. Suh, M. K. Kwak, and H. E. Jeong, "Remote manipulation of droplets on a flexible magnetically responsive film," *Scientific Reports*, vol. 5, no. 1, p. 17843, 2015.

[140] M. Sun, X. Fan, C. Tian, M. Yang, L. Sun, and H. Xie, "Swarming microdroplets to a dexterous micromanipulator," *Advanced Functional Materials*, vol. 31, no. 19, p. 2011193, 2021.

[141] M. Akter, J. Keya, K. Kayano, A. Kabir, D. Inoue, H. Hess, K. Sada, A. Kuzuya, H. Asanuma, and A. Kakugo, "Cooperative cargo transportation by a swarm of molecular machines," *Science Robotics*, vol. 7, no. 65, p. eabm0677, 2022.

[142] X. Dong, G. Z. Lum, W. Hu, R. Zhang, Z. Ren, P. R. Onck, and M. Sitti, "Bioinspired cilia arrays with programmable nonreciprocal motion and metachronal coordination," *Science Advances*, vol. 6, no. 45, p. eabc9323, 2020.

[143] A. F. Demirörs, S. Aykut, S. Ganzeboom, Y. A. Meier, R. Hardeman, J. de Graaf, A. J. Mathijssen, E. Poloni, J. A. Carpenter, C. Ünlü *et al.*, "Amphibious transport of fluids and solids by soft magnetic carpets," *Advanced Science*, vol. 8, no. 21, p. 2102510, 2021.

[144] J. Miao, T. Zhang, G. Li, W. Shang, and Y. Shen, "Magnetic artificial cilia carpets for transport, mixing, and directional diffusion," *Advanced Engineering Materials*, vol. 24, no. 7, p. 2101399, 2022.

[145] S. Sohn, H. Lee, H. Kee, and S. Park, "Reprogrammable magnetically actuated self-assembled cilia array," *Advanced Intelligent Systems*, vol. 5, no. 1, p. 2200227, 2023.

[146] Z. Ren, M. Zhang, S. Song, Z. Liu, C. Hong, T. Wang, X. Dong, W. Hu, and M. Sitti, "Soft-robotic ciliated epidermis for reconfigurable coordinated fluid manipulation," *Science Advances*, vol. 8, no. 34, p. eabq2345, 2022.

[147] Z. Cui, Y. Wang, S. Zhang, T. Wang, and J. M. den Toonder, "Miniaturized metachronal magnetic artificial cilia," *Proceedings of the National Academy of Sciences*, vol. 120, no. 35, p. e2304519120, 2023.

[148] Y. Collard, F. N. Piñan Basualdo, A. Bolopion, M. Gauthier, P. Lambert, and N. Vandewalle, "Controlled transitions between metastable states of 2d magnetocapillary crystals," *Scientific Reports*, vol. 12, no. 1, p. 16027, 2022.

[149] F. N. Piñan Basualdo and S. Misra, "Collaborative magnetic agents for 3d microrobotic grasping," *Advanced Intelligent Systems*, 2023.

[150] B. Yigit, Y. Alapan, and M. Sitti, "Programmable collective behavior in dynamically self-assembled mobile microrobotic swarms," *Advanced Science*, vol. 6, no. 6, p. 1801837, 2019.

[151] Y. Collard, G. Grosjean, and N. Vandewalle, "Magnetically powered metachronal waves induce locomotion in self-assemblies," *Communications Physics*, vol. 3, no. 1, p. 112, 2020.

[152] L. Wang, J. Wang, J. Hao, Z. Dong, J. Wu, G. Shen, T. Ying, L. Feng, X. Cai, Z. Liu *et al.*, "Guiding drug through interrupted bloodstream for potentiated thrombolysis by c-shaped magnetic actuation system in vivo," *Advanced Materials*, vol. 33, no. 51, p. 2105351, 2021.

[153] F. Ongaro, C. M. Heunis, and S. Misra, "Precise model-free spline-based approach for magnetic field mapping," *IEEE Magnetics Letters*, vol. 10, pp. 1–5, 2018.

[154] S. Andersson-Engels, J. Johansson, and S. Svanberg, "Multicolor fluorescence imaging system for tissue diagnostics," in *Bioimaging and Two-Dimensional Spectroscopy*, vol. 1205. SPIE, 1990, pp. 179–189.

[155] P. P. Laissue, R. A. Alghamdi, P. Tomancak, E. G. Reynaud, and H. Shroff, "Assessing phototoxicity in live fluorescence imaging," *Nature methods*, vol. 14, no. 7, pp. 657–661, 2017.

[156] N. Senthilnathan, C. M. Oral, A. Novobilsky, and M. Pumera, "Intelligent magnetic microrobots with fluorescent internal memory for monitoring intragastric acidity," *Advanced Functional Materials*, vol. 34, no. 29, p. 2401463, 2024.

[157] Y. Wang, J. Shen, S. Handschuh-Wang, M. Qiu, S. Du, and B. Wang, "Microrobots for targeted delivery and therapy in digestive system," *ACS Nano*, 2022.

[158] Y. Zhang, L. Zhang, L. Yang, C. I. Vong, K. F. Chan, W. K. Wu, T. N. Kwong, N. W. Lo, M. Ip, S. H. Wong *et al.*, "Real-time tracking of fluorescent magnetic spore–based microrobots for remote detection of c. diff toxins," *Science Advances*, vol. 5, no. 1, p. eaau9650, 2019.

[159] A. Neettiyath and M. Pumera, "Micro/nanorobots for advanced light-based biosensing and imaging," *Advanced Functional Materials*, vol. 35, no. 8, p. 2415875, 2025.

[160] A. Shakoor, T. Luo, S. Chen, M. Xie, J. K. Mills, and D. Sun, "A high-precision robot-aided single-cell biopsy system," in *2017 IEEE International Conference on Robotics and Automation (ICRA)*. IEEE, 2017, pp. 5397–5402.

[161] C. K. Schmidt, M. Medina-Sánchez, R. J. Edmondson, and O. G. Schmidt, "Engineering microrobots for targeted cancer therapies from a medical perspective," *Nature Communications*, vol. 11, no. 1, p. 5618, 2020.

[162] C. Xin, D. Jin, Y. Hu, L. Yang, R. Li, L. Wang, Z. Ren, D. Wang, S. Ji, K. Hu *et al.*, "Environmentally adaptive shape-morphing microrobots for localized cancer cell treatment," *ACS nano*, vol. 15, no. 11, pp. 18 048–18 059, 2021.

[163] H. Chen, Y. Li, Y. Wang, P. Ning, Y. Shen, X. Wei, Q. Feng, Y. Liu, Z. Li, C. Xu *et al.*, "An engineered bacteria-hybrid microrobot with the magnetothermal bioswitch for remotely collective perception and imaging-guided cancer treatment," *ACS nano*, vol. 16, no. 4, pp. 6118–6133, 2022.

[164] M. M. Frigault, J. Lacoste, J. L. Swift, and C. M. Brown, "Live-cell microscopy–tips and tools," *Journal of cell science*, vol. 122, no. 6, pp. 753–767, 2009.

[165] A. Stylianou, V. Gkretsi, V. Huntošová, and A. Theodosiou, "Fluorescence microscopy of the cell and cell interactions to study dynamic cellular processes," in *Bioimaging in Tissue Engineering and Regeneration: Advanced Microscopy and Preclinical Imaging*. Springer, 2024, pp. 1–28.

[166] S. Mukhtar, A. Arbabi, and J. Viegas, "Advances in spectral imaging: A review of techniques and technologies," *IEEE Access*, 2025.

[167] J. Ohn, J. Yang, S. E. Fraser, R. Lansford, and M. Liebling, "High-speed multicolor microscopy of repeating dynamic processes," *genesis*, vol. 49, no. 7, pp. 514–521, 2011.

[168] T. Zimmermann, *Spectral Imaging and Linear Unmixing in Light Microscopy*. Berlin, Heidelberg: Springer Berlin Heidelberg, 2005, pp. 245–265.

[169] Y. Fu, Y. Zheng, H. Huang, I. Sato, and Y. Sato, "Hyperspectral image super-resolution with a mosaic rgb image," *IEEE Transactions on Image Processing*, vol. 27, no. 11, pp. 5539–5552, 2018.

[170] L. Uguen, R. Piedevache, G. Russias, S. Helmer, D. Tregoat, and S. Perrin, "Single-pixel-based hyperspectral microscopy," *Applied Physics Letters*, vol. 125, no. 7, 2024.

[171] Z. Wei, K. Wu, Y. Qin, H. Cheng, and C. Gu, "Dual-type hyperspectral microscopic imaging system based on fourier transform imaging spectrometer," in *Fifteenth International Conference on Information Optics and Photonics (CIOP 2024)*, vol. 13418. SPIE, 2024, pp. 617–621.

[172] M. M. Antony, C. S. Sandeep, and M. V. Matham, "Hyperspectral vision beyond 3d: A review," *Optics and Lasers in Engineering*, vol. 178, p. 108238, 2024.

[173] Q. Li, Y. Yang, M. Tan, H. Xia, Y. Peng, X. Fu, Y. Huang, and X. Ma, "Rapid detection of single bacteria using filter-array-based hyperspectral imaging technology," *Analytical Chemistry*, vol. 96, no. 43, pp. 17 244–17 252, 2024.

[174] Q. Lv, K. Liang, C. Tian, Y. Zhang, Y. Li, J. Deng, W. Yue, and W. Li, "Unveiling thymoma typing through hyperspectral imaging and deep learning," *Journal of Biophotonics*, vol. 17, no. 11, p. e202400325, 2024.

[175] Y. Shechtman, L. E. Weiss, A. S. Backer, M. Y. Lee, and W. Moerner, "Multicolour localization microscopy by point-spread-function engineering," *Nature photonics*, vol. 10, no. 9, pp. 590–594, 2016.

[176] C. Yang, V. Hou, L. Y. Nelson, and E. J. Seibel, "Mitigating fluorescence spectral overlap in wide-field endoscopic imaging," *Journal of Biomedical Optics*, vol. 18, no. 8, pp. 086 012–086 012, 2013.

[177] J. Mao and H. He, "Deep learning in fluorescence imaging and analysis," *Journal of Intelligent Medicine*, vol. 1, no. 1, pp. 42–62, 2024.

[178] H. Zhuge, B. Summa, J. Hamm, and J. Q. Brown, "Deep learning 2d and 3d optical sectioning microscopy using cross-modality pix2pix cgan image translation," *Biomedical Optics Express*, vol. 12, no. 12, pp. 7526–7543, 2021.

[179] C. Bouchard, T. Wiesner, A. Deschênes, A. Bilodeau, B. Turcotte, C. Gagné, and F. Lavoie-Cardinal, "Resolution enhancement with a task-assisted gan to guide optical nanoscopy image analysis and acquisition," *Nature Machine Intelligence*, vol. 5, no. 8, pp. 830–844, 2023.

[180] P. Isola, J.-Y. Zhu, T. Zhou, and A. A. Efros, "Image-to-image translation with conditional adversarial networks," in *Proceedings of the IEEE conference on computer vision and pattern recognition*, 2017, pp. 1125–1134.

[181] E. Hershko, L. E. Weiss, T. Michaeli, and Y. Shechtman, "Multicolor localization microscopy and point-spread-function engineering by deep learning," *Optics express*, vol. 27, no. 5, pp. 6158–6183, 2019.

[182] S. Liu, W. Zou, H. Sha, X. Feng, B. Chen, J. Zhang, S. Han, X. Li, and Y. Zhang, "Deep learning-enhanced snapshot hyperspectral confocal microscopy imaging system," *Optics Express*, vol. 32, no. 8, pp. 13 918–13 931, 2024.

[183] H. Sha, H. Li, Y. Zhang, and S. Hou, "Deep learning-enhanced single-molecule spectrum imaging," *Apl Photonics*, vol. 8, no. 9, 2023.

[184] B. Dai, S. You, K. Wang, Y. Long, J. Chen, N. Upreti, J. Peng, L. Zheng, C. Chang, T. J. Huang *et al.*, "Deep learning–enabled

filter-free fluorescence microscope," *Science Advances*, vol. 11, no. 1, p. eadq2494, 2025.

[185] O. Ronneberger, P. Fischer, and T. Brox, "U-net: Convolutional networks for biomedical image segmentation," in *Medical image computing and computer-assisted intervention–MICCAI 2015: 18th international conference, Munich, Germany, October 5-9, 2015, proceedings, part III 18*. Springer, 2015, pp. 234–241.

[186] N. C. Shaner, P. A. Steinbach, and R. Y. Tsien, "A guide to choosing fluorescent proteins," *Nature methods*, vol. 2, no. 12, pp. 905–909, 2005.

[187] A. Hoppe, K. Christensen, and J. A. Swanson, "Fluorescence resonance energy transfer-based stoichiometry in living cells," *Biophysical journal*, vol. 83, no. 6, pp. 3652–3664, 2002.

[188] D. Qin, Y. Xia, and G. M. Whitesides, "Soft lithography for micro- and nanoscale patterning," *Nature protocols*, vol. 5, no. 3, p. 491, 2010.

[189] B. Jung, V. I. Vullev, and B. Anvari, "Revisiting indocyanine green: effects of serum and physiological temperature on absorption and fluorescence characteristics," *IEEE Journal of Selected Topics in Quantum Electronics*, vol. 20, no. 2, pp. 149–157, 2013.

[190] B. J. Nelson, I. K. Kaliakatsos, and J. J. Abbott, "Microrobots for minimally invasive medicine," *Annual Review of Biomedical Engineering*, vol. 12, pp. 55–85, 2010.

[191] H. Ceylan, I. C. Yasa, U. Kilic, W. Hu, and M. Sitti, "Translational prospects of untethered medical microrobots," *Progress in Biomedical Engineering*, vol. 1, no. 1, p. 012002, 2019.

[192] A.-I. Bunea and R. Taboryski, "Recent advances in microswimmers for biomedical applications," *Micromachines*, vol. 11, no. 12, p. 1048, 2020.

[193] M. Kaynak, P. Dirix, and M. S. Sakar, "Addressable acoustic actuation of 3d printed soft robotic microsystems," *Advanced Science*, vol. 7, no. 20, p. 2001120, 2020.

[194] D. Li, C. Liu, Y. Yang, L. Wang, and Y. Shen, "Micro-rocket robot with all-optic actuating and tracking in blood," *Light: Science & Applications*, vol. 9, no. 1, p. 84, 2020.

[195] P. Wrede, O. Degtyaruk, S. K. Kalva, X. L. Deán-Ben, U. Bozuyuk, A. Aghakhani, B. Akolpoglu, M. Sitti, and D. Razansky, "Real-time 3d optoacoustic tracking of cell-sized magnetic microrobots circulating in the mouse brain vasculature," *Science Advances*, vol. 8, no. 19, p. eabm9132, 2022.

[196] A. Aziz, R. Nauber, A. S. Iglesias, M. Tang, L. Ma, L. M. Liz-Marzán, O. G. Schmidt, and M. Medina-Sánchez, "Nanomaterial-decorated micromotors for enhanced photoacoustic imaging," *Journal of Micro and Bio Robotics*, vol. 19, no. 1, pp. 37–45, 2023.

[197] H.-C. Park, H. Guan, A. Li, Y. Yue, M.-J. Li, H. Lu, and X. Li, "High-speed fiber-optic scanning nonlinear endomicroscopy for imaging neuron dynamics in vivo," *Optics Letters*, vol. 45, no. 13, pp. 3605–3608, 2020.

[198] X. Yang, W. Shang, H. Lu, Y. Liu, L. Yang, R. Tan, X. Wu, and Y. Shen, "An agglutinate magnetic spray transforms inanimate objects into millirobots for biomedical applications," *Science robotics*, vol. 5, no. 48, p. eabc8191, 2020.

[199] V. Iacovacci, A. Blanc, H. Huang, L. Ricotti, R. Schibli, A. Menciassi, M. Behe, S. Pané, and B. J. Nelson, "High-resolution spect imaging of stimuli-responsive soft microrobots," *Small*, vol. 15, no. 34, p. 1900709, 2019.

[200] D. Li, D. Dong, W. Lam, L. Xing, T. Wei, and D. Sun, "Automated in vivo navigation of magnetic-driven microrobots using oct imaging feedback," *IEEE Transactions on Biomedical Engineering*, vol. 67, no. 8, pp. 2349–2358, 2019.

[201] E. U. Saritas, P. W. Goodwill, L. R. Croft, J. J. Konkle, K. Lu, B. Zheng, and S. M. Conolly, "Magnetic particle imaging (mpi) for nmr and mri researchers," *Journal of Magnetic Resonance*, vol. 229, pp. 116–126, 2013.

[202] W. Choi, D. Oh, and C. Kim, "Practical photoacoustic tomography: realistic limitations and technical solutions," *Journal of Applied Physics*, vol. 127, no. 23, 2020.

[203] K. König, "Multiphoton microscopy in life sciences," *Journal of Microscopy*, vol. 200, no. 2, pp. 83–104, 2000.

[204] L. Abdeladim, K. S. Matho, S. Clavreul, P. Mahou, J.-M. Sintes, X. Solinas, I. Arganda-Carreras, S. G. Turney, J. W. Lichtman, A. Chessel *et al.*, "Multicolor multiscale brain imaging with chromatic multiphoton serial microscopy," *Nature Communications*, vol. 10, no. 1, pp. 1–14, 2019.

[205] W. R. Zipfel, R. M. Williams, R. Christie, A. Y. Nikitin, B. T. Hyman, and W. W. Webb, "Live tissue intrinsic emission microscopy using multiphoton-excited native fluorescence and second harmonic generation," *Proceedings of the National Academy of Sciences*, vol. 100, no. 12, pp. 7075–7080, 2003.

[206] J. Li, S. Thiele, B. C. Quirk, R. W. Kirk, J. W. Verjans, E. Akers, C. A. Bursill, S. J. Nicholls, A. M. Herkommer, H. Giessen *et al.*, "Ultrathin monolithic 3d printed optical coherence tomography endoscopy for preclinical and clinical use," *Light: Science & Applications*, vol. 9, no. 1, pp. 1–10, 2020.

[207] Q. Ji, J. Moughames, X. Chen, G. Fang, J. J. Huaroto, V. Laude, J. A. I. Martínez, G. Ulliac, C. Clévy, P. Lutz, K. Rabenorosoa, V. Guelpa, A. Spangenberg, J. Liang, A. Mosset, and M. Kadic, "4d thermomechanical metamaterials for soft microrobotics," *Communications Materials*, vol. 2, no. 1, pp. 1–6, 2021.

[208] S. R. Dabbagh, M. R. Sarabi, M. T. Birtek, S. Seyfi, M. Sitti, and S. Tasoglu, "3d-printed microrobots from design to translation," *Nature Communications*, vol. 13, no. 1, p. 5875, 2022.

[209] A. Accardo, M.-C. Blatché, R. Courson, I. Loubinoux, C. Thibault, L. Malaquin, and C. Vieu, "Multiphoton direct laser writing and 3d imaging of polymeric freestanding architectures for cell colonization," *Small*, vol. 13, no. 27, p. 1700621, 2017.

[210] M. Schmid, D. Ludescher, and H. Giessen, "Optical properties of photoresists for femtosecond 3d printing: refractive index, extinction, luminescence-dose dependence, aging, heat treatment and comparison between 1-photon and 2-photon exposure," *Optical Materials Express*, vol. 9, no. 12, pp. 4564–4577, 2019.

[211] C. Xu, W. Zipfel, J. B. Shear, R. M. Williams, and W. W. Webb, "Multiphoton fluorescence excitation: new spectral windows for biological nonlinear microscopy." *Proceedings of the National Academy of Sciences*, vol. 93, no. 20, pp. 10 763–10 768, 1996.

[212] A. Fedorov, R. Beichel, J. Kalpathy-Cramer, J. Finet, J.-C. Fillion-Robin, S. Pujol, C. Bauer, D. Jennings, F. Fennessy, M. Sonka, J. Buatti, S. Aylward, J. V. Miller, S. Pieper, and R. Kikinis, "3d slicer as an image computing platform for the quantitative imaging network," *Magnetic Resonance Imaging*, vol. 30, no. 9, pp. 1323–1341, 2012.

[213] M. Harreguy, V. Marfil, N. Grooms, C. Gabel, S. Chung, and G. Haspel, "Ytterbium-doped fibre femtosecond laser offers robust operation with deep and precise microsurgery of c. elegans neurons," *Scientific Reports*, vol. 10, no. 1, pp. 1–7, 2020.

[214] C. J. Sheppard, "Multiphoton microscopy: a personal historical review, with some future predictions," *Journal of Biomedical Optics*, vol. 25, no. 1, p. 014511, 2020.

[215] A. Vogel and V. Venugopalan, "Mechanisms of pulsed laser ablation of biological tissues," *Chemical Reviews*, vol. 103, no. 2, pp. 577–644, 2003.

[216] A. Pitzschke, B. Lovisa, O. Seydoux, M. Haenggi, M. F. Oertel, M. Zellweger, Y. Tardy, and G. A. Wagnières, "Optical properties of rabbit brain in the red and near-infrared: changes observed under in vivo, postmortem, frozen, and formalin-fixated conditions," *Journal of Biomedical Optics*, vol. 20, no. 2, p. 025006, 2015.

[217] M. Mesradi, A. Genoux, V. Cuplov, D. Abi-Haidar, S. Jan, I. Buvat, and F. Pain, "Experimental and analytical comparative study of optical coefficient of fresh and frozen rat tissues," *Journal of Biomedical Optics*, vol. 18, no. 11, p. 117010, 2013.

[218] A. Yaroslavsky, P. C. Schulze, I. V. Yaroslavsky, R. Schober, F. Ulrich, and H. Schwarzmaier, "Optical properties of selected native and coagulated human brain tissues in vitro in the visible and near infrared spectral range," *Physics in Medicine & Biology*, vol. 47, no. 12, pp. 2059–2073, 2002.

[219] B. D. Lucas and T. Kanade, "An iterative image registration technique with an application to stereo vision," in *Proceedings of the 7th International Joint Conference on Artificial Intelligence - Volume 2*, 1981, p. 674–679.

[220] M. Kaya, A. Denasi, S. Scheggi, E. Agbahca, C. Yoon, D. H. Gracias, and S. Misra, "A multi-rate state observer for visual tracking of magnetic micro-agents using 2d slow medical imaging modalities," in *Proceedings of the IEEE/RSJ International Conference on Intelligent Robots and Systems (IROS)*, 2018, pp. 1–8.

[221] G. Collins, J. Federici, Y. Imura, and L. H. Catalani, "Charge generation, charge transport, and residual charge in the electrospinning of polymers: A review of issues and complications," *Journal of Applied Physics*, vol. 111, no. 4, p. 044701, 2012.

[222] Z. Wu, Y. Zhang, N. Ai, H. Chen, W. Ge, and Q. Xu, "Magnetic mobile microrobots for upstream and downstream navigation in biofluids with variable flow rate," *Advanced Intelligent Systems*, vol. 4, no. 7, p. 2100266, 2022.

[223] R. M. Boutilier, J. S. Park, and H. Lee, "High-speed two-photon laser scanning microscopy imaging of in vivo blood cells in rapid circulation at velocities of up to 1.2 millimeters per second," *Current Optics and Photonics*, vol. 2, no. 6, pp. 595–605, 2018.

[224] G. de Vito, P. Ricci, L. Turrini, V. Gavryusev, C. Müllenbroich, N. Tiso, F. Vanzi, L. Silvestri, and F. S. Pavone, "Effects of excitation light polarization on fluorescence emission in two-photon light-sheet microscopy," *Biomedical Optics Express*, vol. 11, no. 8, pp. 4651–4665, 2020.

[225] J. J. Huaroto, M. Richter, M. Malafaia, J. Kim, C. Kim, J.-O. Park, J. Sikorski, and S. Misra, "MagNeed–needle-shaped electromagnets

for localized actuation within compact workspaces," *IEEE Robotics and Automation Letters*, vol. 8, no. 6, pp. 3908–3915, 2023.

[226] X. Yan, Q. Zhou, M. Vincent, Y. Deng, J. Yu, J. Xu, T. Xu, T. Tang, L. Bian, Y.-X. J. Wang *et al.*, "Multifunctional biohybrid magnetite microrobots for imaging-guided therapy," *Science Robotics*, vol. 2, no. 12, p. eaaq1155, 2017.

[227] M. Ussia, M. Urso, M. Kratochvilova, J. Navratil, J. Balvan, C. C. Mayorga-Martinez, J. Vyskocil, M. Masarik, and M. Pumera, "Magnetically driven self-degrading zinc-containing cystine microrobots for treatment of prostate cancer," *Small*, vol. 19, no. 17, p. 2208259, 2023.

[228] J. Vyskocil, C. C. Mayorga-Martinez, E. Jablonska, F. Novotny, T. Ruml, and M. Pumera, "Cancer cells microsurgery via asymmetric bent surface au/ag/ni microrobotic scalpels through a transversal rotating magnetic field," *ACS Nano*, vol. 14, no. 7, pp. 8247–8256, 2020.

[229] Y. Li, D. Dong, Y. Qu, J. Li, S. Chen, H. Zhao, Q. Zhang, Y. Jiao, L. Fan, and D. Sun, "A multidrug delivery microrobot for the synergistic treatment of cancer," *Small*, vol. 19, no. 44, p. 2301889, 2023.

[230] M. Medina-Sánchez and O. G. Schmidt, "Medical microbots need better imaging and control," *Nature*, vol. 545, no. 7655, pp. 406–408, 2017.

[231] Y. Xiao, J. Zhang, B. Fang, X. Zhao, and N. Hao, "Acoustics-actuated microrobots," *Micromachines*, vol. 13, no. 3, p. 481, 2022.

[232] H. Zhou, C. C. Mayorga-Martinez, S. Pané, L. Zhang, and M. Pumera, "Magnetically driven micro and nanorobots," *Chemical Reviews*, vol. 121, no. 8, pp. 4999–5041, 2021.

[233] H. Shen, S. Cai, Z. Wang, Z. Ge, and W. Yang, "Magnetically driven microrobots: Recent progress and future development," *Materials & Design*, vol. 227, p. 111735, 2023.

[234] X. Yi, L. Guo, Q. Zeng, S. Huang, D. Wen, C. Wang, Y. Kou, M. Zhang, H. Li, L. Wen *et al.*, "Magnetic/acoustic dual-controlled

microrobot overcoming oto-biological barrier for on-demand multidrug delivery against hearing loss," *Small*, vol. 20, no. 44, p. 2401369, 2024.

[235] F. C. Landers, L. Hertle, V. Pustovalov, D. Sivakumaran, C. M. Oral, O. Brinkmann, K. Meiners, P. Theiler, V. Gantenbein, A. Veciana *et al.*, "Clinically ready magnetic microrobots for targeted therapies," *Science*, vol. 390, no. 6774, pp. 710–715, 2025.

[236] S. Pane, M. Zhang, V. Iacovacci, L. Zhang, and A. Menciassi, "Contrast-enhanced ultrasound tracking of helical propellers with acoustic phase analysis and comparison with color doppler," *APL Bioengineering*, vol. 6, no. 3, 2022.

[237] S. Martel, M. Mohammadi, O. Felfoul, Z. Lu, and P. Pouponneau, "Flagellated magnetotactic bacteria as controlled mri-trackable propulsion and steering systems for medical nanorobots operating in the human microvasculature," *The International journal of robotics research*, vol. 28, no. 4, pp. 571–582, 2009.

[238] A. C. Bakenecker, A. von Gladiss, H. Schwenke, A. Behrends, T. Friedrich, K. Lüdtke-Buzug, A. Neumann, J. Barkhausen, F. Wegner, and T. M. Buzug, "Navigation of a magnetic micro-robot through a cerebral aneurysm phantom with magnetic particle imaging," *Scientific Reports*, vol. 11, no. 1, p. 14082, 2021.

[239] Z. Chen and M. M. Sánchez, "Microrobots in gynaecological care and reproductive medicine," *Nature Reviews Electrical Engineering*, vol. 1, no. 12, pp. 759–761, 2024.

[240] J. Jang, J. Kim, H. J. Lee, and J. H. Chang, "Transrectal ultrasound and photoacoustic imaging probe for diagnosis of prostate cancer," *Sensors*, vol. 21, no. 4, p. 1217, 2021.

[241] Q. Zhang, C. Wu, K. Long, C. Huang, X. Zhong, X. Bai, L. Cheng, L. Jin, Y. Liang, and B.-O. Guan, "In vivo endoscopic ultrasound imaging with a rotational-scanning, all-optical ultrasound probe," *Optics Letters*, vol. 48, no. 7, pp. 1926–1929, 2023.

[242] M. Gu, X. Gan, A. Kisteman, and M. G. Xu, "Comparison of penetration depth between two-photon excitation and single-photon excitation in imaging through turbid tissue media," *Applied Physics Letters*, vol. 77, no. 10, pp. 1551–1553, 2000.

[243] F. Wang, Y. Zhong, O. Bruns, Y. Liang, and H. Dai, "In vivo NIR-II fluorescence imaging for biology and medicine," *Nature Photonics*, vol. 18, no. 6, pp. 535–547, 2024.

[244] D. Y. Kim, K. Hwang, J. Ahn, Y.-H. Seo, J.-B. Kim, S. Lee, J.-H. Yoon, E. Kong, Y. Jeong, S. Jon *et al.*, "Lissajous scanning two-photon endomicroscope for in vivo tissue imaging," *Scientific Reports*, vol. 9, no. 1, p. 3560, 2019.

[245] Y. Liu, J. L. Huang, and X. Li, "Focus-tunable two-photon fiberscope enabling in vivo imaging at selected depths," *Optics Letters*, vol. 50, no. 13, pp. 4194–4197, 2025.

[246] A. D. C. Fonseca, C. Gluck, J. Droux, Y. Ferry, C. Frei, S. Wegener, B. Weber, M. El Amki, and D. Ahmed, "Acoustic trapping and navigation of microrobots in the mouse brain vasculature," *bioRxiv*, pp. 2023–01, 2023.

[247] M. S. Sidhu and N. Dhingra, "Ablation of materials using femtosecond lasers and electron beams," in *Terahertz, Ultrafast Lasers and Their Medical and Industrial Applications*. IntechOpen, 2022.

[248] L. J. Mortensen, C. Alt, R. Turcotte, M. Masek, T.-M. Liu, D. C. Côté, C. Xu, G. Intini, and C. P. Lin, "Femtosecond laser bone ablation with a high repetition rate fiber laser source," *Biomedical Optics Express*, vol. 6, no. 1, pp. 32–42, 2014.

[249] M. S. Sidhu, M.-Y. Choi, S.-Y. Woo, H.-K. Lee, H.-S. Lee, K.-J. Kim, S. C. Jeoung, J.-S. Choi, C.-K. Joo, and I.-H. Park, "Femtosecond laser-assisted selective reduction of neovascularization in rat cornea," *Lasers in Medical Science*, vol. 29, no. 4, pp. 1417–1427, 2014.

[250] Y. Wu, Y. Leng, J. Xi, and X. Li, "Scanning all-fiber-optic endomicroscopy system for 3D nonlinear optical imaging of biological tissues," *Optics Express*, vol. 17, no. 10, pp. 7907–7915, 2009.

[251] K. Murari, Y. Zhang, S. Li, Y. Chen, M.-J. Li, and X. Li, "Compensation-free, all-fiber-optic, two-photon endomicroscopy at 1.55 μm," *Optics Letters*, vol. 36, no. 7, pp. 1299–1301, 2011.

[252] B. Camli, L. Andrus, A. Roy, B. Mishra, C. Xu, I. Georgakoudi, T. Tkaczyk, and A. Ben-Yakar, "Two photon imaging probe with highly efficient autofluorescence collection at high scattering and deep imaging conditions," *Biomedical Optics Express*, vol. 15, no. 5, pp. 3163–3182, 2024.

[253] A. Carovac, F. Smajlovic, and D. Junuzovic, "Application of ultrasound in medicine," *Acta Informatica Medica*, vol. 19, no. 3, p. 168, 2011.

[254] L. Li, L. Zhu, C. Ma, L. Lin, J. Yao, L. Wang, K. Maslov, R. Zhang, W. Chen, J. Shi *et al.*, "Single-impulse panoramic photoacoustic computed tomography of small-animal whole-body dynamics at high spatiotemporal resolution," *Nature biomedical engineering*, vol. 1, no. 5, p. 0071, 2017.

[255] L. Lin, P. Hu, J. Shi, C. M. Appleton, K. Maslov, L. Li, R. Zhang, and L. V. Wang, "Single-breath-hold photoacoustic computed tomography of the breast," *Nature communications*, vol. 9, no. 1, p. 2352, 2018.

[256] L. Li and L. V. Wang, "Recent advances in photoacoustic tomography," *BME Frontiers*, vol. 2021, p. 9823268, 2021.

[257] S. Harvell-Smith, L. D. Tung, and N. T. K. Thanh, "Magnetic particle imaging: tracer development and the biomedical applications of a radiation-free, sensitive, and quantitative imaging modality," *Nanoscale*, vol. 14, no. 10, pp. 3658–3697, 2022.

[258] M. Goetz and T. D. Wang, "Molecular imaging in gastrointestinal endoscopy," *Gastroenterology*, vol. 138, no. 3, pp. 828–833, 2010.

[259] J. M. Jabbour, M. A. Saldua, J. N. Bixler, and K. C. Maitland, "Confocal endomicroscopy: instrumentation and medical applications," *Annals of biomedical engineering*, vol. 40, no. 2, pp. 378–397, 2012.

[260] M. J. Gora, M. J. Suter, G. J. Tearney, and X. Li, "Endoscopic optical coherence tomography: technologies and clinical applications," *Biomedical optics express*, vol. 8, no. 5, pp. 2405–2444, 2017.

[261] H. Guo, Y. Li, W. Qi, and L. Xi, "Photoacoustic endoscopy: A progress review," *Journal of Biophotonics*, vol. 13, no. 12, p. e202000217, 2020.

[262] H. Han, X. Ma, W. Deng, J. Zhang, S. Tang, O. S. Pak, L. Zhu, E. Criado-Hidalgo, C. Gong, E. Karshalev *et al.*, "Imaging-guided bioresorbable acoustic hydrogel microrobots," *Science Robotics*, vol. 9, no. 97, p. eadp3593, 2024.

[263] J.-Y. Bouguet *et al.*, "Pyramidal implementation of the affine lucas kanade feature tracker description of the algorithm," *Intel corporation*, vol. 5, no. 1-10, p. 4, 2001.

[264] J. Shi and C. Tomasi, "Good features to track," in *1994 Proceedings of IEEE Conference on Computer Vision and Pattern Recognition*. IEEE, 1994, pp. 593–600.

[265] J. Powers and F. Kremkau, "Medical ultrasound systems," *Interface Focus*, vol. 1, no. 4, pp. 477–489, 2011.

[266] F. Šuligoj, C. M. Heunis, S. Mohanty, and S. Misra, "Intravascular tracking of micro-agents using medical ultrasound: Towards clinical applications," *IEEE Transactions on Biomedical Engineering*, vol. 69, no. 12, pp. 3739–3747, 2022.

[267] R. Ansari, E. Z. Zhang, A. E. Desjardins, and P. C. Beard, "All-optical forward-viewing photoacoustic probe for high-resolution 3d endoscopy," *Light: Science & Applications*, vol. 7, no. 1, p. 75, 2018.

[268] Y. Tang, S. Anandasabapathy, and R. Richards-Kortum, "Advances in optical gastrointestinal endoscopy: a technical review," *Molecular Oncology*, vol. 15, no. 10, pp. 2580–2599, 2021.

[269] Z. He, P. Wang, Y. Liang, Z. Fu, and X. Ye, "Clinically available optical imaging technologies in endoscopic lesion detection: current status and future perspective," *Journal of Healthcare Engineering*, vol. 2021, no. 1, p. 7594513, 2021.

[270] O. C. Mora, P. Zanne, L. Zorn, F. Nageotte, N. Zulina, S. Gravelyn, P. Montgomery, M. De Mathelin, B. Dallemagne, and M. J. Gora, "Steerable oct catheter for real-time assistance during teleoperated endoscopic treatment of colorectal cancer," *Biomedical Optics Express*, vol. 11, no. 3, pp. 1231–1243, 2020.

[271] W. Liang, H.-C. Park, K. Li, A. Li, D. Chen, H. Guan, Y. Yue, Y.-T. A. Gau, D. E. Bergles, M.-J. Li *et al.*, "Throughput-speed product augmentation for scanning fiber-optic two-photon endomicroscopy," *IEEE Transactions on Medical Imaging*, vol. 39, no. 12, pp. 3779–3787, 2020.

[272] C. Wang, H. Liu, J. Ma, H. Cui, Y. Li, D. Wu, Y. Hu, D. Wu, Q. Fu, L. Liang *et al.*, "Spiral scanning fiber-optic two-photon endomicroscopy with a double-cladding antiresonant fiber," *Optics Express*, vol. 29, no. 26, pp. 43 124–43 135, 2021.

[273] H. Guan, W. Liang, A. Li, Y.-T. A. Gau, D. Chen, M.-J. Li, D. E. Bergles, and X. Li, "Multicolor fiber-optic two-photon endomicroscopy for brain imaging," *Optics Letters*, vol. 46, no. 5, pp. 1093–1096, 2021.

[274] C. Wang, H. Liu, J. Ma, Q. Fu, Y. Li, Y. Chen, Y. Gao, J. Tian, X. Luo, F. Yu, C. Zhao, R. Wu, A. Wang, and L. Feng, "Lensed fiber-optic two-photon endomicroscopy for field-of-view enhancement," *Photonics*, vol. 10, no. 3, p. 342, 2023.

[275] U. Nam, S. Lee, A. Ahmad, H.-g. Yi, and J. S. Jeon, "Microphysiological systems as organ-specific in vitro vascular models for disease modeling," *BioChip Journal*, vol. 18, no. 3, pp. 345–356, 2024.

[276] J. Lin, Q. Cong, and D. Zhang, "Magnetic microrobots for in vivo cargo delivery: A review," *Micromachines*, vol. 15, no. 5, p. 664, 2024.

[277] J. G. Fujimoto, C. Pitris, S. A. Boppart, and M. E. Brezinski, "Optical coherence tomography: an emerging technology for biomedical imaging and optical biopsy," *Neoplasia*, vol. 2, no. 1-2, pp. 9–25, 2000.

[278] X. Hui, M. O. Malik, and M. Pramanik, "Looking deep inside tissue with photoacoustic molecular probes: a review," *Journal of biomedical optics*, vol. 27, no. 7, pp. 070 901–070 901, 2022.

[279] L. G. Rodriguez, S. J. Lockett, and G. R. Holtom, "Coherent anti-stokes raman scattering microscopy: A biological review," *Cytometry Part A: The Journal of the International Society for Analytical Cytology*, vol. 69, no. 8, pp. 779–791, 2006.

[280] J.-X. Cheng and X. S. Xie, *Coherent Raman scattering microscopy*. CRC press, 2016.

[281] H. Yu, J. Park, K. Lee, J. Yoon, K. Kim, S. Lee, and Y. Park, "Recent advances in wavefront shaping techniques for biomedical applications," *arXiv preprint arXiv:1502.05475*, 2015.

[282] I. M. Vellekoop, "Feedback-based wavefront shaping," *Optics express*, vol. 23, no. 9, pp. 12 189–12 206, 2015.

[283] R. Horstmeyer, H. Ruan, and C. Yang, "Guidestar-assisted wavefront-shaping methods for focusing light into biological tissue," *Nature photonics*, vol. 9, no. 9, pp. 563–571, 2015.

[284] Z. Yu, H. Li, T. Zhong, J.-H. Park, S. Cheng, C. M. Woo, Q. Zhao, J. Yao, Y. Zhou, X. Huang *et al.*, "Wavefront shaping: a versatile tool to conquer multiple scattering in multidisciplinary fields," *The Innovation*, vol. 3, no. 5, 2022.

[285] A. Lombardini, V. Mytskaniuk, S. Sivankutty, E. R. Andresen, X. Chen, J. Wenger, M. Fabert, N. Joly, F. Louradour, A. Kudlinski *et al.*, "High-resolution multimodal flexible coherent raman endoscope," *Light: Science & Applications*, vol. 7, no. 1, p. 10, 2018.

[286] A. Lukic, S. Dochow, H. Bae, G. Matz, I. Latka, B. Messerschmidt, M. Schmitt, and J. Popp, "Endoscopic fiber probe for nonlinear spectroscopic imaging," *Optica*, vol. 4, no. 5, pp. 496–501, 2017.

[287] F. Akhoundi, Y. Qin, N. Peyghambarian, J. K. Barton, and K. Kieu, "Compact fiber-based multi-photon endoscope working at 1700 nm," *Biomedical optics express*, vol. 9, no. 5, pp. 2326–2335, 2018.

[288] G. Hall, W. Liang, Z. M. Bhujwalla, and X. Li, "Shg fiberscopy assessment of collagen morphology and its potential for breast cancer optical histology," *IEEE Transactions on Biomedical Engineering*, vol. 71, no. 8, pp. 2414–2420, 2024.

[289] Lys Medical, "Iriscope," accessed: October 20, 2026. [Online]. Available: https://lysmedical.com/iriscope/

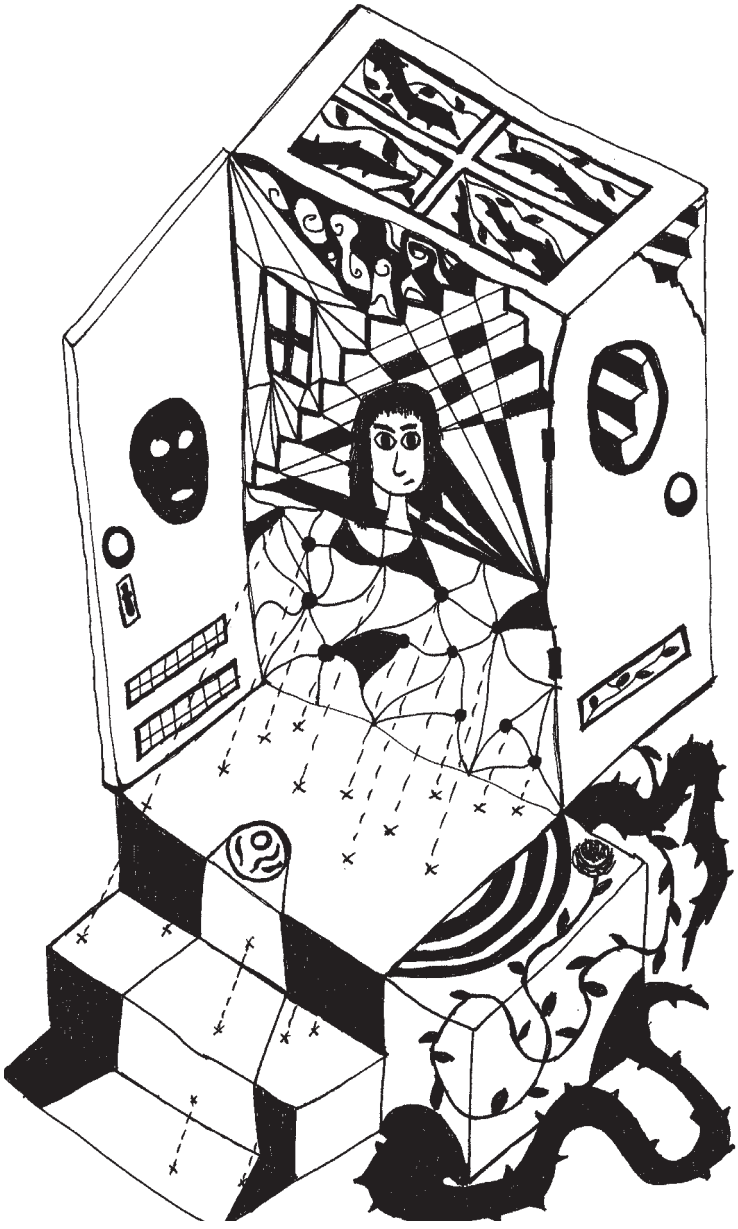
[290] H. Ruan, T. Haber, Y. Liu, J. Brake, J. Kim, J. M. Berlin, and C. Yang, "Focusing light inside scattering media with magnetic-particle-guided wavefront shaping," *Optica*, vol. 4, no. 11, pp. 1337–1343, 2017.

[291] B. Thuilot, P. Martinet, L. Cordesses, and J. Gallice, "Position based visual servoing: keeping the object in the field of vision," in *Proceedings 2002 IEEE International Conference on Robotics and Automation (Cat. No. 02CH37292)*, vol. 2. IEEE, 2002, pp. 1624–1629.

[292] L. Yang and L. Zhang, "Motion control in magnetic microrobotics: From individual and multiple robots to swarms," *Annual Review of Control, Robotics, and Autonomous Systems*, vol. 4, no. 1, pp. 509–534, 2021.

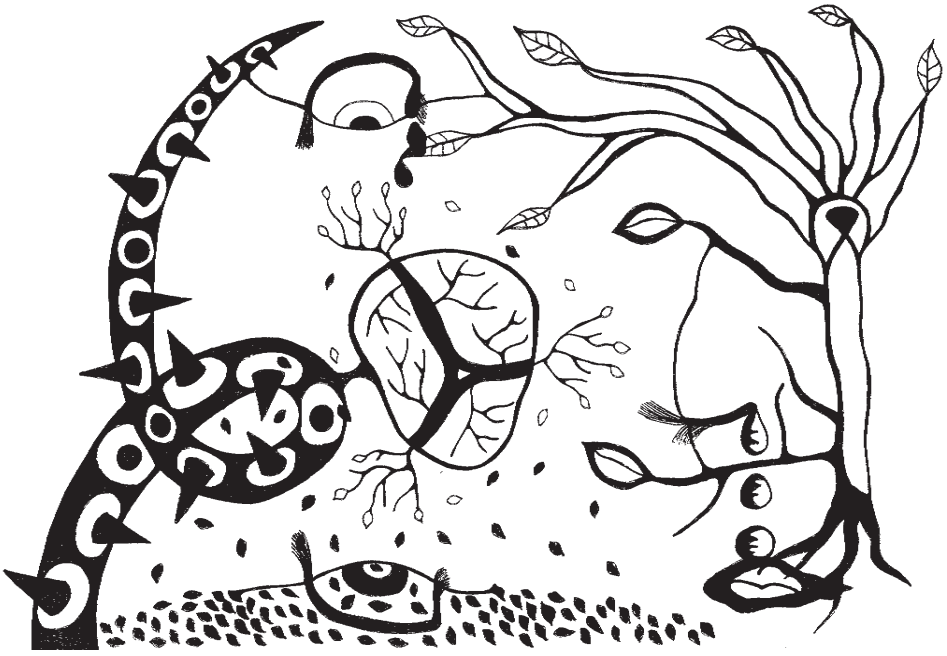
[293] P. Erkoc, I. C. Yasa, H. Ceylan, O. Yasa, Y. Alapan, and M. Sitti, "Mobile microrobots for active therapeutic delivery," *Advanced Therapeutics*, vol. 2, no. 1, p. 1800064, 2019.

[294] D. Zhang, T. E. Gorochowski, L. Marucci, H.-T. Lee, B. Gil, B. Li, S. Hauert, and E. Yeatman, "Advanced medical micro-robotics for early diagnosis and therapeutic interventions," *Frontiers in Robotics and AI*, vol. 9, p. 1086043, 2023.



In the Andean worldview, the conclusion of a journey is not a finality, but a PACHAKUTI*—a cosmic turning point where navigating the unknown reconstitutes the self.*

— JJJHS



Acknowledgments

To those reading these acknowledgments, whether out of scientific curiosity, friendship, or simply to find your name: thank you for being here. Over the past few years, I have spent much of my time reading, conducting experiments, and exploring new ideas. Yet what I will remember most are the people who made this work possible and these years meaningful.

First, I thank my promotor, **Prof. Sarthak Misra**, for your trust and for giving me the opportunity to pursue a PhD. From you, I learned to think carefully about what I wanted to communicate and how every detail in a figure, presentation, or piece of writing should serve that purpose. I also learned to take initiative, find my own way through problems, and reach out to the right people when I needed help. These lessons have shaped both the way I approached my work and the way I supervised students. Thank you also for your availability and the time you devoted to reviewing my work. From storyboards and paper drafts to this thesis, your prompt feedback made each round of revisions smoother and helped me keep moving forward. I also thank **Prof. Gert-Willem Römer** and **Prof. Jutta Arens** for their guidance and feedback, particularly during the final stages of preparing this thesis. I am grateful to the members of my doctoral committee for the time they devoted to assessing my thesis.

Before I arrived in Enschede, several people helped me find my way into research. **Emir**, you helped me take my first steps in scientific research in Peru and publish my first paper. Your recommendation letters also supported my application for the scholarship that took me to France. **Cédric** and **Kanty**, thank you for welcoming me into your laboratory during the first year of my master's. Later, **Pierre**, you placed your trust in me and opened the doors of your laboratory in Brussels for my master's thesis. I am grateful to each of you for these opportunities.

My years at SRL brought together science, friendship, music, and more than a few stories that probably belong outside a laboratory report. **Michiel**, as the first PhD student in MAESTRO, you were among my first contacts at SRL while I was still in Belgium. From our early video call to our "smol yoses", research discussions, and the quieter days after our more senior colleagues left, we shared good moments. I will certainly remember our failed

attempt to ride one bicycle home after a night out! My best wishes to you and Jessica. **Yu-Hsiang**, we went from that first video call to sharing an office, research frustrations, and countless conversations about life. I loved discovering that you knew Tatsuro Yamashita and considered him a classic. Your German exclamations and willingness to join our breaks as our favourite non-smoker made many days memorable. I am glad to see the life you and Tra have built together, and honored to have you as my paranymph. **Sumit** and **Christoff**, you were the first to welcome me in person, and we connected through music almost immediately. **Sumit**, our post-rock conversations led me to discover Indian bands such as Parekh & Singh, Peter Cat Recording Co., and Mad Orange Fireworks. I will never forget the night Ritwick's bicycle and I both ended up in a pond. You returned with Venkat and Ritwick to retrieve the bicycle, then took me home, lent me clothes, and put on Opeth while mine dried. My phone, unfortunately, did not survive. **Christoff**, I remember your hand-rolled cigarettes, and it is exciting to see what you have built with Flux Robotics. Then there was our unofficial *YOS band*: **Luigi** on guitar and vocals, Christoff on keyboards, Sumit on drums, and me on guitar or bass. Thursday jams at Vrijhof and our performance at Tankstation remain among my favourite memories of Enschede. **Luigi**, you also introduced me to nonlinear optics, which later became central to my research. I have not forgotten that you lent me money when I first arrived and could not yet access my own funds. Thank you for the science and your generosity. **Mert**, during our first video call, you explained things so effortlessly that I wondered whether you were a genius or I was completely lost. Your electrospinning tutorials taught me that the fabrication protocol came first; baklava or ice cream had to wait until afterwards. From electrospinning and spectrofluorometry to fluorescence microscopy, HeLa cells, and spheroids, your help supported several of my studies. I also appreciated our discussions about your own work. Even after you left SRL, the mysterious USB drive with laboratory backups that I found in Z213 suggested you had thought of everything. **Jakub**, I admired your ability to integrate complex systems long before I could make sense of your barely commented code. Learning EtherCAT while taking over MagNeed was quite an introduction. I also remember the gatherings at your home with Janine, conversations ranging from science to nonsense, and your unmistakable, loud "Pardon?!", which helped sharpen my English listening skills. **Hugo**, or *Professeur Daguerre*, I am

glad we have stayed in touch. Seeing you become a professor in Besançon, where I did my master's, has been a particular pleasure. Thank you for bringing me Pontarlier and my diploma, and for the lively debates about French cheese and TGV. **Theodosia**, thank you for inviting me to be your paranymph, my first time in that role, and for our brainstorming sessions around the demonstration for your final SRL paper. I still fondly remember trying Pani Puri for the first time at your place. **Venkat**, It has been impressive to see the research you are developing with talented students. I must also mention your cat, for whom I have always had a soft spot. To **Chen, Zhengya, Chuang, Zihan, Kaixuan, and Zhuoyue**, thank you for welcoming me to the former Groningen branch of SRL, defeating me at table tennis and pool, and introducing me to some exceptionally spicy Thai food. **Adriana**, I remember your curiosity after my research presentation there, when you were still considering your next steps. It was a pleasure to see you return as a PhD colleague. **Lukas** and **Simon**, I remember our first drinks at Café Het Bolwerk and have enjoyed watching your research develop. Simon's mechanisms and Lukas's enormous robot continue to impress me. Good luck with the final stages of your PhDs. **Amine**, I have always admired your support for your wife's artistic work, and I hope you both keep pursuing what you love. **Franco**, I still wonder how we survived watching Argentina face the Netherlands in a bar full of Dutch supporters during the 2022 World Cup. I also remember **Hellen** with affection; I am grateful our paths crossed. **Yuxin**, thank you for making time to meet and discuss our paper, and for patiently hearing out my sometimes naive ideas about how to respond to the reviewers. I hope the final stages of your PhD go well. **Antonio**, I appreciate your thoughtful manner, and your work on new directions in fluorescence means I still have someone at SRL who speaks my scientific language. **Vihang**, it was good to help you settle in, even if I was often a busy buddy. Keep pursuing those creative designs. **Tao**, I enjoyed our honest conversations about your research and my defense preparations, and I hope you achieve what you are working towards. **Zhen**, all the best as you begin your PhD.

Several people kept our work running behind the scenes. **Rob**, you always seemed able to get whatever we needed, and your laugh was unmistakable in the corridors. **Jeanine**, your ability to manage Sarthak's schedule and untangle administrative problems was remarkable. **Wendy**, thank you for helping me with the final arrangements after taking over

SRL's administrative responsibilities. **Yolanda** and **Lianne**, thank you for always being willing to help.

To my colleagues across the Biomechanical Engineering Department: **Ander**, speaking Spanish with you made my first days here easier. **Dennis**, thank you for sharing sweets and mandarins; I even grew used to the white noise from your laptop. **Hein**, I always enjoyed your questions about Maxwell. Those lighthearted moments of canine updates provided the perfect antidote to the stress of the PhD.

To the students I have supervised, working with you taught me to adapt my guidance to different interests and ways of approaching research. **Dionne**, your independence and impressive programming skills, back in the days before ChatGPT could come to our rescue, made working with you a pleasure. Our work on non-magnetic fields started with you. **Anna**, I always enjoyed our conversations after research update meetings. I appreciated your enthusiasm for robotics and your persistence when experiments did not turn out as we had hoped. **Guillem**, during your short stay, you helped us address an important question: where could our two-photon endomicroscopy probe actually be applied? **Nicholas**, your motivation and interests in microrobotics, computational simulations, and artificial intelligence made supervising you both challenging and rewarding. Exploring generative adversarial networks together was exciting, and your results provided an important foundation for our subsequent deep-learning paper. **Cátia**, your interest in 3D printing helped us develop prototypes for our experimental characterizations. **Ronalt**, finding the direction of your project took some exploration, and your work on lens-in-fiber systems produced interesting results. Finally, **Jasper**, I have enjoyed shaping your research project with you and hearing about the games you develop with your girlfriend. It has been good to see your progress, and I look forward to seeing where our experiments take us.

My research also took me beyond SRL to the Chair of Laser Processing. **Christian**, I appreciated your willingness to discuss my experiments and share your own work, always with your characteristic directness. **Martijn**, thank you for the discussions that helped improve two of my papers. **Matthias**, I am particularly grateful for your help in getting in touch with Gert-Willem so that he could review my thesis. Your support at that critical stage meant a lot to me. **Hasib**, I fondly remember crossing paths in the laboratory outside regular working hours. **Daniel**, I always enjoyed

our conversations as we switched between Spanish and English. **Namitha**, it was good to catch up during my later visits to the lab.

Ivo and **Femi**, when a power surge damaged the laser I had been using, you gave me access to your laser and laboratory space so I could continue my experiments. Thank you for your trust and for making it possible to complete this work. **Mohammad** and **Yeganeh**, thank you for your company during those literally dark days in the optics lab. Seeing your work in plasmonics and fundamental optics also gave me a welcome change of perspective. **Tom**, from confocal imaging at BIC to assembling my optical setup and later relocating it to Carré, you helped me at every stage. I could not have done much of that work without you. **Franck**, thank you for taking the time to guide me through a post-mortem rat dissection and for providing fixed tissue samples for my experiments. You are also one of the funniest French people I have ever met. **Nick**, thank you for the SEM images that supported several of my publications.

I also thank my colleagues from the former Optical Sciences Group. **José** and **Daniel**, thank you for our early discussions at SRL about optical fibers and tapers, and for later teaching me how to cleave fibers. You gave me my first cleaver, and I used that very same one to complete the final study in this thesis. **Alejandro** and **Luis**, thank you for the scientific conversations, Friday borrels at Carré, and the time we spent together at my place and in the city center. **Alejandro**, I am especially grateful for offering me a place to stay for more than two weeks while I was moving. I will never forget our fusion of ceviche, tortillas, and shrimp. You also introduced me to chips with hot sauce, a combination I have enjoyed ever since. Through you, I also met **Carlos** and **Cheko**, whose friendship and willingness to help I greatly value.

In all my years in Enschede, I got to know just one fellow Peruvian: **Kevin**. Thank you for the gatherings with your EEMCS/DIAM friends, the evenings at your home, and for always inviting me to El Rico Latino. Dancing salsa there now and then reminded me that I needed no lessons. I also remember the move we somehow managed with your mini skateboard. Your birthday lomo saltado made the distance from Peru feel smaller.

My friends in Eindhoven (now in Best) gave me somewhere to escape the demands of the PhD. **Roy** and **Yuxshua**, we have known each other since school. After your years in São Paulo, who would have imagined we would reunite in the Netherlands? I will remember our spontaneous barbecues and

the meals and drinks we shared. Through you I met **Nicholas**, whose wide-ranging knowledge and love of Brazilian music have made our conversations a pleasure. **Yuxshua**, you also introduced me to Maggie, for which I will always be grateful. Our trips to London and Tromsø brought us closer, while our recent Phasmophobia nights made the final thesis rush more bearable. **Roy**, having you beside me as a paranymph means a lot. You have all been my family away from home.

Jorge y **Luis**, mis mejores amigos, gracias por estar siempre ahí. Siempre he podido contar con ustedes para conversar de lo que sea, con la confianza que dan tantos años de amistad. Recuerdo con mucho cariño cuando coincidimos en Amsterdam en 2021 y pudimos volver a pasar tiempo juntos. Hoy estamos en distintas partes del mundo, cada uno siguiendo su propio camino, pero la distancia no ha cambiado esa confianza. **Julio** y **Cintia**, gracias por esa amistad que no depende de hablar todos los días.

A mis queridos tíos, **Violeta, Raquel, Reinaldo, Bertha, Flor, Javier, Félix, Esaud, Juan, Edilberto, Manuela, Víctor, Jeanette, y Ruben**. Gracias por haber estado presentes de tantas maneras. A sus respectivas parejas y a mis primos, gracias también por los momentos compartidos y por el cariño que siempre he encontrado en nuestra familia.

A mis hermanos, gracias por su apoyo y por tantos recuerdos de infancia. Como hermano menor, aprendí de ustedes muchas de las cosas que sé hoy. **Efraín**, todavía me fascinan aquellos dibujos de Dragon Ball y recuerdo nuestros aviones hechos con cajas de pasta de dientes, no siempre para alegría de nuestras hermanas. **Regina y Paola**, gracias por enseñarme matemáticas, aunque nunca olvidaré mi confusión al aprender a despejar una incógnita y la respuesta de Paola: "¡Porque me conviene!" ¿Quién iba a decir que las matemáticas me acompañarían hasta aquí? A mis sobrinos, **Christina, Luciana, Marcelo, Paolo, Caetana y Pía**, me alegra verlos crecer, aunque sea desde lejos. **Marcelo**, mi ahijado, espero poder acompañarte en muchas de tus aventuras. Aunque no siempre encontremos tiempo para hablar, los tengo muy presentes.

A mi madre, **Rita**, gracias por estar pendiente de mí a lo largo de los años y por el cariño que me has dado. Guardo con amor los recuerdos del tocadiscos de casa y nuestros bailes al ritmo de Ram Jam, así como tu máquina de coser en la sala, que tanto despertaba mi curiosidad. Gracias también por tu ejemplo de perseverancia y por todo el esfuerzo que has hecho para salir adelante. Hoy reconozco parte de tu cariño en mi propia

manera de querer. Me alegra mucho que puedas compartir conmigo este momento.

A mi padre, **Juan**, a quien tanto admiro y extraño. Tus libros, tus dibujos, tu música y los objetos que dejaste en casa despertaron muchas preguntas en mí. Hoy en dia nadie sabe como llegó el recuerdo de la Estela Raimondi a casa, pero no puedo ignorar como siempre estuve girando la cabeza para encontrar los ojos entre sus figuras. No imaginaba entonces que, años después, esa fascinación encontraría un lugar en la identidad visual de esta tesis. Me habría encantado conversar contigo sobre lo que he descubierto y sobre la vida que estoy construyendo. En esa curiosidad que me acompaña sigo encontrando algo de ti.

Finalmente, **Maggie**, mi compañera de vida y aventuras. Compartir contigo estos últimos tres años ha cambiado mi manera de ver el mundo. He aprendido a mirarlo con más cariño, a disfrutar de las cosas sencillas y, sobre todo, a comprender que mi valor como persona va mucho más allá de mis títulos, publicaciones o logros. Todavía me hace sonreír recordar cómo nos conocimos en Ámsterdam y aquella primera cita en Zaandam, sin imaginar todo lo que terminaríamos compartiendo. Gracias por estar al otro lado del teléfono después de tantas jornadas agotadoras en el laboratorio, por escuchar pensamientos que difícilmente compartiría con alguien más y por recordarme que mañana siempre habrá otra oportunidad para volver a intentarlo. Admiro la fortaleza con la que afrontas tus propios desafíos y el cariño que, a pesar del trabajo y la distancia, sigues dedicando a nuestra relación y a Maxwell. Gracias también por mostrarme Barcelona y por sacarme tantas veces de casa. Desde una simple caminata por el Volkspark o el centro de Enschede hasta nuestros viajes a la costa Amalfitana y Santorini. Y cómo olvidar Tromsø, donde también cumplí mi sueño de ver las auroras boreales. ¡Qué afortunados hemos sido! Gracias por tu comprensión, incluso cuando nuestras vacaciones no fueron del todo vacaciones y mi laptop terminó acompañándonos más de una vez. Todo esto me recuerda por qué te sigo eligiendo cada día. Y a nuestro querido **Maxwell**, que llegó para cambiar nuestras vidas sin necesidad de decir una sola palabra. Gracias por las alegrías cotidianas y por enseñarnos que una familia también puede tener cuatro patas, mucho pelo y un cariño inmenso. No sé qué nos espera después de esta etapa, pero me hace feliz saber que estaremos juntos para descubrirlo. Los amo, y todavía nos quedan muchas aventuras por vivir.

About the author



Juan Julian Jesus Huaroto Sevilla was born on 30^{th} May 1992 in Trujillo, La Libertad, Peru. He received a degree in mechanical engineering from the Universidad Nacional de Ingeniería (National University of Engineering), Lima, Peru, in 2019. During his studies, he actively participated in student engineering competitions, including amateur rocketry (C'SPACE) and the HYDROCONTEST challenge for energy-efficient vessels, both held in France. He also worked on the design and modeling of soft robotic actuators at Universidad Peruana Cayetano Heredia (Cayetano Heredia University), Lima, before receiving the French-Peruvian scholarship "Alberto Benavides de La Quintana", which allowed him to complete a master's degree in automation and robotics at the Université Marie et Louis Pasteur, Besançon, France. During his master's, he completed research internships at two institutions. At the FEMTO-ST Institute (Franche-Comté Électronique Mécanique Thermique et Optique – Sciences et Technologies), France, he developed a system to characterize 4D-printed microrobots. At TIPS (Transfers, Interfaces and Processes), Université Libre de Bruxelles, Belgium, he designed a system to study fluid transport in artificial vascular networks inspired by the lymphatic system. In October 2021, he began his doctoral studies in the Surgical Robotics Laboratory at the University of Twente, The Netherlands, under the supervision of Prof. Sarthak Misra. His doctoral research covered areas of magnetic actuation and fluorescence imaging strategies for microrobotics.